Spring 2015

Development of a FAst Compton TELescope (FACTEL)

Manuel Grégory Julien
University of New Hampshire, Durham

DEVELOPMENT OF A FAST COMPTON TELESCOPE (FACTEL)

By

Manuel Julien

B. Sc. in Physics from University of Montréal (June 2000)

M. Sc. in Physics from University of Montréal (August 2003)

DISSERTATION

Submitted to the University of New Hampshire

in partial fulfillment

of the requirement for the degree of

Doctor of Philosophy

in

Physics

May 2015

This dissertation has been examined and approved in partial fulfillment of the requirements for the degree of Doctor of Philosophy in Physics by:

Dissertation Director, James M. Ryan, Professor of Physics

Mark L. McConnell, Professor of Physics

Karsten Pohl, Professor of Physics

James Connell, Associate Professor of Physics

Peter F. Bloser, Research Associate Professor of Physics

On December 22, 2014

Original approval signatures are on file with the University of New Hampshire Graduate School.

To my family and

my friends at the University of New Hampshire

ACKNOWLEDGMENTS

I would like to first thank my advisor James Ryan for inviting me to UNH to develop the FACTEL prototype, and for his guidance and support. Through his wisdom and experience, Jim assured guidance over the grand lines of the project, and support in stressful times. Secondly, I would like to thank Peter Bloser, the senior research scientist in charge of the project. As the responsible for the project, Peter was the cornerstone that provided me with guidance, help and support on a daily basis during the development of the instrument. As I did the "actual work" of developing the instrument, Peter was the supervisor with which I would discuss all my results.

On the laboratory side, the first person to thank is Jason Legere. Jason designed the instrument and provided all the hardware experience and knowledge to actually build FACTEL. As Jim was the mentor for support and guiding the project, Peter the mentor behind the physics, data analysis and simulations, Jason was the mentor for everything material in the laboratory. Whether it be sewing FRP beams, gluing detectors, tweaking electronic boards, setting NIM modules or dealing with the aDAQ computers, Jason is the one who thought and supervised me for all these steps. Finally I would like to thank Christopher Bancroft, the electronics engineer who built our cards and helped us with everything related to electronics.

I would also want to thank Mark McConnell, the third voice of the project "high-council" he formed with Jim and Peter. His third opinion, advice, and experience were of course invaluable in steering the project towards its ultimate success.

I thank my family for their unfailing support, my mother who came visit me here in the US regularly, my father, my brother and his wife, and of course my nephew which might not have helped much for the development of FACTEL, but just made me an uncle and gave me another reason to finish this work and keep working on bettering our world.

To finish I would like to thank the University of New Hampshire and its Physics department professors who have welcomed me here in the USA to give me the chance to complete a Ph. D. in Physics and allow me to work on the FACTEL project. The competence and devotion of all of the University professors and personnel to the transmission of knowledge is commendable and admirable, and I thank them all for all they have thought me.

I also acknowledge NASA Grant NNH07ZDA001N-APRA.

TABLE OF CONTENTS

LIST OF TABLES

LIST OF FIGURES

PHYSICAL CONSTANTS

(Particle Physics Booklet, July 2010)

Quantity	Symbol	Value
Speed of light in vacuum	c	299 792 458 m s^{-1}
Planck constant	h	6.626 068 96(33)×10^{-34} J s
Electron charge magnitude	e	1.602 176 478(40)×10^{-19} C
Electron-Volt	eV	1.602 176 478(40)×10^{-19} J
Electron Mass	m_e	0.510 998910(13) MeV/c^2
Pi	π	3.141 592 653 589 793…
Permeability of free space	μ_0	4π×10^{-7} N A^{-2}
Permittivity of free space	$\varepsilon_0=1/\mu_0 c^2$	8.854 187817...×10^{-12} F m^{-1}
Boltzmann constant	k_B	1.380 648 8(13)×10^{-23} J K^{-1}
Wien's displacement constant	b	2.897 768 5(51)×10^{-3} m K
Barn	$barn$	1×10^{-28} m^2
Thomson cross section	σ_T	0.665 245 855 8(27) barn

ABSTRACT

Development of a FAst Compton TELescope (FACTEL)

by

Manuel Julien

University of New Hamsphire, May 2015

This dissertation describes the development of a FAst Compton TELescope (FACTEL) instrument. It is designed to be the prototype of a larger Advanced Scintillators COmpton Telescope (ASCOT) aimed for general astronomical observations in the medium energy gamma-ray range between 500 keV and 50 MeV. This dissertation presents the instrument and the observation results from the successful 2011 balloon campaign which took place on September 23rd and 24th at Fort Sumner, New Mexico (Flight 624N). The instrument was at float altitude for twenty-six hours at an average 36 km altitude. The FACTEL prototype achieved a 1-ns Time-of-flight resolution between the two detectors layers of the instrument.

INTRODUCTION

The medium-energy gamma-ray range, from 500 keV to 10 MeV, is an exciting observational window through which numerous astronomical phenomena involving nuclear and relativistic particle interactions can be studied. This thesis will present the development of a FAst Compton TELescope (FACTEL), the prototype for a next generation instrument aimed at studying these phenomena.

Most photons emitted by the production and destruction of many elements and their isotopes have energies within the 500 keV to 10 MeV window, while charged particles accelerated within the most extreme environments will also emit radiation within that energy range. Sources emitting medium-energy gamma rays extend from our atmosphere to cosmological objects. Terrestrial gamma-ray flashes (TGF) in the Earth's atmosphere, solar flares, isotopes in moons and asteroids, supernovae, their remnants, isotopes diffusing in the galactic plane, positrons, neutrons, neutron stars, pulsars, black holes, binary systems with a compact object, gamma-ray bursts (GRB) and active galactic nuclei (AGN) are all among the many natural astronomical sources that emit radiation within the MeV range.

Instruments capable of opening that window, such as the COMPton TELescope (COMPTEL) [1] instrument onboard the Compton Gamma-Ray Observatory (CGRO), have been developed to study this vast array of sources. The observational difficulty in this energy range is that the instrument itself, as well as the Earth's atmosphere, are strong radiation sources. The challenge of MeV astronomy is to

prevent as much as possible the intense background present from contaminating the data. What ultimately limited the COMPTEL instrument was not observational time but background in the data [2].

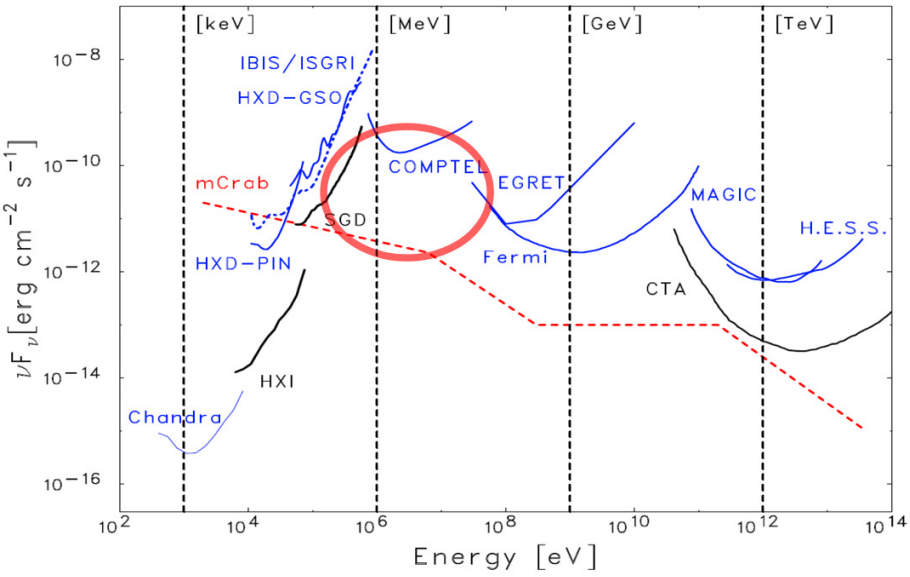

Figure I.1: Compared sensitivities of gamma-ray instruments, the red ellipse shows the sensitivity hole between 500 keV and 50 MeV. [6]

This intense background limits the sensitivity of instruments and figure I.1 highlights the so-called "sensitivity hole" in the MeV band. At lower energies, X rays can be focused and instruments can be relatively easily shielded from surrounding radiation, leading to the excellent sensitivities of instruments such as the Chandra X-ray Observatory [3,4]. For energies above 100 MeV, the scarcity of sources in that range means instruments such as the Fermi Gamma-ray Space Telescope [5] have a lower background environment allowing the sensitivity it achieved. However, the intense background in the 500 keV to 50 MeV band has left instruments making observations in that energy band not as sensitive compared to instruments observing other energy bands. In fact, as of today no instrument has exceeded COMPTEL sensitivity within that band (COMPTEL was launched in 1991 and deorbited in 2000).

Sensitivity is a key aspect of astronomical instruments because it permits the discovery of new weaker sources. A sensitivity improvement by one order of magnitude has always been a very exciting prospect for any astronomy branch because it unveils a whole new domain to study, with new sources being discovered and allowing more refined observations of already known sources. Still, no progress has been accomplished in medium-energy gamma-ray observations for the last two decades because of the intense background instruments have to face.

The answer to the sensitivity hole background problem has finally come with the recent development of so-called fast and bright scintillators [7]. Lanthanum bromide ($LaBr_3$:Ce) has a timing figure of merit five times faster than sodium iodine (NaI:Tl) (0.5 vs 2.6, see eq. 3.1) which was used for COMPTEL. This offers the prospect of substantially improving the Time-of-Flight (ToF) background rejection technique used by Compton telescopes, while providing excellent energy resolution. Improving the resolution of the Time-of-Flight technique leads to better background rejection (see sections 2.6.2 and 3.1), which leads to an improved signal to noise ratio in the data, leading to an improved sensitivity for the instrument. Thus, a ToF resolution improvement would directly lead to new Compton telescopes with a multiple factor sensitivity improvement over COMPTEL, filling the sensitivity hole.

Ultimately, our goal is to provide the scientific community with a new instrument with an unprecedented sensitivity that will unveil one further layer of our understanding of our Universe. Our goal is to bring MeV astronomy on par with GeV astronomy, a goal illustrated in figures I.2 and I.3.

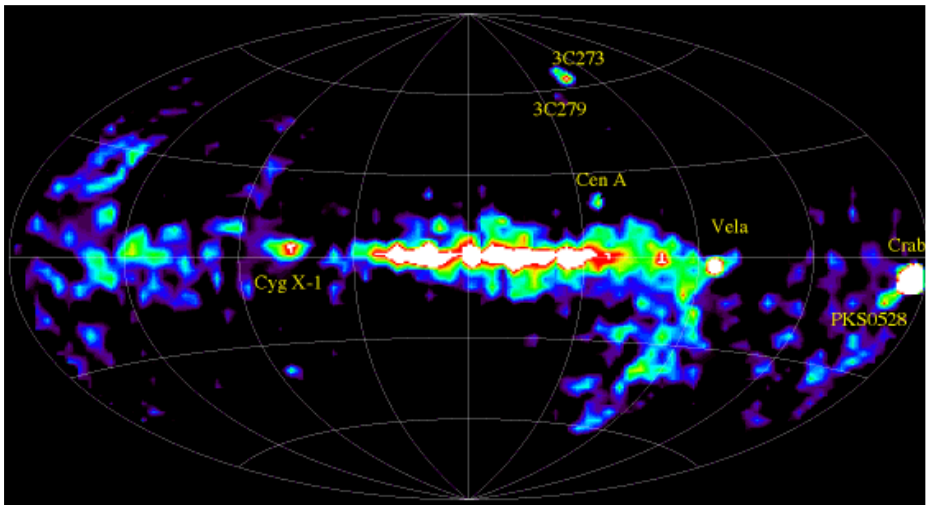

Figure I.2: COMPTEL 1 to 30 MeV All-Sky Map, the low sensitivity gives a coarse image and a mostly black sky. (See figure credits)

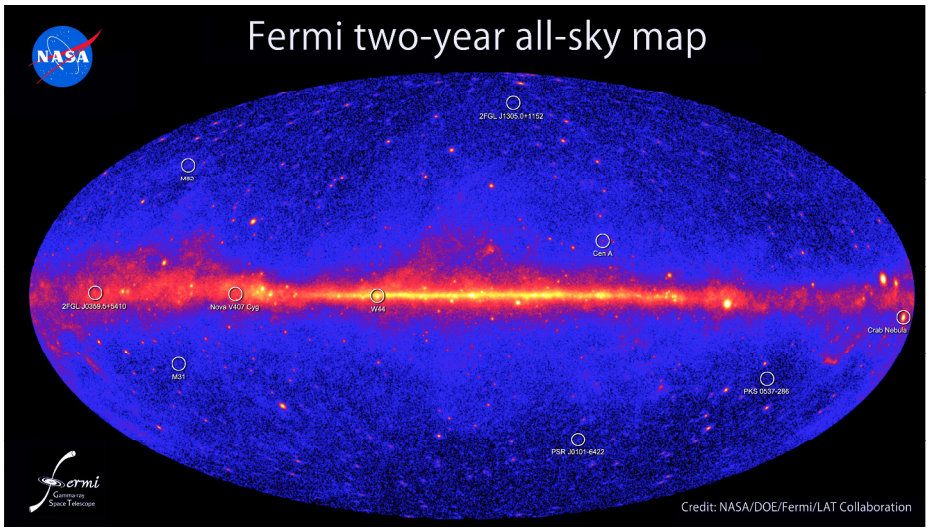

Figure I.3: Fermi two-year all-sky map for energies above 1 GeV, the sensitivity shows many sources and a filled sky. (See figure credits)

This dissertation presents the successful development of a FAst Compton TELescope (FACTEL) prototype using $LaBr_3$ to achieve an unprecedented Time-of-Flight (ToF) resolution and, consequently, a much reduced background. The possibilities demonstrated by the FACTEL prototype, when applied to build a larger "true" telescope, will give MeV astronomy the much awaited sensitivity improvement it lacked for two decades.

This dissertation is divided in six chapters. The first chapter covers the astronomical sources we want to observe and the mechanisms by which they produce gamma rays. The second chapter discusses how these gamma rays interact with matter, how to build a Compton Telescope and the issues pertaining to this class of instruments. The third chapter presents the FACTEL prototype: the concept, the components, materials, its calibration, and how the instrument compares to the developed simulations. We present the flight simulations in the fourth chapter while the fifth chapter covers the results from the balloon flight conducted from NASA's Columbia Scientific Balloon Facility (CSBF) in Fort Sumner, New Mexico, on September 23, 2011. We present basic environmental data, singles events and telescope results, and most importantly that FACTEL achieved the ~1-ns Time-of-Flight resolution required to envision the next generation of sensitive gamma-ray telescopes. The sixth and final chapter will present the concept of a next generation telescope called the Advanced Scintillator COmpton Telescope (ASCOT) along preliminary performance results from initial simulations. We will finally discuss the current state of the medium-energy gamma-ray field and how this new telescope based on the FACTEL prototype would answer the needs of the field.

The background present in the 500 keV to 50 MeV gamma-ray window has made progress in the MeV astronomy field difficult, but new more sensitive observations will be rewarding as a new aspect of our Universe will be unveiled. The results obtained with the FACTEL prototype allow us to envision the next generation telescope that will fill the sensitivity hole.

CHAPTER 1

Gamma-Ray Astronomy

1.1 Introduction

Gamma-ray astronomy is the study of astronomical phenomena and objects emitting gamma rays. Gamma rays are photons with an energy above 100 keV. Having no upper energy limit, the gamma-ray part of the electromagnetic spectrum covers many orders of magnitudes (keV, MeV, GeV, TeV, etc.). The vastly different interaction channels of these gamma rays with media requires us to specify our region of interest because instruments can typically only cover a small part of the gamma-ray range, see fig. I.1. Our program, being a direct evolution of the COMPTEL instrument, focuses on the so-called medium-energy gamma-ray range, broadly from 100 keV to 50 MeV and more restrictively from 500 keV to 10 MeV. Our instrument was not built for the observation of a specific phenomenon but for general high sensitivity observations, thus many phenomena could be studied with it.

The astronomical phenomena producing gamma rays within the medium-energy gamma-ray range can essentially be categorized within two classes: nuclear astrophysics and relativistic particle accelerators. Gamma rays were initially discovered as one type of radiation emitted by decaying radioactive isotopes: alpha radiation, beta radiation, gamma radiation, etc. It is thus no surprise that many nuclear reactions emit gamma rays. Since many astronomical phenomena involve nuclear reactions, these all

become part of what is called nuclear astrophysics. On the other hand, many astronomical sources present high-energy environments with intense gravity, electric or magnetic fields, or very high temperatures. These environments accelerate particles to energies which will lead to the emission of gamma rays, and thus become the second category of gamma ray emitting phenomena called relativistic particle accelerators.

Before proceeding to specific scientific topics, we first make a list of known phenomena observable with the instrument we are proposing. In the nuclear astrophysics field, a Compton telescope can provide observations of the nuclear lines from the galactic center, the positron annihilation 511 keV line, SN Ia supernovae, core collapse SN, the ^{44}Ti isotope, classical novae, nuclear gamma-ray lines from cosmic rays, gamma-ray lines from X-ray binaries, supernovae remnants, solar flare lines, long lived radioactive isotopes diffusing within the interstellar medium, radioactive isotopes within celestial objects without atmospheres, and possibly dark matter annihilation and decay. For relativistic particle accelerators, a Compton telescope can observe the continuum emission from the galactic center, the galactic bulge, the high-energy interstellar clouds, novae, X-ray and gamma-ray binaries, black holes and accreting objects, gamma-ray bursts (GRB), active galactic nuclei (AGN), magnetars and isolated pulsars, pulsar wind nebulae, starburst galaxies, the Sun at high energy, terrestrial gamma-ray flashes, and possibly limits of modern physics.

As seen, a general purpose Compton telescope is relevant for the observation of many interesting astronomical phenomena. For the purpose of this work, one topic from each of the two classes will be discussed: X-ray binaries for the relativistic particles accelerator field and long lived radioactive isotopes for the nuclear astrophysics field. A brief summary of other relevant topics for a Compton telescope will be provided, as well as a review of gamma-ray production mechanisms.

1.2 X-Ray Binaries

X-ray binaries are a class of binary star systems emitting X-ray radiation. They consist of a normal donor star losing mass that is accreted onto the second component of the system, which is a compact object: a white dwarf, a neutron star, or a black hole. To further narrow our discussion about the advancements a new more sensitive Compton telescope would bring to this field, we now focus on the canonical X-ray binary: Cygnus X-1. Cygnus X-1 was discovered in 1964 [8] and is one of the strongest X-ray sources seen from Earth. The system is located in the Cygnus constellation at a distance of about 6100 ly [9] and is composed of a blue O9.7 Iab [10] supergiant star of about 19 solar masses [11], HDE 226868, and the Cygnus X-1 black hole of about 15 solar masses [11] orbiting each other with a period of 5.6 days [12]. An artist's impression of the Cygnus X-1 system is shown in figure 1.1:

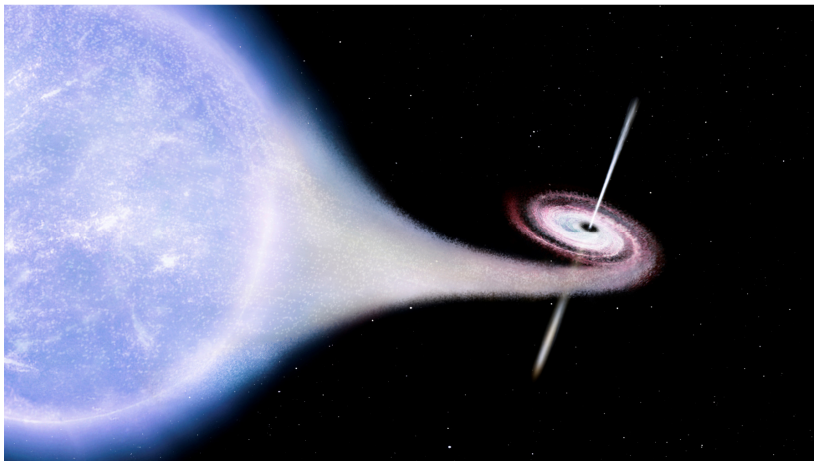

Figure 1.1: Artist's impression of the Cygnus X-1 system: a blue supergiant looses mass that is accreted by the Cygnus X-1 black hole.

The Cygnus X-1 system has been studied from radio waves to high energy gamma rays. For the purpose of this work, we remind a few of the recent

observations within the gamma-ray range: between 20 keV and 2 MeV with INTEGRAL SPI [13], up to about 10 MeV with the CGRO [14], above 30 MeV with AGILE [15] and FERMI [16], and at very high energies (>100 GeV) with MAGIC [17].

Binary systems are systems composed of two stars orbiting each other. An example plot of their gravitational equipotentials is shown in figure 1.21 [81, p. 687]. The Lagrangian points L_1, L_2, L_3, L_4 and L_5 are unstable equilibrium points where the gravitational forces due to M_1 and M_2 are balanced by the centrifugal force. The inner Lagrangian point L_1 plays a central role in close binary systems. If the atmosphere of one star expands enough to fill its Roche lobe (the L_1 equipotential), then gases can escape through the inner Lagrangian point L_1 and be drawn towards its companion.

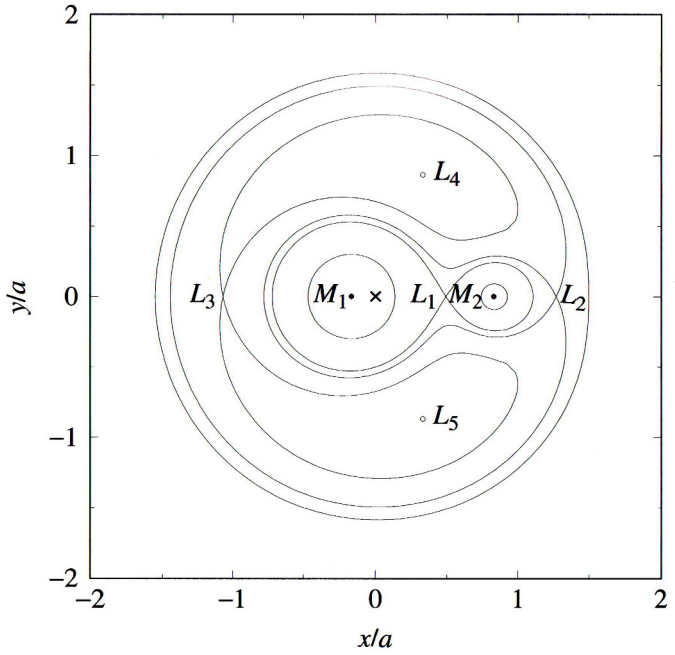

Figure 1.21: Equipotentials for M_1=0.85 $M_\odot$, M_2=0.17 $M_\odot$, and a=5×10^8 m = 0.718 $R_\odot$. The system center of mass × is at the origin. From one of the masses center, the first equipotential is a sphere, the second "8-shaped" is the Roche lobes, and the third the "dumbbell". L_1, L_2, L_3, L_4 and L_5 are the Lagrangian points. [81]

The Cygnus X-1 system exhibits two distinct gamma-ray emission states. In the high/soft state (high fluence, lower energy spectrum), the accretion rate on the black hole is high (compared to the low state), the cooler accretion disk comes closer to the black hole, and the spectrum is dominated by the softer thermal emission of the disk. In the low/hard state (low fluence, higher energy spectrum), the accretion rate is low, and the processes producing higher-energy gamma rays in the hotter region close to the black hole dominate the spectrum. Figure 3 of Sabatini et al. [15] shows a spectrum of each of these two states and is reproduced here in figure 1.2; those spectra themselves are slightly modified versions of figures 5 and 7 of McConnell et al. [14].

A detailed description of the physical mechanisms of a Black-Hole X-ray Binary (BHXB) was published by Esin et al. [18]. BHXBs can display five different emission states: the quiescent state, the low state, the intermediate state, the high state and the very high state. Cygnus X-1 spends most of its time (90% [15]) in the low/hard state and the rest in the high/soft state. Esin et al. use one model to develop a unified picture of the five spectral states observed in BHXBs: a standard thin accretion disk outside a transition radius and a hot advection-dominated accretion flow (ADAF) inside the transition radius close to the black-hole. The different spectral states then correspond to different values of the two main parameters: the mass accretion rate and the transition radius. In the usual low/hard state, the accretion rate is low and the transition radius large. The emission is then dominated by the region close to the black-hole, the ADAF. Electrons in the hot ADAF cool mainly via three processes: bremsstrahlung, synchrotron radiation, and inverse Compton scattering [18]. In the high/soft state, the accretion rate crosses a critical value where the ADAF can no longer be in thermal equilibrium and the cool disk begins to encroach into the ADAF. The disk then comes to a small transition radius

and the ADAF is restricted to a corona above the disk. The emission is then dominated by the cooler accretion disk where electrons mainly produce a softer thermal component. Also, through the study of the fig. 1.2 spectra and the processes contributing to them, the parameters for the initial electron population both in the accretion disk and the ADAF are investigated.

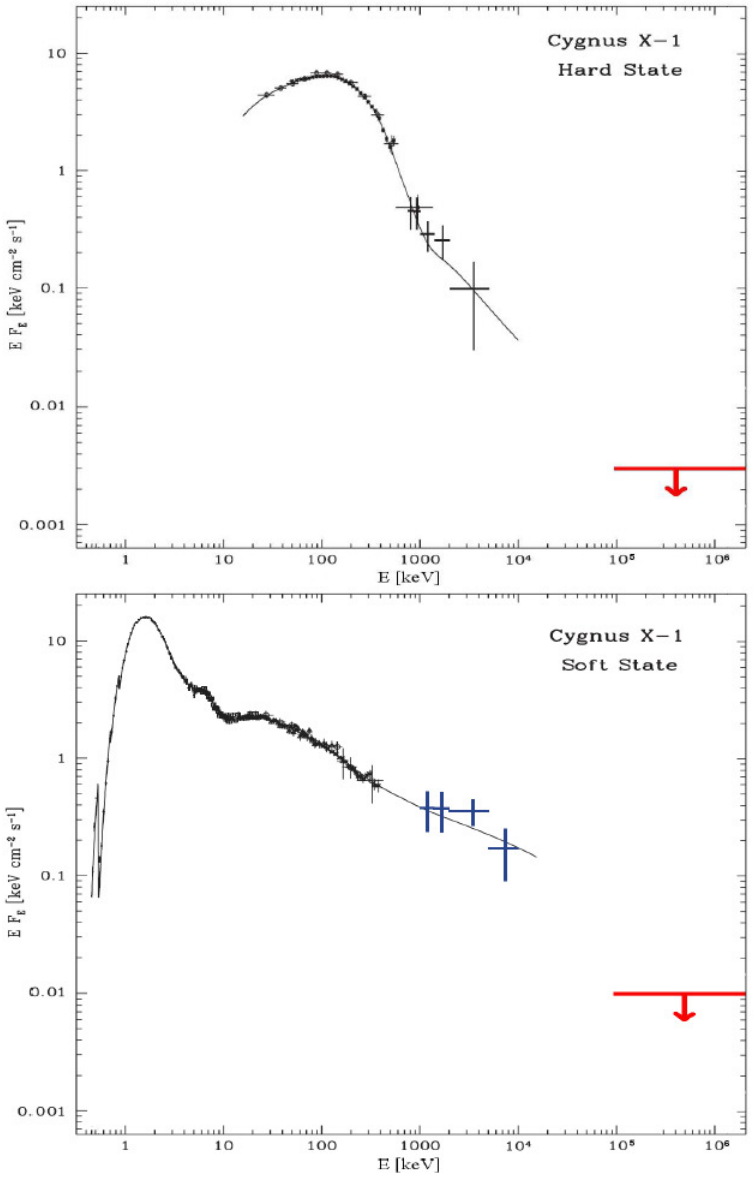

Figure 1.2: Spectral energy distributions of the hard and soft states of the Cygnus X-1 BHXB. The low/hard state has a lower flux than the high/soft state, but its emission peak is at a higher energy, see text for details. COMPTEL points are the ones above 800 keV, AGILE upper limits are in red, see [14, 15] for data details.

The model presented is now the accepted theoretical framework from which new models are developed. An important further aspect is the characterization of the non-thermal component of the soft state (above 500 keV). To quote Sabatini et al. [15]: "Gamma-ray data in the Cyg X-1 soft state are of crucial importance for theoretical modeling because they constrain the high energy part of the spectrum, most likely dominated by non-thermal emission. Of particular interest are observations that can determine a clear cutoff in the spectra at high energies, since the cutoff energy is a function of the compactness of the inner source region."

The parts of these spectra under 500 keV having been well measured, the next step is the energy band between 500 keV and 50 MeV, and the consequence of fig. I.1 shown in the introduction can be directly seen in the spectra of fig. 1.2: points are scarce and the error bars large. Nothing has yet improved upon COMPTEL result in the medium-energy gamma-ray band, published by McConnell et al. [14]. As Jourdain et al. said [13]: "So far, the MeV region of the spectrum was best explored by the Compton Gamma-ray Observatory (CGRO)." This is where the new sensitive telescope we are proposing answers the call: as a direct evolution of COMPTEL, it is the best suited instrument to make the next generation observations needed to further our understanding of X-ray Binaries.

The required observations need increased sensitivity in the 1 to 10 MeV part of X-ray binaries emission spectra. The relevant quantity to measure, aside from the energy and flux, is the photon spectrum power-law index Γ (also called the spectral index, the photon index, etc.) The photon spectral index is the main tool for constraining models of how processes contribute to the total spectrum, the distributions and energy of the emitting particles, and ultimately our understanding of these binary systems. The data from COMPTEL (the last four-five points in the fig. 1.2 spectra) are not precise enough to sufficiently constrain that photon index at

higher energies to discriminate between different theoretical models. An example from [14], modeling the soft state of Cygnus X-1 is shown in figure 1.3.

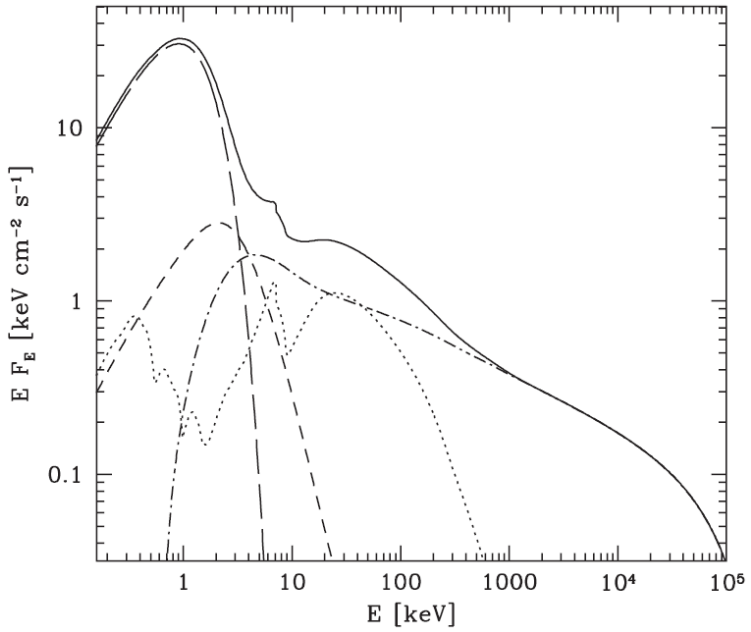

Figure 1.3: Components of the EQPAIR fit for the soft state. All spectra are intrinsic, i.e., corrected for absorption. The long-dashed, short-dashed, dot-dashed, and dotted lines correspond to the unscattered blackbody, scattering by thermal electrons, the scattering by nonthermal electrons, and Compton reflection/Fe Kα fluorescence, respectively. The solid curve is the total spectrum. [14]

To summarize, new more precise observations of the spectrum between 1 and 10 MeV help constrain the processes, particle populations, and BHXBs models. The COMPTEL data have provided results, but now the next step of understanding BHXBs requires more precise observations. As pointed by Sabatini et al. [15], the characterization of the non-thermal component of the spectra at higher energies is of crucial importance in constraining the theoretical models. For example, the cutoff energy relates to the compactness of the inner source region. The relevance of a new more sensitive telescope for observations in the 1 to 10 MeV band is then evident for the study of binary systems.

1.3 Galactic Diffuse Isotopes

For the nuclear astrophysics field, an important topic is the study of long lived radioactive isotopes diffusing throughout the galactic plane, specifically ^{26}Al. Nuclear astrophysics includes the study of nucleosynthesis, which in turn lead to stars and more specifically to supernovae structure. With a half-life of 7.17×10^5 years, ^{26}Al is a "long" lived isotope compared to the supernovae (SN) timescales, yet is a "short" lived isotope with respect to galactic evolution timescales. This means it has the time to diffuse in the inter-stellar medium (ISM), yet it has not the time to diffuse too far, it then "must be continuously produced by one or more nucleosynthetic source to be observed" [19]. Most of the emission is attributed to young, massive stars and active star forming regions [20]. At the galactic scale, the study of the ^{26}Al isotope in the galaxy is a way to study the chemical evolution of the galaxy, specifically the evolution of metallicity in the galactic plane (metallicity gradient), and a way to constrain models of stellar evolution. At the stellar level, the study of the ^{26}Al isotope (and the ratio ^{60}Fe/^{26}Al) is another probe to the SN mechanism and Wolf-Rayet stars [19], [21].

^{26}Al was the first radioactive nucleus ever detected in the galaxy through its 1.809 MeV signature nuclear line. The observation was made from the HEAO 3 satellite and reported in 1984 by Mahoney et al. [22]. The two main contributors to the galactic ^{26}Al are SN II and Wolf-Rayet stars [21]. A complete review of ^{26}Al research can be found in Prantzos and Diehl [23]. The basis for the SN II theory comes from the 1995 paper by Woosley, Thomas and Weaver [24]. The theory behind the Wolf-Rayet wind component can be found in Sabatini et al. [19].

Areas of research are a precise map of the ^{26}Al distribution in the galaxy and the ratio ^{60}Fe/^{26}Al. The map serves to locate star forming regions which can then be

further studied, while the $^{60}Fe/^{26}Al$ ratio helps to constrain SN II and Wolf-Rayet theoretical models.

Timmes et al. [25] found, based on calculations [24], that the expected ratio of $^{60}Fe/^{26}Al$ from a Core Collapse SuperNovae (CCSN) is 0.16. Then the first detection of the galactic ^{60}Fe gamma-ray lines with RHESSI [26] found a flux of 16±5 % of the 1809 keV ^{26}Al line for each of the ^{60}Fe lines. That coincidental confirmation would have implied that all galactic ^{26}Al and ^{60}Fe would come from CCSN. However, by then CCSN theoretical models had much evolved and the ratio is now believed to be much higher, from 40% to unity depending on the model [21], implying another source of galactic ^{26}Al that does not produce ^{60}Fe. The natural candidates to fill the gap are Wolf-Rayet stars, which eject ^{26}Al and no ^{60}Fe [19]. One also needs to keep in mind the different half-lives of these isotopes while analyzing results: ^{26}Al has a half-life of 7.17×10^5 years, while ^{60}Fe has a half life of 2.6×10^6 years. The decay processes of these isotopes can be found in equations 1.16, 1.17 and 1.20.

On the observational side of the study of the galactic $^{60}Fe/^{26}Al$ flux ratio, the goal is more sensitive measurements of both fluxes, ^{60}Fe being the weakest one. An imaging telescope such as the one we propose, being a more sensitive version of COMPTEL, could measure and image both emissions, and help progress in the fields of elemental galactic evolution, star formation regions, Type II Supernovae and Wolf-Rayet stars.

A second objective is the mapping of the ^{26}Al isotope in the galaxy. The latest and best results are those of Plüschke S. et al. [20], shown in figure 1.4:

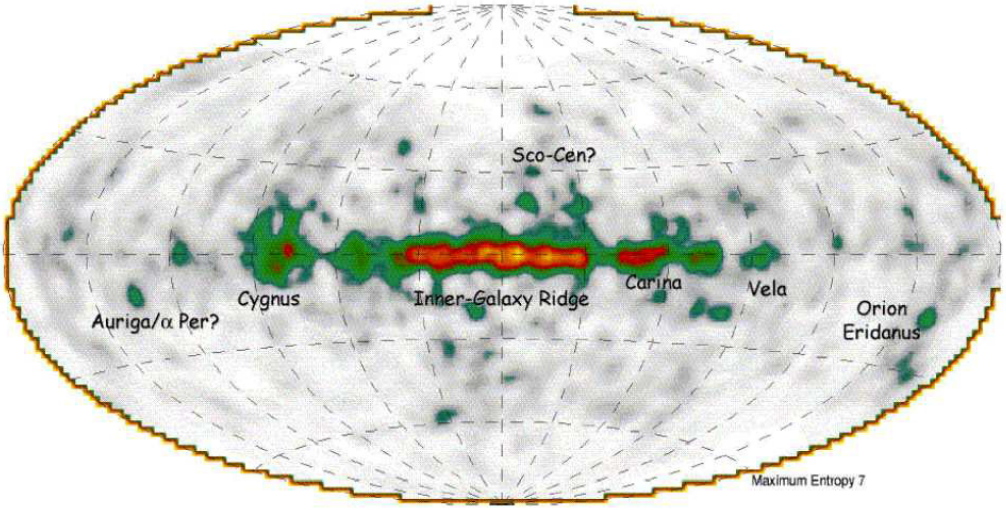

Figure 1.4: COMPTEL Galactic ^{26}Al map. ^{26}Al has been clearly detected in the Inner Galaxy Ridge, Cygnus and Carina regions, and less clearly in the Scorpius Centaurus, Auriga, Vela and Orion regions. (Credit [20], Reference [27])

Figure 1.4 is like the all-sky map shown in the introduction (fig. I.2): the low sensitivity of COMPTEL provides only a coarse image. The same way the Cygnus X-1 results from COMTEL [14] have been cited for over a decade because no instrument has provided better results in the medium-energy gamma-ray band, the result of fig. 1.4 has been the Galactic ^{26}Al reference map since its publication. Bringing the fig. 1.4 map to the level of fig. I.3 shown in the introduction would obviously be a tremendous step forward: clear identification of many regions of interest, localization and study of point sources, and then modeling to constrain and aid observations with other instruments. For example, because SN II produce ^{26}Al and ^{60}Fe, while Wolf-Rayet winds only eject ^{26}Al, a sufficiently sensitive telescope could detect the presence of ^{60}Fe and thus discriminate between SN II and Wolf-Rayet dominated regions. INTEGRAL SPI observations of the ^{60}Fe emission can be found in [82]: the average flux for the two ^{60}Fe lines is $(4.4\pm0.9)\times10^{-5}$ ph cm^{-2} s^{-1}rad^{-1} for the inner Galaxy region, they also find the flux ratio of ^{60}Fe/^{26}Al gamma rays as 0.148 ± 0.06. The galactic ^{26}Al science topic is also a subject for which the large Field

of View (FoV) of a Compton Telescope such as the one we are proposing is an advantage: it allows sensitive observations of large regions of the sky, precisely what is needed (FoV of 40 degrees with under 3 degrees of angular resolution).

1.4 Other Science Topics

All the science topics relevant for Compton telescopes identified at the beginning of this chapter are interesting and important subjects which could be detailed as the X-Ray binaries and diffusing isotopes topics. However for the brevity of this work we will skip a full presentation of each topic and instead provide a short presentation of three more. Ultimately, research for many of these topics is limited the same way: COMPTEL was deorbited 14 years ago, no instrument has provided better results in its energy window since, and the sensitivity in that range is trailing compared to instruments in other energy windows.

The relativistic particle accelerators we listed are different objects with different emission processes, however the necessary measurement is the same as for the X-ray binary topic: a location, image, and a measurement of the continuum spectrum between 1 and up to 50 MeV to help constrain the theoretical models.

The topics in the nuclear astrophysics field are also different in their nature and processes. But again the measurements needed are basically those presented for the diffusing galactic isotopes case: a much improved sensitivity/imaging capability for the topics requiring source identification, and better sensitivity to measure weak nuclear lines to constrain models.

1.4.1 Gamma-Ray Bursts (GRB)

The first observation of a Gamma-ray burst came on July 2, 1967, with the military Vela satellites. The observation of the 1970 August 22 gamma-ray burst by Vela satellites is shown in figure 1.5, it is a reproduction of fig. 1 of [28]. Now shown to have an extra-galactic origin, GRBs are among the most energetic explosions in the Universe, capable of outshining its host galaxy in the gamma-ray range for a few seconds. They are detected at the rate of about one per day. A recent review of the topic was published by Gehrels, Ramirez-Ruiz and Fox [29]. Gamma-ray bursts emission goes from the keV range up to the TeV range.

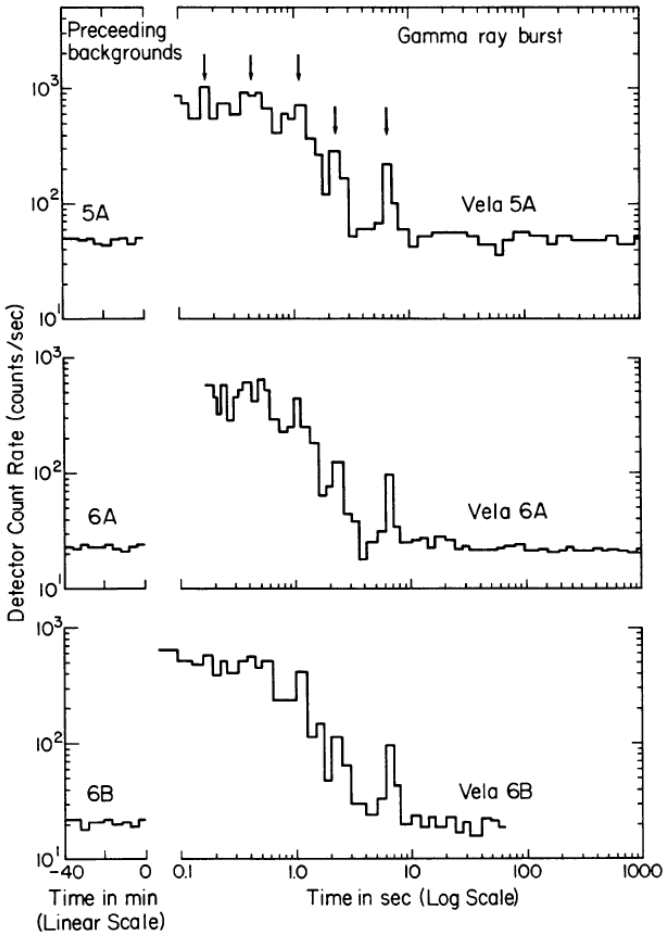

Figure 1.5: A Gamma-Ray Burst observation with the Vela satellites. The picture shows the count rate as a function of time for the gamma-ray burst of 1970 August 22 as recorded by three Vela spacecraft.

The science available through the study of gamma-ray bursts is well summarized in one paragraph [29]:

> "Although interesting on their own, GRBs are now rapidly becoming powerful tools to study detailed properties of the galaxies in which they are embedded and of the Universe in general. Their apparent association with massive star formation and their brilliant luminosities make them unique probes of the high-redshift Universe and galaxy evolution. Absorption spectroscopy of GRB afterglows is being used to study the interstellar medium (ISM) in evolving galaxies, complementary to the traditional studies of quasar absorption line systems. Possibly the most interesting use of GRBs in cosmology is as probes of the early phases of star and galaxy formation, and the resulting reionization of the Universe at $z \sim 6$–20. GRBs are bright enough to be detectable, in principle, out to much larger distances than the most luminous quasars or galaxies detected at present. Thus, promptly localized GRBs could serve as beacons that, shining through the pregalactic gas, provide information about much earlier epochs in the history of the Universe."

To understand GRBs, the first step is a model of the central engine, which is believed to be a black-hole (BH) or a neutron star (NS) with a high accretion mass rate (recently formed by a supernova or hypernova). To produce the luminosities of GRBs, the central engine has to process more than 10^{-2} solar masses of material per second through a region the size of a NS or a BH [29]. From there, the theoretical model is built up to the stellar environment. Figure 1.6 shows a diagram exhibiting GRB activity over successive decades in radius ranging from 10^6 cm to 1 pc, it a reproduction of figure 14 of [29]. Without entering into the physical details [29], the topics of the GRB process are the central engine, the accretion flow, the jet production, collimation, stability and confinement, the dissipation and cooling effects

within the jet, the jet interaction with the external environment, and finally the beaming of the produced gamma rays.

As for the observational needs in this field, improved precision of the continuous spectrum in the MeV band is needed: the evolution of the flux in time and the spectral index of the spectrum. The new data is then used to constrain theoretical models, which in turn help us to further our understanding of the phenomenon.

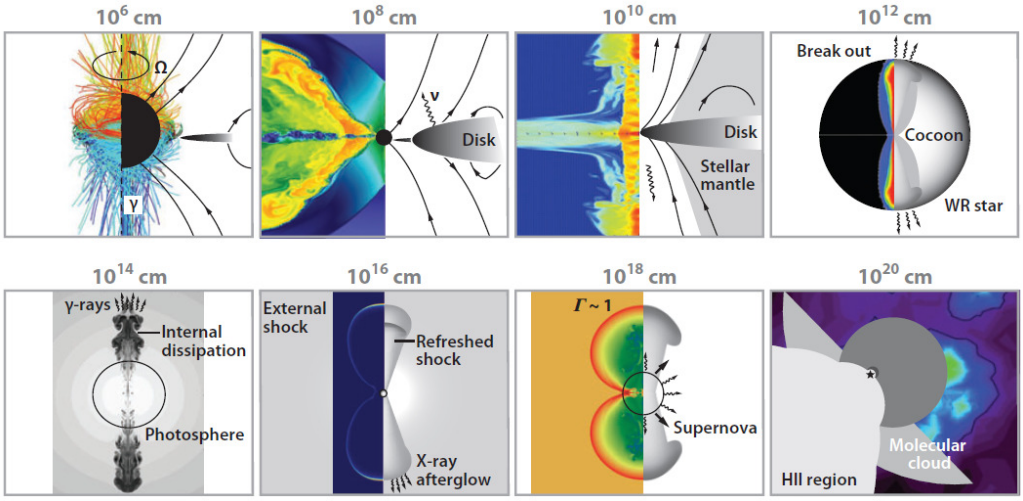

Figure 1.6: Diagram exhibiting GRB activity over successive decades in radius ranging from 10^6 cm to 1 pc. At 10^6 cm, the relevant aspect is the BH or NS and its magnetosphere. At 10^8 cm is the accretion disk in a corona. At 10^{10} cm the remaining of the stellar interior starts to play a role. 10^{12} cm is the size of the massive star progenitor. 10^{14} cm involves the relativistic jets and photosphere interactions. 10^{16} cm involves the external shock. 10^{18} cm is the supernova region and 10^{20} cm the stellar region.

1.4.2 The 511 keV emission from positron annihilation

The first observed gamma-ray line origination from outside the solar system was the 511 keV emission from positron annihilation in the galaxy. Whenever a particular astrophysical process creates positrons, these will eventually annihilate with an electron producing gamma rays. This makes the 511 keV emission line an

interesting study topic for gamma-ray telescopes because it is directly linked to positron creation and the processes creating them.

The first positrons of extraterrestrial origin were directly detected by De Shong et al. [30], while the first detection via annihilation emission from the galactic center came later in 1972 by Johnson et al. [31]. The detection of solar positron annihilation was made with the OSO-7 satellite and reported by Chupp et al. [32]. Since then, the positron 511 keV line study field has thrived and a modern review of the research field can be found in Prantzos et al. [33] published in 2010.

Many sources and processes produce positrons that can be studied via the 511 keV annihilation line. One process is the β^+ decay of radioactive isotopes, which produces positrons. The β^+ decay occurs when a proton converts to a neutron in the nucleus, thus proton rich environments where heavier nuclei can capture protons are important positron emitters. These environments are massive star cores, novae and supernovae explosions. Astrophysically important positron emitting isotopes are ^{56}Ni, ^{22}Na, ^{44}Ti and ^{26}Al [33]. The knowledge about these isotopes populations is then used to further the study of their sources: SNIa for ^{56}Ni, novae for ^{22}Na, supernovae for ^{44}Ti, and massive stars for ^{26}Al. Many non-nuclear processes can produce positrons: inelastic p-p collisions, and e^--e^+ pair creation either through γ-γ interactions, reactions of gamma rays with matter, or through various particles interacting with intense electromagnetic fields. These intense electromagnetic fields can be found around pulsars, magnetars, black holes and galactic black holes. A detailed presentation of the physical processes producing positrons can be found in [33].

Like the ^{26}Al topic presented in section 1.3, imaging resolution and line sensitivity are the key aspects in need of improvement. Because 511 keV is on the low energy boundary for a telescope such as COMPTEL, the best data does not come

from COMPTEL but from the SPI instrument of the INTEGRAL satellite. Figure 1.7 shows the 511 keV map derived from 5 years of INTEGRAL/SPI data [34]. The image is like the others presented so far: coarse and mostly absent of signal.

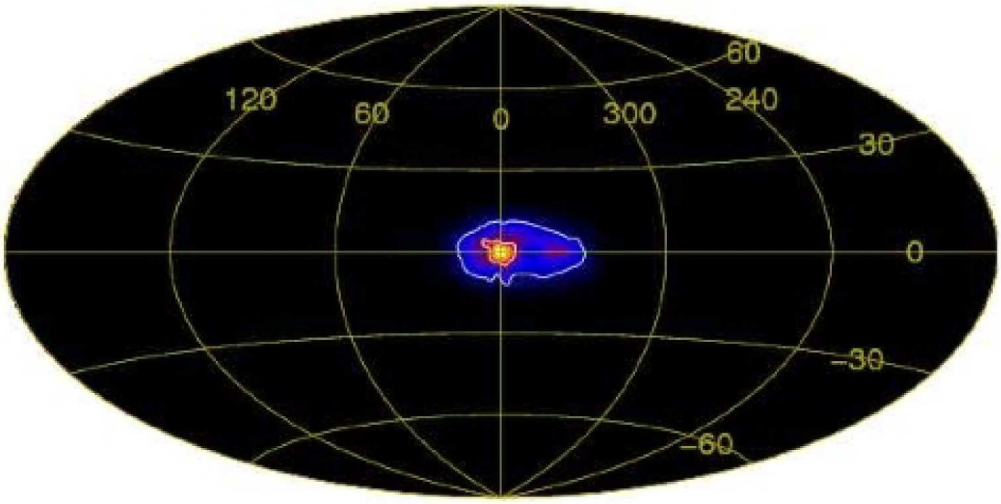

Figure 1.7: 511 keV line map derived from 5 years of INTEGRAL/SPI data [34]

Again, sensitivity is the instrumental property required to fill this image with sources, while angular resolution coupled with a better sensitivity would clarify the morphology of the underlying source population(s). As seen in fig. I.1, 500 keV was under the lower energy limit of COMPTEL (800 keV), and we see that a new Compton Telescope that could reach 500 keV would provide the required more sensitive observations.

1.4.3 Solar Flares

Solar flares are yet still not a completely solved problem. They emit electro-magnetic radiation from radio-waves to gamma rays and many processes contribute to the gamma-ray portion of their spectrum. Nuclear lines, neutron capture, positron annihilation and bremsstrahlung all supply the MeV spectrum of solar flares. Solar

flare gamma-ray spectroscopy provide measurements of the elemental abundances in the ambient solar material, as well as insights on the accelerating processes of ions and magnetohydrodynamics within the solar atmosphere. A modern review of the solar flare topic by Fletcher et al. can be found in [35].

A solar flare gamma-ray spectrum from the early 1970's from Chupp et al. [32], already mentioned in the 511 keV line section, is shown in figure 1.8, it is a reproduction of fig. 4 of [32]. The nuclear lines are evident: 511 keV from positron annihilation, 1173 and 1333 keV from ^{60}Co, 2.2 MeV from neutron capture by protons (see eq. 1.12), 4.4 MeV from ^{12}C and 6.1 MeV from ^{16}O. A more recent solar flare gamma-ray spectrum from the RHESSI satellite is shown in figure 1.9, it is a reproduction of fig. 1 of [36]. The nuclear lines measure elemental abundances for the particular flare, while the overall spectrum is used to constrain the processes of solar-flare models.

Imaging is also crucial for solar flares because the precise location of the gamma-ray emission is critical to constraining models. A RHESSI-STEREO composite image of the emission evolution is shown in figure 1.10.

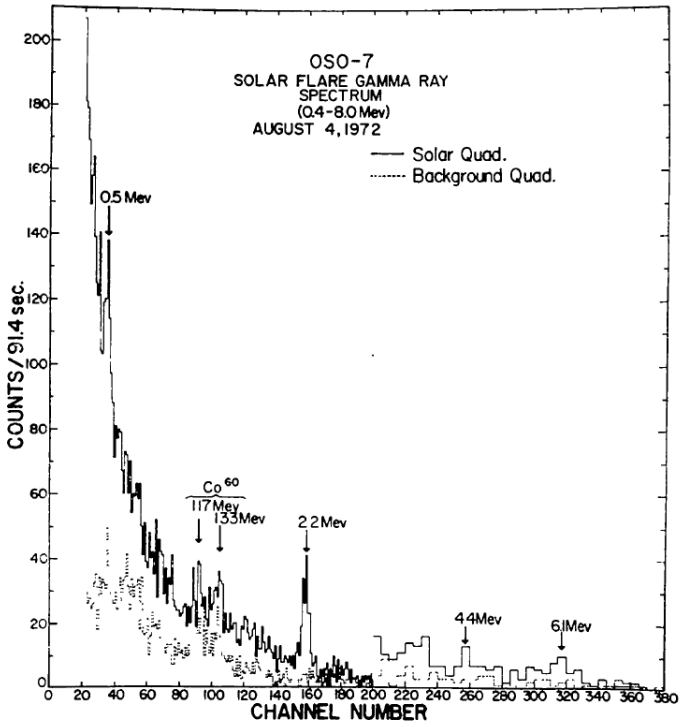

Figure 1.8: OSO-7 Solar flare gamma-ray spectrum, August 4, 1972, 0624-0633 UT [32]

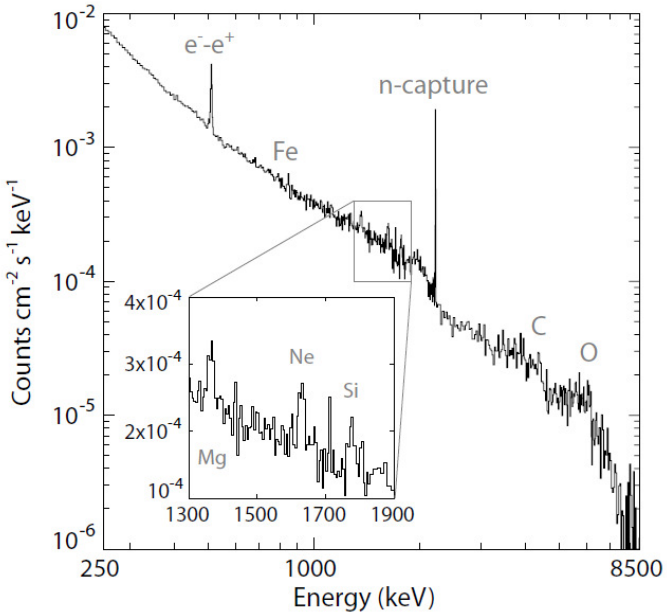

Figure 1.9: RHESSI γ-ray count spectrum of the 2002 July 23 solar flare. The positron-annihilation line (511 keV), the neutron-capture line (2.223 MeV), and six nuclear de-excitation lines are labeled. The narrow line at 1.712 MeV is the single-escape peak of the neutron-capture line.

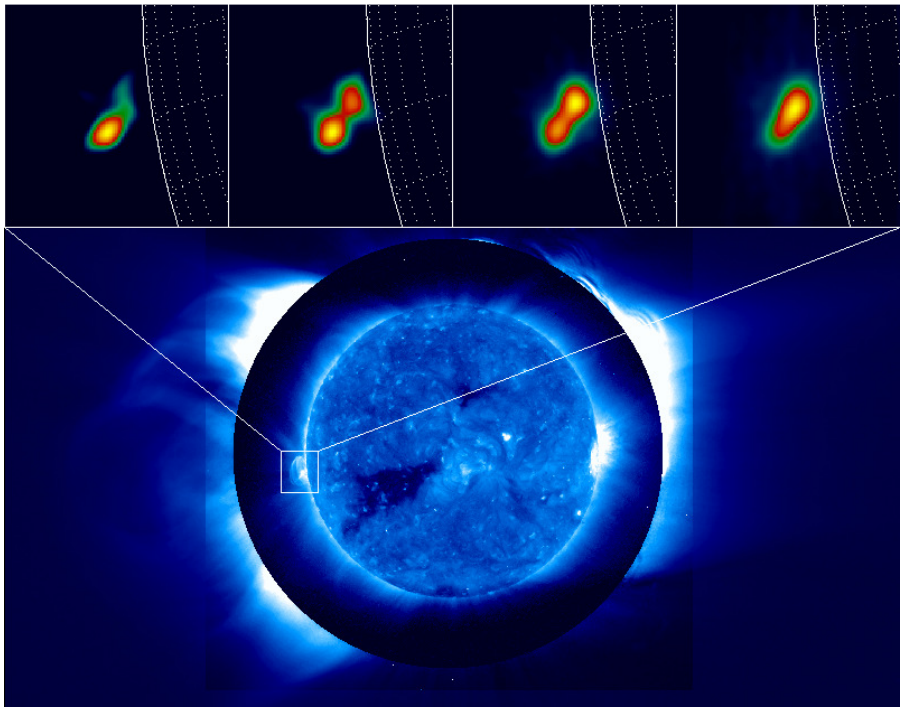

Figure 1.10: RHESSI-STEREO composite image. It shows two X-ray sources merging during a Coronal Mass Ejection eruption.

Of note at the end of the review article [35] is a small section on future observational progress listing areas where observations should be improved. The second point of the section is relevant for a new sensitive Compton Telescope:

> "**Sensitive high-energy observations.** *RHESSI* has made it abundantly clear that the key to non-thermal processes involved in the disruption of coronal plasmas (i.e., flares and CMEs) can readily be detected even in the tenuous middle corona. There is a vast parameter space awaiting sensitive instruments."

1.5 Gamma-Ray Emission Processes

We review in this section the main gamma-ray emission mechanisms: thermal emission, charged particles interacting with electromagnetic fields (bremsstrahlung

and cyclotron/synchrotron radiation), inverse Compton scattering, nuclear transitions, and particle annihilations and decays.

1.5.1 Thermal Emission

Thermal emission is blackbody radiation, the electromagnetic radiation emitted by a body in thermodynamic equilibrium with its environment. The blackbody radiation intensity spectrum, shown in figure 1.11, is given by Plank's law [37, eq. 5.182]:

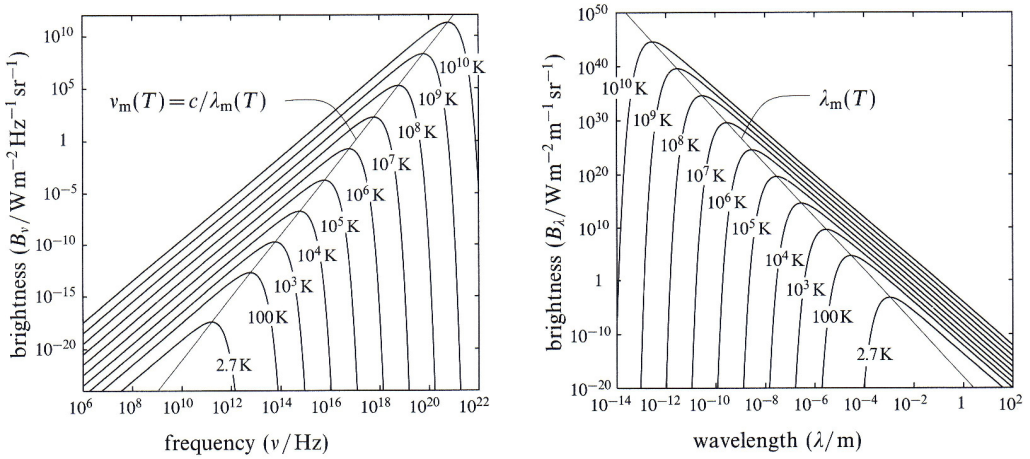

Figure 1.11: Blackbody radiation spectra

$$B_\upsilon(T) = \frac{2\,h\,\upsilon^3}{c^2}\left[\exp\left(\frac{h\,\upsilon}{k_B\,T}\right) - 1\right]^{-1} \quad , \tag{1.1}$$

where B_υ is the surface brightness per unit frequency [W m^{-2} Hz^{-2} sr^{-1}], T the temperature [°K], h the Planck constant, υ the frequency [Hz], c the speed of light, and k_B Boltzmann's constant. The peak maximal wavelength λ_{max} is related to the

temperature T through Wien's displacement law [37, eq. 5.189] where b is a constant equal to 2.9×10^{-3} [m °K]:

$$\lambda_{max} = \frac{b}{T}\,. \tag{1.2}$$

X-rays and gamma rays can be produced through thermal emission by sources with material reaching extreme temperatures. An example already covered is the long dashed curve in fig. 1.3 (the multi-component fit of the Cygnus X-1 soft state spectrum [14]) which corresponds to the blackbody radiation. The 1 keV maximum corresponds to a 2.3×10^{6} °K temperature. However, that component of the spectrum looses significance above 20 keV, and much more extreme environments would be needed to reach MeV energies. Temperatures required to produce 1 MeV photons are of the order of 10^{11} °K, so MeV gamma-ray astronomy usually deals with the "non-thermal components" of a source emission spectrum.

1.5.2 Charged particles interacting with electromagnetic fields

A much more common source of gamma rays is the interactions of charged particles (typically electrons) with the electric or magnetic fields present around celestial objects. Accelerated energetic charged particles emit radiation. When an energetic charged particle is deflected by an electric field and produces a photon, the process is called bremsstrahlung, and when it is deflected by a magnetic field and emits a photon, the process is called cyclotron radiation. When the particle interacting with a magnetic field has a relativistic speed, cyclotron radiation is known as synchrotron radiation as it is much more focused in the forward direction. Gamma-ray astronomy usually deals with synchrotron radiation rather than cyclotron radiation.

1.5.2.1 Bremsstrahlung

Bremsstrahlung comes from the German words ***bremsen*** "to brake" and ***strahlung*** "radiation" thus meaning "braking radiation". Bremsstrahlung occurs when a charged particle interacts with an electric field and emits a photon, typically when an electron is deflected by the Coulomb field of an atomic nucleus, figure 1.12 shows a diagram of the process. Bremsstrahlung is basically an electron-ion collision that produces a photon from the electron kinetic energy, with the nucleus absorbing the momentum change.

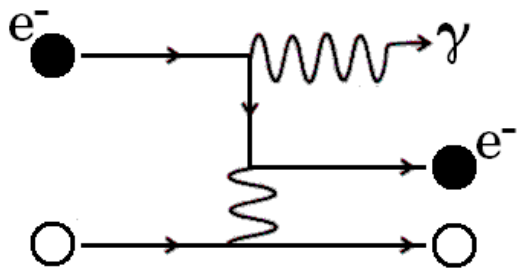

Figure 1.12: Bremsstrahlung diagram, an electron interacts with a nucleus electric field and emits a photon

For mono-energetic electrons traveling in a homogeneous material where the much heavier ions are assumed to be at rest, the spectrum of bremsstrahlung radiation is flat up to the electron maximal kinetic energy where it falls to zero: all of the electron kinetic energy is given to the created photon. Below the maximal kinetic energy of the electron, the total intensity per unit frequency I_v [W s m^{-2}] is [38, p.15]:

$$I_v(E_e) = \frac{Z^2\, e^6\, n}{12\,\pi^3\,\varepsilon_0^3\, c^3\, m_e^2\, v_e}\, ln\left(\frac{192\, v_e}{Z^{1/3}\, c}\right) \quad , \tag{1.3}$$

where E_e and v_e are the electron energy and velocity, Z and n [m^{-3}] the atomic number and number density of the material, e, ε_0, c and m_e the usual physical constants.

For an astrophysical application, the initial electrons have an energy distribution (power-law, or thermal) and the material might be composed of many ion species with temperature distributions.

A detailed treatment of bremsstrahlung radiation can be found in the literature [39]. Solar flares are a well established source for which the hard X-rays (HXRs) come from bremsstrahlung radiation [35], [79].

1.5.2.2 Synchrotron Radiation

Synchrotron radiation is emitted when a relativistic charged particle interacts with a magnetic field. While strong electric fields are usually constrained close around atoms, magnetic fields can reach astronomical distances. When a charged particle enters a region containing a magnetic field, it starts gyrating along the field lines, its trajectory becomes a helix, and it will radiate energy as photons, a diagram of synchrotron radiation is shown in figure 1.13:

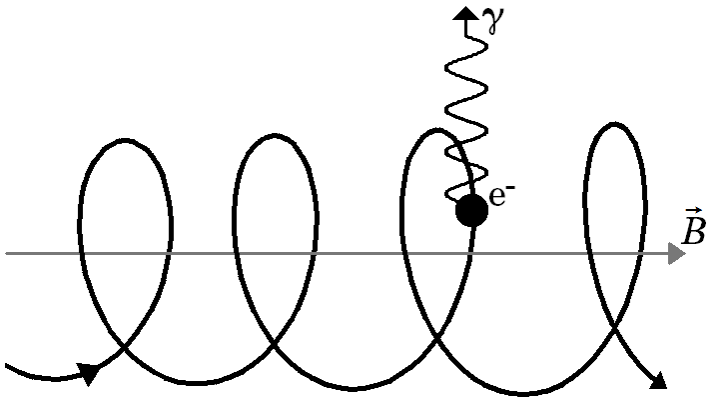

Figure 1.13: Synchrotron radiation diagram, an electron gyrates along a magnetic field line and emits a photon

For a particle of mass m and charge q, the cyclotron frequency (or Larmor frequency, or gyro-frequency) ν_C [Hz] in a magnetic flux density B [T] is given by [37, eq. 7.265]:

$$\upsilon_C = \frac{q\,B}{2\,\pi\,\gamma\,m} \quad , \tag{1.4}$$

where γ is the Lorentz factor. At low speeds, for electrons $\nu_{Ce} = 28\times10^9\,B$ Hz, while for protons $\nu_{Cp} = 15.2\times10^6\,B$ Hz.

The photons are emitted at discrete energies following harmonics rising from the trajectory cyclic nature. However, Doppler broadening widens the discrete emission line from each harmonic with the resulting total continuous spectrum peaking at a frequency ν_{Ch} [Hz] given by [37, eq. 7.292]:

$$\upsilon_{Ch} = \frac{3}{2}\,\gamma^2\,\upsilon_C\,\sin(\theta) \quad , \tag{1.5}$$

where γ is the Lorentz factor and θ is the pitch angle (the angle between $\boldsymbol{v}$ and $\boldsymbol{B}$). The emission spectrum $P(\nu\ \mathbf{[Hz]})$ itself for a single electron is given by [37, eq. 7.290]:

$$P(\upsilon) = \frac{\sqrt{3}\,e^3\,B\,\sin\theta}{4\,\pi\,\varepsilon_0\,c\,m_e}\,F\left(\frac{\upsilon}{\upsilon_{Ch}}\right) \ \text{[W Hz}^{-1}\text{]}, \tag{1.6}$$

where $F(x)$ is a spectral function using $K_{5/3}$, the modified Bessel function of the 2nd kind of order 5/3, given by [37, eq. 7.294]:

$$F(x) = x\int_x^\infty K_{5/3}(y)\,\mathrm{d}y \quad . \tag{1.7}$$

A plot of the $F(x)$ spectral function is shown in figure 1.14. A complete treatment of synchrotron radiation can be found in the literature [39], where the equations 1.6 and 1.7 can be recognized in [39, eq. 14.91].

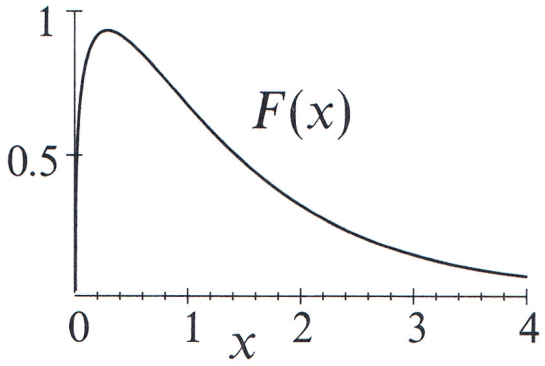

Figure 1.14: Plot of the spectral function giving the synchrotron emission spectrum for a single electron

Synchrotron radiation is mostly emitted perpendicular to the magnetic field line, or parallel to the electron velocity, see fig. 1.13, another diagram of the effect is shown in figure 1.15.

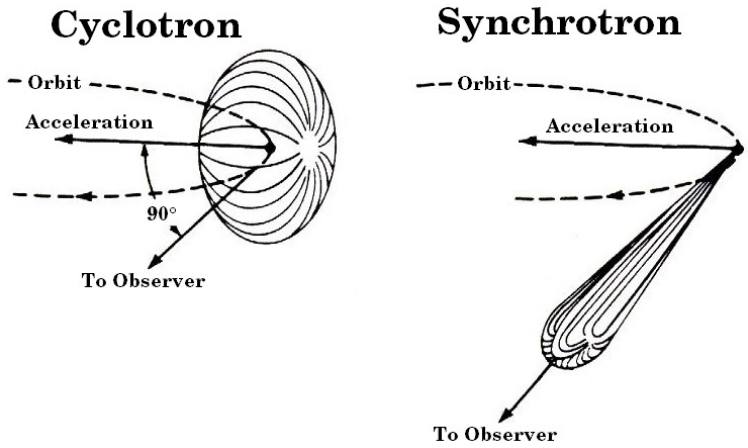

Figure 1.15: Synchrotron emission is beamed parallel to the electron velocity

Astronomical sources of synchrotron radiation are sources with strong magnetic fields and relativistic particles, typically pulsars and black holes jets. As for bremsstrahlung, the initial electrons typically have a continuous energy distribution (power-law, or thermal).

1.5.3 Inverse Compton Scattering

Inverse Compton scattering is the up-energizing of a low-energy photon interacting with an ultra-relativistic electron, a diagram of this process is shown in figure 1.16:

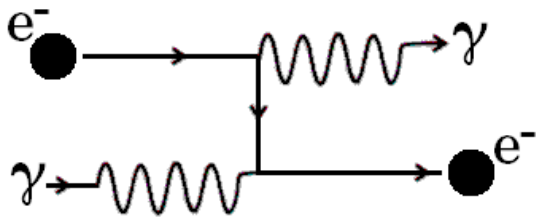

Figure 1.16: Inverse Compton scattering diagram, a low-energy photon is up-energized by a high-energy electron

The reference for inverse Compton scattering is the review article from Blumenthal and Gould "Bremsstrahlung, Synchrotron Radiation, and Compton Scattering of High-Energy Electrons Traversing Dilute Gasses" [40]. They show the spectral emissivity $I(\upsilon)$ is:

$$I(\upsilon)\,\mathrm{d}\upsilon = \frac{3\,\sigma_T\,c\,N(\upsilon_0)}{16\,\gamma^4\,\upsilon_0^2}\,\upsilon\left[2\,\upsilon\ln\left(\frac{\upsilon}{4\,\gamma^2\,\upsilon_0}\right) + \upsilon + 4\,\gamma^2\,\upsilon_0 - \frac{\upsilon^2}{2\,\gamma^2\,\upsilon_0}\right], \qquad (1.8)$$

where the initial photon field is assumed to be monochromatic with a frequency υ_0, $N(\upsilon_0)$ is the number density of the photon field, σ_T the Thompson cross section, c the speed of light, and γ the Lorentz factor of the electron. A theoretical inverse Compton spectrum example is shown in figure 1.17.

Some results of interest are:

The maximum energy of the emitted photon is: $E_{\max} \approx 4\,\gamma^2 E_0$ (1.9)

The average energy of the emitted photons is $E_{\mathrm{avrg}} \approx 4/3\,\gamma^2 E_0$ (1.10)

The electron energy loss rate is given by:

$$P = -\frac{\mathrm{d}E}{\mathrm{d}t} = \frac{4}{3}\left(\frac{v^2}{c^2}\right)\sigma_T\,\gamma^2 c\,U_{\mathrm{rad}}\,, \qquad (1.11)$$

where U_{rad} is the radiation energy density. The reader is referred to [40] for the complete details.

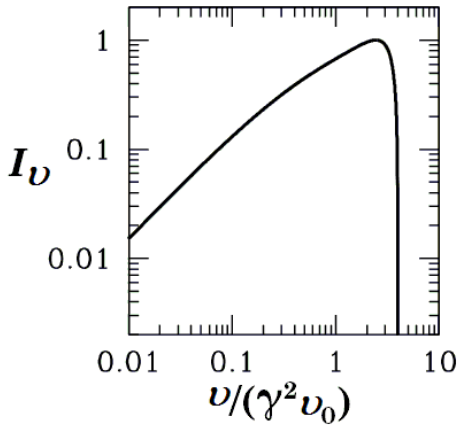

Figure 1.17: Theoretical spectrum of photons created via inverse Compton scattering, the end of the spectrum shows that $E_{\mathrm{max}} \approx 4\gamma^2 E_0$

Equations 1.9 and 1.10 show that the energy gain for the initial photon is of order γ^2, which for γ values between 100 and 1000 can lead to an energy gain of a factor 10^6. This is how thermal keV photons emitted by a hot accretion disk or a pulsar can be up-energized to GeV energies by ultra-relativistic electrons.

1.5.4 Nuclear Transitions

Gamma rays were discovered through nuclear energy transitions, making them a *de facto* classical gamma-ray source. Most natural nuclear reactions leave the new nuclei in an unstable excited state with an excess of energy that will be promptly emitted as a gamma ray, leading to a multitude of natural nuclear lines. Those lines are discrete because neutrons and protons in nuclei form a quantum system with discrete

states and shells with an energy spacing typically in the MeV range, up to the binding energy of a nucleon. The gamma rays produced by nuclear transitions are thus a signature of the reaction that occurred and of the nuclei involved, figure 1.18 for example shows the decay diagram of ^{22}Na.

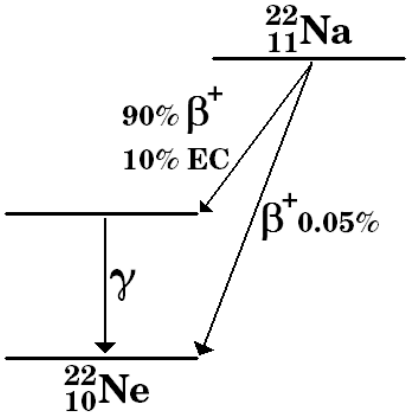

Figure 1.18: ^{22}Na Decay diagram, ^{22}Na undergoes a β^+ decay and a 1275 keV gamma ray is emitted

Most nuclei created in supernovae are unstable and decay emitting gamma rays that help understanding the SN phenomenon. In the laboratory, instruments can be accurately calibrated using standard radioactive sources that emit gamma rays of a known energy. Because nuclear transitions are a major source of gamma rays, a few important reactions are now presented [73]:

Wherever neutrons are created in an astronomical environment, hydrogen atoms are usually present. This will lead to a neutron capture reaction that will in turn produce a signature gamma-ray:

$$^1_0\mathrm{n} + {}^1_1\mathrm{H} \rightarrow {}^2_1\mathrm{H} + \gamma(2.223\ \mathrm{MeV}) \qquad (1.12)$$

For supernovae studies, a number of nuclei of particular interest are produced during the explosion:

^{56}Ni has a half-life of 6.077 days and decays to ^{56}Co:

$$^{56}_{28}\mathrm{Ni} \rightarrow {}^{56}_{27}\mathrm{Co} + \mathrm{e}^{+} + \upsilon_e + \gamma(158, 270, 480, 750, 812\ \mathrm{keV}) \quad (1.13)$$

^{56}Co itself has a half-life of 77.27 days and decays to ^{56}Fe:

$$^{56}_{27}\mathrm{Co} \rightarrow {}^{56}_{26}\mathrm{Fe} + \mathrm{e}^{+} + \upsilon_e + \gamma(847, 1038, 1238, 1771, 2598\ \mathrm{keV}) \quad (1.14)$$

^{44}Ti has a half-life of 63 years and decays to ^{44}Sc:

$$^{44}_{22}\mathrm{Ti} + \mathrm{e} \rightarrow {}^{44}_{21}\mathrm{Sc} + \upsilon_e + \gamma(67.9, 78.3\ \mathrm{keV}) \quad (1.15)$$

^{44}Sc will quickly (4 hours) decay to ^{44}Ca producing a 1157 keV gamma ray.

Longer lived isotopes provide means to study the ejected material as it diffuses in the inter-stellar media. The decay schemes of ^{26}Al and ^{60}Fe are:

^{26}Al has a half-life of 7.17×10^{5} years and decays to ^{26}Mg:

$$^{26}_{13}\mathrm{Al} + \mathrm{e} \rightarrow {}^{26}_{12}\mathrm{Mg} + \upsilon_e + \gamma(1809\ \mathrm{keV}) \quad (1.16)$$

^{60}Fe has a half-life of 2.6×10^{6} years and decays to ^{60}Co:

$$^{60}_{26}\mathrm{Fe} \rightarrow {}^{60}_{27}\mathrm{Co} + \mathrm{e} + \overline{\upsilon_e} + \gamma(58.6\ \mathrm{keV}) \quad (1.17)$$

^{60}Co itself decays quickly compared to ^{60}Fe with a 5.27 years half-life following the decay scheme of eq. 1.20.

A final series of decay schemes are those of the main isotopes used to calibrate laboratory instruments in the MeV range:

^{137}Cs has a half-life of 30.17 years and decays to ^{137}Ba:

$$^{137}_{55}\mathrm{Cs} \rightarrow {}^{137}_{56}\mathrm{Ba} + \mathrm{e} + \overline{\upsilon_e} + \gamma(661.7\ \mathrm{keV}) \quad (1.18)$$

^{22}Na has a half-life of 2.6 years and will decay to ^{22}Ne following the decay scheme shown in figure 1.18:

$$^{22}_{11}\mathrm{Na} \rightarrow {}^{22}_{11}\mathrm{Ne} + \mathrm{e}^{+} + \upsilon_e + \gamma(1274.5\ \mathrm{keV}) \tag{1.19}$$

And finally, ^{60}Co has a half-life of 5.27 years and decays to ^{60}Ni:

$$^{60}_{28}\mathrm{Co} \rightarrow {}^{60}_{29}\mathrm{Ni} + \mathrm{e} + \overline{\upsilon_e} + \gamma(1173,\ 1333\ \mathrm{keV}) \tag{1.20}$$

1.5.5 Particle Annihilations and Decays

Particles such as positrons and neutral pions created in the various processes occurring in the Universe will annihilate or naturally decay producing gamma rays. For annihilations, anti-matter particles such as positrons created by high-energy processes or nuclear reactions can find electrons to create positronium, annihilate with and create two 511 keV gamma rays (anti-parallel spins), a diagram of this process is shown in figure 1.19.

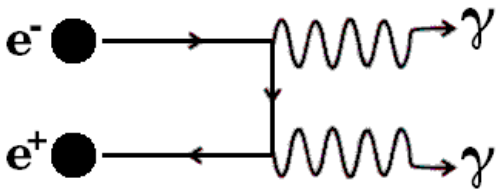

Figure 1.19: Positron Annihilation diagram, an electron and a positron annihilate creating two 511 keV gamma rays

The density of the medium and the kinetic energy of the positrons will affect the annihilation rate, and if the electron and positron have parallel spins, they will annihilate producing three gamma rays. Detecting 511 keV gamma-ray radiation is a clear signature of positron annihilation, as shown in figures 1.7 from SPI, 1.8 and 1.9.

For particles decays, the focus is mainly on neutral mesons composed of a quark and an anti-quark that will quickly react with each other. The main one is the neutral pion π^0 with a 135 MeV/c^2 rest mass created when cosmic-rays (high-energy protons) interact via the strong force with various nuclei of a target media. The π^0 decays quickly as the quark and anti-quark annihilate following a scheme similar to normal annihilation, depicted in figure 1.20. For the neutral pion decay, the two resulting gamma rays will have an energy spectrum peaking at around ~70 MeV.

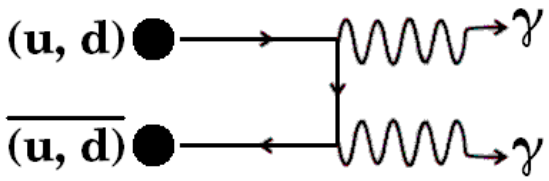

Figure 1.20: Neutral pion decay diagram, a quark and an anti-quark annihilate creating two gamma rays

1.6 Summary

This chapter presented the astronomical sources of medium-energy gamma rays and the processes by which they produce gamma rays. A Compton telescope based on the prototype we developed is meant to study everything in the 500 keV to 10 MeV energy band. This band covers many topics both in the nuclear astronomy and relativistic particle accelerators broad categories.

X-ray binary systems are composed of a star having its material accreted into a compact object such as a neutron star or a black hole. The dynamics of the accretion disk and the NS/BH corona and fields lead to various processes to emit gamma rays. Different rates of accretion create different states of emission for binary systems: the high/soft state and the low/hard state. The spectra of those states inform us about the processes and dynamics occurring around binary systems, and more precise measurements can help us refine theoretical models. The range between 1 and 10

MeV involves non-thermal processes and the current best observations from COMPTEL are not sensitive enough to settle many questions. More sensitive observations of the non-thermal part of the binary systems spectra would bring crucial new data to help us progress in their understanding.

Diffusing isotopes in the interstellar medium inform us about the chemical evolution of the galaxy as well as provide us tools to study supernovae and Wolf-Rayet stars. ^{26}Al has a half-life long enough to diffuse to the inter-stellar medium from its creation site, yet not long enough compared to galactic timescales to diffuse too far. This means the observed ^{26}Al has been produced in a nearby system, and has to be continuously produced to be observed, which informs us about star forming regions. What is sought for in this case is sensitivity combined to image resolution to refine the ^{26}Al map and better identify structures in the galaxy, which in turn lead to progress about the chemical evolution of the galaxy, the SN II phenomenon and Wolf-Rayet stars.

The other topics (GRBs, galactic positrons and solar flares) further showed sensitivity to be the main need of the field: sensitivity to measure the spectral index of the relativistic particle accelerators spectra, and sensitivity to refine maps by detecting lower fluxes in the nuclear astrophysics category.

The processes by which these sources produce gamma rays were surveyed. Thermal emission is rarely relevant above 1 MeV, however it does provides the X-rays that will be up-energized by inverse Compton scattering. Bremsstrahlung radiation is emitted when an electron interacts with an atomic electric field, while synchrotron radiation is emitted by relativistic particles in magnetic fields. Gamma rays can also be produced when ultra-relativistic electrons interact via inverse Compton scattering with local photons, by many nuclear transitions, particle annihilations and decays.

The medium-energy gamma-ray astronomy field is rich with numerous exciting phenomena to study. However, as shown in fig. I.1 of the introduction and throughout this chapter, the field needs a new more sensitive instrument to make progress.

CHAPTER 2

Compton Telescopes

2.1 Introduction

This chapter introduces the instrument class known as Compton telescopes. We start by reviewing the gamma-ray interaction channels with matter, then how to build a Compton telescope. We will then discuss the issues of Compton telescopes, their limits, the background they experience, and the various techniques used to mitigate that background.

2.2 Gamma Ray Interaction processes with Matter

Gamma rays interact with matter, including instruments, mainly via three processes. Under 400 keV, gamma rays interact primarily via the photoelectric effect. Between 400 keV and 5 MeV, gamma rays interact predominantly via the Compton effect. Above 5 MeV, gamma rays primarily interact via pair production. The cross sections of these processes depend on the energy of the gamma ray and the atomic number of the material; a plot of the dominant interaction process in function of these two parameters is shown in figure 2.1 [41, p. 712]. This plot explains many of the choices made for building instruments in the medium-energy gamma-ray astronomy field, but before proceeding to Compton telescopes, we review the three interaction processes.

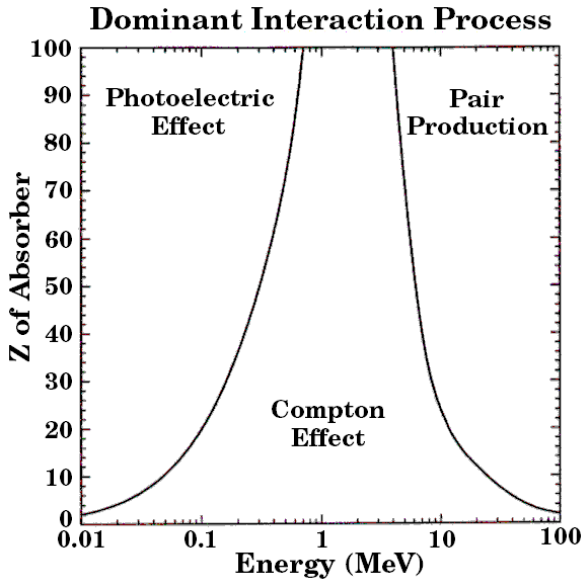

Figure 2.1: Gamma ray dominant interaction process with matter in function of its energy and the *Z* of the absorber (Evans, 1955 [41])

2.2.1 Photoelectric effect

The photoelectric effect is the absorption of a gamma ray by an atom which then ejects an electron called photoelectron, a diagram of the process is shown in figure 2.2. The effect was discovered in the 19th century and its explanation earned Albert Einstein his 1921 Physics Nobel Prize [42].

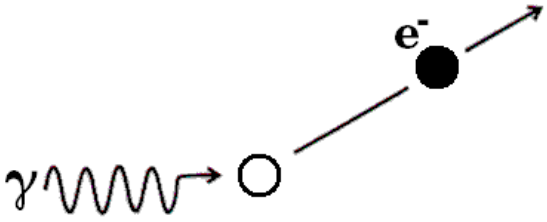

Figure 2.2: Photoelectric effect diagram, a gamma ray is absorbed by an atom which ejects an electron

The maximal kinetic energy of the ejected electron $Ek_{\text{e\_max}}$ is the energy of the incoming gamma ray E_γ minus the work function Φ of the material:

$$Ek_{\text{e\_max}} = E_\gamma - \Phi \tag{2.1}$$

The liberated electron will then quickly lose its energy by interacting with other atoms. The photoelectric effect is the dominant interaction process with matter for gamma rays with an energy under ~400 keV, see fig. 2.1. There is no single analytic expression for the photoelectric effect cross section, but for energies above the K-absorption edge, the cross section for the emission of a K shell electron is given by eq. 7-15 of [43]:

$$\sigma_{\text{phot}} = \frac{32\,\pi\,\sqrt{2}\,Z^5}{3\,(137)^4}\left(\frac{m_e\,c^2}{E_\gamma}\right)^{\frac{7}{2}}, \tag{2.2}$$

where $\boldsymbol{Z}$ is the material atomic number, $\boldsymbol{E_\gamma}$ the energy of the incoming gamma ray, $\boldsymbol{m_e}$ the electron mass and $\boldsymbol{c}$ the speed of light. This result is valid for $\boldsymbol{E_\gamma} << \boldsymbol{m_e c^2}$. As the energy increases, the 7/2 exponent goes to 1, see [43] for details; however Compton Scattering dominates before reaching such energies.

2.2.2 Compton Effect

The Compton effect was discovered by Arthur H. Compton who published his article "A Quantum Theory of the Scattering of X-Rays by Light Elements" in 1923 [44], which earned him the 1927 Physics Nobel Prize. The Compton effect is the scattering of an incoming gamma ray by a static electron, a diagram of the process is shown in figure 2.3. Unlike the photoelectric effect where the incoming photon is fully absorbed, the Compton effect produces an electron and a new photon of lower energy.

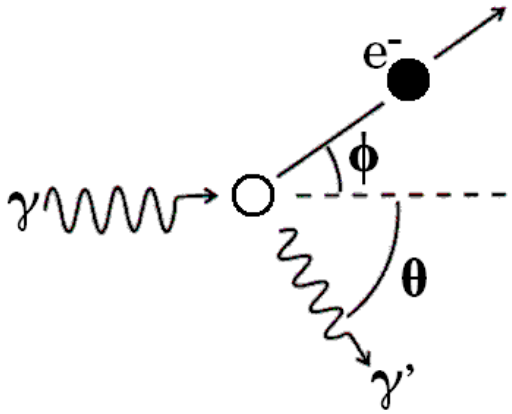

Figure 2.3: Compton effect diagram, a gamma ray is scattered by an electron

The energy of the scattered photon $E_{\gamma'}$ may be found with the conservation of relativistic energy and momentum, it is given by:

$$E_{\gamma'} = E_{\gamma}\left[1 + \frac{E_{\gamma}}{m_e\, c^2}(1 - \cos\theta)\right]^{-1} \tag{2.3}$$

The kinetic energy of the electron E_{e} is given by:

$$E_{\mathrm{e}} = E_{\gamma} - E_{\gamma'} \tag{2.4}$$

And the electron scatter angle ϕ given by:

$$\sin\phi = \frac{E_{\gamma'}}{c\,\gamma\, m_e\, v}\sin\theta \tag{2.5}$$

E_{γ} is the energy of the incoming gamma ray, θ the photon scatter angle, γ the electron Lorentz factor, and v its speed. The details of the problem can be found in Compton's paper [44].

The differential cross section is given by Klein-Nishina formula [80]:

$$\frac{d\sigma}{d\Omega} = \left(\frac{e^2}{4\,\pi\,\varepsilon_0\, m_e\, c^2}\right)^2 \frac{P(E_{\gamma},\theta)^2}{2}\left\{P\left(E_{\gamma},\theta\right) + P\left(E_{\gamma},\theta\right)^{-1} - 1 + \cos^2\theta\right\} \tag{2.6}$$

$$P\left(E_{\gamma},\theta\right) = \frac{E_{\gamma'}}{E_{\gamma}} = \left[1 + \frac{E_{\gamma}}{m_e\, c^2}(1 - \cos\theta)\right]^{-1}$$

One can integrate eq. 2.6 to get the total Compton Scattering cross section for one electron (eq. 7-16 of [43]):

$$\sigma_C = \pi \left(\frac{e^2}{4\,\pi\,\varepsilon_0\,m_e\,c^2}\right)^2 \left\{\left[1 - \frac{2(\gamma+1)}{\gamma^2}\right]\ln(2\gamma+1) + \frac{1}{2} + \frac{4}{\gamma} - \frac{1}{2(2\gamma+1)^2}\right\} \qquad (2.7)$$

$$\gamma = \frac{E_\gamma}{m_e\,c^2}$$

Finally, one can find the total Compton scattering cross section of an atom to incident gamma rays of energy E_γ by multiplying eq. 2.7 by its atomic number Z.

The Compton effect is the interaction process exploited for building Compton telescopes such as the prototype we built to observe the medium-energy gamma-ray range, between 500 keV and 10 MeV. It is the dominant interaction process with matter for gamma rays with an energy between 400 keV and 5 MeV, see fig. 2.1.

2.2.3 Pair Production

Pair production is the dominant interaction process with matter for gamma rays with an energy above ~5 MeV, see fig.2.1. Pair production is the process by which an energetic particle creates a particle and its anti-particle by interacting with a fourth particle necessary to absorb momentum. In our case, it is the production of an electron-positron pair by a gamma ray interacting with a nucleus or an electron, a diagram of this process is shown in figure 2.4.

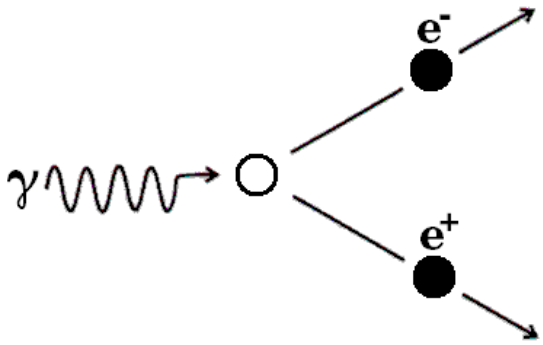

Figure 2.4: Pair production diagram, a gamma ray creates an electron-positron pair by interacting with a particle

Whenever a photon has two times the rest mass of a certain particle, it could "energetically" create the particle and its anti-particle. However momentum needs to be conserved, so a fourth particle is needed (photons do not decay by themselves creating pairs, they need to interact with another particle). For a gamma ray to create two particles of mass m by interacting with a particle of mass M, a minimal energy E_γ is required:

$$E_\gamma = 2\,mc^2\left(1+\frac{2m}{M}\right) \tag{2.8}$$

Equation 2.8 shows that the heavier the target particle, the closer the minimal photon energy E_γ is to the rest mass/energy of the two particles to be created. To create an electron-positron pair (1022 keV/c^2) from a hydrogen nucleus (938.272 MeV/c^2), the gamma ray needs at least 1023.11 keV of energy; heavier nuclei only makes the process marginally easier. The process dominates above 5 MeV when gamma rays can create electron-positron pairs by interacting with the electrons of the material; which becomes possible above 3.066 MeV (for an electron as the target, M=m=511 keV/c^2).

The cross section for electron-positron pair production is given by eq. 7-17 of [43]:

For $2\,m_e c^2 \ll E_\gamma \ll 137\,m_e c^2\,Z^{-1/3}$

$$\sigma_{\text{pair}} = \frac{Z^2}{137}\left(\frac{e^2}{4\,\pi\,\varepsilon_0\,m_e\,c^2}\right)^2\left[\frac{28}{9}\ln\left(\frac{2\,E_\gamma}{m_e c^2}\right) - \frac{218}{27}\right] \tag{2.9}$$

2.3 Compton Telescopes

A Compton telescope exploits the Compton effect to make observations in the 500 keV to 10 MeV energy range: this is the range in which gamma rays primarily interact via Compton scattering with low-Z detecting materials, see fig. 2.1. To build a Compton telescope, the energy and direction of the incoming gamma ray must be recovered from the products of a Compton scatter, see fig. 2.3 and equations 2.3, 2.4 and 2.5. The energy of the incoming gamma ray is easily recovered using eq. 2.4:

$$E_\gamma = E_{\text{e}} + E_{\gamma'} \tag{2.10}$$

The initial photon direction cannot be recovered without the electron momentum vector, which is usually unavailable except in special instruments able to track the recoil electron. However, with the velocity vector of the scattered photon and the energy values, the direction of the initial photon can be constrained to lie on the mantle of a cone of opening θ around the scattered photon velocity vector by inverting eq. 2.3:

$$\theta = \cos^{-1}\left[1 - m_e c^2\left(\frac{1}{E_{\gamma'}} - \frac{1}{E_\gamma}\right)\right] \tag{2.11}$$

Using eq. 2.10 to replace E_γ in eq. 2.11:

$$\theta = \cos^{-1}\left[1 - m_e c^2\left(\frac{1}{E_{\gamma'}} - \frac{1}{E_{\text{e}}+E_{\gamma'}}\right)\right] \tag{2.12}$$

Thus, with the two energy measurement of $E_{\gamma'}$ and E_e (the energy of scattered photon and the energy of the recoil electron), and the measurements positions, the initial photon energy can be recovered and its incoming direction constrained to a cone mantle.

2.3.1 Compton Telescope Concept

A Compton telescope starts with a detector in which the incoming gamma ray interacts via a Compton scatter: the Compton target. This is the first detector and is commonly referred to as D1. As seen from figure 2.1, to maximize the chance of a Compton scatter interaction in D1, low Z materials are favored. To measure the energy of the recoil electron, the D1 material is usually a scintillator coupled to a photomultiplier tube that measures the scintillation light. To let the scattered gamma ray escape the detector, the D1 material is usually not dense, or the detector made thin so that the thickness is smaller than the interaction length. The scattered photon must then be measured. Knowing that it has a lower energy than the initial photon, we see from fig. 2.1 that the photoelectric effect will often be the next interaction process. The second detector is the absorber, which is commonly referred as D2, for which a high Z material is favored to maximize the probability of a photoelectric interaction. To measure the energy of all the generated electrons in D2, the D2 material is again typically a scintillator that is coupled to a photomultiplier tube. The vector between the locations of the two energy deposits gives the direction vector of the scattered gamma ray. A diagram summarizing the Compton Telescope concept is shown in figure 2.5:

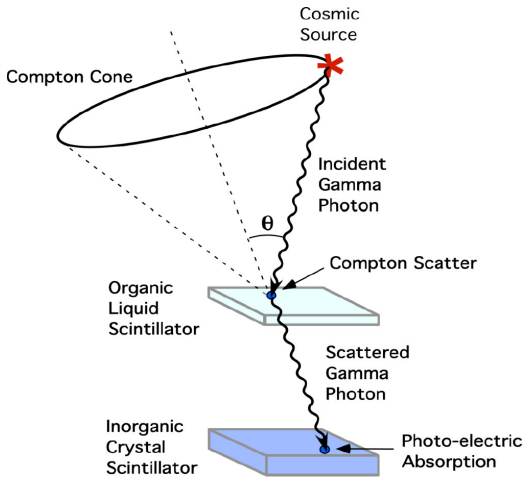

Figure 2.5: Compton telescope concept. An astronomical gamma ray interacts via the Compton effect with D1, a thin low Z scintillator detector that serves as the Compton target. The scattered gamma ray then often interacts via the photoelectric effect in D2, a high Z scintillator detector that serves as the absorber. The detectors are position sensitive to compute the axis of the Compton cone.

2.3.2 Image Reconstruction

One cone from one event does not yield an image, neither does many cones from multiple events. Then to produce an image, the circles from multiple events are projected onto a map and then some technique is used to reconstruct an image. A diagram of intersecting circles from the events of the 5 May 1991 gamma-ray burst observed by COMPTEL is shown in figure 2.6 [45].

Reconstructing an image from the event circles is not a trivial problem, and many techniques have been used. One well known method is the maximum-likelihood method [46] (1990), a more recent one (2000) was developed by Parra [47]. The paper from Parra [47] is also interesting for its references to other reconstruction methods. Because no imaging was performed with the FACTEL prototype, it is beyond the scope of this work to fully present any reconstruction method. The interested reader is refereed to [46], [47], and the references therein for further information on reconstruction algorithms.

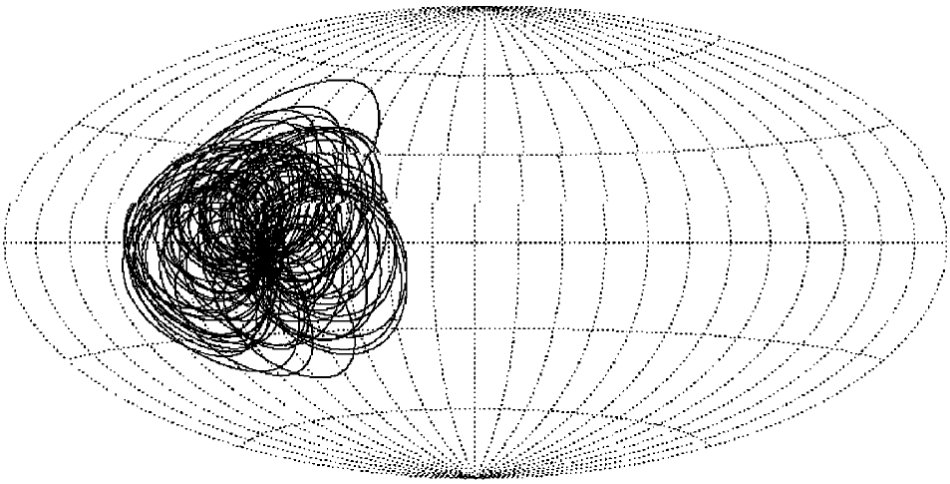

Figure 2.6: Intersecting circles from the events of the 5 May 1991 gamma-ray burst observed by COMPTEL

An important aspect of Compton Telescopes is the Angular Resolution Measurement (ARM), which is the difference between the computed angle derived from the energy measurements $\theta_{Compton}$ and the source actual angle θ_{Geo}:

$$ARM = \theta_{Compton} - \theta_{Geo} \tag{2.13}$$

When the source direction is known (θ_{Geo}), an ARM spectrum (or distribution) can be computed from multiple events. An ideal ARM spectrum should be centered on zero and as narrow as possible. The energy resolution of the detectors and the position resolution of the interactions affect the computed angle $\theta_{Compton}$, thus the ARM. A measured example from COMPTEL is shown in figure 2.7, it is a reproduction of figure 2 of [48]:

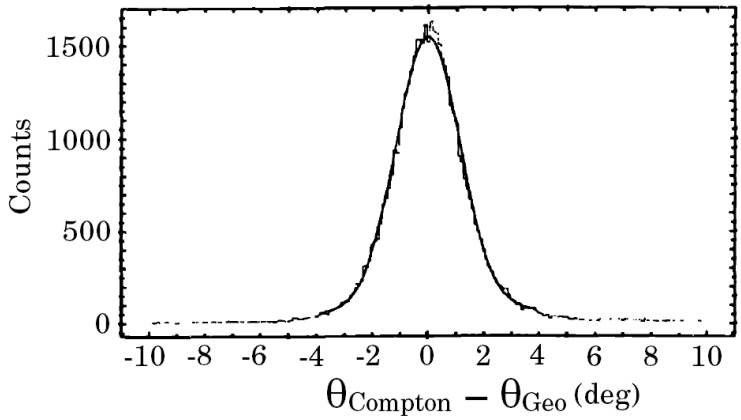

Figure 2.7: COMPTEL ARM distribution of 4.4 MeV gamma rays, the FWHM is 2.71° [48]

2.3.3 Energy Resolution

Because a Compton telescope measures the energy of the incoming gamma rays, it is a radiation spectrometer. A crucial aspect of Compton telescopes is how precise and accurate that measurement can be. This precision is expressed as the telescope energy resolution. Ideally, for a mono-energetic beam of gamma rays of energy $\boldsymbol{E}$, when a detector fully absorbs the gamma rays, it will record a spectrum following the normal distribution. The energy resolution definition for a detector is the Full Width at Half Maximum (FWHM) divided by the photon energy, this is shown in figure 2.8 and equation 2.14:

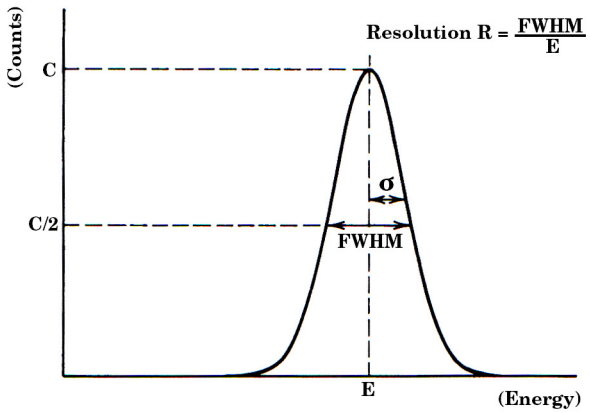

Figure 2.8: Energy Resolution Definition, it is the FWHM of the energy distribution divided by its mean value (the center) E.

$$Resolution\ R = \frac{FWHM}{E} \tag{2.14}$$

In practice, the resolution value is to be as small as possible: the smaller the resolution, the closer to the real energy the measured energy is. Also, the smaller the resolution and the better the telescope will be able to resolve two neighboring emission lines. Standard fitting software usually yields a Gaussian standard deviation σ, it is related to the ***FWHM*** by:

$$FWHM = 2\sqrt{2\ln 2}\,\sigma \approx 2.35482\,\sigma \tag{2.15}$$

2.3.4 Other Aspects of Compton Telescopes

Other attributes of a Compton Telescope are important. Some are the energy range, the field of view, the effective area, the sensitivity and the background rejection capabilities. The four first will be discussed here, and the fifth detailed in section 2.5.

The instrument energy range comes from the fact that detectors are themselves intrinsically sensitive to a certain energy range of incoming particles: they will not detect a particle with a too low energy while their response to high energy particles might level (saturate) and make measurements poor. Scintillator detectors used in the medium-energy gamma-ray range will typically have an energy range between 10 keV and 20 MeV. The energy range of the complete instrument will be a combination of the detectors energy range, geometry and other factors. A Compton telescope energy range always falls within 50 keV to 50 MeV.

The field of view (FoV) is a measure of the solid angle of acceptance. It is measured in steradians or square degrees; the full sphere is 4π steradians, or 41253 square degrees. The field of view is a classic case of quantity versus quality: larger FoV instruments will usually need longer times to make a detection because they observe

more background, while smaller FoV instruments can usually detect sources quicker by being focused. Some instruments have a large field of view while having the background from one part of the field of view not contaminating the measurements in another part of the field of view. Each instrument has its specific characteristics and one concept is favored over another depending on the application: if the need is a large continuous survey, a large FoV instrument will be favored, while if in-depth observations of specific regions of the sky are needed, a smaller FoV instrument will be favored. For a Compton telescope, the FoV is given by the area (solid angle) encompassed by the cone with the maximal angle of acceptance (the largest accepted scatter angle).

The effective area is a measure of the instrument "size" and is measured in units of area [cm^2]. A Compton telescope effective area is not simply the D1 detectors area, or the D2 detectors area, or the sum of those, but a calculation that also involves the incident gamma ray energy and the materials quantum efficiencies. It is an expression of the instrument photon collection ability and is usually computed by simulations.

A gamma-ray telescope sensitivity is a measure of the minimum flux it can measure at a given confidence level assuming a given observational time. It is measured in [Energy cm^{-2} s^{-1}] or [Photons cm^{-2} s^{-1}]. Like the effective area, the sensitivity is a calculation that depends on the gamma ray energy and other quantities such as the efficiency and the background reduction capabilities. Sensitivity is a critical property of a Compton Telescope: it expresses how faint the objects the telescope can study can be. Each new improvement step in sensitivity can lead to the discovery of new classes of objects in our universe. The FACTEL prototype we built is designed to significantly improve a Compton telescope sensitivity by improving its background rejection capabilities. As shown in fig. I.1 of the introduction, the medium-energy

gamma-ray range, from 500 kev to 50 MeV, trails in sensitivity compared to instruments in other energy ranges. A new step in sensitivity is what could transform fig. I.2 into the equivalent of fig. I.3 for the MeV range: a sky filled with many identified sources. For some historical perspective, HEAO C-1 launched in 1979 had "a sensitivity level of approximately 10^{-4} photons cm^{-2} s^{-1} over the energy range from 50 keV to 10 MeV" [22], while COMPTEL launched in 1991 had "a sensitivity in the 1.809 keV regime of 0.8 to 1.4×10^{-5} ph cm^{-2} s^{-1}" [20]. {A language note: increasing a telescope sensitivity, i.e. improving its sensitivity, actually refers to decreasing its sensitivity value, i.e. lowering the numerical sensitivity value.}

A final point is that Compton telescopes must operate above the Earth atmosphere which completely absorbs gamma rays, as shown in figure 2.9. Observations in the 500 keV to 50 MeV range must be conducted above the atmosphere either aboard a balloon or a satellite. This introduces many challenges to instrument design in terms of size (mass, volume), power consumption, telemetry, orbits, cost, thermal issues, vacuum operation, and the radiation background the instrument must endure.

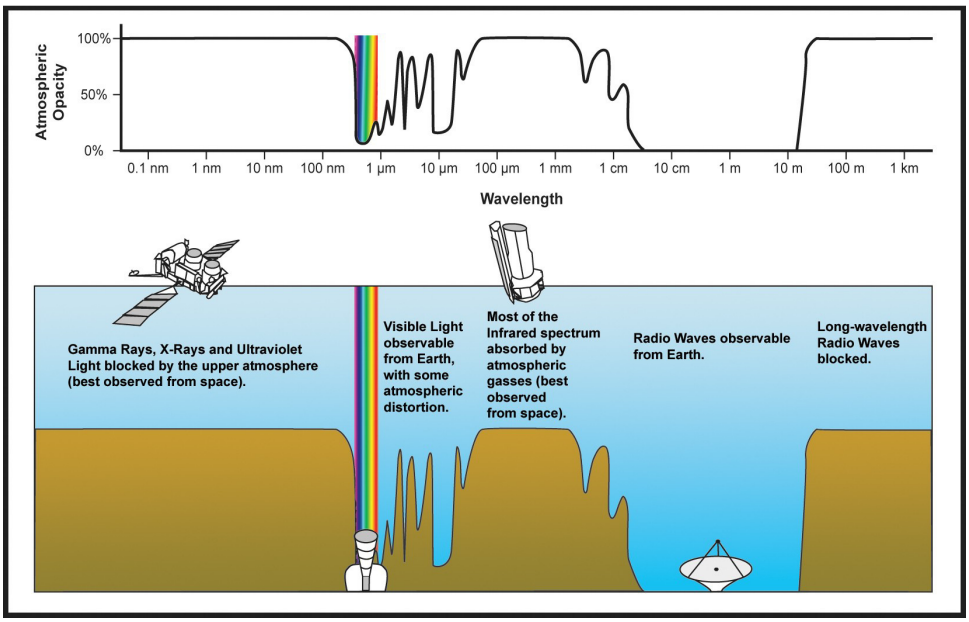

Figure 2.9: Atmospheric Electromagnetic Opacity, the atmosphere absorbs all gamma rays

2.4 The COMpton TELescope (COMPTEL) Instrument

The most successful Compton telescope was the COMpton TELescope (COMPTEL) [1] launched onboard the Compton Gamma-Ray Observatory (CGRO) in April 1991 by NASA as part of the Great Observatories Program, a diagram of the CGRO is shown in figure 2.10. The CGRO was deorbited in June 2000.

COMPTEL was a Compton Telescope built by the Max Planck Institute for Extraterrestrial Physics, the University of New Hampshire, the Netherlands Institute for Space Research and ESA Astrophysics Division. It successfully observed the gamma-ray universe between 0.8 and 30 MeV while it was in operation between 1991 and 2000. COMTEL had two layers of scintillators coupled to photomultiplier tubes. The first layer D1, the Compton target, was composed of NE 213A liquid scintillator (based on toluene), and the second layer D2, the absorber, was composed of NaI:Tl crystals. A schematic diagram of COMPTEL is shown in figure 2.11. COMPTEL was 2.6 m tall and had a diameter of 1.7 m. A detailed description of the COMPTEL experiment and its operating characteristics was described by Schönfelder et al. [1].

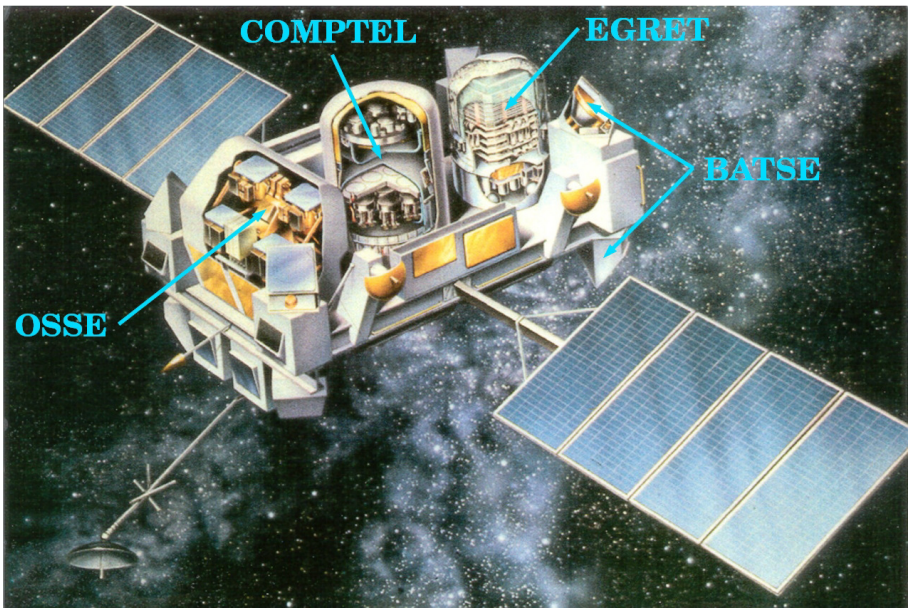

Figure 2.10: The CGRO Satellite, the instruments were BATSE (20 keV to 8 MeV), OSSE (50 keV to 10 MeV), COMPTEL (800 keV to 30 MeV), and EGRET (20 MeV to 30 GeV)

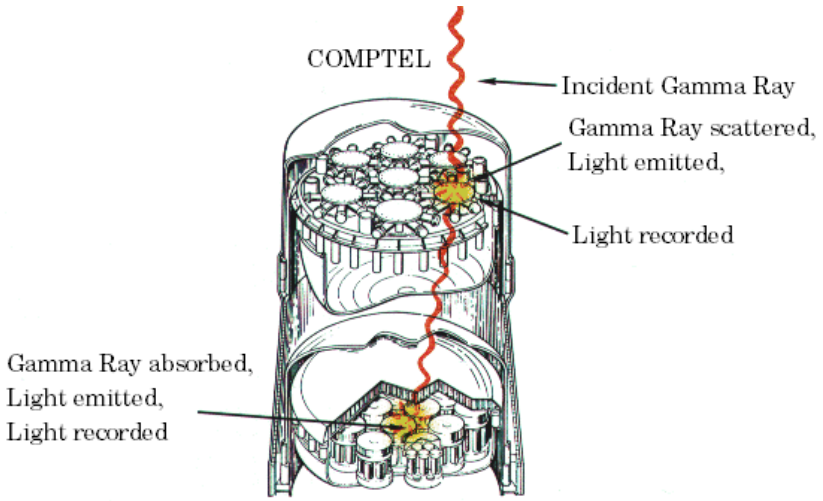

Figure 2.11: COMPTEL Diagram, the incident gamma ray Compton scatters in a D1 detector where one energy deposit is recorded, the scattered gamma ray is then absorbed in a D2 detector where a second energy deposit is recorded.

The first detector layer D1 recorded the energy of the recoil electron $\boldsymbol{E_1}$, while the second detector layer D2 absorbed the scattered gamma ray and recorded its energy as $\boldsymbol{E_2}$. Equations 2.10 and 2.12 are updated to:

$$E_\gamma = E_1 + E_2 \tag{2.16}$$

$$\theta = \cos^{-1}\left[1 - m_e c^2 \left(\frac{1}{E_2} - \frac{1}{E_1 + E_2}\right)\right] \tag{2.17}$$

COMPTEL results have already been presented in this work: an all-sky map in fig. I.2, parts of Cygnus X-1 spectra in fig. 1.2, the ^{26}Al all sky map in figure 1.4, and the events circles from a GRB in fig. 2.6.

The main characteristics of the COMPTEL instrument were [1]:

Energy Range: 0.8 to 30 MeV
Angular Resolution: between 1° and 2°
Energy Resolution: 8.8% FWHM at 1.27 MeV
Field of View: ~1 Steradian
Effective Area: between 10 and 50 cm^2 (depending on E)
Sensitivity: Could detect sources 20 times weaker than the Crab nebula within 14 days.

2.5 Compton Telescope Background

Space exposes Compton telescopes to the intense high-energy radiation environment above the atmosphere. High-energy particles are abundant both from space and Earth albedo: gamma rays, neutrons, cosmic-rays/protons, alpha particles, electrons, positrons, muons, etc. Contrary to other energy bands, like the optical or X ray bands, where the detectors can be shielded from the radiation coming from the sides or the back of the instrument with little material, gamma-ray astronomy must contend with penetrating radiation. All the high-energy particles mentioned can interact with the satellite, the instrument, and the detectors to produce gamma rays that can enter the normal data stream. While other telescopes receive a signal only through the telescope aperture, a gamma-ray telescope is bathing in an environment of gamma rays incoming from all directions. This background radiation ("background noise" or the "background") competes with the signal to be studied and is, of course, unwanted. Suppressing as much as possible the background noise leads directly to improving a Compton telescope sensitivity by improving the signal to noise ratio. The

sources of background signal that are relevant to Compton telescopes will now be reviewed.

2.5.1 Gamma-Ray Background

The first type of background for Compton telescopes is gamma rays themselves: gamma rays produced locally (within the satellite) can enter the data stream and mimic astronomical gamma rays. Many processes can create background gamma rays:

- Astronomical gamma rays can interact with the satellite passive material prior to entering the detectors and create background gamma rays originating from the spacecraft.
- Cosmic or albedo high-energy charged particles such as electrons can create a gamma ray via bremsstrahlung by interacting with the satellite material.
- Protons can create neutral pions that will decay producing gamma rays.
- Protons, neutrons and ions can interact with a nucleus and trigger a nuclear reaction that will create an excited or unstable nucleus that will decay producing gamma rays.
- Positrons annihilation produces 511 keV gamma rays.

These gamma rays are the foremost source of background noise for Compton telescopes, and have been studied in detail and categorized into four types (A, B, C and D) of gamma ray background events; the basis for these categories comes from Kappadath [51].

Type A events are gamma rays produced within the satellite passive material which then interact "normally" by Compton scattering into a D1 detector and then being absorbed in a D2 detector, a diagram is shown in figure 2.12. This process is the same as for the astronomical gamma rays to be observed, making type A events particularly difficult to suppress.

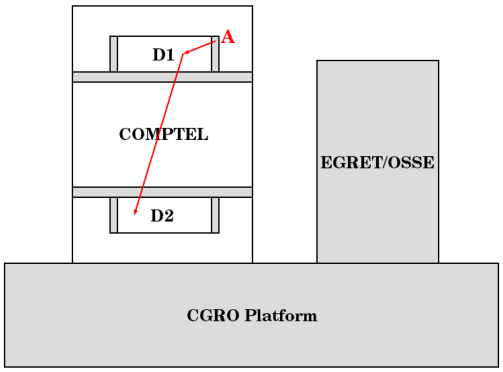

Figure 2.12: Type A Background event: a locally produced gamma ray enters the valid data stream

Type B events are random coincidence events: two independent gamma rays interacting in the D1 and D2 layers within the correct time interval to trigger a valid event measurement by the instrument. This process is shown in figure 2.13. The two photons may both be of cosmic origin, or one from space and one produced within the satellite, or both originating from the structure of the satellite.

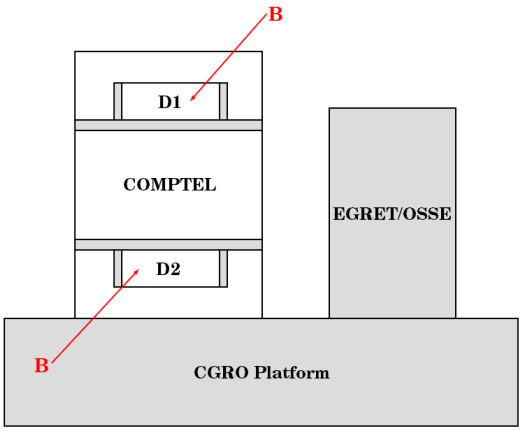

Figure 2.13: Type B Background event: two random gamma rays interact in each detector layer within the right time interval

Type C events are created from two gamma rays emitted quasi-simultaneously by the same source within the satellite passive material. Typically, these come from excited nuclei created by nuclear reactions that emit multiple gamma rays as they de-excite. As for the Type B events, if these gamma rays then interact within each detector layer within the right time window, the interactions will be registered as the two parts of a valid event. This process is shown in figure 2.14. An example of a type C background event is when a nuclear reaction produces a positron: the positron will quickly annihilate with an electron and produce two 511 keV gamma rays. This would not seem to be a problem because the gamma rays are emitted in opposite directions, however the nuclear decay could occur between the detectors, or the outgoing gamma ray could interact and be deflected back into one detector.

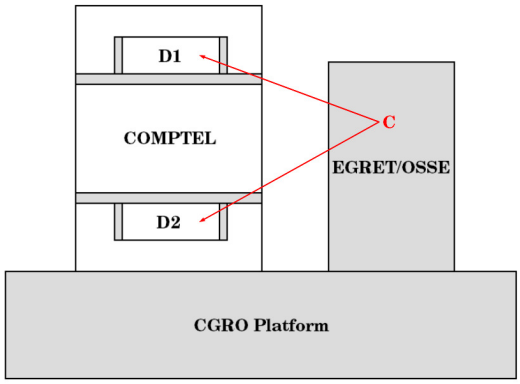

Figure 2.14: Type C Background event: two gamma rays from a nuclear reaction interact in each detector layer within the right time interval

The final Type D background events are cosmic-ray induced gamma-ray showers. Cosmic rays are high-energy protons or ions. When a proton in the GeV range interacts with the material of the satellite, the initial proton energy will be dissipated by a cascade effect creating an electromagnetic shower in the satellite. A diagram of this process is shown in figure 2.15. Just as for the Type B and C events, if two photons interact in the D1 and D2 layers within the right time interval, the instrument will register a valid event.

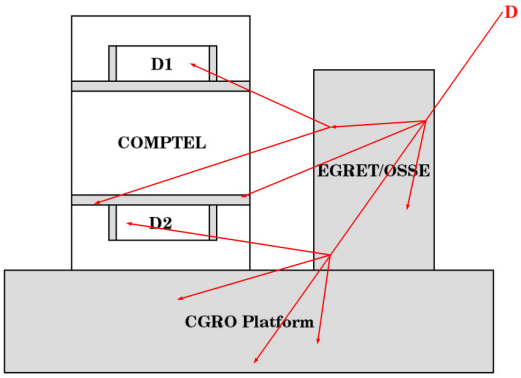

Figure 2.15: Type D Background event: a cosmic ray creates a shower and two gamma rays interact in each detector layer within the right time interval

2.5.2 Neutron Background

Neutrons are the second most important source of background events for Compton telescopes, and both high-energy and low-energy neutrons can lead to background. Like gamma rays, neutrons are neutral particles and relativistic neutrons are in many ways like gamma rays: a neutron going at 90% of the speed of light (1.2 GeV of kinetic energy) and interacting in both detector layers will appear much like a gamma ray for the instrument. Medium to low energy neutrons can interact multiple times with the spacecraft and thermalize, then the low-energy thermal neutron can be captured creating a gamma ray, see eq. 1.12. Thermal neutrons are particularly problematic for the D1 detectors. As described in section 2.3.1, the D1 detectors are the Compton target, and to maximize a Compton scatter interaction, low Z materials such as organic scintillators, partly composed of hydrogen, are used. Through the neutron capture process of eq. 1.12, a thermal neutron entering a D1 detector can lead to the creation of a 2.2 MeV gamma ray directly within the detecting material of the first layer. Then, this gamma ray can enter the data stream by interacting in a D1 and a D2 detector. Another important reaction is high-energy neutrons interacting

with carbon nuclei leading to the prompt emission of a gamma ray, $^{12}C(n, \gamma X)$. Neutrons usually not interacting with the anti-coincidence shields, the reaction they produce within the D1 detector may lead to a valid gamma-ray D1 to D2 event.

2.5.3 Charged Particles and Nuclear Activation

Any charged particle with sufficient energy can produce gamma rays, and any charged particle entering the spacecraft will inevitably interact with the electrons or nuclei of the material, losing its energy. Electrons can produce gamma rays via bremsstrahlung, positrons will annihilate with electrons and create gamma rays, protons will knock off electrons that can create gamma rays, and muons and ions will also create gamma rays. Evidently, anything that is not a gamma ray is a potential source of background events for a gamma-ray telescope. Gamma rays can also produce background through electromagnetic cascades, photo-activation, and interactions with the spacecraft rather than with the detectors.

The final source of background events in Compton telescopes is nuclear activation. Some nuclear reactions create isotopes with half-lives longer than a few seconds, those unstable nuclei will build up within the spacecraft material and decay randomly over an extended time period, many decays create gamma rays and add to the background. As an example, the activation background for the COMPTEL instrument was studied extensively by Weidenspointner et al. [52]. The authors found that eight isotopes contributed mainly to this type of background: ^{2}H, ^{22}Na, ^{24}Na, ^{28}Al, ^{40}K, ^{52}Mn, ^{57}Ni and ^{208}Tl. For example, the aluminum (^{27}Al) that composes a substantial part of the spacecraft mass can be activated by neutrons or protons to create ^{24}Na. ^{24}Na has a half-life of 14.96 hours and will decay producing both a 1368.6

and a 2754.0 keV gamma rays (a C type background event). The reactions for ^{24}Na creation by neutrons or protons interacting with ^{27}Al are as follow:

$$^{27}_{13}\mathrm{Al} + \mathrm{n} \rightarrow {}^{24}_{11}\mathrm{Na} + \alpha \tag{2.18}$$

$$^{27}_{13}\mathrm{Al} + \mathrm{p} \rightarrow {}^{24}_{11}\mathrm{Na} + 3\mathrm{p} + \mathrm{n} \tag{2.19}$$

^{24}Na will then decay within a day to ^{24}Mg following:

$$^{24}_{11}\mathrm{Na} \rightarrow {}^{24}_{12}\mathrm{Mg} + \mathrm{e} + \overline{\upsilon_{\mathrm{e}}} + \gamma(1368.6, 2754.0\ \mathrm{keV}) \tag{2.20}$$

A spacecraft is composed of many materials with many isotopes, and because the spacecraft is bombarded by many particle species with a wide energy range, the possible reactions are numerous and many isotope species can be created. The unstable isotopes can have a wide range of half-lives, some of them decaying within seconds while others can build up within the satellite for years. This makes nuclear activation a complex problem.

2.6 Compton Telescopes Background Suppression

Most of the events registered by a Compton telescope orbiting the Earth are background events. The Earth albedo and the basics of space physics create an intense radiation environment in which the instrument resides, while the astronomical signals are comparatively weak. In practice, the astronomical signals are overwhelmed by the background events, and most of the work of developing a Compton telescope is to find ways to mitigate and suppress as much as possible the background noise to extract the weak astronomical signal. The basic tools of Compton telescopes background suppression will now be reviewed.

2.6.1 The Dome and Anti-Coincidence Panels

The first layer of background suppression is the dome and the anticoincidence panels. The dome provides a mechanical structure for the instrument, protects it from dust and micrometeorites and protects the detectors and photomultiplier tubes from lower energy radiation such as light and X-rays. Photomultiplier tubes are sensitive to light and the instrument must be operated in complete darkness. The second basic background suppression component are the anti-coincidence panels, commonly referred to as the "ACPs", the "panels", the "Antis", or the "AC panels". For COMPTEL, the anti-coincidence systems also served as a dome, as seen in figures 2.10 and 2.11. Each of the COMPTEL layers was enclosed in two anti-coincidence systems. These were plastic scintillator round slabs that surrounded each detector layer. The anti-coincidence panels help suppress background events by detecting any charged particles traversing them. Charged particles such as protons, electrons, positrons or ions will inevitably interact with the material of the instrument, depositing some energy. By surrounding the detectors with an anti-coincidence box, a signal will be generated by any charged particle crossing the panels. This signal from the anti-coincidence panels will trigger an electronic flag used to suppress the events that would be registered by the telescope in coincidence with that signal The anti-coincidence panels do not filter neutrons, or background gamma rays such as gamma rays produced by charged particles interacting with the dome or produced by a nuclear reaction within the spacecraft (activation), however they do provide a valuable and critical layer of background suppression.

2.6.2 The Time of Flight (ToF) technique

An important technique of background suppression for Compton telescopes is the Time of Flight (ToF) technique. The ToF suppression capability of a Compton telescope directly improves overall background suppression capabilities. Improving the ToF is the main driver for the FACTEL project and where it takes its name "FAst Compton TELescope".

The Time of Flight measurement is the time difference between the D1 signal and the D2 signal. The time when the D1 detector is triggered is T_1 and T_2 the time when the D2 detector is triggered. Then the Time of Flight is defined as:

$$ToF = T_2 - T_1 \tag{2.21}$$

For a gamma ray Compton scattering in a D1 detector and then being absorbed in a D2 detector, the Time of Flight value will be positive and correspond to the distance divided by the speed of light: the time it takes for a gamma ray to travel from the D1 layer to the D2 layer. The ToF technique is a powerful tool that can identify many background events. The ToF value of an event is required to be within a certain window to be considered valid.

Random coincidences like type B background events will have an uniformly distributed ToF spectrum, thus most of the type B events will be rejected by being outside the proper ToF window. All the events coming upwards, either from the spacecraft or from the Earth albedo, will be from the D2 layer to the D1 layer (D2→D1). As the D2 detector will have been triggered before the D1 detector, T_2 will be smaller than T_1, the ToF value will be negative, and the event will be rejected. Many of the type C events (two gamma rays emitted by the same source) coming from the lower parts of the spacecraft will not be within the proper ToF window and

will be rejected. Neutrons not going fast enough will not have a ToF value within the designated ToF window for photons traveling from a D1 to a D2.

Only events with one interaction in a D1 detector, one interaction in a D2 detector and having its ToF value within the designated ToF window will be retained as a valid event. The center of the ToF window corresponds to the ToF value given by a photon traveling from the D1 to the D2 layers (D1→D2).

As an example, figure 2.16 shows a schematic representation of the ToF distribution of events from COMPTEL [52] when pointed at the local zenith:

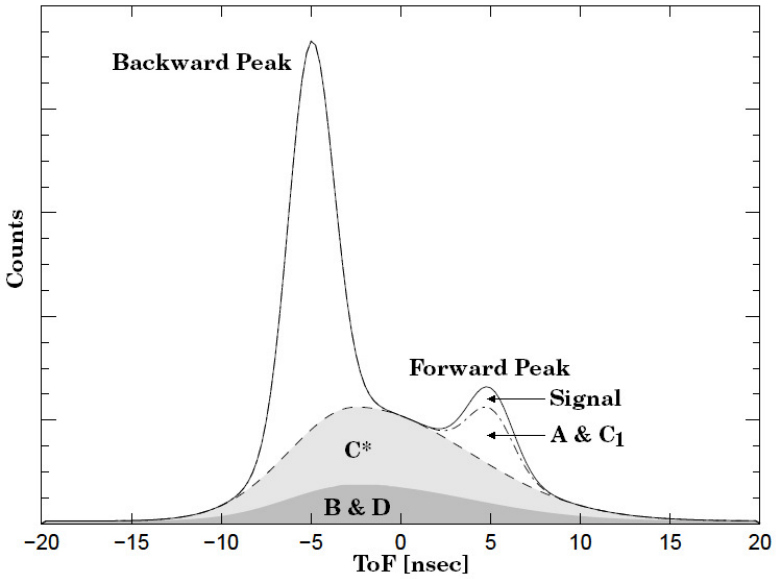

Figure 2.16: Schematic representation of the ToF distribution of events from COMPTEL. Three major components can be discerned: the ToF backward and forward peak, centered at ToF values of about −5 ns and +5 ns respectively, and an underlying continuum distribution. [52]

Three major components can be identified in figure 2.16:

- The ToF backward peak centered at a ToF value of about −5 ns
- The ToF forward peak centered at a ToF value of about +5 ns
- An underlying continuum distribution

The backward peak is composed of all types of background events originating in and around the D2 layer, but most are upward moving gamma rays from Earth albedo. The forward peak contains the celestial signal as well as background events originating in and around the D1 layer. The ToF continuum is dominated by background events originating in the instrument structure between the two detectors and the spacecraft structure in general. The relative magnitudes of the different components are only represented approximately. {From [52] fig. 3 caption with modifications.}

The signal portion of the distribution is small compared to the rest of the distribution, and this is the medium-energy gamma-ray astronomy situation: a small signal within a large background. However, as we see in fig. 2.16, the ToF measurement alone can be used to identify most of the background events. For example, most of the events are in the backward peak (D2→D1) coming from the lower massive parts of the spacecraft, see figure 2.10, or originating from the Earth albedo. Of note are the type A background events, gamma rays locally produced and scattering normally in the telescope: they are effectively mixed with the astronomical signal. The distribution of type B random coincidences and type D cascades takes a bell shape because of the spacecraft geometry. Type C background events coming from multiple gamma-rays decays must be separated into the events occurring near D1, noted as C_1, and the events coming from the rest of the spacecraft, referred to as C*. The C_1 events near D1 have a ToF distribution much like a normal Compton scatter: while the first photon interacts quickly in D1, the second travels to D2 and interacts with a time of flight value within the ToF window. The C* events will however exhibit a distribution influenced by the spacecraft geometry and mass distribution.

Figure 2.16 is important because FACTEL results will be compared to this figure to assess the success of our prototype.

The ToF resolution is the FWHM of a peak, and is expressed in time units: COMPTEL had a 4 ns ToF resolution. For COMPTEL, the accepted ToF window was from 4 to 8 ns, corrected for path length.

2.6.3 Pulse Shape Discrimination (PSD)

Pulse Shape Discrimination (PSD) is a technique to discriminate between gamma-ray and neutron interactions, thus providing a way to reject background events originating from neutrons. Gamma rays interact primarily with electrons in a material either by the photoelectric effect or by Compton scattering. Neutrons must strike a nucleus to interact. Ultimately, the energy deposits in detectors come from charged particles losing their energy by interacting with electrons. (Charged particles like electrons and protons lose their energy "normally" by interacting with electrons, while neutral particles such as gamma rays and neutrons must produce an energetic charged particle to lose energy.) The difference between gamma rays and neutrons is that gamma rays produce fast electrons (light particles) while neutrons produce slow particles such as protons or alphas (heavy particles). For certain scintillators, this leads to a difference in the signal shape: electrons are light particles that excite states that decay quickly compared to a heavier proton that loses its energy by exciting states that decay more slowly, this is shown in figure 2.17 [53].

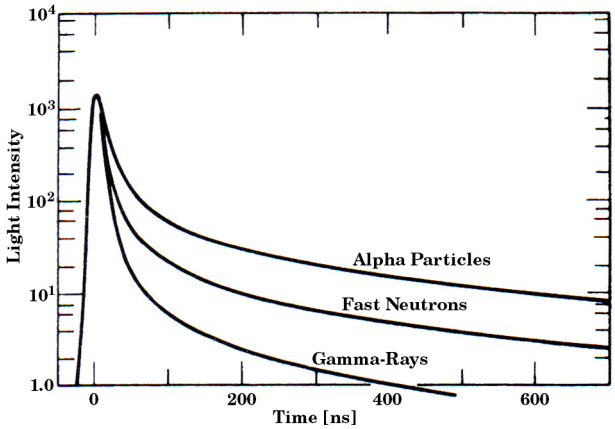

Figure 2.17: The time dependence of scintillation pulses in stilbene when exited by radiations of different types [53]

By analyzing what fraction of the signal is within the signal tail compared to its peak, the particles species interacting in the detector can be identified. This technique is known as Pulse Shape Discrimination (PSD) and it is widely used in gamma-ray and neutron instruments to distinguish the two species. When a scatter plot of the "fraction of the signal in the tail" (y axis) versus the "energy deposit" (x axis) is constructed, gamma-ray and neutron interactions can clearly be identified, as seen in figure 2.18.

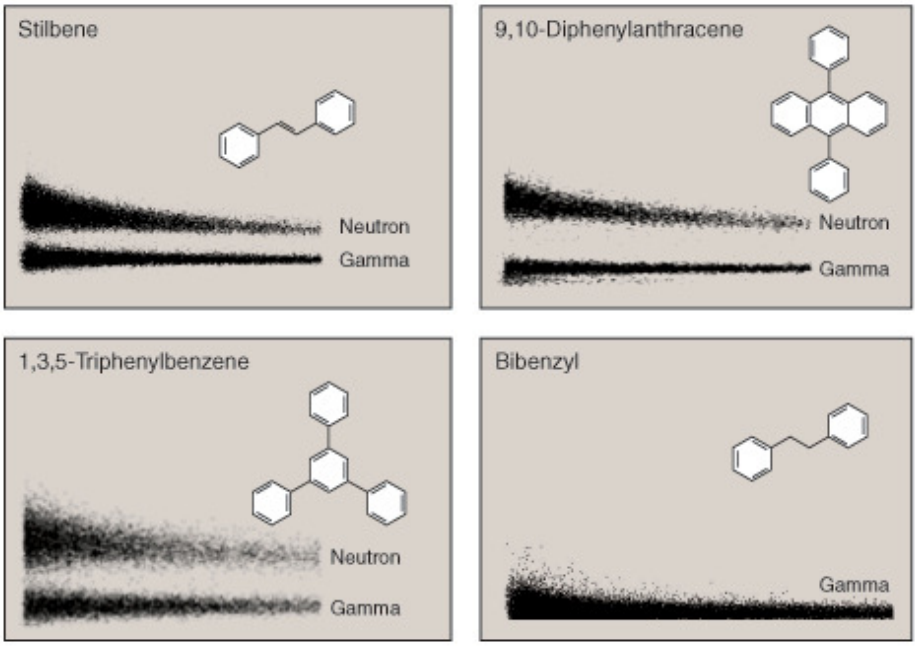

Figure 2.18: PSD for different materials [See Figure Credit]

As seen in fig. 2.18, different materials have different PSD capabilities. A spectrum with only the "fraction of the signal in the tail" or "Delayed Charge / Total Charge" can also be produced to discriminate between gamma-ray and neutron interactions, an example is shown in figure 2.19. It is the projection on the y-axis of a fig. 2.18 plot.

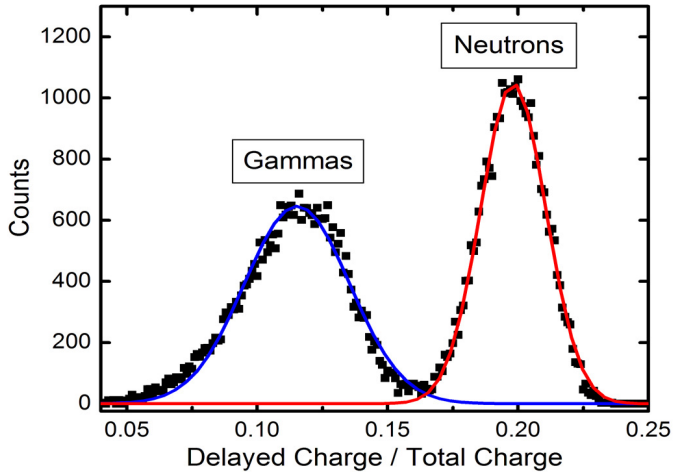

Figure 2.19: Gamma ray and neutron interactions are clearly discriminated using PSD with Plastic Scintillators [See Figure Credit]

For Compton Telescopes, D1 detectors often have PSD properties to suppress the events generated by neutrons.

2.6.4 Materials

The last method for background mitigation is the choice of materials. Material choices is a passive rather than active (ToF, PSD) method of background suppression. The method consists to carefully choose materials to avoid certain background channels: bombarding particles are thus less likely to create background events. Lessons in material choices were learned from the COMPTEL experience and analysis.

The first choice is to borate the top anti-coincidence panel. The anti-coincidence panels are composed of an organic plastic scintillator, which contains hydrogen that thermal neutrons can interact with releasing a 2.2 MeV gamma ray in the vicinity of the D1 detectors. The 2.2 MeV gamma rays coming from the sides or under the D1 layer are not of critical concern because the Compton angle formula (eq. 2.17) will lead to large angles and those events will be rejected. However, 2.2 MeV gamma rays coming from the aperture above D1 are of concern because they can be registered as valid gamma rays.

The hydrogen-neutron capture process is a process occurring both within the celestial phenomena to be studied and within an instrument. In the later case it is background to be mitigated. The solution to mitigate this problem is to add a small fraction (1%) of ^{10}B to the top anti-coincidence panel. ^{10}B is an isotope that has one of the largest thermal neutron capture cross-section and is commonly used for thermal neutron shielding. The reaction for ^{10}B neutron capture is as follow:

$$^{10}_{5}\mathrm{B} + \mathrm{n} \rightarrow {}^{7}_{3}\mathrm{Li}^{*} + \alpha \tag{2.22}$$

$$^{7}_{3}\mathrm{Li}^{*} \rightarrow {}^{7}_{3}\mathrm{Li} + \gamma(478\ \mathrm{keV}) \tag{2.23}$$

The resulting 478 keV gamma ray is of lesser concern because it falls below the usual energy range of Compton telescopes, for example the COMPTEL energy range was from 0.8 to 30 MeV. 478 keV is close to the 511 keV annihilation line from positrons, however the energy resolution is good enough for this not to be a problem.

Thus, by borating the top anti-coincidence panel, problematic 2.2 MeV gamma rays are shifted to 478 keV gamma rays that are of lesser concern.

The second material choice again concerns neutron capture by hydrogen, but is much more radical: deuterate the D1 scintillator material. The thermal neutron

capture process by hydrogen within a D1 detector is particularly critical because it creates a 2.2 MeV gamma ray directly within the detecting material of the telescope, putting that gamma ray in a good position to enter the normal data stream. Neutron capture by hydrogen (eq. 1.12) produces deuterium, so the solution is to deny the opportunity for thermal neutrons to be captured by hydrogen nuclei. We do this by replacing those hydrogen atoms in the scintillator with deuterium atoms. This change does not significantly modify the scintillation properties; however it does solve the neutron capture problem in D1. One minor drawback of this solution is the increase of the material neutron cross-section: deuterium is composed of two nucleons instead of one nucleon for hydrogen, so it inevitably increases the cross-section for nuclear reactions. The new material is thus more prone to interact with neutrons, however PSD can be used to detect and suppress these events. The anti-coincidence panels could also be deuterated; however this is currently a costly option.

The final material solution to limit background events is to reduce as much as possible passive materials and metals in the vicinity of the D1 detectors. The ToF measurement along with the computed scatter angle can filter much of the background occurring in the instrument, however there is a region close around the D1 layer where the ToF technique is not effective against type C events, while the scatter angle cannot filter all type A background events. The solution is to limit as much as possible passive materials, especially metals, around the D1 detectors to limit background particles interaction targets. Metals are particularly problematic because they are denser and will interact with electrons and protons creating gamma rays, and metals are more likely to be activated by protons and neutrons to create long-lived unstable isotopes. A commonly used material for spacecraft is aluminum which produces ^{24}Na when interacting with protons and neutrons (see equations 2.18, 2.19 and 2.20). ^{24}Na has a half-life of 14.96 hours and decays producing 1368.6 and 2754.0

keV gamma rays. Background events can thus be significantly mitigated by limiting the amount of passive materials and particularly metals around the D1 layer.

2.6.5 Summary of background suppression

The solutions to the various background types for Compton telescopes are now summarized.

- Type A background events are single gamma rays and are countered by material choices around the D1 layer.
- Type B random coincidences are mostly filtered by the ToF value.
- Type C multiple gamma rays decays are solved by material choices around the D1 layer and the ToF value for the rest of the instrument.
- Type D gamma ray showers events are suppressed with the ToF value.
- For neutrons, pulse-shape discrimination, time of flight, no metals around the D1 detectors, borating the top anti-coincidence panel and deuterating the D1 scintillator provides a combined solution to neutron background events.
- Charged particles are detected by the anti-coincidence panels.
- Limiting metals around the D1 detectors limits the activation problem.

2.7 Summary

This chapter introduced the theory behind scintillator based Compton telescopes, specifically the COMPTEL experience. Gamma rays interact with matter mainly via three processes: the photoelectric effect, Compton effect, and pair production. To build a Compton telescope to observe the gamma rays in the medium-energy range (500 keV to 30 MeV), a first D1 layer serves as a Compton target for the

incoming celestial gamma rays, then a second D2 layer serves as the absorber for the scattered gamma ray. We reviewed how to retrieve the energy and direction of the incoming gamma ray, then outlined the principal characteristics of a Compton telescope: the energy resolution, the ARM, the energy range, the Field of View, effective area and sensitivity. We presented a successful past Compton telescope, COMPTEL, in orbit between 1991 and 2000. The principal sources of background events that limited COMPTEL sensitivity were type A single gamma rays, type B random coincidences, type C multiple gamma rays decays, type D gamma ray showers, neutrons, and high-energy charged particles. To suppress those background events, we use a dome and anti-coincidence panels, the Time of Flight (ToF) technique, and the Pulse Shape Discrimination (PSD) technique. For a next generation of instruments, based on the COMPTEL experience, we propose to borate the top anti-coincidence panel, deuterate the D1 detectors material, and limit the passive materials (especially metals) around the D1 detector layer.

CHAPTER 3

The FACTEL Instrument

3.1 Introduction

We focus in this chapter on the development of the FAst Compton TELescope (FACTEL) prototype. We review the components and material choices, then the instrument calibration (detectors, ToF, PSD) and its simulations validation.

As seen in the last sections of the second chapter, a Compton Telescope can only be operated in space. This places the instrument in an intense radiation environment that creates many unwanted background sources that need to be suppressed in the analysis. From the COMPTEL experience, we developed new techniques in material choices to mitigate background events, and described how the Time of Flight system plays a key role in suppressing many types of background events. The material lessons gained from COMPTEL are one aspect of the development of a future Compton telescope, but the real breakthrough is the recent development of "fast" inorganic crystal scintillators. Cerium doped lanthanum bromide ($LaBr_3$:Ce) offers a timing figure of merit five times better than the thallium doped sodium iodine (NaI:Tl) used by COMPTEL: 0.5 for $LaBr_3$:Ce versus 2.6 for NaI:Tl (these numbers will be explained shortly). The COMPTEL 4-ns ToF resolution can now realistically be brought down under 1 ns, leading to a dramatic background suppression improvement, leading to an improved sensitivity for the telescope, finally leading to a telescope capable of observing fainter fluxes from

astronomical gamma-ray sources. This improvement is shown in figures 3.1 and 3.2. The background types (A, B, C and D) have been detailed in section 2.5.1, and a representation of a COMPTEL ToF spectrum is shown in fig. 2.16. The point to understand with these two figures is that by having a low ToF resolution (wide peaks), the astronomical signal observed by COMPTEL had to compete with the background sources. This led to a low signal to noise ratio, and consequently to a low sensitivity. On the other hand, fast scintillators allow a small ToF resolution window, which better separates the real signal from background sources. This leads to an increased signal to noise ratio, and consequently an increase in sensitivity. In the case of figures 3.1 and 3.2, the improvement in the signal to noise ratio is around a factor 20.

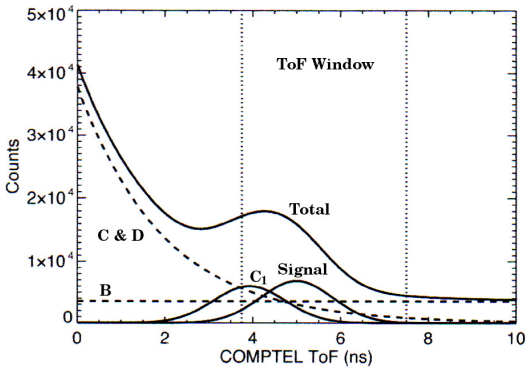

Figure 3.1: COMPTEL ToF spectrum from 4.2 to 6 MeV

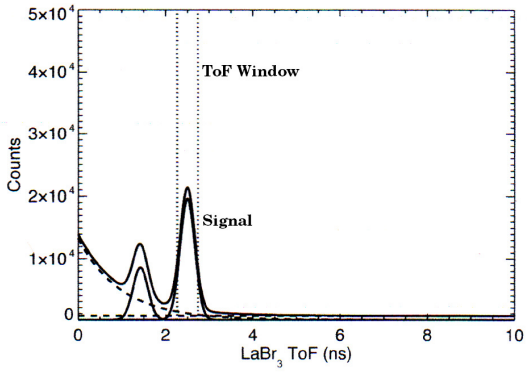

Figure 3.2: Estimated ToF spectrum of a Compton Telescope using $LaBr_3$ for D2

Figures 3.1 and 3.2 are the reason why the FACTEL prototype exists, they come from the proposal submitted to the NASA that led to the funding of the FACTEL project. As shown, by using fast scintillators the valid events ToF window can be drastically restricted, suppressing most background events. A 500-ps ToF window versus 4 ns makes it much more difficult for background events to infiltrate the valid events stream. The valid signal is no longer buried in the noise as is the case for a 4-ns ToF window. The goal of the FACTEL project was to build a small Compton Telescope prototype to show that a sub-nanosecond ToF window was

achievable. We show in the rest of this work how we were successful in achieving a ~1-ns ToF window and why we fell short of our objective of 500 ps.

3.2 Concept and Materials

The FAst Compton TELescope (FACTEL) prototype is a small Compton Telescope designed to demonstrate that a sub-nanosecond ToF resolution is achievable. Based on COMPTEL, it is a two-layer Compton telescope, D1 and D2. The D1 layer is composed of deuterated organic liquid scintillator detectors that serve as the Compton target. The D2 layer is composed of $LaBr_3$ fast crystal scintillator detectors that absorb the scattered gamma ray. Since timing is crucial for the project, the combination of scintillators-photomultiplier tubes (PMT) was chosen over semi-conductor detectors. Background suppression is key to the sensitivity of a Compton Telescope, and a very narrow ToF window is key to background suppression. While semi-conductor detectors have their advantages (Energy resolution, positioning), they do not match the speed of a scintillator-PMT combination. Since speed is what narrows the ToF window, our development path was to use scintillators-PMT combinations.

Considering the project scale, we opted for three cylindrical detectors of 1 inch (2.54 cm) of diameter and 1 inch (2.54 cm) in length for each layer, totaling six detectors. The three D1 detectors will be referred to as D11, D12 and D13 while the three D2 detectors will be referred to as D21, D22 and D23. Since 1 ns at the speed of light is 30 cm, the final distance between the two telescope layers was chosen to be 31.75 cm: with a 31.75 cm on-center distance between the layers, the D1→D2 ToF peak would be near 1 ns, while the D2→D1 ToF peak would be near –1 ns. With a 1 ns peak width (0.5 ns on each side), the ToF peaks would be well separated. The pitch

between the detectors of a layer is 2 1/8″ (5.40 cm). An engineering model of the FACTEL instrument is shown in figure 3.3; the only difference between the initial model shown in fig. 3.3 and the final instrument is that the D2 electronic cards were flipped to put the D2 layer closer to the D1 layer. All the components of the instrument will be described in the next sections. For a quick overview, a picture of one D1 detector, one D2 detector, and one PMT is shown in figure 3.14. Then one detector is glued to one PMT, sled into a tube, and the assemblies mounted horizontally side by side, see figure 3.10. The D1 detector layer is within an anti-coincidence panel box shown in figure 3.8. Figure 3.3 is to be compared to the picture of the final instrument shown in figure 3.11.

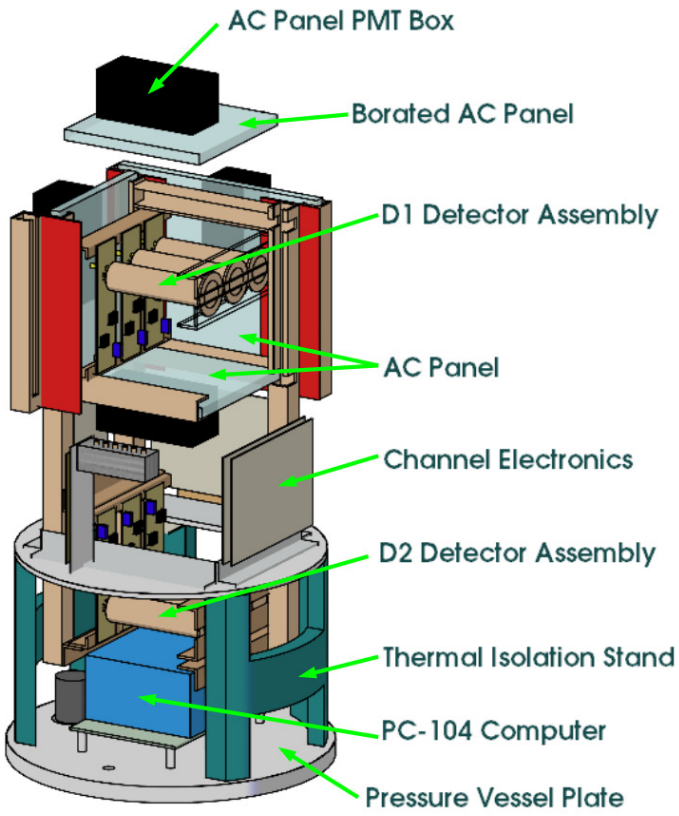

Figure 3.3: The FACTEL Engineering Model. The D1 layer is composed of deuterated organic liquid scintillator detectors, the D2 layer is composed of $LaBr_3$ detectors. The detectors are 1″x1″ cylinders, the layers are separated by 31.75 cm, detectors in a layer are separated by 5.40 cm. The D1 layer is enclosed in an anti-coincidence box.

3.2.1 The D1 Detectors

The scintillator chosen for the D1 detectors was Eljen Technologies EJ-315. It is an organic liquid scintillator based on benzene with 99% of its hydrogen replaced by deuterium to prevent thermal neutrons from being captured by hydrogen. The liquid is enclosed in a 1.5 mm thick borosilicate glass cell of one inch diameter and 1.26″ in length (2.54×3.20 cm). The cell is sealed by an aluminum plug and 9% of the cavity filled with an inert gas. The schematics of the D1 cells are shown in figure 3.4.

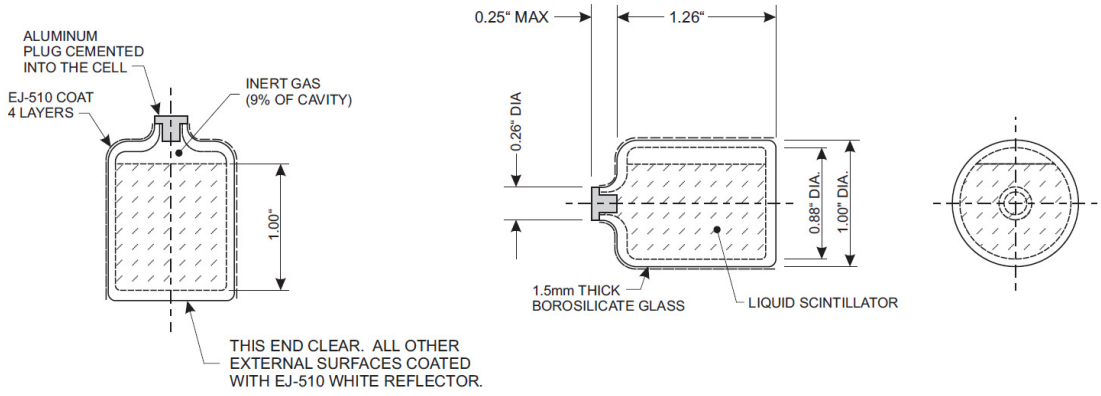

Figure 3.4: Schematics diagrams of a D1 cell

A reflective Teflon tape layer covers the cell top and side, as well as an electrical tape layer outside used for mechanical fixation and light protection.

EJ-315 is pulse-shape discrimination capable, and its properties are listed below:

Light Output (% of anthracene)	60%
Photons produced by a 1 MeV electron	9200
Wavelength of Maximum Emission	425 nm
Decay Time, Short Component	3.5 ns
Specific Gravity	0.954
No. of D Atoms per cm^3	4.06×10^{22}
No. of H Atoms per cm^3	2.87×10^{20}
No. of C Atoms per cm^3	4.10×10^{22}

These data are only valid for the D11 and D13 detectors: D12 was provided by our partner group for the project based at the Los Alamos National Laboratory (LANL), the Space Science and Applications Group (ISR-1). The D12 detector contains deuterated toluene doped with PPO ($C_{15}H_{11}NO$) and p-Terphenyl ($C_{18}H_{14}$). The physical cell has the same dimensions as the other D1 detectors. D12 aimed at testing new detector materials being developed and the FACTEL prototype was a good opportunity to conduct such test. It is not the focus of this work to compare and analyze both materials properties. The supplied D12 detector could function like the other D1 detectors, with perhaps a few improved properties. The D12 detector was thus treated the same way as D11 and D13 in every aspect of signal treatment and analysis.

3.2.2 The D2 Detectors

The three cerium doped lanthanum bromide ($LaBr_3$:Ce) D2 detectors were provided by Saint-Gobain Crystals as their N20×20/B380 product. Lanthanum bromide based scintillator D2 detectors were chosen for their very fast timing

properties. The FACTEL concept was motivated in part because $LaBr_3$ exists: $LaBr_3$ made a sub-nanosecond ToF window a possibility.

The $LaBr_3$ crystal detectors are cylinders of 2 cm in diameter and 2 cm in length, encased within reflective Teflon protected by a thin aluminum housing. Lanthanum bromide being highly hygroscopic, a glass light guide seals the crystal and serves as a window for the PMT. The schematic diagram of a D2 detector cell provided by Saint-Gobain is shown in figure 3.5.

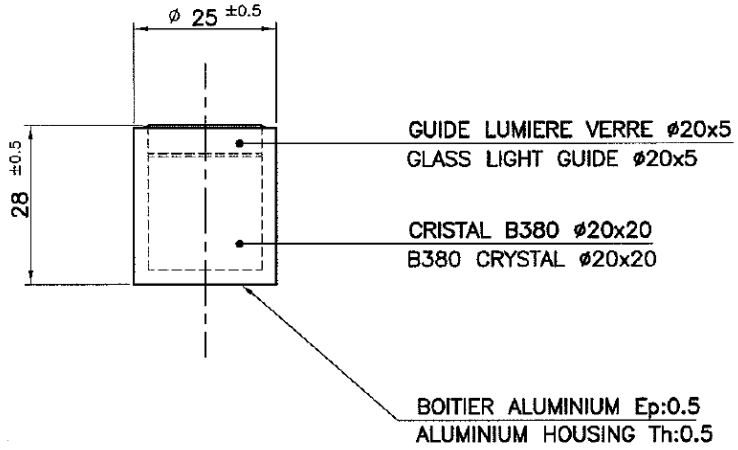

Figure 3.5: Schematic diagram of a D2 cell

Lanthanum bromide is dense at 5.08 g/cm^3, and is a high Z material with Lanthanum at Z=57 and Bromine at Z=35, improving the photoelectric effect probability and making it a good gamma ray absorber. A comparison between $LaBr_3$:Ce and NaI:Tl, which has been commonly used for decades in multiple scintillation detectors such as the COMPTEL D2 detectors, follows:

	$LaBr_3$:Ce	NaI:Tl
Density [g/cm^3]	5.08	3.67
Average Z	40.5	32
Energy Resolution at 662 keV	~3%	~7%
Light Yield [photons/keV]	63	38
Decay Time [ns]	16	250
Timing FoM	0.5	2.6
Wavelength of maximum emission [nm]	380	415

The Timing Figure of Merit is a measure of scintillator properties and is computed according to equation 3.1:

$$\textit{Timing FoM} = \sqrt{\frac{\textit{Decay Time}\ [\text{ns}]}{\textit{Light Yield}\ [\text{photons/keV}]}} \tag{3.1}$$

By all accounts (except for cost and availability), lanthanum bromide is superior to sodium iodine as a scintillator.

However, one working with $LaBr_3$ detectors must be aware of the intrinsic background of lanthanum. Natural lanthanum is composed at of 99.91% of stable ^{139}La and of 0.09% of unstable ^{138}La. ^{138}La has a half-life of 1.05×10^{11} years, has a 66.4% probability to decay via electron capture following equation 3.2, and a 33.6% probability to undergo a beta decay following equation 3.3:

$$^{138}_{57}\mathrm{La} + \mathrm{e} \rightarrow {}^{138}_{56}\mathrm{Ba} + \upsilon_\mathrm{e} + \gamma(1436\ \mathrm{keV}) \tag{3.2}$$

$$^{138}_{57}\mathrm{La} \rightarrow {}^{138}_{58}\mathrm{Ce} + \mathrm{e} + \overline{\upsilon_\mathrm{e}} + \gamma(789\ \mathrm{keV}) \tag{3.3}$$

The electron in eq. 3.3 has an energy up to 255 keV, while the electron capture in eq. 3.2 creates a hole in the electronic structure of the created ^{138}Ba atom and a 35

keV X-ray will be emitted by the filling of the K-shell vacancy. The total self-background rate of $LaBr_3$, including the ^{227}Ac contamination discussed below, is rather low at 0.393 counts per second per cm^3.

The self-background from lanthanum bromide also includes ^{227}Ac contamination. Actinium is chemically similar to lanthanum and will easily mix with it. ^{227}Ac comes from the uranium 235 decay chain following:

$$^{235}_{92}U \rightarrow \alpha + ^{231}_{90}Th \rightarrow e + ^{231}_{91}Pa \rightarrow \alpha + ^{227}_{89}Ac \qquad (3.4)$$

^{227}Ac is a trace element, but its chemical similarity with lanthanum allows it to find its way into rare-earth compounds. ^{227}Ac has a 27.77 years half-life and a 1.38% chance to decay emitting an alpha particle of about 5 MeV. The alpha particles produced by ^{227}Ac will leave a peaked continuous spectrum between 1750 and 2600 keV in a $LaBr_3$ detector, see figure 3.6.

In total, the self-background of a $LaBr_3$ detector is shown in figure 3.6 [55] (note that the part above 1600 keV is magnified by a factor 10):

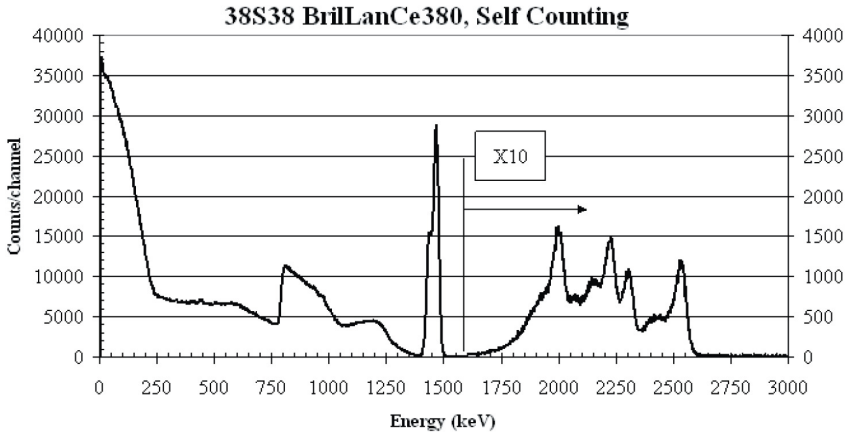

Figure 3.6: The self-background of $LaBr_3$. The peak at 1471 keV comes from the decay of ^{138}La, the continuum above 1600 keV comes from ^{227}Ac decays.

The self-background of $LaBr_3$ is of course undesirable for a gamma-ray telescope. However, a gamma ray interacting in a D2 detector then in a D1 detector would be rejected by its negative time of flight, while a gamma ray emitted by a D2 detector then interacting in a D1 detector before interacting back in a D2 detector is a rare occurrence. This leaves the type B background event case where a random gamma ray would interact in a D1 detector at the same time a D2 detector would be triggered by a self-background particle. However, the rather low 0.393 counts per second per cm^3 self-background rate is not a problem for our small prototype (18.85 cm^3 of $LaBr_3$).

On the positive side, the $LaBr_3$ self-background can be used for self-calibration. The sharp peak at 1471 keV (1436+35) can be (and has been) used both for laboratory calibrations and in-operation calibration. The counting rate is too low for a "quick" calibration in a few minutes, however the cumulated events over a longer time period can be used to confirm the laboratory calibration: even a few dozen events can be enough to confirm that the D2 detectors are operating normally.

3.2.3 The Photomultiplier Tubes

The photomultiplier tubes, Hamamatsu R4998, were chosen because they were the fastest one inch (26 mm) PMTs available at the time FACTEL was built. A diagram of a R4998 PMT from Hamamatsu documentation is shown in figure 3.7 [56].

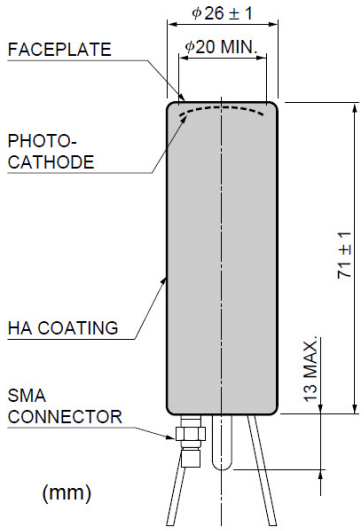

Figure 3.7: Schematic diagram of a Hamamatsu R4998 PMT

The 20-mm diameter photocathode is a Bialkali type, its response maximum occurs at 420 nm, and the ten stages offer a 5.7×10^6 gain. For timing performance, the anode pulse risetime is 0.7 ns and the PMTs were operated at around 2000 V. Each PMT has a different gain, and although the company certifies the gain within a certain range, the range is rather wide and the actual gain of one specific PMT can be very different from one to another. Each PMT was thus tested and paired with one detector, this procedure will be covered in the calibration section.

3.2.4 The Anti-Coincidence Panels

The six anti-coincidence panels form a box around the D1 layer, see figures 3.3 and 3.8. Normally, either a box enclosing both detector layers with large panels, or two boxes one around each detectors layer would be built (as was done for COMPTEL, see fig. 2.11). The FACTEL anti-coincidence panels were restricted to a single box around D1 for cost and complexity considerations. Restricting the use of passive materials was our goal and large panels would have added much weight for no

real advantage: the ToF value already filters D2→D1 events and only D1→D2 events are of interest, thus shielding the D1 layer from charged particles is the only real necessity. The drawback of this solution is to add a substantial material layer between the D1 and D2 layers, which is very undesirable: it can absorb transiting gamma rays and can produce background events between the detector layers. A larger instrument such as the one presented in the sixth chapter of this work would be completely enclosed in an anti-coincidence box and would not possess a material layer between the D1 and D2 detectors layers.

The top anti-coincidence panel is composed of EJ-254, while the five others are composed of BC-408. BC-408 is a plastic scintillator from Saint-Gobain Crystals, based on polyvinyltoluene with a 1.032 g/cm^3 density. It suited the FACTEL shielding needs by stopping X-rays under 100 keV and detecting charged particles; its specifications can be found in [57]. EJ-254 from Eljen Technology is another plastic scintillator based on polyvinyltoluene but with 1% boron added to mitigate the effect of neutron capture by hydrogen. EJ-254 has a 1.021 g/cm^3 density and is based on the same material as BC-408, thus possesses the same basic properties.

This work will not have a section dedicated to the anti-coincidence (AC) panel calibration, so the specific details will now be reviewed. Each AC panel has an identifying number: AC4 (+Z) is the top panel, AC1 (-Z) is the panel between the D1 and D2 layers, AC6 (+Y) is the panel in front of the detectors, AC2 (-Y) is the panel behind the pre-amplifier boards, AC3 (+X) is the front panel in fig. 3.3, and AC5 (-X) is the panel behind in the same figure. Thus, AC4 is the borated EJ-254 AC panel while the others panels are composed of BC-408. All the panels are 6 mm thick, AC1 and AC4 are 17.7×17.0 cm, AC2 and AC6 are 21.8×17.0 cm, and AC3 and AC5 are 26.9×21.8 cm. The AC panels are each separated in two parts with a light guide between that brings the scintillation light to a photomultiplier tube. For mechanical

stability and light protection, there is an aluminum sheet 1.27 mm thick on each panel side. On one side of each panel is an aluminum box containing a PMT, a small pre-amplifier card and a second longer electronic card. These boxes are 5″×2″×2″ (12.7×5.1×5.1 cm) with a 0.05″ (1.3 mm) thickness, and the PMTs are Hamamatsu R1924A one inch (26 mm) with a 4.3 cm length. Finally, the panels and boxes are covered with a few layers of dark plastic (Electrical tape - Polyvinyl Chloride). A picture of the anti-coincidence box is shown in figure 3.8.

Figure 3.8: FACTEL Anti-Coincidence panels box around the D1 detector layer, see text for a description

The anti-coincidence panels energy threshold is about 400 keV, meaning that if any particle deposits 400 keV_{ee} in any panel, the anti-coincidence veto electronic signal is triggered.

3.2.5 Other Materials of FACTEL

The other materials of the structure of the FACTEL instrument are also important: limiting as much as possible passive mass and particularly metals was our

priority. Besides metallic screws and nuts and the electronic wires, here is a review of the main materials of FACTEL.

Fiberglass Reinforced Plastic (FRP) is the strong metal-less material used for the frame and the core mechanical structure of FACTEL. All the frame beams are made of FRP, and in the many pictures of the FACTEL prototype shown in this work, the FRP structure is easily recognizable as the olive green beams. A picture of FACTEL frame is shown in figure 3.9. The beams were provided by McMASTER-CARR. All beams are square tubes 1 inch (2.54 cm) wide and 1/8″ (3.2 mm) thick. FRP is composed at 70% by silica (SiO_2, 2.634 g/cm^3) and at 30% by polyester ($C_{10}H_8O_4$, 1.5 g/cm^3).

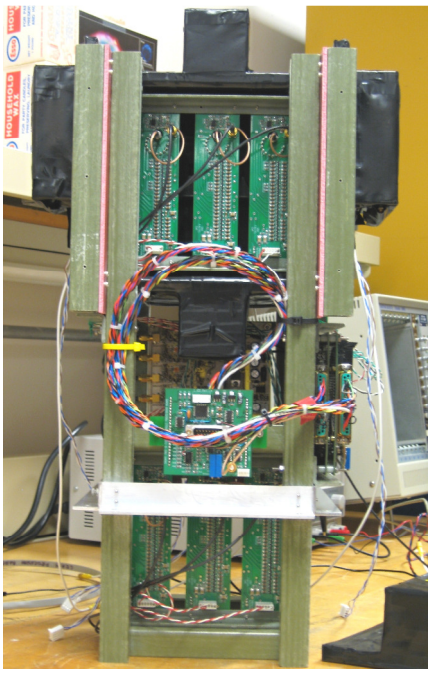

Figure 3.9: FACTEL frame, the FRP structure is easily recognizable as the olive green beams

The tubes surrounding the detector assemblies (PMT-Detector) are composed of Bakelite, sold as Garolite by McMASTER-CARR. The mounting rings directly in front of the detectors supporting the tubes and linking them to the frame are also

composed of Bakelite. This material is in the immediate vicinity of the detectors and is metal-less. A picture of the D1 detectors in their tubes attached to the frame is shown in figure 3.10.

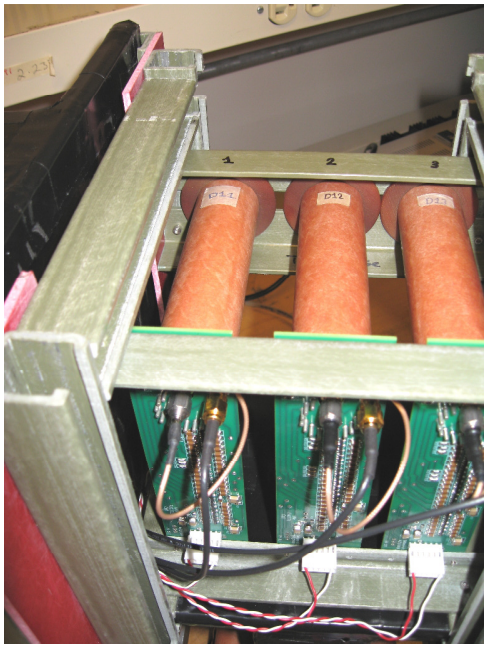

Figure 3.10: The Bakelite tubes surrounding the detector assemblies are in orange/brown, as the mounting rings linking the assemblies tubes to the structure

Between the detectors tip and the mounting rings are small pieces of neoprene foam. To secure the PMTs-Detectors inside the Bakelite tubes, electrical tape (polyvinyl chloride) was coiled around the PMTs and the detectors up to the point where the PMT-Detectors were supported by the tubes. These few layers (2.85 mm for the D1 detectors) do count for some passive mass directly around the D1 detectors.

For the FACTEL prototype, the first metal source close to the D1 detectors material is the aluminum plug used to seal the D1 cells, see figure 3.4. The second metal source in the vicinity of a D1 detector is its PMT photocathode, focusing electrode and dynodes. The third metal source close to the D1 detectors are the

aluminum plates of the AC4 and AC6 anti-coincidence panels. The bulk of the metallic mass around the D1 layer comes from the twelve aluminum plates from the anti-coincidence panels. As for neutron capture mitigation, the most relevant sources of hydrogen close to the D1 detectors are: the electrical tape around the cells and PMTs, the thick electrical tape rings liking the assemblies to the Bakelite tubes, the Bakelite tubes, the Neoprene foam between the cells and mounting rings, and the Bakelite mounting rings.

For the dome and the pressure vessel, the bottom of the pressure vessel is a cylindrical aluminum plate, seen at the bottom of figure 3.11. The bottom plate is 3/4″ (1.9 cm) thick and has an 18″ (45.7 cm) diameter. The aluminum dome is 24.75″ (62.9 cm) tall, has a 15″ (38.1 cm) diameter and is 1/8″ (3.2 mm) thick. The dome was surrounded by a layer of insulating foam protected by a duct tape layer. Pictures of the completed FACTEL instrument prior to the balloon flight and its dome are shown in figures 3.11 and 3.12.

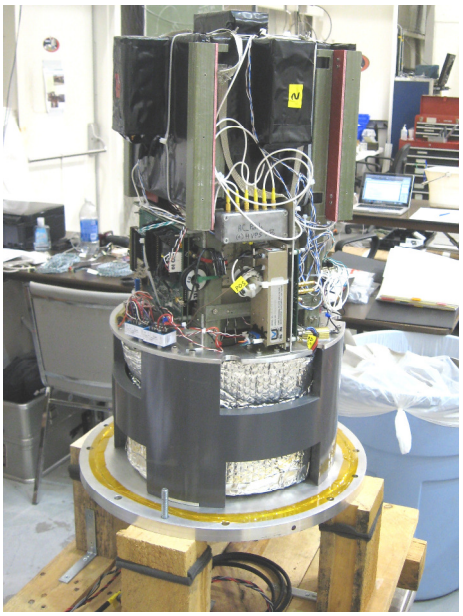

Figure 3.11: The assembled FACTEL prototype prior to the balloon flight

Figure 3.12: The FACTEL prototype pressure vessel

3.2.6 Electronic Boards

Most of the electronic boards of the FACTEL prototype were custom made at the University of New Hampshire. We do not describe precisely the engineering details and components of each board: only their roles in the FACTEL instrument are described.

The first electronic boards are the six preamplifier boards connected directly to the PMTs, these can be easily seen in figure 3.3 and the pictures of figures 3.9 and 3.10. The preamplifier boards supply bias to the PMTs and provide the first amplification stage of the PMT signals before sending them for further analysis to the "Channel" board. The second electronic board of the analysis process is the "Channel" board, it can be seen in the back of the frame in fig. 3.9, behind the AC1 PMT box and the front board. The channel board receives the six signals from the preamplifier boards, amplifies and digitalizes them before sending its information to the "Summer" boards. The third electronic boards are the "Summer" boards. The FACTEL instrument has two summer boards, one for the D1 detectors and one for the D2 detectors. The summer boards receive the signals from the channel board and perform the main signal analysis before sending their information to the PIC board. The summer boards can be seen at the bottom of fig. 3.8 and on the side of the instrument in fig. 3.9. The fourth step of the electronic process is the Programmable Interface Controller (PIC) microcontroller board. The PIC controls the signals of the interfaces (the summer boards) following the FACTEL operation program. The PIC is programmed with BASIC software written at UNH. The PIC receives the signals from the summer boards and sends its own data to the onboard PC-104 computer. The PIC board can be seen at the center front of fig. 3.9 connected to the summer boards. Finally, the information is sent to the PC-104 onboard computer, seen as the blue box at the bottom of the fig. 3.3 engineering diagram. The PC-104 runs a Linux

system and operated the FACTEL prototype during the balloon flight. A block diagram of the FACTEL electronic system is shown in figure 3.13.

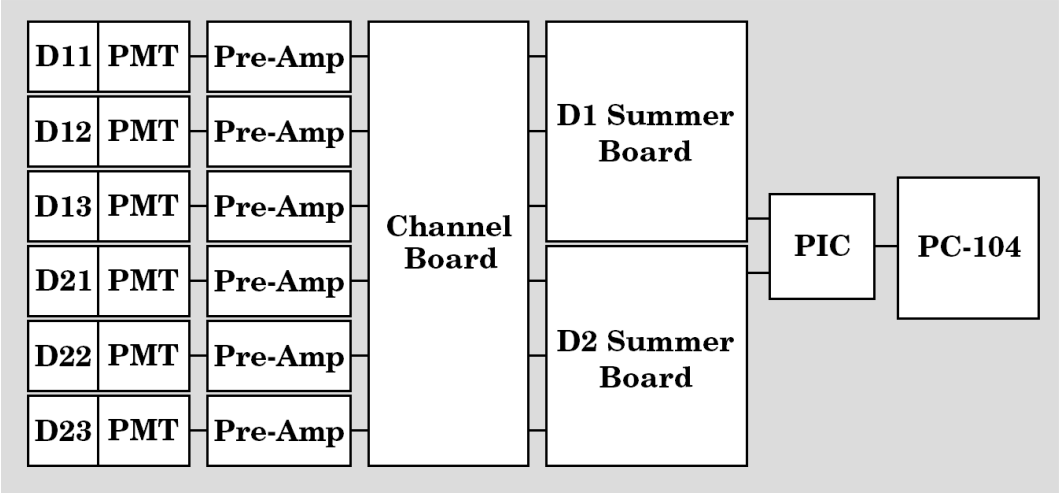

Figure 3.13: Block diagram of the FACTEL prototype electronic system, the signals from the PMTs are pre-amplified and then sent to a channel board, the signals then go to a summer board, then to the PIC controller, and finally to the onboard PC-104 computer.

The PC-104 cycles between FACTEL operational modes, operates the PIC board and records the data into a hard drive. The data files from a FACTEL run are recovered from the PC-104. The PC-104 also records time, temperatures, pressures, and various voltages.

Other electronic components of the FACTEL instrument are the power supply for the AC panels, seen in the middle of fig. 3.11, and temperature control boxes, seen as two white boxes under the summer boards in the center-left of the same figure. The FACTEL flight also flew a test for a Silicon Photo-Multiplier (SiPM) experiment, it included an electronic board and a small detector assembly in the D1 layer anti-coincidence box; however this experiment is not part of this work.

The FACTEL electronic components also brought the two greatest disappointments of the project. First, PSD did not function for the final instrument,

and secondly an electronic noise issue severely degraded the overall performance of the instrument.

The first disappointment of the final instrument was pulse-shape discrimination. The D1 EJ-315 detectors are PSD capable, and their PSD capabilities have been successfully tested with laboratory instruments, as will be shown in the calibration section. For the final instrument, the problem came from the non-validity of previous electronic solutions to our fast signals case. As seen in figure 2.17, PSD electronics normally works for signals in the hundreds of nanoseconds range, however the aim of FACTEL was a sub-nanosecond ToF. FACTEL PMTs are fast and operated at their maximum speed, leading to fast rising signals (~1 ns range) with fast decays. This made standard PSD solutions for instruments invalid for the FACTEL prototype, thus PSD was not available for the final FACTEL instrument.

One could point that PSD was successfully tested with FACTEL D1-PMT assemblies, and ask what the difference was between those tests and the final instrument? The answer is power: PSD was successfully tested by analyzing the signals from the preamplifier boards using standard NIM laboratory equipment. NIM crates can be massive pieces of equipment and modules can consume hundreds of watts. On the other hand, electronics onboard satellites are small, light and typically function in the milliwatt range. For the FACTEL detector assemblies, NIM modules equipment were able to analyze the D1 signals accurately enough to achieve PSD. However, the solution implemented on the flight electronic board could not achieve successful pulse-shape discrimination, this problem has been solved since.

The second disappointment from the FACTEL instrument was an electronic noise issue that degraded every aspect of the telescope. In the latest stage of instrument integration, a few weeks before the balloon flight, an electronic noise

source that almost ruined the experiment was uncovered. Each subsystem functioned properly when individually tested, however when the final instrument was assembled, digital noise from the PC-104 computer was picked up by high-impedance analog lines and increased the baseline noise of the entire system.

Initially, the increased baseline noise caused the D1 sub-system to trigger continuously at a ~5 kHz rate while the normal background rate in the D1 layer is in the ~5 Hz range. This locked up the instrument because the electronics were constantly processing noise, and good events were missed in the dead time. Applying aluminum foil on the inside sides of the anti-coincidence panels and grounding the foil and other parts of the instrument directly solved the D1 triggering problem.

Two other aspects of the FACTEL prototype were degraded by the increased baseline noise: the D2 detectors energy resolution was degraded to NaI levels (7% instead of 3%) and ToF was also impacted. This noise issue was solved later, leading us to the conviction that the FACTEL prototype could have performed better than it did.

3.3 The Calibration of FACTEL

This section reviews the calibration of the FACTEL instrument. This includes the energy calibration, Time of Flight and Pulse-Shape discrimination. A picture of key FACTEL components is shown in figure 3.14; it shows a D1 Cell, a D2 detector, and one R4998 PMT.

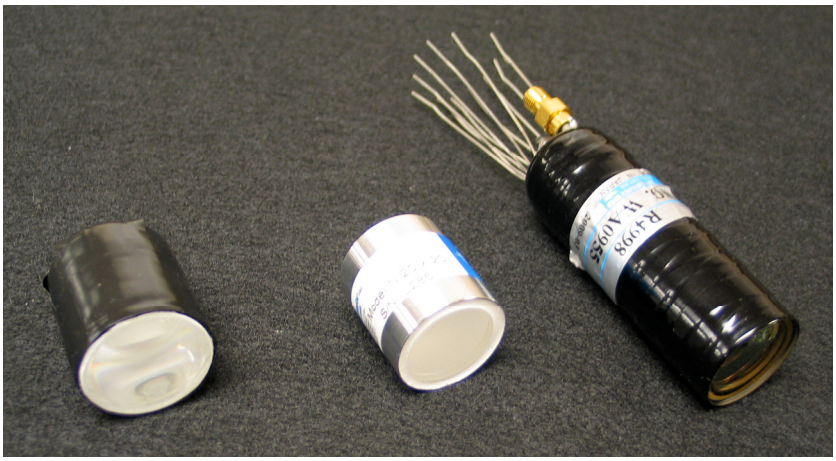

Figure 3.14: Deuterated Liquid D1 (left), $LaBr_3$ D2 (center), and R4998 PMT (right)

NOTE. Because this chapter presents many results acquired over the years the instrument was developed, various results are marked with "stamps" to guide the reader. Figures marked with the "LAB" stamp LAB indicate results not taken with the final version of the instrument, but most probably taken with NIM standard laboratory equipment as the various parts of the instrument were tested. Figures marked with the "FI" stamp FI indicate results taken with the Final Instrument as it flew for the balloon test flight. Also, laboratory runs and simulations were noted by a letter and a number for easy retrieval of information concerning the runs and simulations. Laboratory runs and tests are noted with an "R" followed by a number: laboratory run 655 is thus R655. The FACTEL balloon flight conducted September 23, 2011, is R654 in our notation. The Geant 4 simulations performed follow the same convention, albeit an "S," for "Simulation," is used instead of an "R:" simulation 55 is thus S55.

3.3.1 The PMTs and the Pairing

Each PMT has a different gain, and before gluing the detectors with epoxy, each PMT was tested and paired with a detector. The six R4998 PMTs Hamamatsu sent us in 2009 had the serial numbers WA0800, WA0952, WA0954, WA0955, WA0971 and WA0974, henceforth referred as TXXX with XXX being the last three numbers of their serial number. T974 was mishandled and broken, its replacement R4998 PMT with serial number WA1330 was sent to us in March 2011. The parameter that varied significantly between the PMTs was their "Anode Luminous Sensitivity", and according to the test sheets from Hamamatsu, they are as follow for each PMT:

	Serial Number	Anode Luminous Sensitivity [A/lm]
	WA0800	389
	WA0952	384
	WA0954	684
	WA0955	334
	WA0971	555
X	WA0974	338
	WA1330	174

The first five PMTs were tested for their gain (T974 was broken early on, while WA1330 was received late in the project). For this test, each PMT was coupled to the same $LaBr_3$ detector and the same preamplifier board set at the same voltage (2000V). Then laboratory runs were performed for ^{22}Na and ^{137}Cs sources, those were R187 to R196. ^{22}Na spectra examples from these runs are shown in figure 3.15:

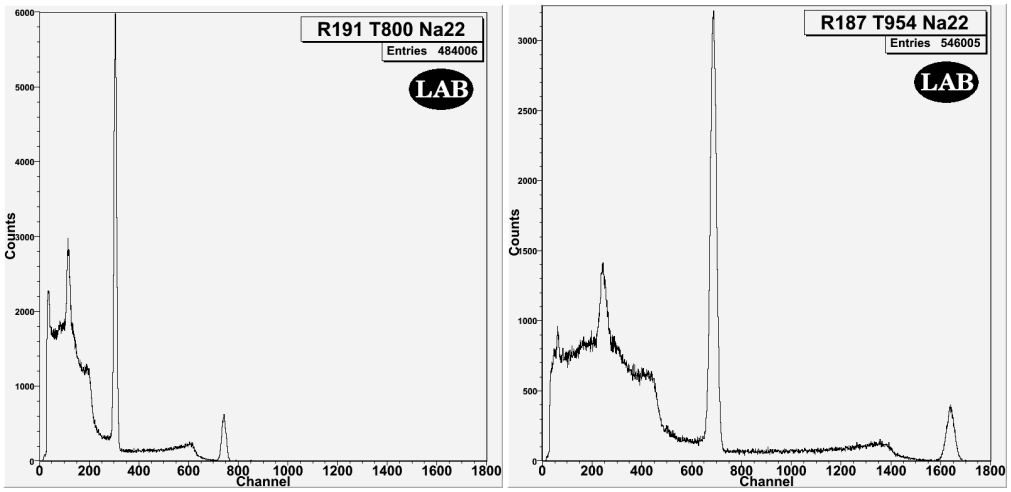

Figure 3.15: ^{22}Na Spectrum with T800 (left), ^{22}Na Spectrum with T954 (right), different PMTs have different intrinsic gains

The actual gain of the PMTs varied by over a factor 2, see fig. 3.15, a graph of the test results is shown in figure 3.16. The PMT with the lowest gain was T800. Comparing the other PMTs to T800, the relative gains are 112% for T955, 158% for T952, 199% for T971 and 224% for T954. For energy resolution, the averaged results are 4.5% at 511 keV, 2.5% at 1275 keV, and 3.9% at 662 keV. A ^{137}Cs spectrum from R188 is shown in figure 3.17, the ~32 keV X-rays peak is clearly visible.

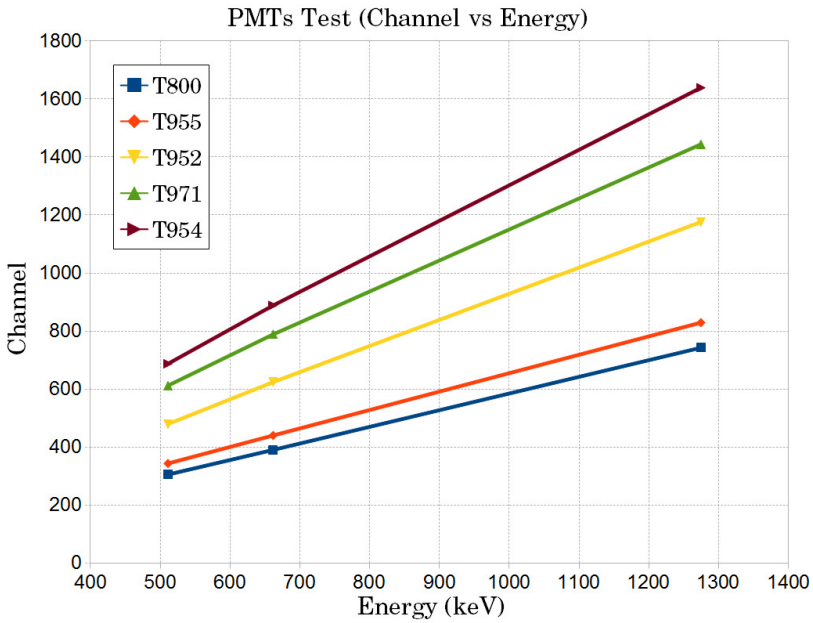

Figure 3.16: FACTEL PMTs gain comparison

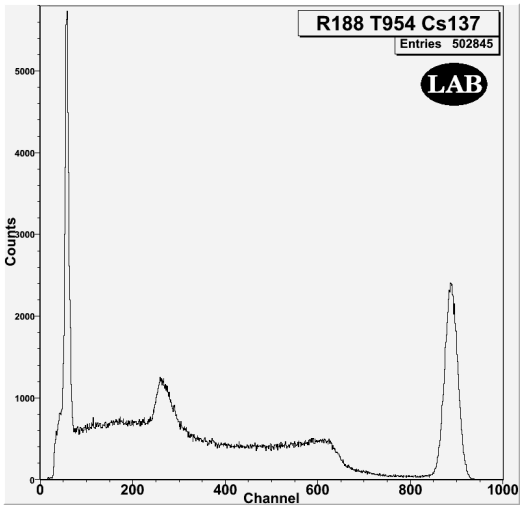

Figure 3.17: The ^{137}Cs spectrum from R188, the features from right to left are the 662 keV photopeak around channel 880, the Compton edge around channel 625, the backscatter peak around channel 260, and the 32 keV photopeak around channel 60.

The next step was to choose which PMT to couple to which detector. The two EJ-315 D1 cells from Eljen were equivalent, as were the D2 detectors from Saint-Gobain. The $LaBr_3$ detectors are bright and fast, they produce many photons quickly, leading to high instantaneous currents in the PMTs causing them to saturate quickly. To mitigate this effect, the lower gain PMTs were chosen for the $LaBr_3$ detectors and their operating voltages were set to 2000 V. The D1 detectors are conventional scintillators with conventional characteristics, the PMTs with the highest gain were thus coupled to the D1 detectors and were operated at 2200 V. The pairings were as follow:

D11: T954 PMT, EJ2 Cell, Preamp board 1, 2200 V

D13: T971 PMT, EJ1 Cell, Preamp board 3, 2200 V

D21: T800 PMT, L285 D2, Preamp board 4, 2000 V

D23: T955 PMT, L273 D2, Preamp board 6, 2000 V

The last D1 cell from LANL, the last PMT (WA1330) from Hamamatsu, and the last D2 detector from Saint-Gobain were received later. WA1330 has a very low anode luminous sensitivity compared to the other PMTs: about 50% of our weakest PMT T955, with an anode luminous sensitivity of 174 A/lm compared to 334 A/lm. On the other hand, the D1 cell from our LANL partner group was brighter than the other D1 cells. It thus made sense to use our weakest D1 PMT (T952) with our brightest D1 cell, and use the weak WA1330 PMT for the last D2 detector. To mitigate the weak gain of WA1330, the D22 PMT was operated at 2200 V, like the D1 detectors, instead of 2000 V. The solution functioned well as D22 has a similar calibration curve compared to the other D2s, see fig. 3.34. Although a difference can be noted as it rises faster at first and then saturates more quickly. The fact that the last D1 from LANL was received after the other D1s had been glued to their PMTs precluded a complete comparison. The last two pairings are as follow:

D12: T952 PMT, LANL D1 Cell, Preamp board 2, 2200 V

D22: WA1330 PMT, $LaBr_3$ Cell, Preamp board 5, 2200 V

3.3.2 Energy Calibration

Energy calibration was a task performed routinely throughout the project: every time one parameter was modified, a re-calibration was necessary. Because FACTEL evolved "up to the last minute" prior to the flight, the final complete calibration was performed post-flight: those runs will thus have numbers above R654 and the **FI** stamp. The FACTEL instrument overall performance was degraded by the electronic noise issue for its final iteration; results from prior laboratory runs stamped **LAB** will still be presented to showcase the potential performance of each subsystem.

3.3.2.1 Radioactive Calibration Sources

This section lists the various radioactive sources used to calibrate the FACTEL instrument and how they were used.

^{241}Am is usually used for the first point of the calibration curve. Its main line is a 59.54 keV gamma ray. It also emits a fainter mix of four gamma-ray lines averaging at 100.44 keV, which was observed with $LaBr_3$ detectors.

^{109}Cd is used for its gamma-ray lines at 22.57 and 88.04 keV. The 22.57 keV line is an average of five X-ray lines and is the lowest energy available to us (that low level threshold is rarely reached). The 88.04 keV line is more commonly used for laboratory calibrations.

^{57}Co is a staple source commonly used to showcase the low-energy resolution of a detector: it emits two close gamma-ray lines at 122.06 keV and 136.47 keV with a ratio of 8 to 1 (85.60% for the 122 keV and 10.68% for the 136 keV). A common test is to see how well a detector can separate these two lines, as seen in figure 3.18. ^{57}Co also has a much fainter and less used gamma-ray line at 692.03 keV, it is usually used for comparison with the 662 keV line from ^{137}Cs.

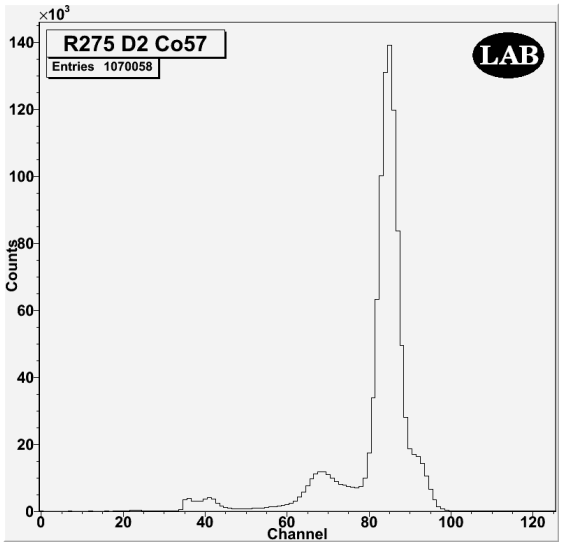

Figure 3.18: A ^{57}Co spectrum with a $LaBr_3$ detector. The 122 keV gamma-ray line is the sharp peak while the 136 keV gamma-ray line is the shoulder on the right side of the peak.

^{133}Ba is a useful source because it emits many close gamma-ray lines used to illustrate resolution. More importantly, a "good" ^{133}Ba calibration run can cement a detector calibration in the low-energy range (<500 keV). ^{133}Ba emits 4 gamma-ray lines between 250 keV and 400 keV: 276.40, 302.85, 356.02 and 383.85 keV. A showcase of our $LaBr_3$ D2 detectors capabilities is shown in figure 3.19, the fit is one decaying exponential for the background and 4 Gaussians for the peaks. ^{133}Ba emits other useful gamma-ray lines: 80.90 keV and 30.85 keV (both are mixes of X-ray lines), and weaker less useful lines at 53.16 keV and 35.14 keV (X-ray mixes). A full ^{133}Ba spectrum is shown in figure 3.20, showing how useful a ^{133}Ba calibration run can be for the low-energy calibration: 6 points can be used.

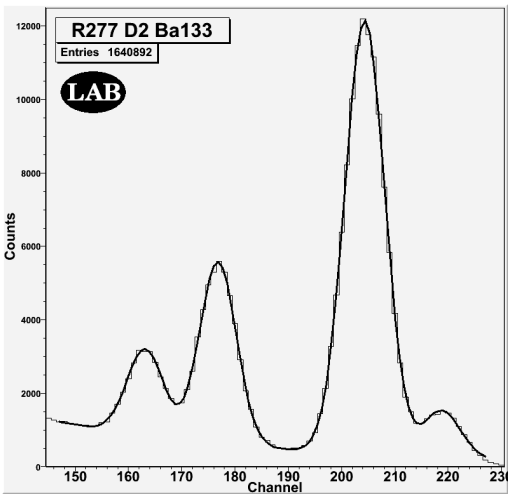

Figure 3.19: Fit of the four ^{133}Ba lines (276.40, 302.85, 356.02 and 383.85 keV)

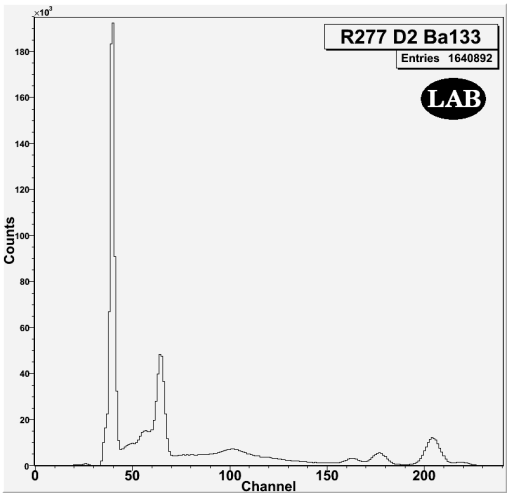

Figure 3.20: The full ^{133}Ba spectrum with a $LaBr_3$ detector, 6 lines can be used for calibration

^{22}Na was the most useful radioactive source for this project. The two gamma-ray lines from ^{22}Na are the 511.00 keV line coming from positron annihilation and the 1274.53 keV line coming the decay product of ^{22}Na (^{22}Mg). The decay diagram of ^{22}Na is shown in fig. 1.18, a spectrum in fig. 3.15, and the decay scheme described in eq. 1.19. The two peaks are well separated in the range of interest for Compton telescopes, and do not have much background. One ^{22}Na run can quickly give a sense of a detector calibration and is usually the first run performed after any modification to the instrument. The ^{22}Na source is also used for Time of Flight calibration, which was critical for the FACTEL project. When the positron emitted by a decaying ^{22}Na nucleus annihilates with an electron, the two 511 keV gamma rays produced are emitted simultaneously in opposite directions. These will induce time correlated interactions in a D1 detector and a D2 detector. This is used to calibrate the ToF system by placing the source between the detectors layers and by varying its position.

^{137}Cs is another staple radioactive source of every nuclear laboratory, its 661.66 keV line is an industry standard to compare detectors, and most documents about a

detector performance will feature a ^{137}Cs spectrum. The ^{137}Cs 30.17-year half-life makes a source steady over the course of a project. ^{137}Cs is a common and widely available isotope because it is a common ^{235}U fission fragment. The 662 keV gamma-ray line in the middle of the range provides a clear assessment of the detector resolution. ^{137}Cs also has a mix of X-rays at 32.06 keV. A ^{137}Cs spectrum from one of our D2 detectors was shown in fig. 3.17, and its decay scheme is outlined in eq. 1.18.

A last common radioactive source is ^{60}Co, which emits two gamma-ray lines at 1173.24 and 1332.50 keV. Along with the 1275 keV line from ^{22}Na which falls between the two ^{60}Co lines, these three points are the cement of the 900 to 1500 keV calibration. The small 160 keV difference between the two peaks also makes ^{60}Co an industry standard for measuring a detector resolution at high energy. A ^{60}Co spectrum from one of our D2 detectors is shown in figure 3.21, and its decay scheme is outlined in eq. 1.20.

The ^{40}K present in the environment can be used to calibrate gamma-ray detectors, however its 1460.83 keV line is too close to the self-background 1471 keV line from ^{138}La to be useful in our case.

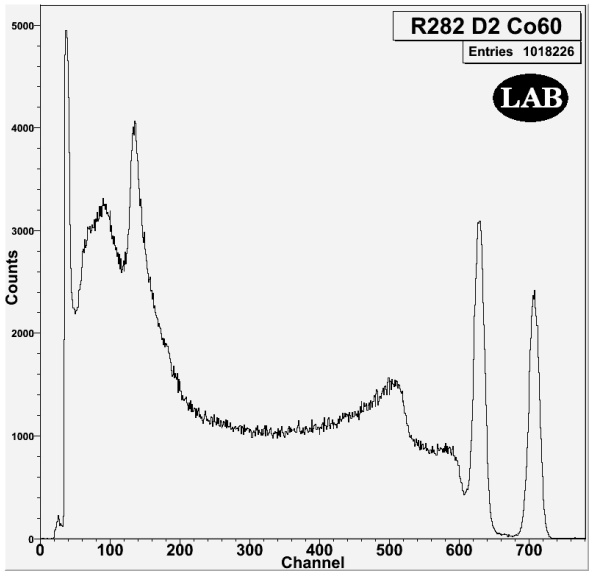

Figure 3.21: A ^{60}Co spectrum with a $LaBr_3$ detector

A first less conventional source to use for instrument calibration is an Americium-Beryllium (AmBe) source. Usually used as a neutron source, it also emits a 4438.91 keV gamma ray. The process starts with a ^{241}Am nucleus decaying emitting an alpha particle, the alpha particle then tunnels into a ^{9}Be nucleus that, in turn, emits a fast neutron. However, it also creates an exited ^{12}C nucleus which decays to its ground state via a 4439 keV gamma ray. These reactions proceed as follow:

$$^{241}_{95}\mathrm{Am} \rightarrow {}^{237}_{93}\mathrm{Np} + {}^{4}_{2}\alpha \tag{3.5}$$

$$^{4}_{2}\alpha + {}^{9}_{4}\mathrm{Be} \rightarrow {}^{12}_{6}\mathrm{C}^{*} + {}^{1}_{0}\mathrm{n} \tag{3.6}$$

$$^{12}_{6}\mathrm{C}^{*} \rightarrow {}^{12}_{6}\mathrm{C} + \gamma(4439\ \mathrm{keV}) \tag{3.7}$$

A gamma ray of 4439 keV energy has a significant chance to interact with a detector via pair production (see sections 2.2 and 2.2.3). The created electron will slow down and deposit its energy, while the positron will slow down and deposit its energy before annihilating with an electron and produce two 511 keV gamma rays. If both 511 keV gamma rays are absorbed by the detector, the total energy deposit will be the initial gamma ray full 4439 keV, if one 511 keV gamma ray escapes the detector, the total energy deposit will be 3928 keV (4439-511), and if both 511 keV gamma rays escape the detector, the total energy deposit will be 3417 keV (4439-1022). This leads to a spectrum with three peaks: a first full absorption peak, followed by two "escape peaks". This is shown in figure 3.22, giving three high-energy calibration points. The peak at 3417 keV having the largest amplitude in fig. 3.22 implies that for our small detectors, the two escapes scenario is the most probable one.

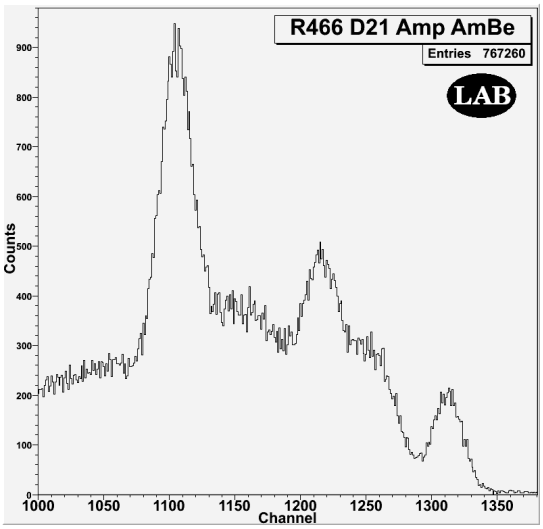

Figure 3.22: AmBe spectrum with a $LaBr_3$ detector, the rightmost peak is at 4439 keV, followed by the two escape peaks 3928 and 3417 keV.

Californium 252, ^{252}Cf, is usually a fast neutron source, however these neutrons can be used to produce 2223 keV gamma rays by exploiting the hydrogen-neutron capture reaction (eq. 1.12). To do so, the ^{252}Cf source is surrounded with household wax blocks that thermalize the neutrons, capture them and emit 2223 keV gamma rays. These gamma rays being above 1022 keV, they have a chance to interact via pair production, leading to three exploitable peaks in the spectrum, as seen in figure 3.23. The three peaks are the full photoelectric absorption peak at 2223 keV, the first escape peak at 1712 keV (2223-511), and the double-escape peak at 1201 keV (2223-1022). The spectrum of fig 3.23 is special because it exhibits the signs of the three interaction processes by which gamma rays interact with matter: the peak around channel 1100 is the photoelectric absorption peak, preceded by a Compton edge and continuum, and two peaks from pair production are present at channels ~650 and ~900. The ratio between the two escape peaks indicates the two escapes scenario is more likely than the one escape scenario, typical of a small detector, thus that the first peak at Ch 1100 comes mainly from photoelectric absorption.

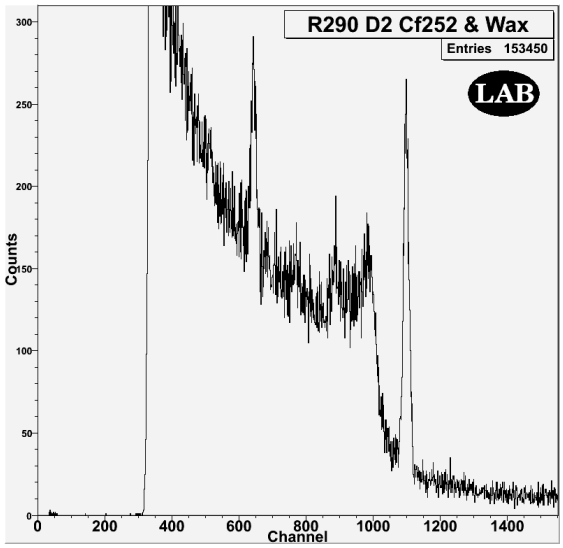

Figure 3.23: ^{252}Cf surrounded by wax spectrum, the rightmost peak is 2.2 MeV, and the peaks at channels ~650 and ~900 are the 1.2 and 1.7 MeV escape peaks.

A last unconventional calibration source is $LaBr_3$ itself. As seen in section 3.2.2, lanthanum-bromide has a self-background which can be exploited for calibration purposes, specifically the 1471 keV peak from ^{138}La. A self-background spectrum from one of our own D2 $LaBr_3$ detector is shown in figure 3.24, the 1471 keV peak is prominent and the spectrum is to be compared to figure 3.6 from Saint-Gobain.

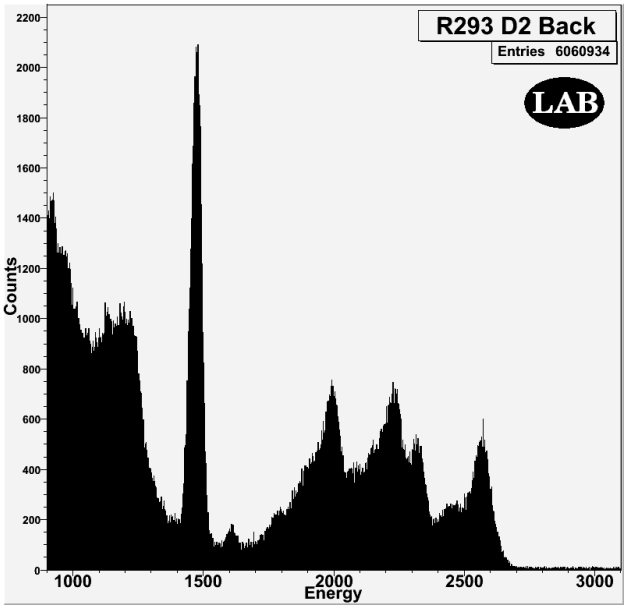

Figure 3.24: $LaBr_3$ self-background

3.3.2.2 D2 Calibration

The $LaBr_3$ D2 detectors are straightforward to calibrate. Because of its density and high Z, gamma rays readily interact with the crystal via the photoelectric effect or multiple Compton scatters, leading to the full absorption of the gamma ray, leading to discrete peaks in the energy spectrum. This section presents the final calibration of the $LaBr_3$ D2 detectors for the assembled instrument. Because of the electronic noise issue leading to the degradation of the performance of the whole instrument, not every line previously used during laboratory calibrations was used for the final instrument calibration. For example, out of the six possible points from ^{133}Ba, only the 80.9 keV and 356.02 keV lines were used for the final calibration. The ^{133}Ba spectrum used for the final calibration of D23 is shown in figure 3.25, the degradation is evident when fig. 3.25 is compared to figures 3.19 and 3.20.

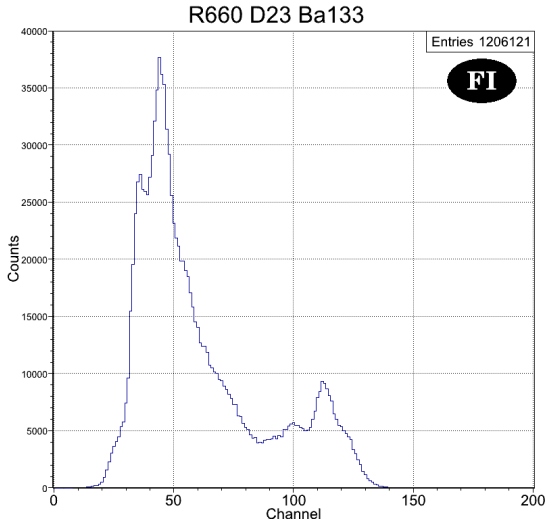

Figure 3.25: Final ^{133}Ba spectrum with D23, only the 81 and 356 keV peaks were used for the detector calibration

The points used for the final D2 detectors energy calibration were: 80.9 and 356.02 keV from ^{133}Ba, 122.06 keV from ^{57}Co, 511 and 1274.53 keV from ^{22}Na,

661.66 keV from ^{137}Cs, 1201 and 2223 keV from ^{252}Cf, 1173.24 and 1332.50 keV from ^{60}Co, 1470 keV from the $LaBr_3$ self-background, and 3416, 3927 and 4438 keV from AmBe. A table with the calibration data for D22 is shown in table 3.1.

Some of the calibration spectra used for the final calibration will now be presented along two laboratory spectra for ^{22}Na and ^{137}Cs.

D22 Calibration Data

Energy (keV)	Channel	Sigma (Cha)	Run #	Slope@ E/Ch	Resolution (%)
511.00	171.504	5.01882	655	3.3699	7.793926
661.66	217.836	5.13313	657	3.3684	6.153621
1173.24	363.197	7.62747	658	3.6966	5.659199
1274.53	391.30	6.81	655	3.8339	4.822644
1332.50	405.284	6.76808	658	3.9225	4.691574
1470	440.819	7.24523	659	4.157	4.824725
356.017	125.428	5.68777	660	3.3989	12.786963
80.898	45.509	5.11274	660	3.4837	51.845896
122.0614	58.8305	6.98331	661	3.4699	46.747420
2223	593.894	7.91944	662	5.6308	4.723706
1201	369.673	7.73486	662	3.7319	5.659749
3416	775.356	12.1369	664	7.889	6.600390
3927	832.097	16.1939	664	9.2631	8.995072
4438	884.761	9.21575	664	11.232	5.492350

Table 3.1: Calibration data for D22

Figure 3.26 shows the ^{22}Na spectrum for D22 from R655, while figure 3.27 shows a previous ^{22}Na spectrum from a laboratory run.

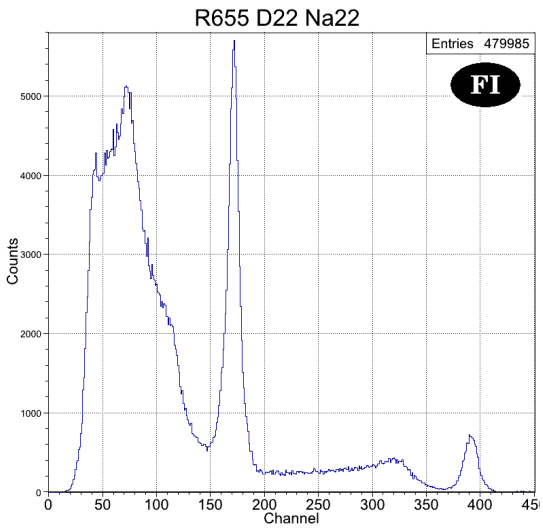

Figure 3.26: ^{22}Na spectrum with D22 from the final instrument

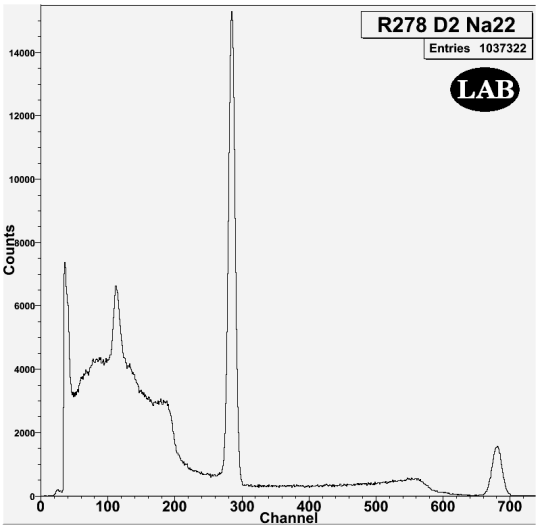

Figure 3.27: ^{22}Na spectrum from the laboratory run R278

Figure 3.28 shows the ^{137}Cs spectrum for D22 from R657, while figure 3.29 shows a previous ^{137}Cs spectrum from a laboratory run.

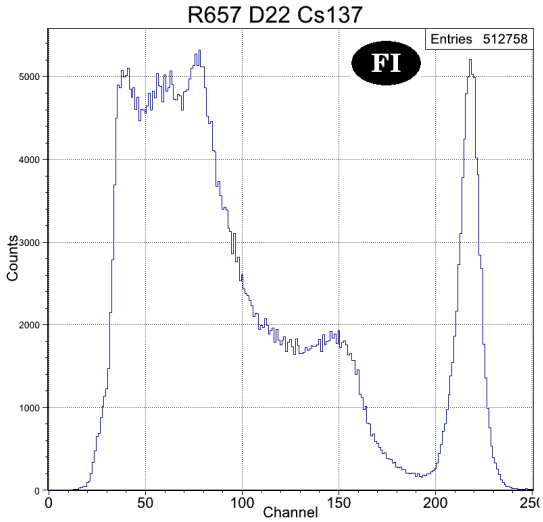

Figure 3.28: ^{137}Cs spectrum with D22 from the final instrument

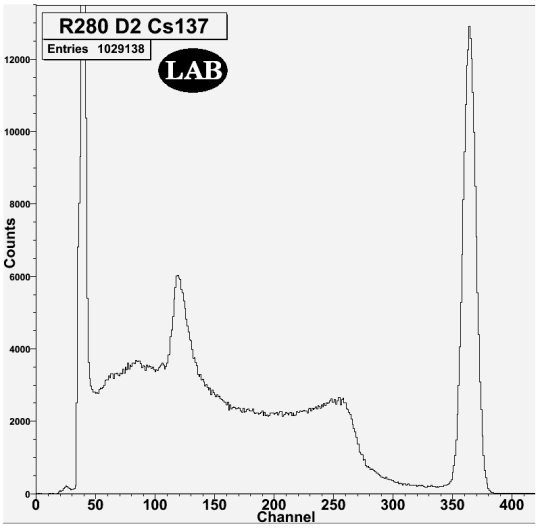

Figure 3.29: ^{137}Cs spectrum from the laboratory run R280

Figure 3.30 shows the ^{57}Co spectrum of D22 from R661, it should be compared to fig. 3.18. Figure 3.31 shows the ^{60}Co spectrum of D22 from R658, and it should be compared to fig. 3.21.

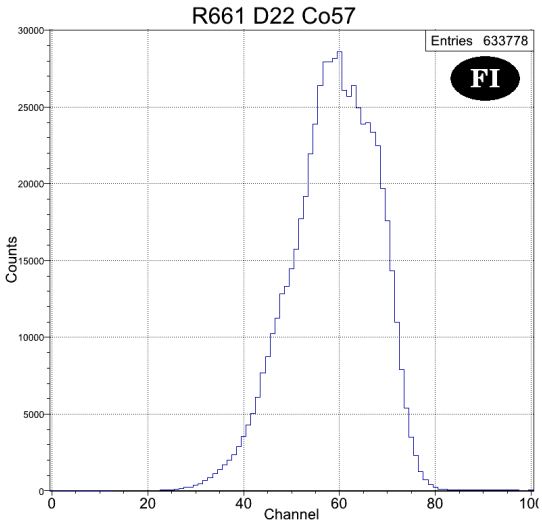

Figure 3.30: ^{57}Co spectrum with D22 from the final instrument

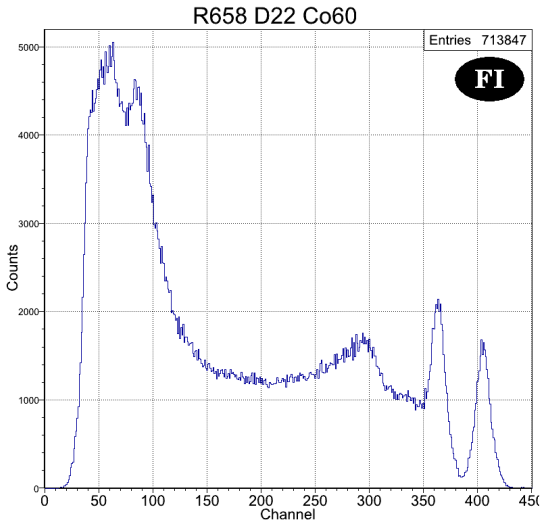

Figure 3.31: ^{60}Co spectrum with D22 from the final instrument

Figure 3.32 shows the AmBe spectrum (with a fit curve) of D22 from R664, it should be compared to fig. 3.22. Finally, figure 3.33 shows the self-background from the three D2 detectors from R659, it should be compared to fig. 3.24.

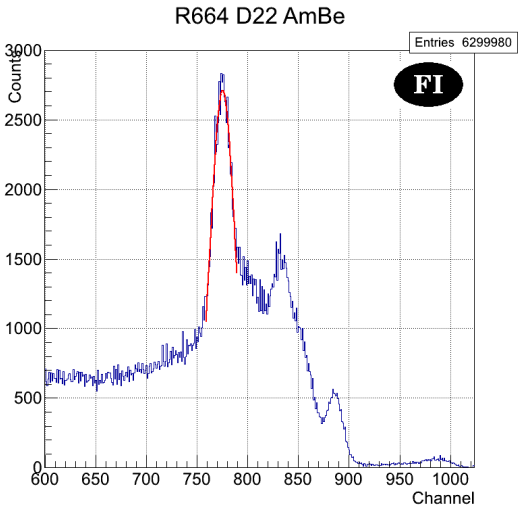

Figure 3.32: AmBe spectrum with D22 from the final instrument

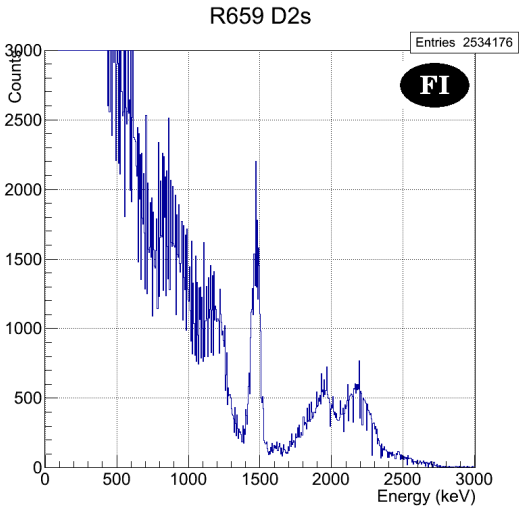

Figure 3.33: $LaBr_3$ self-background from the D2 layer of the final instrument

These points are then used to fit calibration curves, shown in figure 3.34:

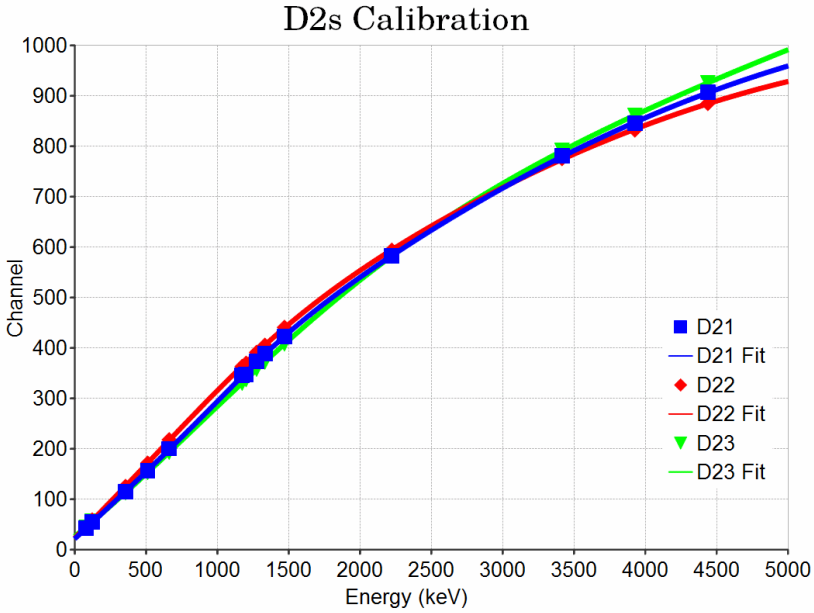

Figure 3.34: FACTEL prototype D2 $LaBr_3$ detectors calibration curves

The data points were fitted following the empirical formula of eq. 3.8:

$$Ch(x) = A + B\,x - \frac{C + D\,x + E\,x^2}{1 + F\,e^{-G\,x}}, \tag{3.8}$$

where Ch [Channel] is the detector response, x [keV] the energy deposit in the detector, and A, B, C, D, E, F and G the fit parameters. The fit parameters values for the three $LaBr_3$ D2 detectors are compiled in table 3.2:

D2s Calibration Parameters

	D21	D22	D23
A	21.0264	13.1839	-186.547
B	0.259784	0.266493	0.061834
C	-55.0496	-103.667	-625.048
D	-0.00911451	0.0101155	-0.0575665
E	0.0000184602	0.0000188198	0.00000144465
F	99.3143	9.61137	1.93489
G	0.00371707	0.00218134	0.00106531

Table 3.2: FACTEL $LaBr_3$ D2 Detectors calibration fit parameters

It might appear strange to use a 7 parameters function for 14 data points, however this function was developed prior to the final energy calibration using many more data points (over 20). The function of eq. 3.8 was carefully chosen. The points at lower energy are very linear, so a line ($A+B\,x$) is the obvious choice, then the non-linearity arising from the PMT saturation must be subtracted. The functions usually used to account for non-linearity in detectors were tested against the data without yielding satisfactory results. The function closest to the non-linear deviation was a parabola ($C + Dx + Ex^2$). However, the parabola lower energy part had to be suppressed so as not to interfere with the lower energy linear calibration. The need was for a continuous Heaviside function to "turn on" the parabola at the appropriate energy. The function also had to approach zero quickly at low energies so as not to impede with the linear function, while approaching unity fast enough at higher energies to properly match the non-linearity. The chosen function $(1+F\ e^{-G\,x})^{-1}$ is based on the logistic function, with one parameter controlling where the function "turns on" and the other controlling how fast the function passes from zero to one. The function described by eq. 3.8 was effective describing the D2 detectors responses, as well as other responses from other detectors our group is using.

The parameters values have to be chosen carefully for the fitting script not to converge on an improper local minimum of the parameter space. For the FACTEL D2 detectors, the B parameter must be positive, the C parameter must be positive and small, and the G parameter must be positive. In practice, one starts the fitting procedure by getting a sense of the A and B parameters by fitting only the low-energy points to a line. Then, one gets a sense of the C, D and E parameters by fitting a parabola to the higher energy points minus the line. Finally, one obtains final values for all parameters by fitting all the data points to the complete function using the previously obtained values as the seeds for the fitting script to converge to the desired

minimum. One should also keep an open mind for the parameters values, the values of the parameters for the D23 line ($\boldsymbol{A}$ and $\boldsymbol{B}$) are not conventional and would not fit the low-energy points properly; however the slow ascent of the logistic function compensates this and the final function fits the data well, so the values were kept nonetheless even if unconventional. A final warning concerning eq. 3.8: it is to be used only within the fitted energy range, it diverges at higher-energy.

As seen in fig. 3.34, the $LaBr_3$ D2 detectors energy response is linear at lower energies, then becomes non-linear due to an electronic saturation effect. The D2 detectors "trustworthy" range in terms of channels is from channel 35 to channel 975. The lower limit set to channel 35 is empirically defined by inspecting spectra (fig. 3.25, 3.28, etc.): the 80.9 keV line from ^{133}Ba is clearly visible. The higher limit of channel 975 is defined by the calibration curves of fig. 3.34. FACTEL D2 $LaBr_3$ detectors have energy ranges of:

$$\begin{aligned} &\textbf{D21: 51 keV} \rightarrow \textbf{5198 keV} \\ &\textbf{D22: 42 keV} \rightarrow \textbf{5918 keV} \\ &\textbf{D23: 37 keV} \rightarrow \textbf{4858 keV} \end{aligned} \tag{3.9}$$

For the energy resolution measurement, only the data from well isolated photopeaks were kept. The nine points kept for this measurement are: 122.06 keV from ^{57}Co, 356.02 keV from ^{133}Ba, 511 and 1274.53 keV from ^{22}Na, 661.66 keV from ^{137}Cs, 2223 keV from ^{252}Cf, 1332.50 keV from ^{60}Co, 1470 keV from the $LaBr_3$ self-background, and 4438 keV from AmBe. The standard deviations for the various lines were averaged to get a fitted curve valid for all three D2 detectors. A data plot of the standard deviation and its fit is shown in figure 3.35.

Often, if photoelectron limited, the resolution is proportional to $E^{-1/2}$; however it does not represent the data satisfactorily (the blue lines in figures 3.35 and 3.36). The fit function used is:

$$\sigma\ (x) = A + B\,x + C\,e^{-D\,x} \tag{3.10}$$

Where x [keV] is the energy and the parameters are A = -4.64064, B = 0.0223813, C = 36.1328, and D = 0.0023828. The line was chosen because the last five points appeared linear, and the decaying exponential was chosen to quickly vanish to zero at higher energies.

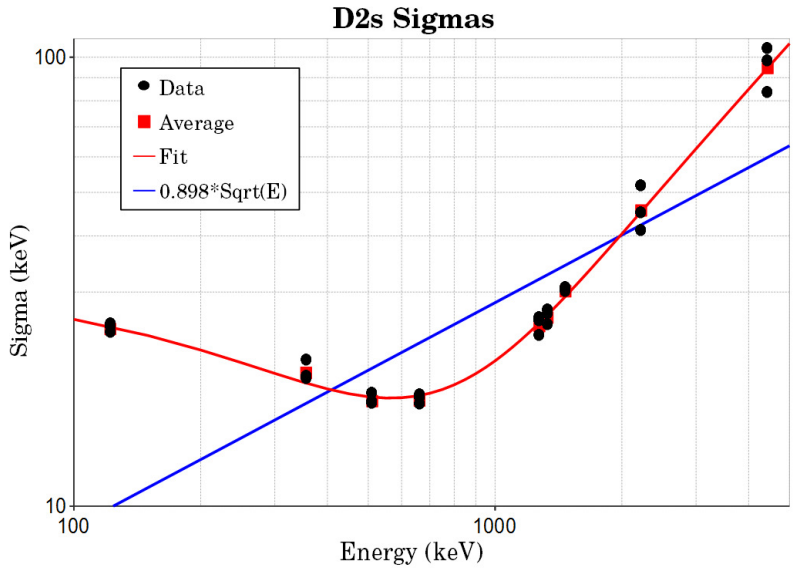

Figure 3.35: FACTEL prototype D2 $LaBr_3$ detectors sigmas of the energy peaks

The resolution R in function of the energy E and σ is directly given by using equations 2.14 and 2.15:

$$R = 100\%\ \frac{2.3548\ \sigma(E)}{E} \tag{3.11}$$

A plot of FACTEL $LaBr_3$ D2 detectors resolution in function of energy is shown in figure 3.36:

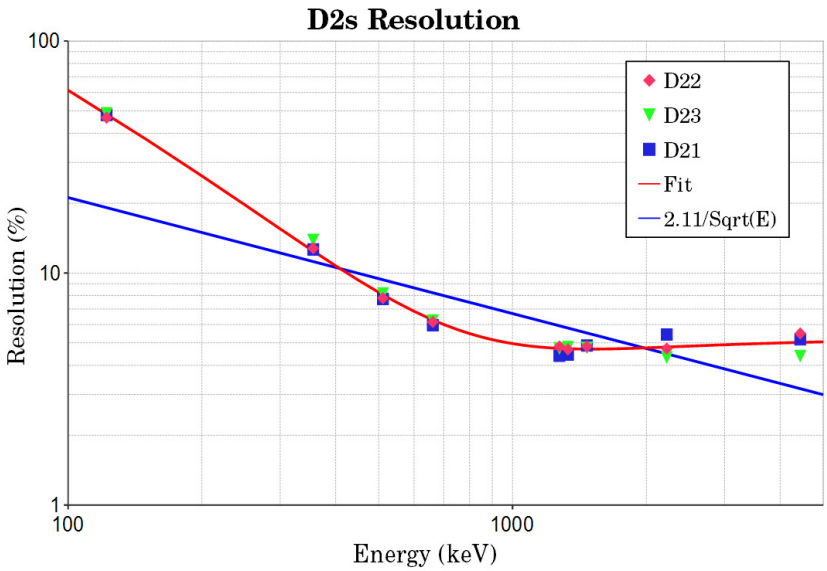

Figure 3.36: FACTEL prototype D2 $LaBr_3$ detectors energy resolution in function of energy

As seen in fig. 3.36, the D2 $LaBr_3$ detectors for the final FACTEL prototype had a 5% resolution above 1 MeV, and about 6% at 662 keV. Due to the electronic noise issue, these results are not the best results achieved and do not reflect the real capabilities of $LaBr_3$ detectors. Our best results are consistent with results in the literature: 4% at 662 keV and <3% above 1 MeV. The square root reference line shown in blue in the last two figures represents the usual response of a conventional linear detector, and we can see that it is inadequate for describing the response of our $LaBr_3$ detectors. {It has been pointed that the last point on the fig. 3.36 curve, the 4.4 MeV point from AmBe, is slightly incorrectly placed and should have been a little bit lower: the current point includes a broadening coming from the fact that the $^{12}C^*$ in equations 3.6 and 3.7 is not exactly at rest. The $^{12}C^*$ not being completely at rest when it emits the 4.4 MeV gamma ray induces a small further broadening implying that the last point in fig. 3.36 should have been slightly lower. This is a small effect not really relevant here, however it is worth pointing it out.}

3.3.2.3 D1 Calibration

The energy calibration of a liquid organic scintillator that interacts with gamma rays via Compton scattering is more complex than calibrating an inorganic crystal scintillator that photoelectrically absorbs gamma rays. One should remember that gamma rays in that energy range interact primarily via the Compton effect, and that the direction of the incoming gamma ray needs to be retrieved. The D1 detectors have been chosen to be targets for incoming gamma rays to Compton scatter. Then the resulting gamma ray from the partial absorption is used to constrain the direction of the initial gamma ray. D1 detectors are chosen for their Compton scattering properties: they are chosen for being good at "not absorbing" gamma rays. Gamma rays will thus not deposit their full energy in a D1 detector, making it difficult to get clear sharp calibration data. Three techniques to calibrate liquid scintillators will now be reviewed: photoelectric absorption at low energy, scatter data, and Compton edge calibration.

First, figure 3.37 presents a D1 spectrum. It is a ^{22}Na spectrum taken with D11 and the equivalent spectrum from a $LaBr_3$ crystal scintillator can be seen in fig. 3.27. As expected, the difference is that the photoelectric absorption peaks are absent for an organic liquid scintillator: it interacts via Compton scattering which produces Compton edges in spectra.

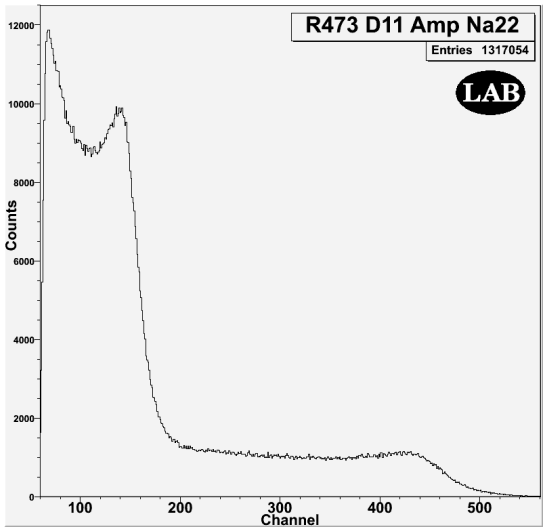

Figure 3.37: ^{22}Na spectrum with D11, the photoelectric peaks are absent because organic liquid scintillators interact via Compton scattering with incoming gamma rays, thus only two Compton edges are present.

The first method to measure energy calibration points for an organic liquid scintillator detector is low-energy photoelectric peaks. As seen in fig. 2.1, there is a region down left where a low Z material will interact predominantly via photoelectric absorption (or numerous Compton scatters) with low-energy gamma rays. Also, the predominance regions do not imply exclusivity: low-energy gamma rays can interact via photoelectric absorption in the Compton region, but with a lower probability. This can be used to measure low-energy calibration points from our lower energy sources: ^{241}Am, ^{109}Cd and ^{57}Co. A ^{57}Co photopeak from a D1 organic liquid scintillator is shown in figure 3.38.

This calibration method was used throughout the FACTEL project evolution to get low-energy calibration points for the D1 detectors, but could not be used for the final instrument calibration: the electronic noise issue combined with the high energy threshold used for the flight made that method impossible to use.

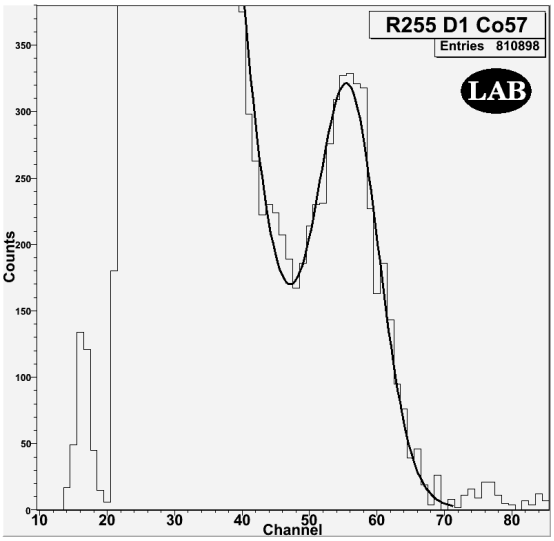

Figure 3.38: ^{57}Co spectrum with D11, organic liquid scintillators interact via the photoelectric effect with low-energy gamma rays

The second method to calibrate the energy response of organic liquid scintillator detectors is to use the telescope in a backward logic. Once the D2 detectors are calibrated, and knowing the initial energy of the gamma rays emitted by the calibration source, it is trivial to retrieve the energy deposit in the D1 detector by reversing eq. 2.16:

$$E_1 = E_\gamma - E_2 \tag{3.12}$$

Hence, a source is placed at an angle in front of the telescope and the energy deposit in a D2 detector will give the energy deposit in the D1 detector. The scatter angle does not need to be known: the initial energy and the energy deposit in the D2 detector are the only values needed to retrieve the energy deposit in the D1 detector. This technique can provide as many points as needed by varying the sources and angles.

An example of this technique is shown in figure 3.39: the laboratory run involved placing a ^{137}Cs source in front of the detectors pair 60° from the zenith and

recording the coincident events. The figure shows the spectrum from each detector, both of them displaying a clear peak used to calibrate the D1 detector. The furthest peak in the D2 detector spectrum, at Ch2=255, is the photoelectric absorption of a 662-keV gamma ray in the D2 detector at the same time that a random interaction occurs in the D1 detector. The events above the peak in the D1 detector spectrum comes from a 662-keV gamma ray Compton scattering in the D1 detector at the same time a random interaction occurs in the D2 detector. The second and tallest peak in the D2 detector spectrum at Ch2=215 is what we are looking for. It comes from the full photoelectric absorption of the resulting gamma rays from 662-keV gamma rays that previously Compton scattered in the D1 detector, leaving the clear peak at Ch1=105 in the D1 detector spectrum. For example, if the peak in the D2 detector is at 400 keV, then the peak in the D1 detector must be at 262 keV.

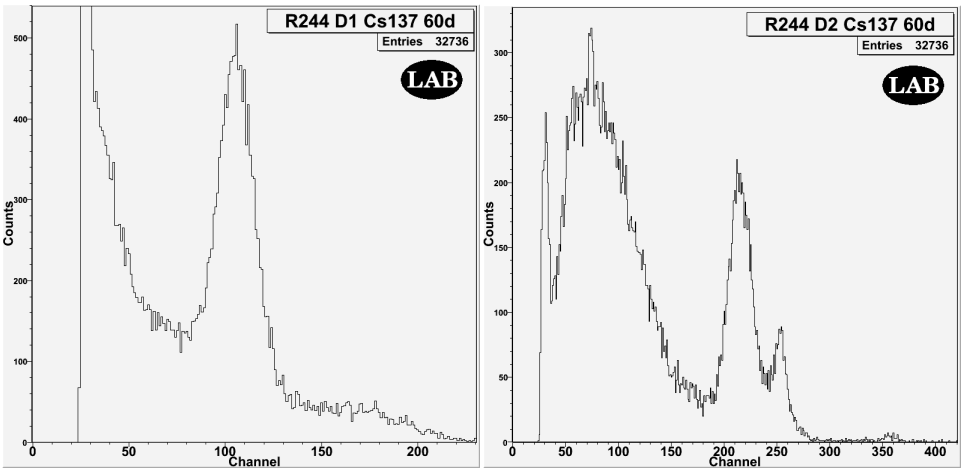

Figure 3.39: D1 detector (left) and D2 detector (right) spectra from R244 (^{137}Cs at 60°), the peaks at Ch1=105 and Ch2=215 are used to calibrate the D1 detector

This Compton scattering technique to calibrate organic liquid scintillators is the only technique used to calibrate the D1 detectors for the final FACTEL instrument prototype. To calibrate the D1 detectors, two ^{22}Na runs were performed leading to four calibration points, and one ^{137}Cs run was performed to retrieve a fifth point.

Because three calibrated D2 detectors lead to three detector pairs with slightly different angles for each D1 detector, fifteen calibration points were used for each D1 detector. (Detector pairs are noted by a "P," then the D1 detector number, then the D2 detector number. For example, P23 is the pair formed by D12 and D23.) A table with the calibration data for D12 is shown in table 3.3. An example of the calibration spectra from P22 from the ^{137}Cs run is shown in figure 3.40.

D12 Calibration Data

Energy (keV)	Channel	Sigma (Cha)	Resol (keV)	Run #	Pair
351.107	130.016	12.0445	19.9868	665	P21
337.847	128.852	11.7965	20.3435	665	P22
337.917	131.927	13.2977	22.9277	665	P23
347.089	133.426	13.4638	22.6006	666	P21
344.589	131.871	13.3806	22.6239	666	P22
342.069	133.433	13.5916	23.1500	666	P23
1070.05	428.787	29.5764	16.1040	666	P21
1065.17	426.57	27.421	14.9988	666	P22
1061.6	428.65	29.7538	16.3296	666	P23
202.069	80.3919	9.24996	26.6706	667	P21
190.969	79.4559	9.49693	28.9743	667	P22
191.799	80.4433	10.495	31.8808	667	P23
778.43	306.887	33.4648	25.0474	667	P21
753.26	298.301	32.5849	25.2037	667	P22
753.44	302.81	32.1802	24.8848	667	P23

Table 3.3: Calibration data for D12

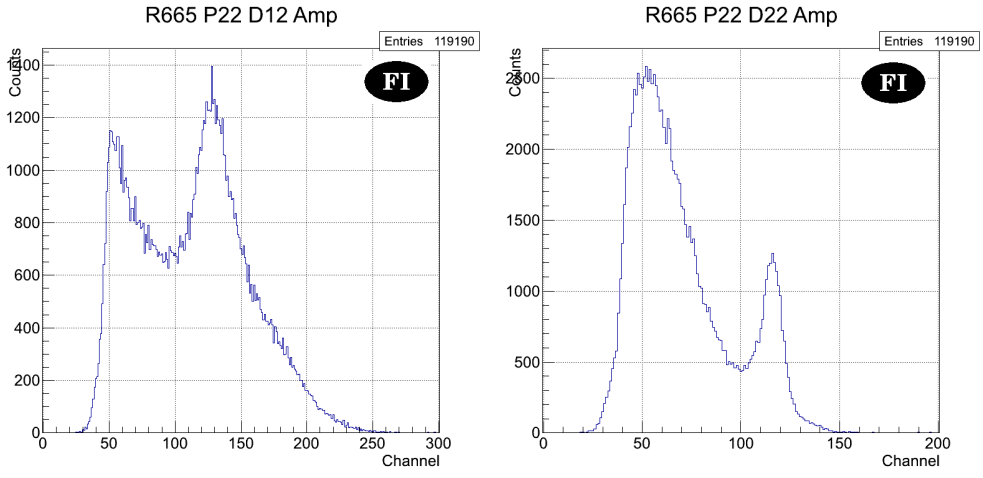

Figure 3.40: D12 detector (left) and D22 detector (right) spectra from R665 (^{137}Cs at ~80°)

A linear function was then used to fit the calibration points to determine the D1 detectors calibration, a plot is shown in figure 3.41:

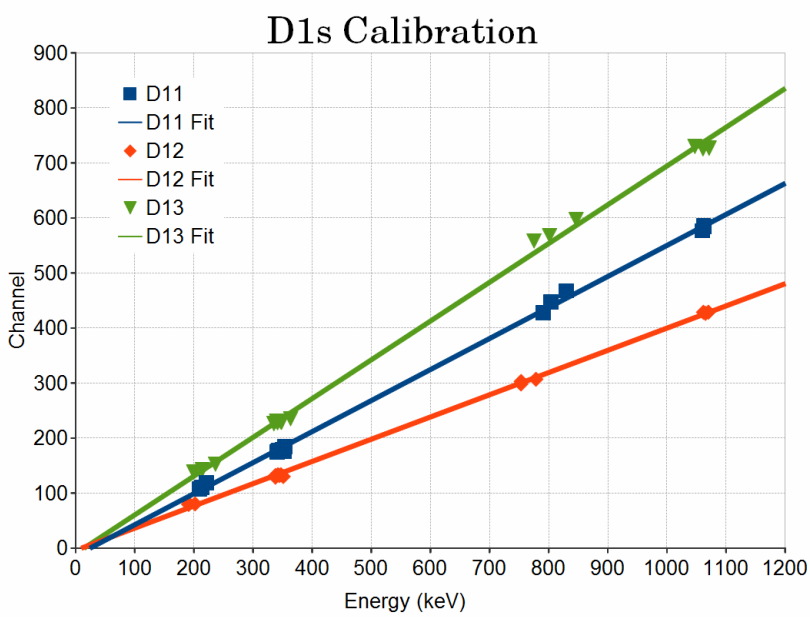

Figure 3.41: FACTEL prototype D1 organic liquid scintillator detectors calibration curves

There are actually 6 points around 350 keV for each detector in fig. 3.41: as seen in table 3.3, the first six points are very close in energy. This is a fortunate coincidence: R666 was a ^{22}Na at 160° run meant to record the most energetic point of the line by using the backscatter of 1275 keV gamma rays, which would give ~1060 keV in a D1, while R665 was a ^{137}Cs at 80° run aiming to have equal deposits in both layers. Organic liquid scintillators are notoriously hard to calibrate, and having six different points from two different laboratory runs spanning two weeks of data acquisition stacking in a tight cluster indicates a precise calibration.

The data points were fitted with a linear function:

$$Ch(x) = A + B\,x \quad , \tag{3.13}$$

where Ch [Channel] is the detector response, x [keV] the energy deposit in the detector, and A and B the fit parameters. The fit parameters values for the FACTEL instrument D1 detectors are compiled in table 3.4:

D1s Calibration Parameters

	D11	D12	D13
A	-13.810146	-4.007502	-10.059542
B	0.563866	0.403811	0.704477

Table 3.4: FACTEL D1 Detectors calibration fit parameters

The D1 detectors "trustworthy" range in terms of channels is from channel 50 to channel 975, then FACTEL D1 organic liquid scintillator detectors have energy ranges shown in equation 3.14. The lower energy thresholds were set to a high value to avoid low-energy noise.

$$\begin{aligned} &\text{D11: } 114\ \text{keV} \rightarrow 1752\ \text{keV} \\ &\text{D12: } 134\ \text{keV} \rightarrow 2423\ \text{keV} \\ &\text{D13: } \ 86\ \text{keV} \rightarrow 1397\ \text{keV} \end{aligned} \tag{3.14}$$

For the D1 detectors energy resolution analysis, one detector actual resolution is convoluted with the geometrical factor allowed by the detectors and geometry. However, the intrinsic resolution of a liquid scintillator detector is usually poor enough for that factor not to have a major impact. To remove the geometrical factor from a laboratory peak, σ_{lab}, one performs a simulation replicating the laboratory run, measures the peak sigma from the simulation, σ_{geo}, and removes it statistically from the laboratory run sigma to get the intrinsic resolution of the detector, σ_{det}, this is summarized in equation 3.15:

$$\sigma_{lab} = \sqrt{\sigma_{det}^2 + \sigma_{geo}^2} \Rightarrow \sigma_{det} = \sqrt{\sigma_{lab}^2 - \sigma_{geo}^2} \quad , \tag{3.15}$$

where σ_{lab} is the laboratory run peak sigma, σ_{det} the intrinsic sigma of the detector, and σ_{geo} the simulation peak sigma. Such analysis has been performed for past iterations of the instrument, but was deemed unnecessary for the final instrument since the electronic noise was degrading resolution to levels that did not reflected the actual capabilities of the detectors.

The data and the fit used for the sigma analysis of the D1 detectors are shown in figure 3.42. Many functions were tested to fit the data and the conventional square root function proved to be the most satisfactory when all the higher-energy points are not included in the fit. All the fits that included these later points missed the lower energy clusters and the mismatch was evident when comparing laboratory data and computer generated spectra. Since those later points are known to have a significant error, although the precise dominant source of error is not well identified (fig. 3.49 would suggest a large geometric effect, σ_{geo}), discarding them was the correct approach.

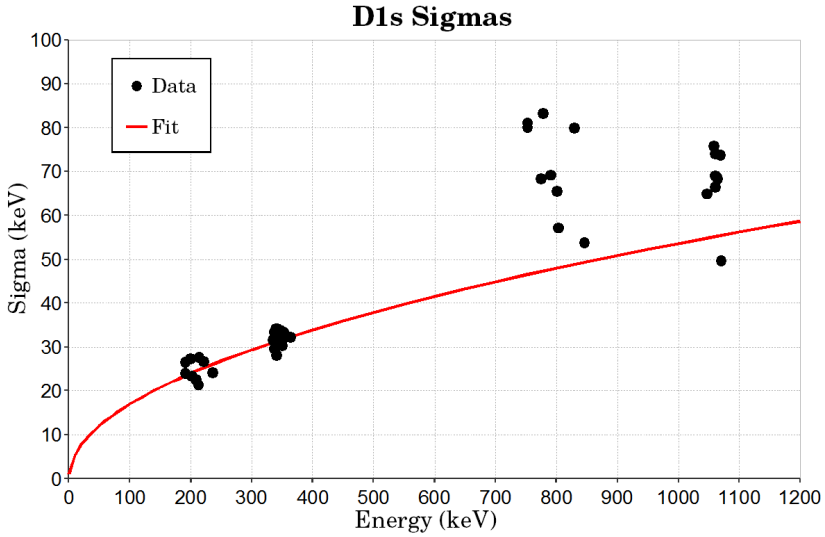

Figure 3.42: FACTEL prototype D1 organic liquid scintillators detectors sigmas of the energy peaks, the later points were discarded due to significant error

The fitting function is a conventional square root function:

$$\sigma(x) = \sqrt{A + B\,x} \tag{3.16}$$

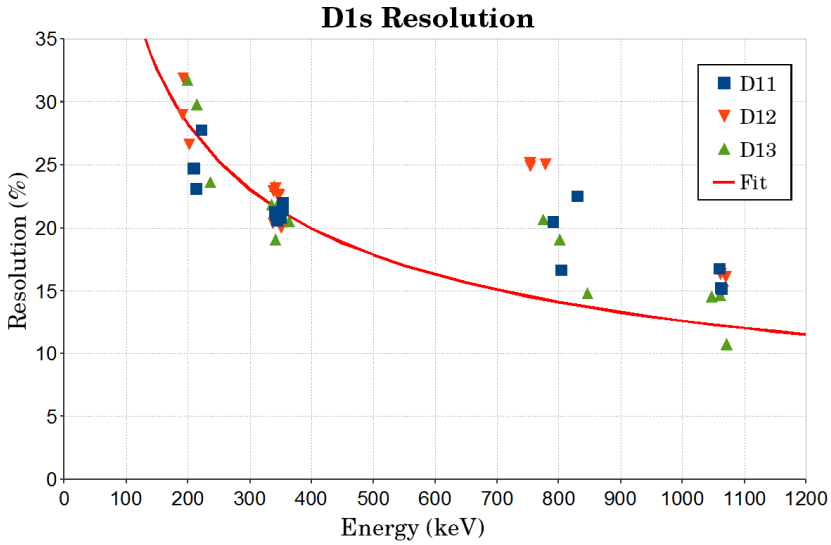

Figure 3.43: FACTEL prototype D1 organic liquid scintillator detectors energy resolution in function of energy

Where x [keV] is the energy and the parameters are A=0.913535 and B=2.8705. The resolution is computed using eq. 3.11 and the result shown in figure 3.43. Those results are conventional and unremarkable for organic liquid scintillator detectors.

The third organic liquid scintillator calibration technique is Compton edge calibration. Compton edge calibration is a quick, efficient and sufficiently precise method to calibrate organic liquid scintillators. However, it requires a previous complete calibration of the detectors, and optionally a set of simulations using the resolution curve to improve the accuracy of the technique. It is thus a quick technique to re-calibrate detectors, and is completely irrelevant for a first calibration. The technique consists in assigning an energy value to a detector Compton edge maximum by using a first calibration, then to use the assigned value to re-calibrate the detector.

For example, after the first calibration is complete, one measures a ^{22}Na spectrum such as the one shown in fig. 3.37 and assigns an energy value to the edges maxima. Afterwards, as long as the detector resolution is not modified substantially, this assigned value can be used to quickly re-calibrate a detector with a single ^{22}Na run. Other clear Compton edges such as the ones from ^{137}Cs and ^{60}Co can be used with this technique. D1 organic liquid scintillator spectra from a ^{137}Cs and ^{60}Co laboratory runs are shown in figures 3.44 and 3.45 respectively. The fit function in this case does not need to be a complicated function with multiple parameters and a fine background account, a quadratic function is sufficient to locate the maximum. Using this technique, an energy value was assigned for the two Compton edges from ^{22}Na and the ones from ^{137}Cs and ^{60}Co, resulting in four calibration points.

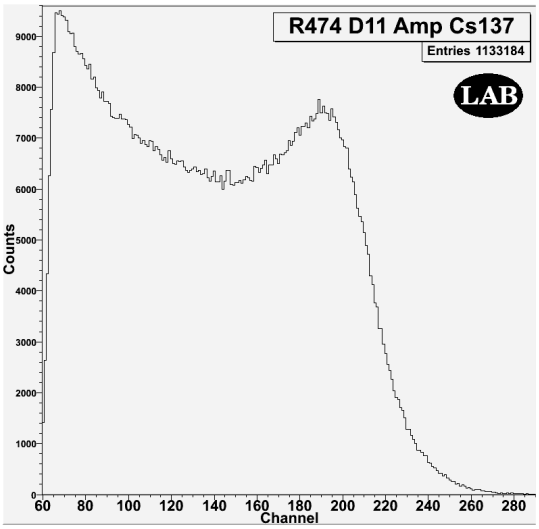

Figure 3.44: ^{137}Cs spectrum with D11

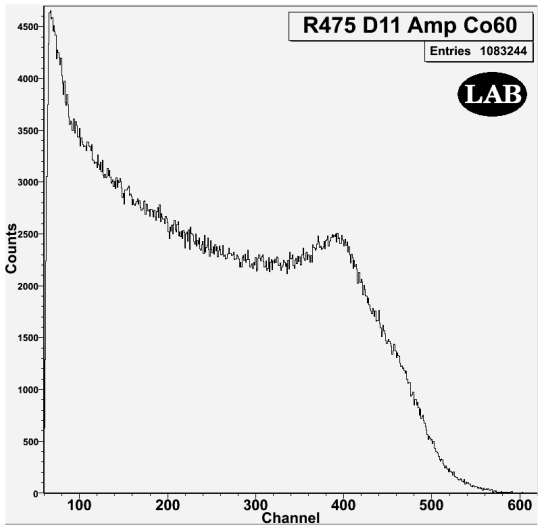

Figure 3.45: ^{60}Co spectrum with D11

The power of this technique is shown by the fact that figures 3.37, 3.44 and 3.45 are actually coming from R473, R474 and R475: three 500 s runs performed in a row that led to the provisional calibration shown in figure 3.46:

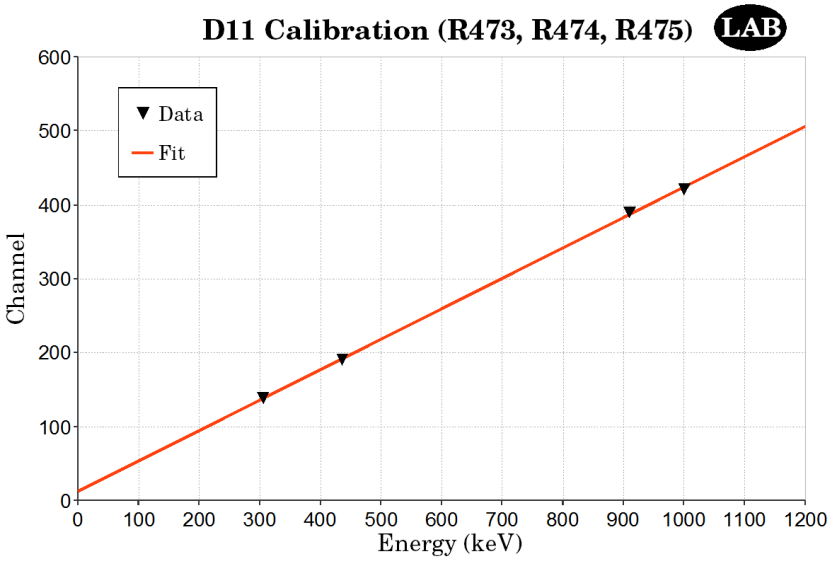

Figure 3.46: Organic liquid scintillator detector energy calibration using the Compton edge technique, the 3 laboratory runs used to perform the calibration took a total of 1500 s

The resulting calibration of fig. 3.46 is precise, but more importantly quick: these three runs were taken in 1500 s while the three runs (R665, R666 and R667) used for the final calibration of the D1 detectors of the FACTEL instrument shown in 3.41 took a full month to complete.

Simulations can be used to refine the energy value given to a Compton edge maximum by the first energy calibration. To do so, one models a D1 detector and then simulates gamma rays of the appropriate energy and records the energy deposits. The resulting spectra, shown in figure 3.47, will show the theoretical Compton edge spectra with a sharp edge and a drastic fall.

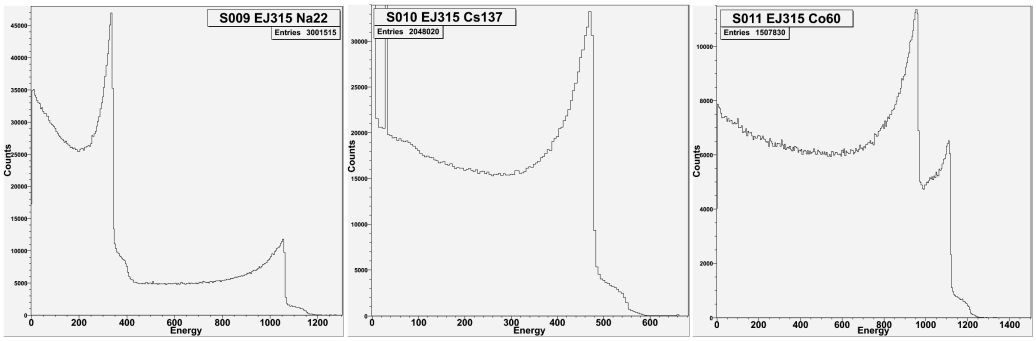

Figure 3.47: Unbroadened D1 Simulations spectra: ^{22}Na (left), ^{137}Cs (middle), ^{60}Co (right). The spectra show the theoretical shapes of Compton edges: a sharp edge followed by a drastic fall.

One then uses the first calibration sigma fit, fig. 3.42 is an example, to broaden these spectra and match the real detector resolution. Theoretically, this is the convolution of the theoretical spectra with a Gaussian function that broadens with energy. In practice, one adds a noise value picked from a Gaussian distribution of the appropriate standard deviation on an event by event basis and lets the statistics fill the spectrum. Once broadened by the appropriate sigma, the spectra from fig. 3.47 are shown in figure 3.48:

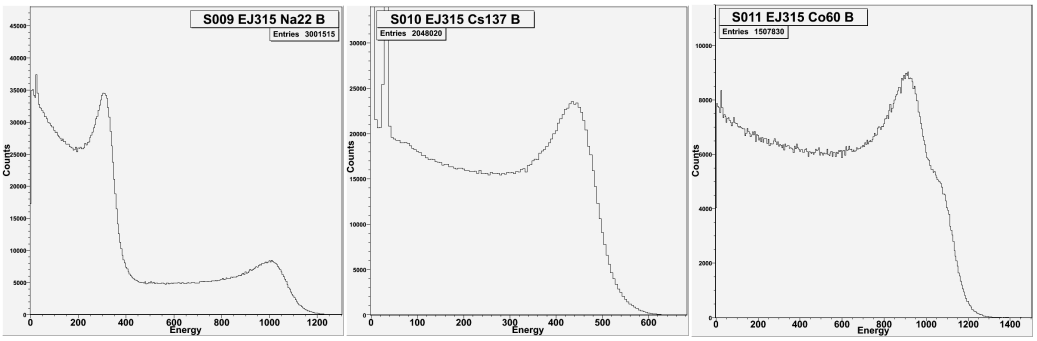

Figure 3.48: Broadened D1 Simulations spectra: ^{22}Na (left), ^{137}Cs (middle), ^{60}Co (right).

Comparing the spectra of fig. 3.48 with figures 3.37, 3.44 and 3.45, one could note that the simulations should have been broadened more. However these runs (R473, R474, R475) were performed at later time than the simulations were broadened. These broadened simulation D1 spectra should be compared to the R396,

R397 and R400 spectra, which are not presented here, and are in better agreement. Here, changing the broadening by 1 or 2% would only move the maxima a few keV, which is inconsequential for a liquid scintillator energy calibration.

Simulations combined with experimental results can provide a second set of energy values for the Compton edges maxima. That second set can be compared with the first set provided by direct calibration. Both sets are then used to choose a refined value for a Compton edge maximum. For the FACTEL project D1 organic liquid scintillators detectors, these values have evolved throughout the project as more experience was gained with the detectors. The final values used were: ^{22}Na 511 keV Compton Edge Maximum (CEM) = 305 keV, ^{137}Cs 662 keV CEM = 436 keV, ^{60}Co 1173 keV CEM = 910 keV, and ^{22}Na 1275 keV CEM = 1000 keV.

The Compton edge calibration technique has been successfully used throughout the majority of the project development to calibrate the D1 detectors, but could not be used for the final instrument calibration. The significant degradation of the detectors resolution meant the values for the Compton edges maximums were now significantly incorrect. Re-broadening the simulations results would have required a sigma measurement from the detectors, which comes from a first calibration that was not yet performed. The Compton edge calibration technique is a re-calibration method, it functions properly as long as the resolution of the detectors does not change significantly. For the final instrument, the resolution loss implied that a full recalibration was required. Furthermore, the D12 detector was not composed of EJ-315 like the D11 and D13 detectors: the D12 detector came from the LANL laboratory and was composed of deuterated toluene rather than deuterated benzene. The EJ-315 simulations were thus invalid for the D12 detector, and no calibration data was available for its sigmas. A full calibration of FACTEL D1 detectors was thus unavoidable and necessary. (As seen in figures 3.42 and 3.43, the D12 detector

resolutions were comparable to the other two detectors, so all three D1 detectors were treated in the same manner.)

3.3.3 Telescope Performance

This section reviews how a Compton Telescope performs. Once a run in telescope (or coincidence) mode has been completed, the first and most useful data analysis tool is a 2D scatter plot where the events are placed within the D1-D2 space. A scatter plot from a ^{22}Na at 30° run (the source was actually closer to 25°) is shown in figure 3.49.

This plot was particularly chosen for its many features. The D1-D2 scatter plot is the main tool used to analyze a scatter run: it provides a quick and complete look on what occurred during the run. (Note: most of the analysis is done in term of channels. All the usual work is done with what the data acquisition system provides, channel integer numbers, and usually only the end products are displayed with physical units (keV and nanoseconds). So unless a unit is specified in a plot axis, the units are channels, such as fig. 3.49.)

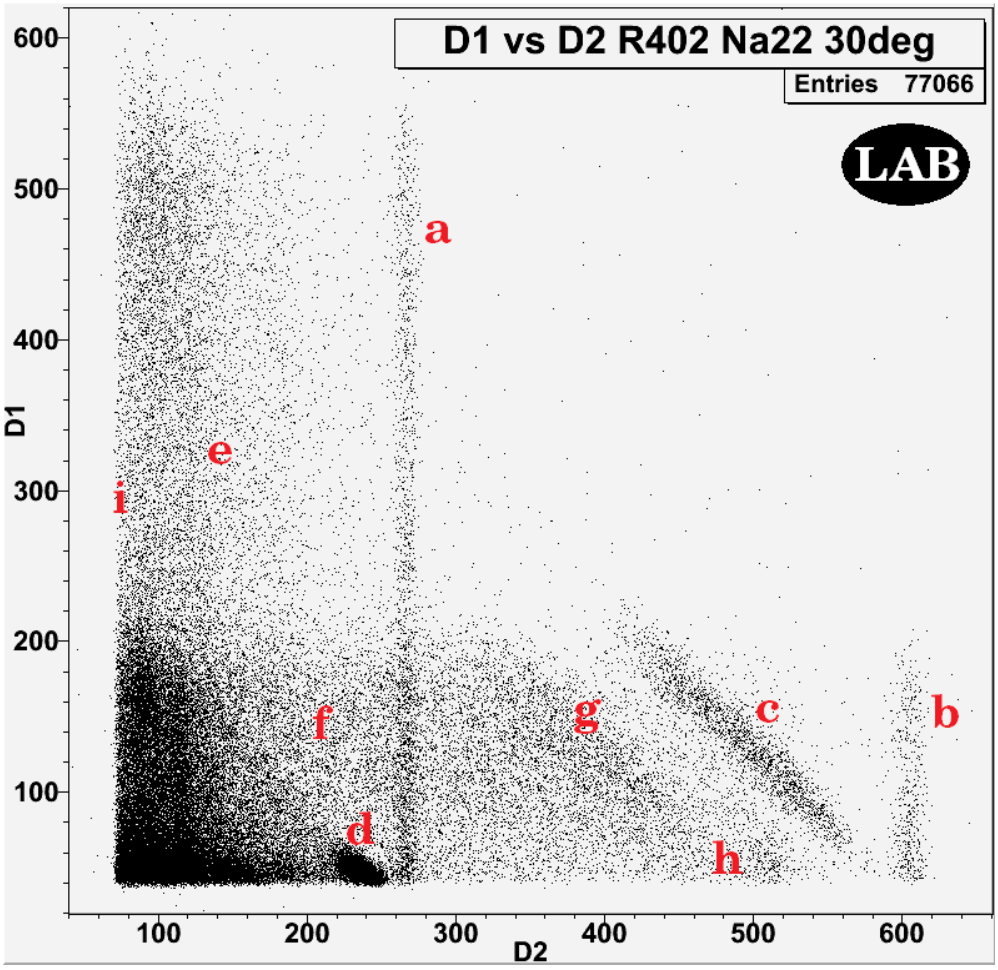

Figure 3.49: D1-D2 scatter plot from a ^{22}Na at ~30° run, see text for details

The first thing that catches the eye in fig. 3.49 are the vertical lines at D2 = 270 (a) and D2 = 605 (b). These are respectively a 511 keV gamma ray being photoelectrically absorbed in the D2 detector while another interaction occurs in the D1 detector, and a 1275 keV gamma ray being photoelectrically absorbed in the D2 detector while another interaction occurs in the D1 detector. This implies that the D2 detector was not properly shielded from the ^{22}Na source. The lack of these vertical lines in further plots indicates the D2 detectors were properly shielded from the source. The 1275 keV line (b) is continuous from D1 channels 60 to 200, this means a 511 keV gamma ray Compton scattered in the D1 detector while a 1275 keV gamma ray was photoelectrically absorbed in the D2 detector: the D2 1275 keV absorption

line (b) is correlated with the Compton continuum of a 511 keV gamma ray Compton scattering in the D1 detector. The same logic applies for the 511 keV absorption line (a): the denser part for D1 channels between 60 and 200 comes from a 511 keV gamma ray being absorbed in the D2 detector while another 511 keV gamma ray Compton scatters in the D1 detector, while the less dense part of the line (a) for D1 channels between 200 and 560 corresponds to a 511 keV gamma ray being absorbed in the D2 detector while a 1275 keV gamma ray Compton scatters in the D1 detector. Along that line (a), the D1 spectrum would look like fig. 3.37 while the D2 spectrum would only be a sharp peak at 511 keV.

The second striking features of the fig. 3.49 plot are the diagonal line from (D2=420, D1=200 to D2=560, D1=80) (c) and the spot at (D2=240, D1=50) (d). These features are the Compton scatters of interest, scatters from the D1 to the D2 detectors. The 511 keV Compton scatter spot is right under the 511 keV D2 line (a) because a 511 keV gamma ray Compton scattering at 30° from the D1 detector to the D2 detector leaves 450.6 keV in the D2 detector and 60.4 keV in the D1 detector. The diagonal (c) follows the constant 1275 keV energy line for the telescope, and points to the base of the D2 1275 keV absorption line (b) which would be D2 = 1275 keV and D1 = 0 keV. The diagonal elongated aspect comes from the Compton scatters angles geometrically allowed by the setup.

The fig. 3.49 plot displays other features. The region (D1 60→560, D2 70→200) (e) involves a 1275 keV gamma ray Compton scattering in the D1 detector while a 511 keV gamma ray Compton scatters in the D2 detector. The region (D1 60→200, D2 70→420) (f) involves a 511 keV gamma ray Compton scattering in the D1 detector while a 1275 keV gamma ray Compton scatters in the D2 detector. The denser region around (D2 = 380, D1 = 150) (g) is a diagonalized version of the 1275 keV Compton edge in D2 (see fig. 3.26) and involves a 1275 keV gamma ray

Compton scattering in the D1 detector, then traveling to the D2 detector and Compton scattering again. The denser region (D2 = 510, D1 = 50) (h) arises from the backscatter of a 1275 keV gamma ray from the D2 detector to the D1 detector (D2 = 1062.2 keV and D1 = 212.8 keV, however the gamma ray Compton scatters again in the D1 detector leading to an incomplete absorption, else those events would be on the 1275 keV diagonal.) {Another interesting plot is a 3D plot (D2, D1, ToF) where the forward, noise and backward cases such as (h) are easy to spot.}

Many other cases could be highlighted by zooming in the lower energy region, cases involving two 511 keV gamma rays, but the observations of fig. 3.49 will be left as is for now. A last point to mention is that the region along the D1 axis (i) is a "forbidden" region for a single Compton scatter event from the D1 to the D2 detectors, these usually imply multiple scatters in one detector. Treating these events as single Compton scatters leads to unphysical results. For example inserting $\boldsymbol{E}_1$ = 1000 keV and $\boldsymbol{E}_2$ = 100 keV into eq. 2.17 leads to cos(θ) = -3.65, which is unphysical. This is a known and inconsequential issue, these events are filtered away by a simple θ calculation.

The D1-D2 scatter plot is a powerful analysis tool, and also our main one. For example, the D1 calibration fits were not actually performed using the spectra of figure 3.40, but were performed on much "cleaner" spectra from 2D cuts of the scatter plot from that pair, this is shown in figure 3.50:

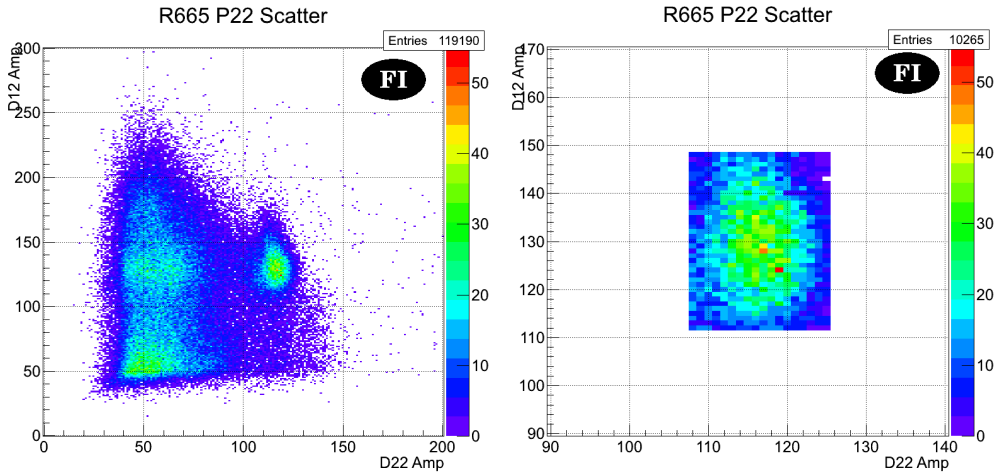

Figure 3.50: D1-D2 scatter plot of P22 from R665 (^{137}Cs at ~80°) (left), and the selected region for the D12 calibration (right)

The D1-D2 scatter plot is for the experienced eye a powerful tool to diagnose a laboratory run, it also permits us to view and quickly select regions of interest, and discern rare cases otherwise buried in 1D plots, such as the 1275 keV backscatter spot at (510, 50) (h) in fig. 3.49.

The second tool is to express the data points from (D2, D1) space to (Total Energy, Angle) space by using equations 2.16 and 2.17. Figure 3.49 then becomes figure 3.51. To visualize the conversion, figures 3.49 and 3.51 are shown side by side in figure 3.52. The reader should observe how the features of fig. 3.49 migrate to fig. 3.51. Note that the angle axis stops at 90°.

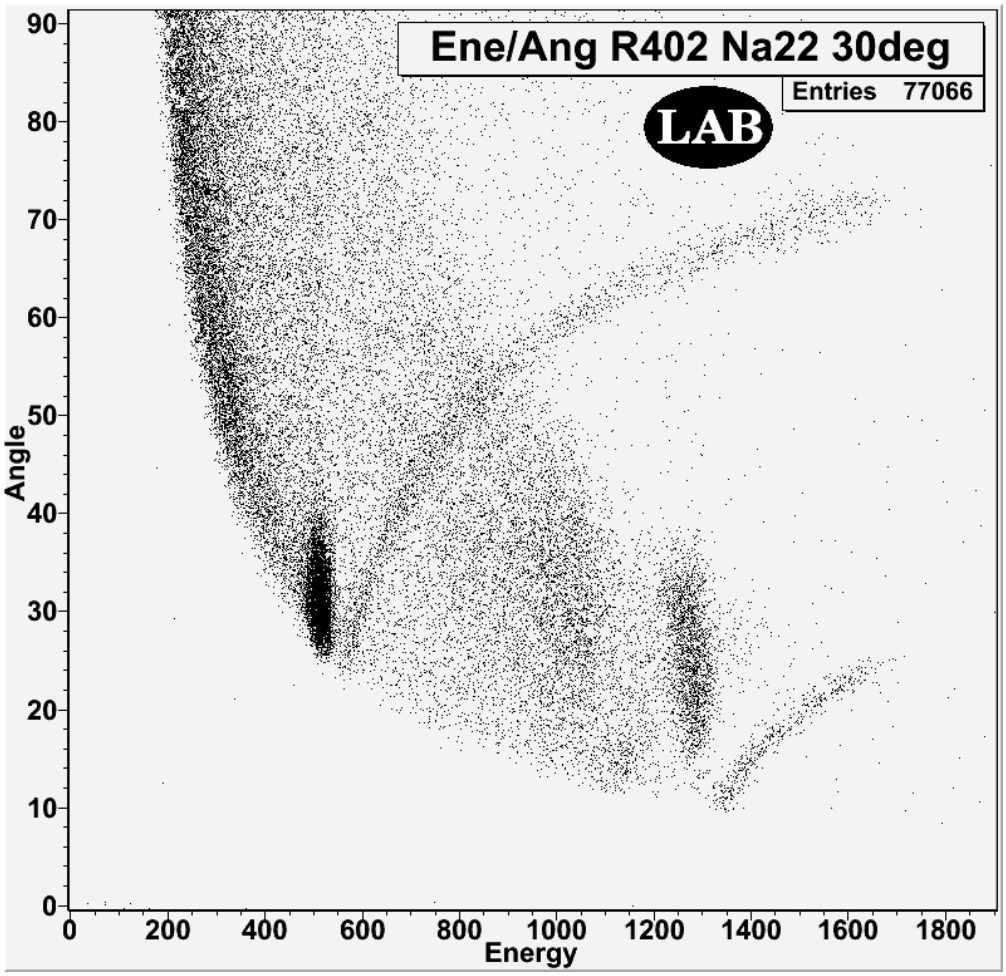

Figure 3.51: Total Energy-Angle scatter plot from a ^{22}Na at ~30° run

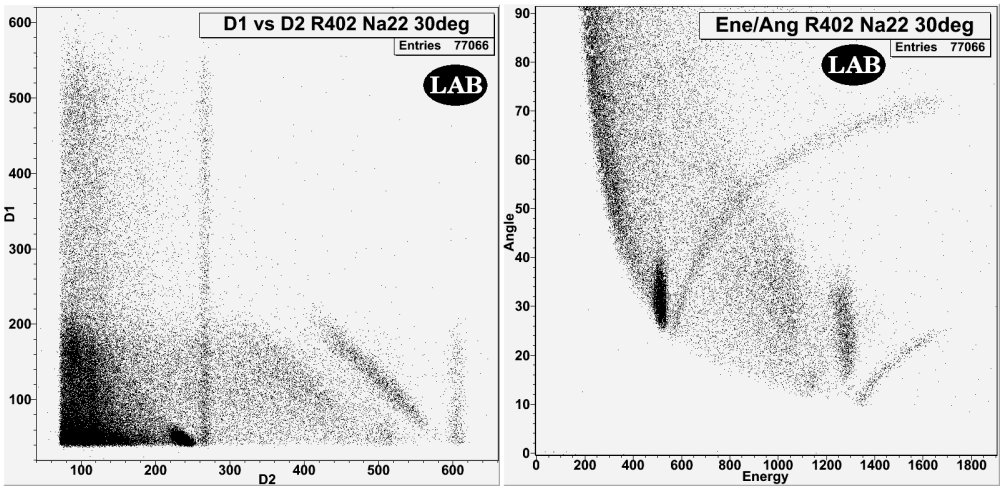

Figure 3.52: Figures 3.49 and 3.51 side by side, notice how the features migrate from one plot to the other

The diagonal lines become vertical lines of constant energy (511 and 1275 keV) with an angle width. (The source was difficult to place at an exact angle, this run aimed for 30° and was noted as such. The 511 keV spot tended to confirm the 30° value, however the 1275 keV spot was at odds with that conclusion. The angle is now believed to have been closer to 25° and that the 511 keV spot is truncated from its lower portion by the D1 detector threshold.) The vertical lines from fig. 3.49 have become curved lines in fig. 3.51: the full absorption of a gamma ray in the D2 detector added to a random coincidence energy in D1 leads to the curve evolving in energy and angle.

A final procedure is to apply an angle cut (from 10° to 45° in our example) and produce a total energy spectrum for the telescope run, this is shown in figure 3.53. The telescope energy resolution at 511 keV is 6.5% and 4.5% at 1275 keV. One published success of the project [58] was to compare these figures to the equivalent ones resulting from a Geant 4 simulation of that laboratory run (S015), the simulations results are shown in figure 3.54. The simulated energy resolution at 511 keV is 5.6% and 4.4% at 1275 keV (these simulated resolutions are dependent on the broadening).

3.3.4 Telescope Operation

A technical aspect of the FACTEL instrument that needs reviewing is the format of the data. The data acquisition program records the scientific data from the telescope in a computer file with a different format depending on the type of run performed. We now review these data acquisition modes.

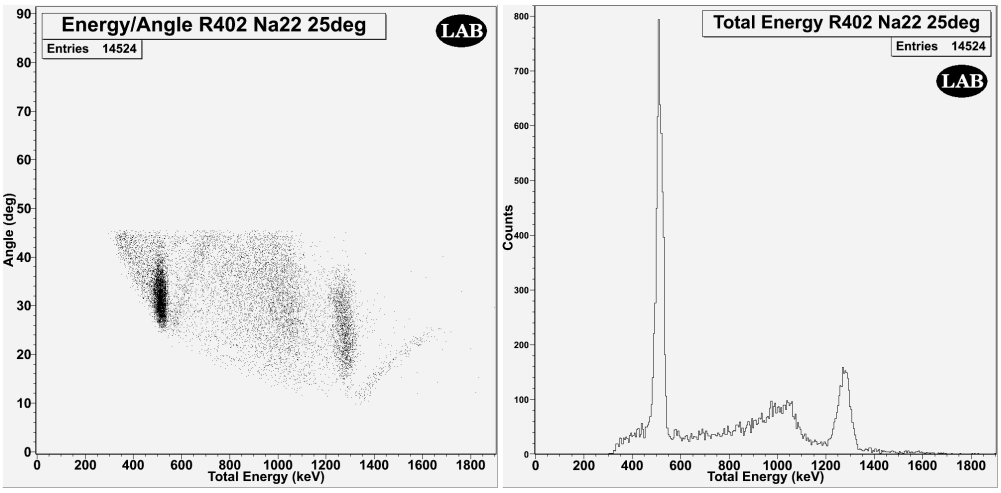

Figure 3.53: Total Energy-Angle scatter plot with angle cuts (10° to 45°) from a ^{22}Na at ~25° laboratory run (left), Total energy spectrum with angle cuts (10° to 45°) from the same laboratory run (right)

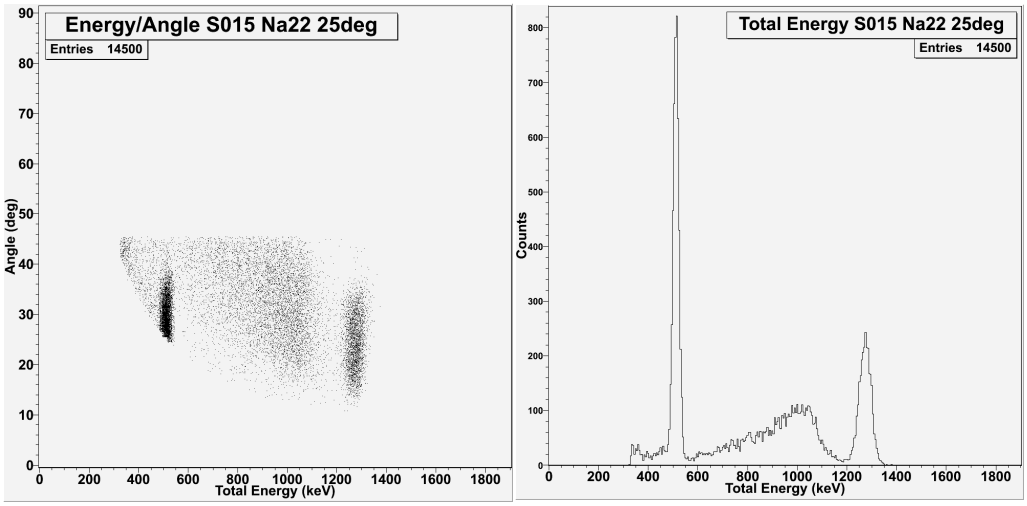

Figure 3.54: Total Energy-Angle scatter plot with angle cuts (10° to 45°) from a ^{22}Na at 25° simulation (left), Total energy spectrum with angle cuts (10° to 45°) from the same simulation (right)

For a D1 singles run, the scientific data from an event is written as five integers on one line of the computer file. The first number is a bit integer which is the anti-coincidence veto flag. A value of 0 means the event has not triggered the anti-coincidence veto, while a value of 1 means enough energy was deposited in one of the

six anti-coincidence panels during the event to trigger the anti-coincidence veto. The second number is a 3 bit integer (0 to 7) representing the address of the triggered detector(s). Each bit is set to 1 if the corresponding detector is triggered, and kept to 0 otherwise. For example, the address number 5 (101) means that the D1 layer first and third detectors have been triggered during the event. The third number is a 10 bit integer (0 to 1023) representing the amplitude of the energy deposit. The physical value of the energy deposit is recovered using eq. 3.13 and the data of table 3.4. The fourth number is a 10 bit integer which was intended to represent the pulse shape discrimination value; however it could not be used for analysis as the PSD electronic circuit did not function properly. The fifth and final value of an event line is always "0000", it was intended to represent the dead time but was never implemented.

For a D2 singles run, the data from an event is written as four integers on one line of the file and follows closely the D1 convention. The first number is a bit integer which is the anti-coincidence veto flag. For the D2 events, the ACV flag is irrelevant because the anti-coincidence box did not enclosed the D2 detector layer. The second number is a 3 bit integer (0 to 7) representing the address of the triggered detector(s) and follows the same convention as for the D1 singles file. The third number is a 10 bit integer (0 to 1023) representing the amplitude of the energy deposit. The physical value of the energy deposit is recovered using eq. 3.8 and the data of table 3.2. The fourth and final value of an event line is always "0000", it was intended to represent the dead time but was never implemented.

For a Telescope/Coincidence run, the data from an event is written as seven integers on one line of the file. The first number is a bit integer which is the anti-coincidence veto flag. The second number is a 10 bit integer (0 to 1023) representing the Time-of-Flight value. The third number is a 3 bit integer (0 to 7) representing the address of the detector(s) triggered by the event in the D1 detector layer. The fourth

number is a 10 bit integer (0 to 1023) representing the amplitude of the energy deposit in the D1 detector layer. The fifth number is a 3 bit integer (0 to 7) representing the address of the detector(s) triggered by the event in the D2 detector layer. The sixth number is a 10 bit integer (0 to 1023) representing the amplitude of the energy deposit in the D2 detector layer. The final seventh number is a 10 bit integer which was intended to represent the pulse shape discrimination value; however it could not be used for analysis.

For the balloon flight, time stamps (a float number) were added at regular intervals in the files, while other data was made available through various other housekeeping files (times, altitudes, rates in the anti-coincidence panels and in the detector layers, pressures, temperatures, and voltages).

For a laboratory FACTEL run in coincidence mode, an address plot example is shown in figure 3.55, the numbers in the cells is the counts number.

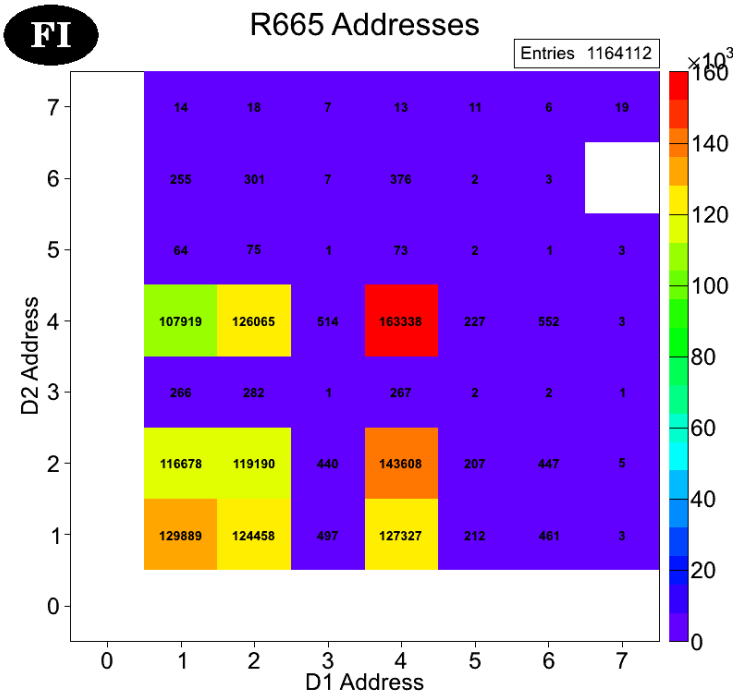

Figure 3.55: Addresses plot from R665

The addresses plot can then be truncated from the "multiple detectors in one layer" events to make a plot of the nine detector pairs counts, this is shown in figure 3.56:

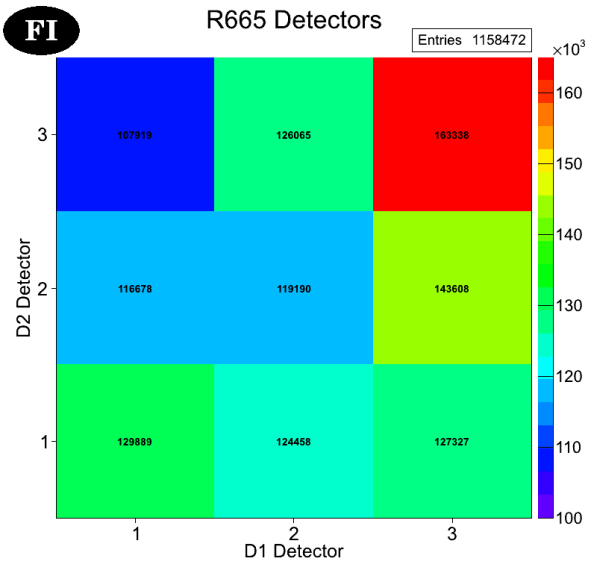

Figure 3.56: Counts for the detector pairs plot from R665

The D13 line (rightmost vertical) usually has more events than the others because D13 had the lowest energy threshold, see eq. 3.14. Energy thresholds and geometrical aspects specific to the laboratory run explain the variations. The address plot is used for the qualitative validation of an experimental run.

3.3.5 Time of Flight Calibration

The Time of Flight was defined by eq. 2.21 as $ToF = T_2 - T_1$, and is a standard time difference ΔT. One would think instinctively to have the D1 detector signal start a counter and the D2 detector signal to stop it, however upwards events with a negative ToF makes this solution unfeasible. The solution is to add a fixed long delay to the D2 signal such that the ToF value will always be large and positive, with ideally $ToF=0$ falling in the center of the ToF channel range.

There are two techniques to calibrate the ToF axis. The first is to add fixed length wires, with a known signal propagation time, to the D1 or D2 detectors signals while performing laboratory runs with a ^{22}Na source placed between the detectors ($ToF=0$). The second technique is to perform laboratory runs while varying the ^{22}Na source position between the detectors. This typically involves performing three runs: one run with the source in the middle, one with the source close to the D1 detector, and a final run with the source close to the D2 detector. A diagram of this second procedure is shown in figure 3.57. ^{22}Na is the source of choice for both methods because the two 511 keV gamma rays created by the positron annihilation are created simultaneously (correlated in time) and emitted in opposite directions.

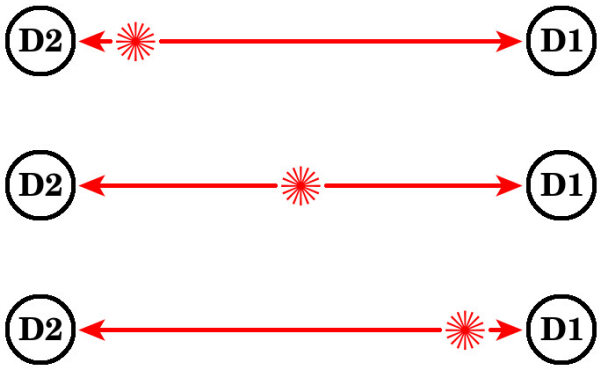

Figure 3.57: ToF Calibration procedure. The 3 laboratory runs to perform are: with the source close to the D2 detector (top), with the source in the middle (middle), and with the source close to the D1 detector (down)

Both calibration methods will lead to the same energy spectra shapes in the detectors, examples are shown in figure 3.58, the D1 spectrum displays a Compton edge while the D2 spectrum also shows a photoelectric absorption peak.

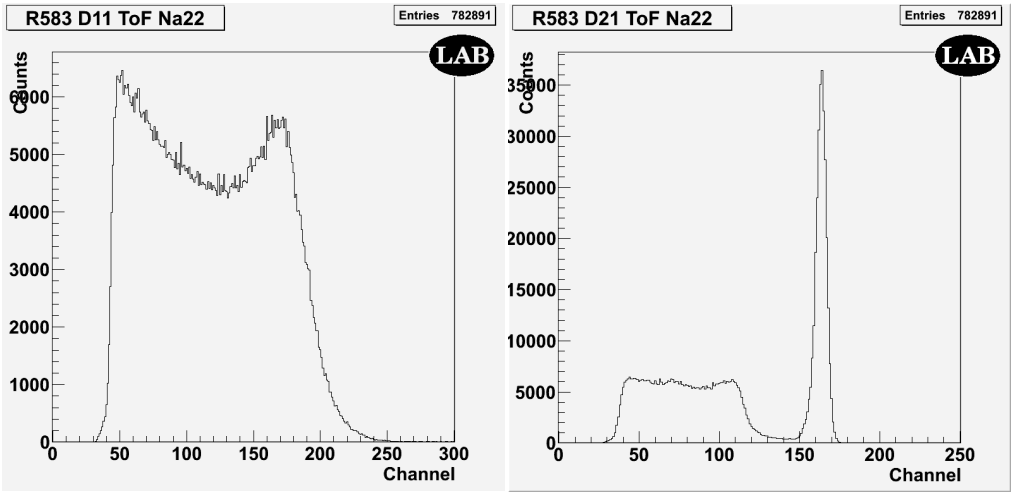

Figure 3.58: D11 (left) and D21 (right) spectra from a ^{22}Na ToF run. The D11 spectrum displays a Compton edge and the D21 spectrum a photoelectric absorption peak, both from interactions with correlated 511 keV gamma rays

A scatter plot of the run is then produced, shown in figure 3.59(left). We then select the region we are the surest a 511 keV gamma ray interacted in each detector: the Compton edge peak in the D1 detector (Ch1 = 145 to 186), and the photoelectric absorption peak in the D2 detector (Ch2 = 158 to 169), the selected region is shown in figure 3.59(right).

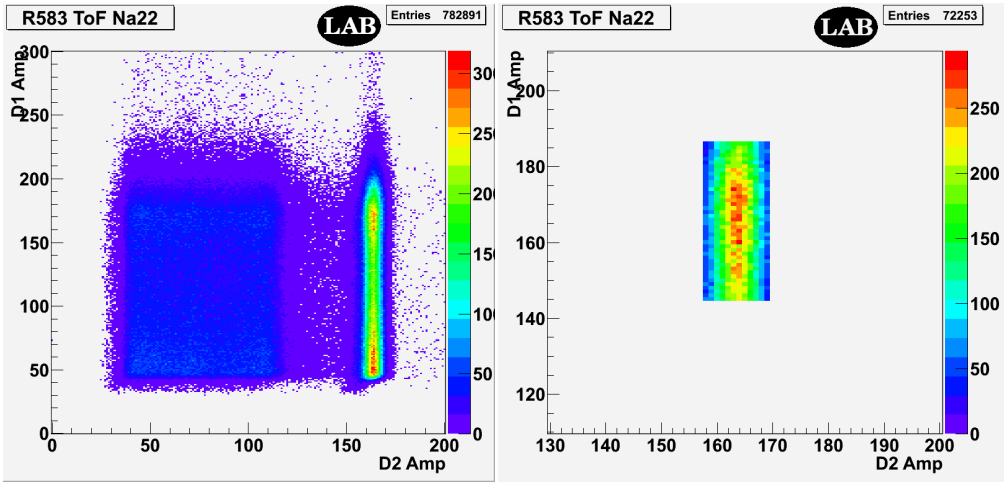

Figure 3.59: ToF Run D1-D2 Scatter plot (left), and the selected region (right)

One calibration example using the second method (moving a ^{22}Na source between the detectors) were laboratory runs 392, 393 and 394. The ToF spectra from the selected regions of these runs with their fits are shown in figure 3.60. These led to the ToF calibration displayed in figure 3.61. Figure 3.61 is remarkable because the ToF resolution was in the 450 ps range, which was under our 500 ps goal, and because the forward and backward peaks for detectors separated by ~15 cm can clearly be distinguished.

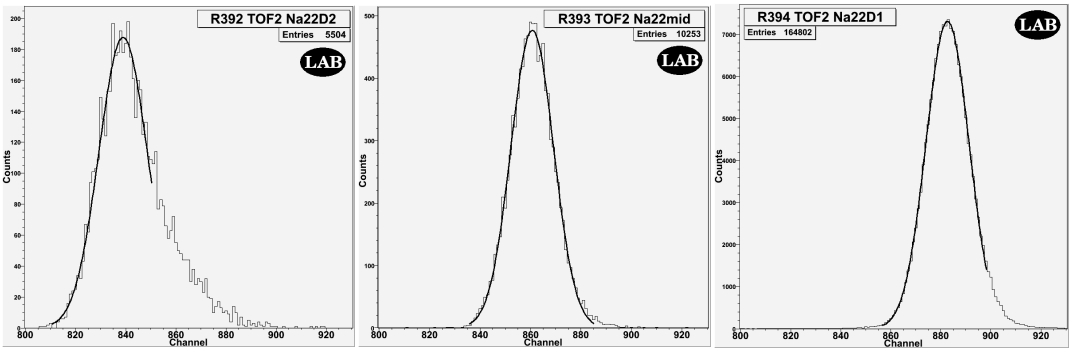

Figure 3.60: ToF Spectra from laboratory runs 392, 393 and 394: ^{22}Na source besides D2 (left), in the middle (middle), and besides D1 (right)

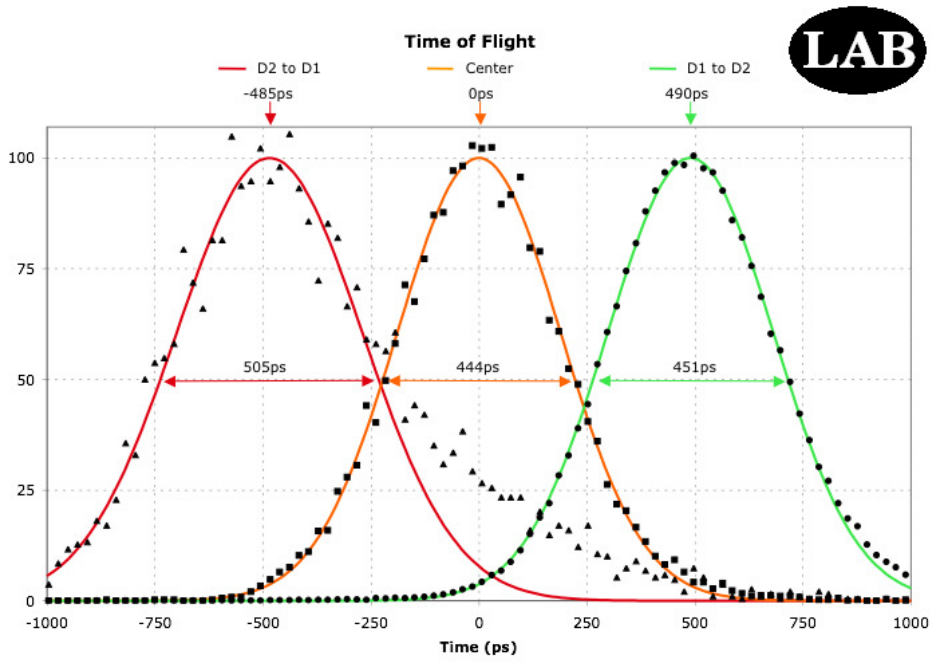

Figure 3.61: ToF Calibration from laboratory runs 392, 393 and 394. A ToF resolution of 450 ps was achieved for the forward peak

These laboratory runs (R392, R393, R394) were performed under optimal conditions: only one D1 detector and one D2 detector, NIM standard laboratory electronics were used, and selected energies were taken in both detectors. The final FACTEL instrument had three D1 detectors and three D2 detectors with different PMTs, used customized low-power electronics, had an electronic noise issue, and a ToF measurement for all of the detectors energy ranges was needed. This last point is important because the timing is dependent on the energy deposit and thus has to be calibrated: the smaller the energy deposits are the longer the signals are delayed. An initial raw ToF spectrum will thus have values over a wide channel range, an example from a ^{60}Co scatter run taken near the final version of the instrument is shown in figure 3.62.

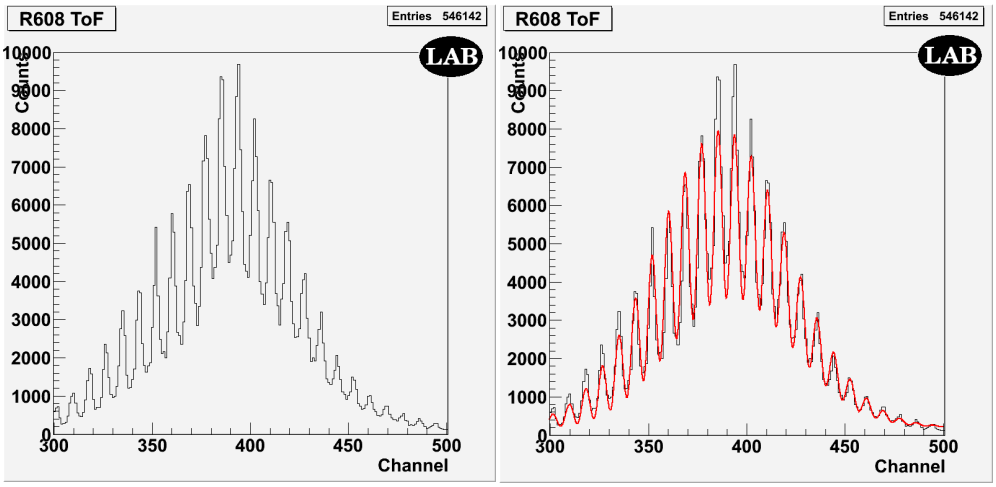

Figure 3.62: Initial raw uncorrected ToF spectrum from a ^{60}Co scatter run (left), the spikes are due to the electronic noise issue FACTEL suffered. A fit of the spectrum (right.)

The spikes in fig. 3.62 are coming from the electronic noise the onboard computer generated. This spectrum confirmed that the PC-104 computer was the electronic noise source. A spectrum fit, shown in figure 3.62 (right), revealed the noise had a ~1.8 GHz frequency (556 ps), which is the PC-104 clock frequency.

The final FACTEL instrument ToF calibration was performed with the laboratory run R668. Laboratory run 668 placed a ^{60}Co source at the center of the instrument, between the two layers and on the D12→D22 line (as precisely as possible). ^{60}Co was chosen because one decay emits two gamma rays of 1173 and 1333 keV correlated in time and not in opposite directions (such as the two 511 keV from ^{22}Na). This permits a calibration of all of the nine detector pairs of the instrument at once. The source was thus at $ToF=0$ for P11, P22, P33, P13 and P31, and slightly off center for P21, P23, P12 and P32. A reminder of FACTEL detector geometry and conventions is shown in figure 3.63. A simple calculation for these last four pairs gives a travel time difference of 29.8 ps between the two paths, which is inconsequential for our purpose.

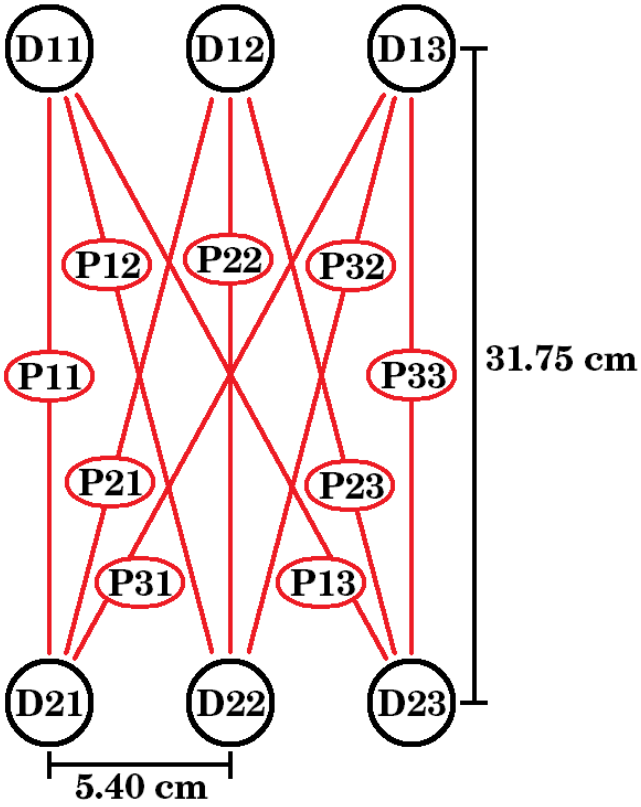

Figure 3.63: FACTEL geometry and pair naming convention

^{60}Co is also our highest energy conventional source, which allows a calibration that covers a wide energy range. The scatter plot of P11 events is shown in figure 3.64.

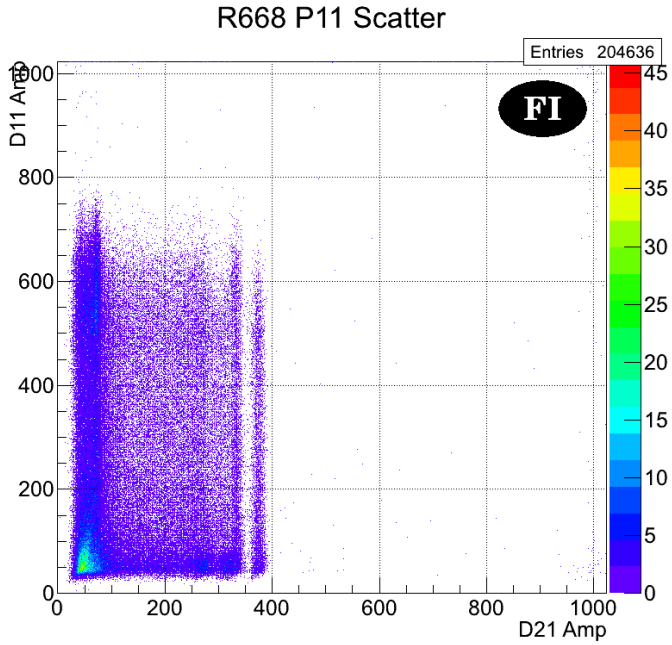

Figure 3.64: P11 Scatter plot from the ToF calibration run R668

The signal from each detector has a delay that is dependent on the magnitude of the energy deposit, and smaller energy deposits carry longer delays. Recovering the real ToF from the laboratory run ToF value ToF_{lab} is given by equation 3.17:

$$ToF_{\text{lab}} = (T_2 + D2_{\text{delay}}) - (T_1 + D1_{\text{delay}})$$
$$\Rightarrow \quad ToF = T_2 - T_1 = ToF_{\text{lab}} + D1_{\text{delay}} - D2_{\text{delay}} \qquad (3.17)$$

where $D1_{\text{delay}}$ and $D2_{\text{delay}}$ are respectively the delays from the D1 and D2 detectors. Although there are nine unique detector pairs spanning nine 2D maps like fig. 3.64, with each location having a different ToF delay combination, those are the combination of only six 1D functions which are intrinsic delays from each detector assembly. The delay from one detector at a given energy is constant regardless of which second detector was triggered or its energy deposit. To extract those lines from

the data, one simply has to analyze one band of data from a scatter plot, figure 3.65 shows example bands from P32.

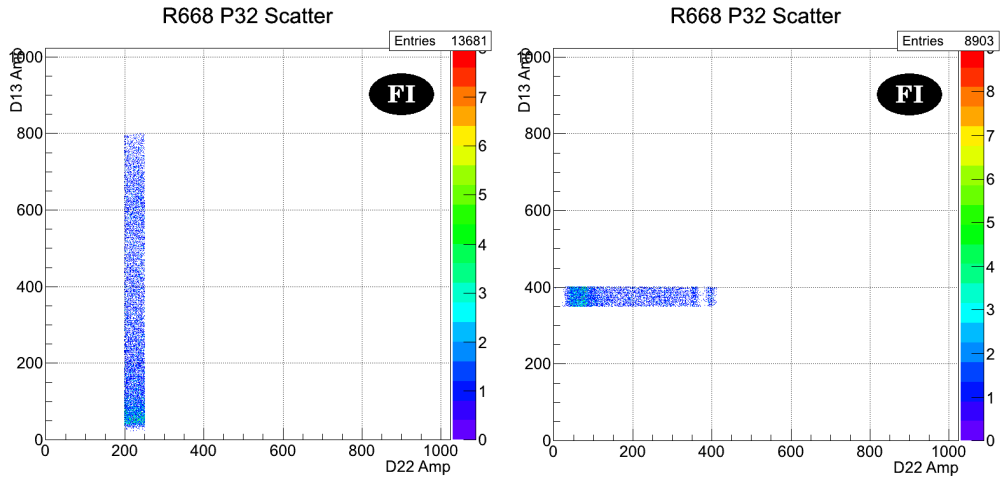

Figure 3.65: ToF Calibration bands from P32, the left plot holds the D13 delay curve, the right plot holds the D22 delay curve, see text for details

Along these bands for one detector, the delay from the second detector of the pair stays constant. The bands also need to be wide enough to have significant data, yet narrow enough for the delay from the second detector to be almost constant. The bands were taken in flat portions of the second detector spectrum, see figures 3.31 and 3.45, and at higher energies for the second detector to ensure an almost constant minimal delay.

About 25 data points were taken along each band, the measured data being the centroid value of a Gaussian fit of the ToF spectrum. The data is then normalized assuming the highest energy point has a delay of zero. For the FACTEL instrument calibration, four bands were taken from each nine pairs, giving six curves for each detector. These curves were then averaged to produce the final delay correction curve. The resulting delay correction curve for the D11 detector is shown in figure 3.66.

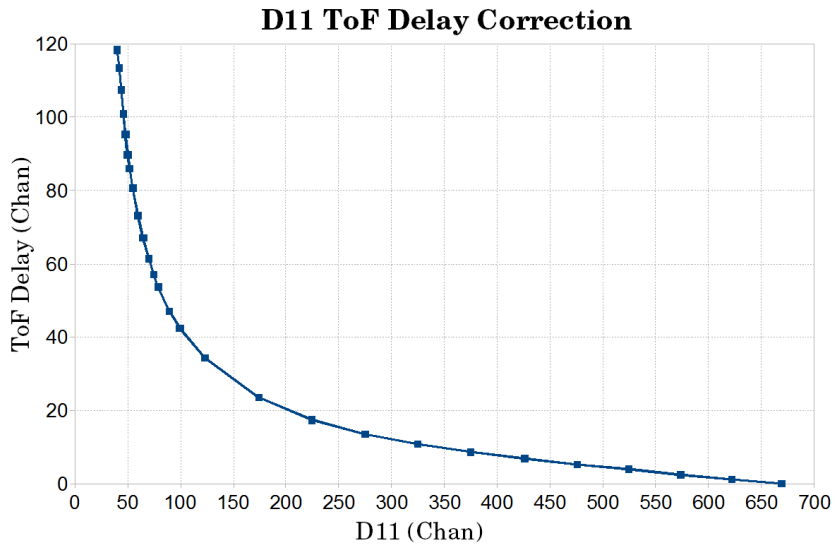

Figure 3.66: ToF Delay correction curve for the D11 detector assembly

The D2 detectors needed a further refinement because the ^{60}Co backscatter peak induced a faulty "bump" at lower energies, this is shown in figure 3.67.

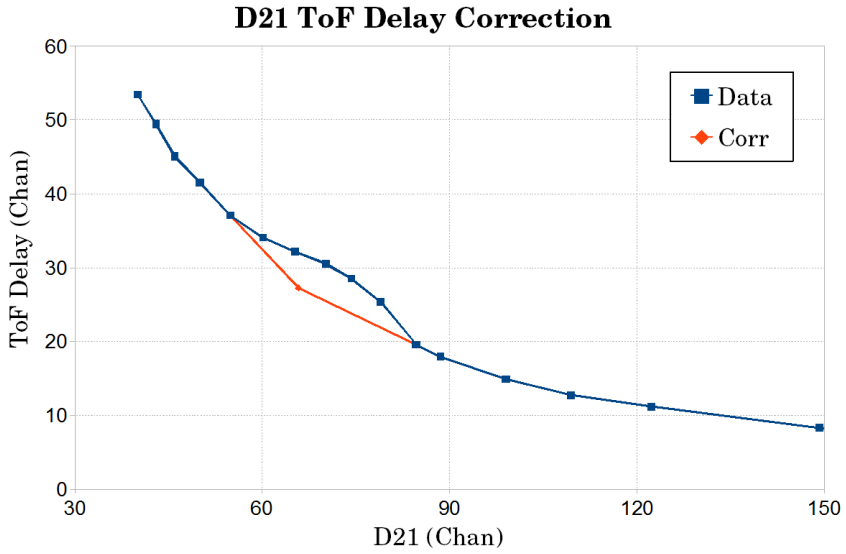

Figure 3.67: ToF Delay correction curve for the D21 detector assembly, the initial correction contains a bump caused by the ^{60}Co backscatter peak, the red line shows the correction of that effect.

Backscatter peaks are a common occurrence for gamma rays detectors, one clear example can be seen in figure 3.29, and details can be found in the literature, see Knoll Ch. 10.III.D.5a [49]. For ~1250 keV gamma rays, a backscatter at 170° will

result in a peak at ~215 keV in the detectors. As seen in fig. 3.31, this region of the D2 detectors (Ch2 50→100) is known to be the ^{60}Co backscatter region. These backscattered gamma rays are further delayed and cause the bump seen in fig. 3.67. To correct this effect, a point at the intersection of the lines formed by the last two trustworthy points before the bump and the first two trustworthy points after the bump was inserted, this is shown in fig. 3.67.

The six final ToF delay correction curves for the FACTEL instrument detectors are shown in figure 3.68:

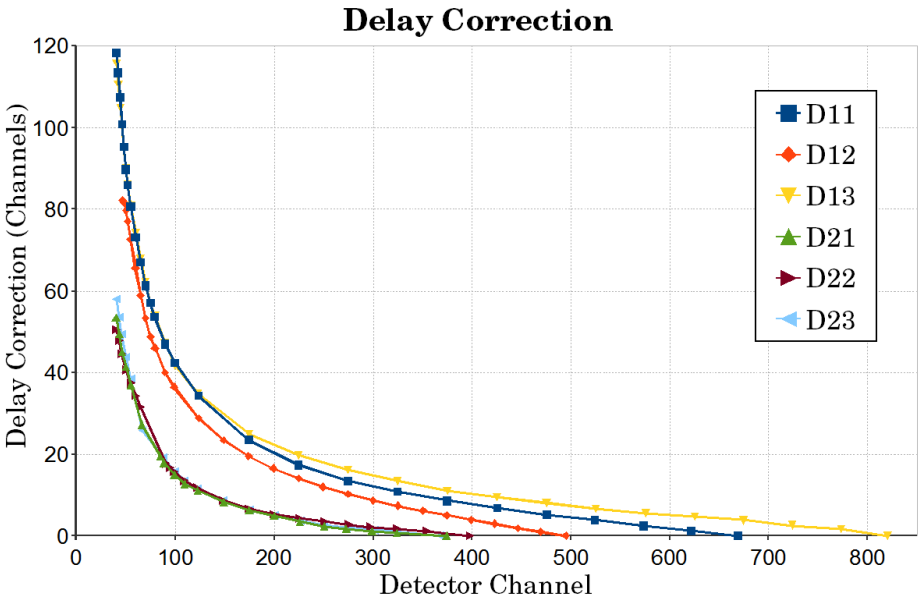

Figure 3.68: ToF delay correction curves for each of the FACTEL instrument detectors

The correction is applied using numerical interpolation from the curves data on an event by event basis following eq. 3.17, where the two delay values are function of the specific detector and the channel of the signal amplitude. For example, the ToF spectrum for the P11 pair, shown in figure 3.69 (left), is corrected to the spectrum shown in fig. 3.69 (right):

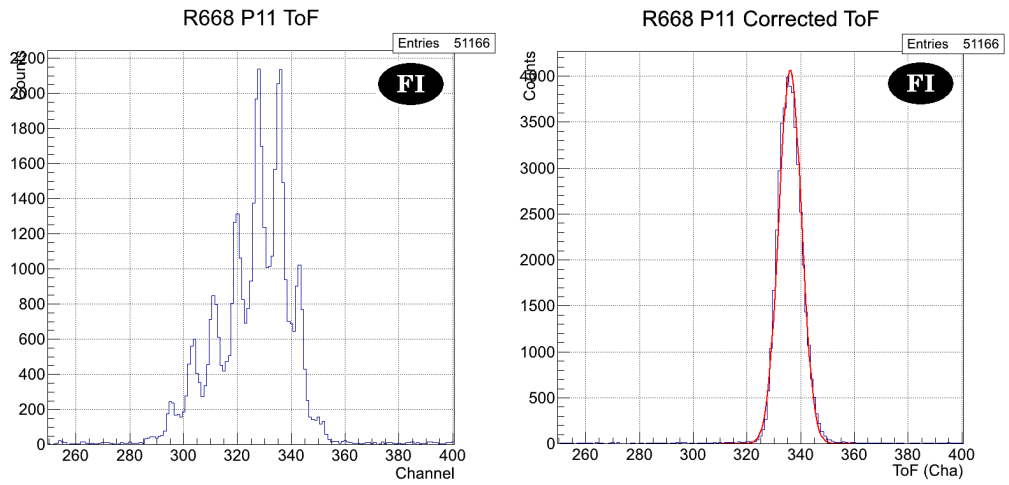

Figure 3.69: R668 P11 pair initial raw uncorrected (left) and corrected (right) ToF spectra, the delays correction curves successfully correct the initial ToF spectrum

For the complete R668 laboratory run, the initial raw uncorrected and corrected ToF spectra are shown in fig. 3.70:

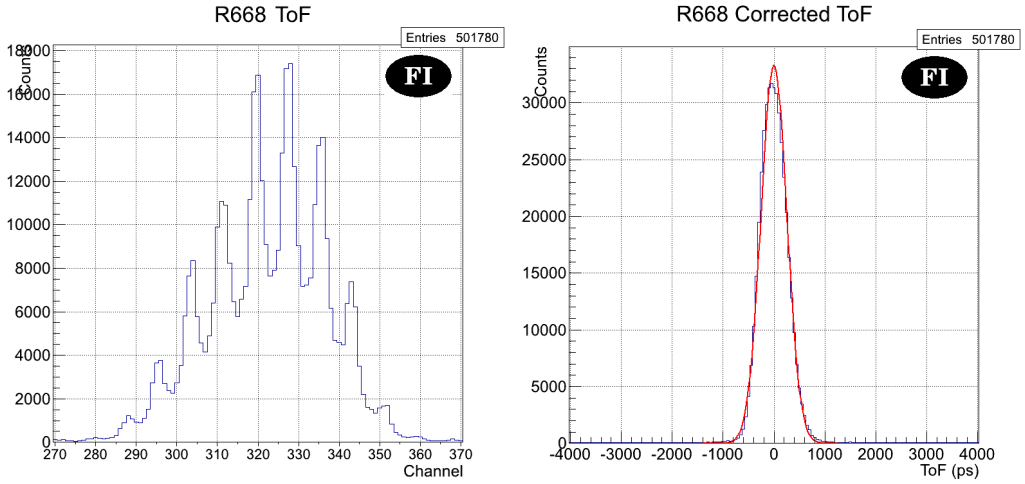

Figure 3.70: R668 initial raw uncorrected (left) and corrected (right) ToF spectra, the corrected spectrum has a sub-nanosecond ToF resolution

The final corrected ToF spectrum is a smooth Gaussian where the delays and spikes from the electronic noise are corrected by the statistics, we were lucky that the digital noise was small/high frequency and could be corrected with enough statistics. This last corrected ToF spectrum from R668, fig. 3.70(right), has a 600 ps ToF

resolution (FWHM), which is an impressive success (although depending on the conversion factor could also be 875 ps, this will be discussed later). This result shows we have successfully built a Compton telescope with a sub-nanosecond ToF resolution.

The last topic to discuss in this ToF section is the conversion factor from channel-space to time-space: channel units to time units. $\boldsymbol{ToF=0}$ is the center of the Gaussian of a $\boldsymbol{ToF=0}$ laboratory run, see figures 3.69 (right) and 3.70(right). Then the conversion factor [ch]→[ps] has to be found. This was performed with laboratory runs 522, 523 and 524. These runs used two D2 $LaBr_3$ detectors and the ToF calibration method of adding delay cables, the calibration plot from these runs is shown in figure 3.71:

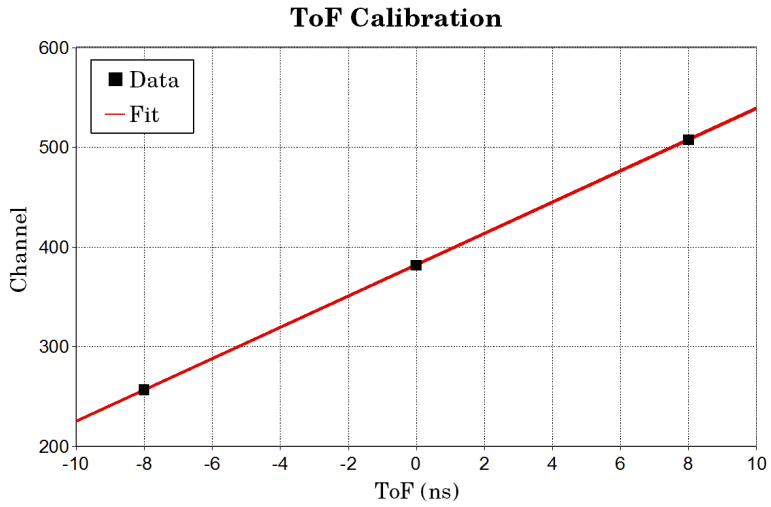

Figure 3.71: ToF Calibration from R522, R523 and R524, the conversion factor found is 63.7 ps/ch

The calibration shown in fig. 3.71 led to a value of 63.691 ps/ch, which is close to the value from the tests our electrical engineer performed prior to the delivery of the electronic board. This value has also been successfully used in a number of tests. However, the analysis from the flight data leads to a 92.95 ps/ch conversion factor. According to our electrical engineer and project engineer, this value should not have

changed between the test and the final instrument integration, yet a 92.95 ps/ch factor had to be used to properly analyze the flight data. This will be discussed in the flight results analysis chapter of this work. However it would seem that in the end, the correct ps/ch conversion factor is indeed 63.691 ps/ch and that the 600 ps ToF resolution of fig. 3.70 is genuine, which is an impressive result.

These last numbers show how critical the delay correction is: one delay correction has to be applied for both detectors, and fig. 3.68 shows these corrections to be anywhere between 0 and 120 channels. A ~75 ps/ch conversion factor implies two corrections between 0 and 9 ns. An initial ToF spectrum such as the one shown in fig. 3.70 initially spans over 5 ns and needs to be corrected to a ~700 ps resolution. An error of a few channels on the correction curves can quickly impact the resolution when one channel is worth ~75 ps. This is the reason the correction curves are critical and need to be carefully sampled, and many points were taken and the correction applied numerically using interpolation from the data points.

3.3.6 Pulse-Shape Discrimination and Neutrons

Neutron pulse-shape discrimination did not function for the final instrument. The PSD capabilities of our D1 detectors were nonetheless tested. As explained in section 3.2.6, our signals were much faster than conventional signals, and conventional electronic solutions were not valid for the FACTEL instrument. However, standard NIM laboratory equipment modules were able to properly analyze the D1 detector signals for PSD. PSD tests would typically use an AmBe source because it is both a neutron and a gamma ray source, see equations 3.5, 3.6 and 3.7. The laboratory run 380 was such an AmBe test that used one of our D1 detector assemblies sending its signal to a Mesytec MPD-4 (Multichannel Pulse-shape

Discriminator) module. The PSD value came from the TAC (Time to Amplitude Converter) output. The results shown in figure 3.72 were obtained and compared to figures 2.18 and 2.19, these are excellent results because gamma rays and neutrons are clearly discriminated.

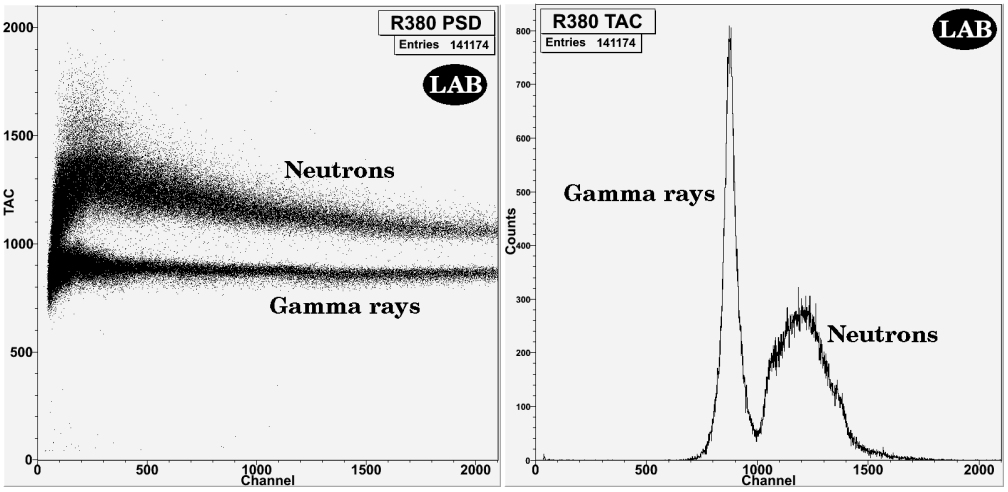

Figure 3.72: PSD results from one of FACTEL D1 detector (R380), the source is AmBe, gamma rays and neutrons are clearly discriminated

A second aspect relative to neutrons to be measured was the deuteration effect of the D1 liquid scintillators. Specifically, we tried to see the neutron capture line from an undeuterated D1 detector to then "not see" the line when doing the same test replacing the undeuterated detector with a deuterated one. This test proved to be an impossible measurement for reasons now detailed.

Neutron capture is a problem for organic based liquid scintillator detectors. A test was conducted using a spare D1 detector from COMPTEL where a ^{252}Cf neutron source was placed 120° off the telescope axis and ~4 m away. The events within the first 90° of the telescope (the front) were recorded and the resulting spectrum is shown in figure 3.73. A strong 2.2 MeV line from neutron capture is clearly visible, as well as the 1.46 MeV line from the ambient ^{40}K.

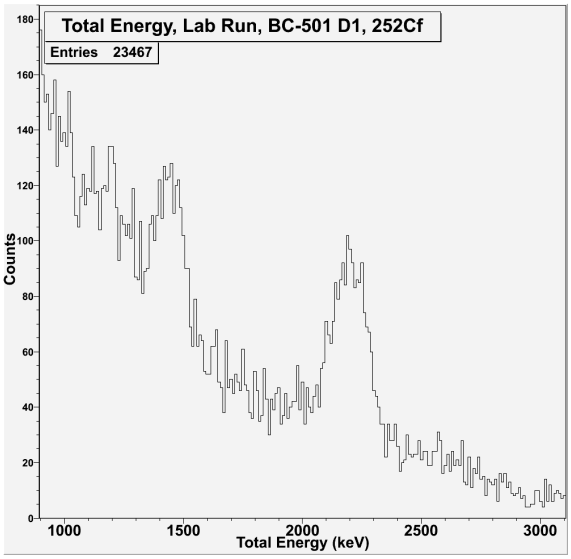

Figure 3.73: COMPTEL undeuterated D1 detector exposed to a ^{252}Cf source from behind, a strong neutron capture line at 2.2 MeV is clearly visible within the field of view of the telescope; the 1.46 MeV line from ambient ^{40}K is also visible

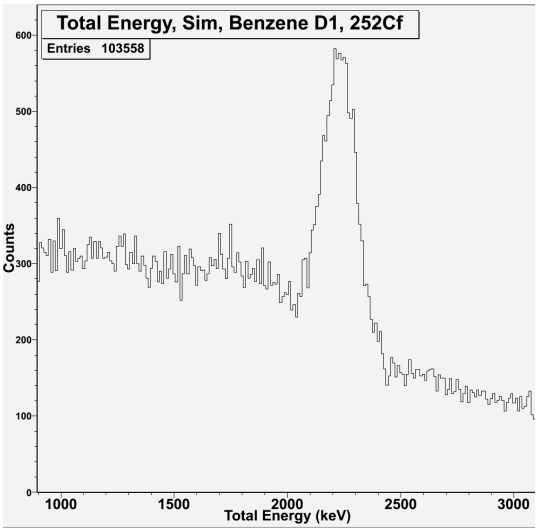

Figure 3.74: Geant 4 Simulation of fig. 3.73 laboratory run, the 2.2 MeV neutron capture line is clearly visible.

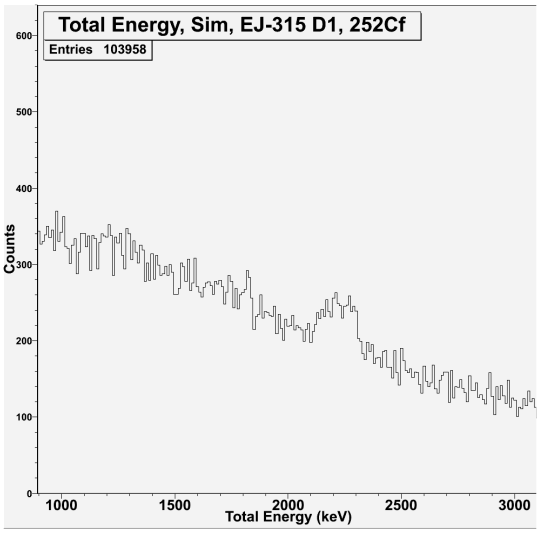

Figure 3.75: Result of the same simulation of fig. 3.74, but with the undeuterated liquid replaced with EJ-515 deuterated liquid scintillator, the 2.2 MeV neutron capture line is clearly mitigated.

Then one Geant 4 simulation of the laboratory run was performed as well as a second simulation where the regular liquid scintillator was replaced with deuterated liquid scintillator. The resulting spectra are shown in figures 3.74 and 3.75: the 2.2 MeV line is clearly mitigated using the deuterated liquid.

This mitigation proved to be impossible to reproduce with a FACTEL D1 cell filled with normal liquid scintillator and another cell filled with deuterated EJ-315. Simulations provided the explanation: our D1 cells are too small for neutron capture to be a problem. COMPTEL D1 detectors were cylinders 28 cm in diameter and 8.5 cm deep, totaling 5234 cm^3. FACTEL D1 detectors contain 9.97 cm^3 of liquid. A neutron penetrating one of COMPTEL D1 detectors has the space and time to thermalize and get captured. Then the emitted 2.2 MeV gamma ray has the volume to interact within the detector and then interact in a D2 detector. For the FACTEL instrument, the detectors small volume makes incoming neutrons likely to exit the detector after only one interaction: neutrons do not have the volume to thermalize. Then, even if a thermal neutron is captured resulting in the emission of a 2.2 MeV gamma ray, the detector is so small that the gamma ray is most likely to exit the detector before interacting. To summarize, COMPTEL D1 detectors were large enough to thermalize neutrons, and large enough to interact with the emitted gamma ray. While the efficiency of FACTEL small D1 detectors to interact with neutrons producing a 2.2 MeV gamma ray, and then detecting it are two small numbers. This is the reason a 2.2 MeV neutron capture line from a FACTEL D1 cell filled with normal organic liquid scintillator could not be obtained, and then we were unable to show its mitigation using a deuterated liquid scintillator cell. The lesson here is that neutron capture is definitely a problem for massive detectors, but not an issue for small detectors. For the FACTEL instrument, deuterating the D1 detectors was

unnecessary as neutrons are seldom captured in small detectors. However, deuterating the D1 detectors would become necessary for a larger volume of detecting material.

3.4 Simulations: Mass Model and Physics

Simulations are now a standard tool in the development and analysis of scientific instruments. Simulations provide an invaluable resource to analyze the performance of an instrument, improve it, and to predict the capabilities of a future instrument. The simulation software used for FACTEL simulations is CERN Geant 4 [59], a Monte Carlo toolkit widely used in the high-energy physics and medical community.

A mass model of the FACTEL prototype was developed, shown in figure 3.76 and is to be compared to figures 3.9 and 3.3. Special care was taken to model the immediate vicinity of the detectors as faithfully as possible, both for material definitions and for geometry. One significant difference between the real instrument and the Geant 4 mass model is the composition of the D12 detector: the mass model uses EJ-315 deuterated benzene for all D1 detectors while the instrument D12 is deuterated toluene. Another difference is that the insulating foam around the dome and its surrounding duct tape were not simulated. These differences are not believed to be significant enough to be noticeable. It is not the goal of this work to review the details of the simulations coding, volumes, materials, objects/classes, variables, logic tricks, analysis steps, physics, etc. Still, some details are important and some developed solutions need to be explained.

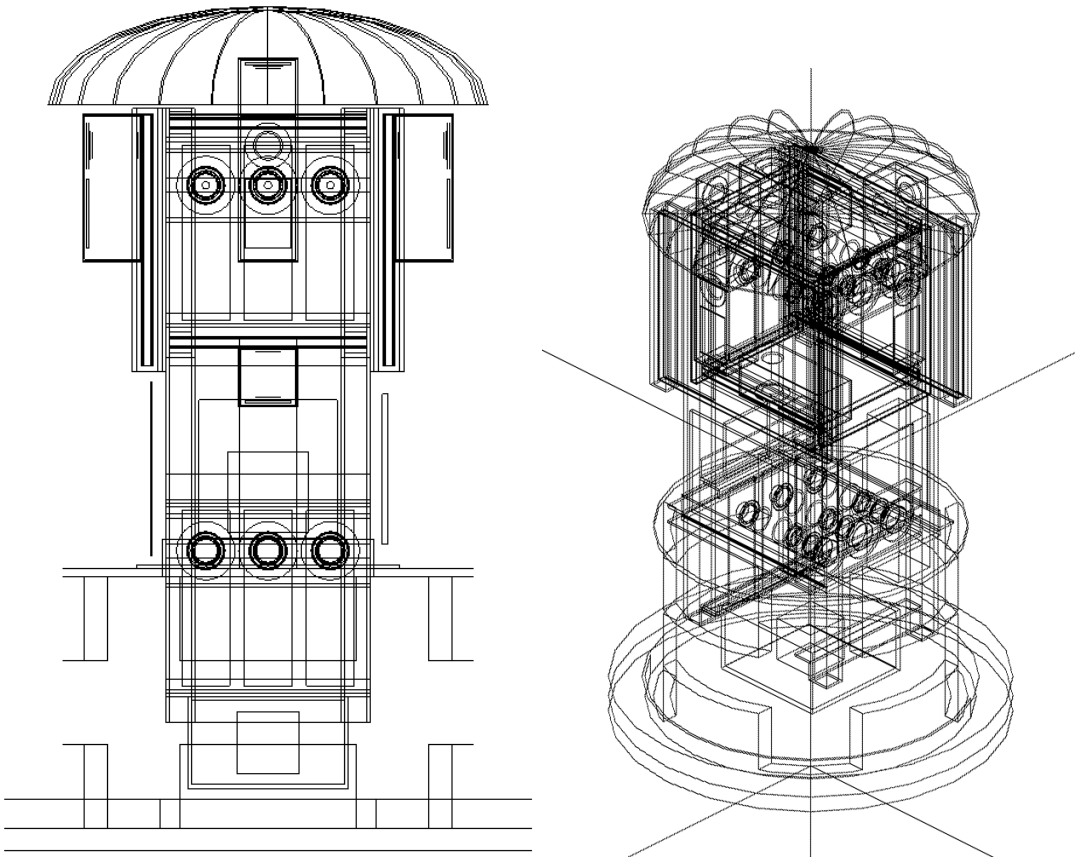

Figure 3.76: FACTEL Geant 4 Mass Model

The simulations energy results need to be broadened to account for the intrinsic statistical deviation of real laboratory measurements. The measured energy deposits in a simulation are exact, meaning that a 510.999 keV gamma ray photoelectrically absorbed in a D2 detector will be measured at 510.999 keV precisely. A million such gamma rays interacting photoelectrically will also each be measured at 510.999 keV precisely, leading to a spiked spectrum. For example, the initial spectrum that led to the spectrum presented in fig. 3.54 is shown in figure 3.77 (the 511 keV line goes much higher). As well, the D1 spectra shown in fig. 3.47 need to be broadened to the ones shown in fig. 3.48 to correctly reproduce laboratory data. One broadens the initial spectra using the sigma data from the energy calibration, see figures 3.35 and 3.42, and equations 3.10 and 3.16, by adding Gaussian noise of the

appropriate sigma to the simulation data. It is suggested to add the noise in a post-simulation analysis: non-broadened simulations can be powerful diagnostic tools.

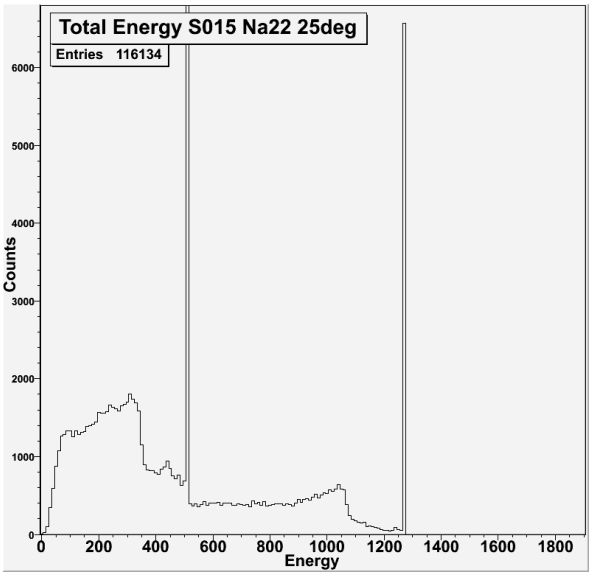

Figure 3.77: Unbroadened simulation spectrum, the photoelectric peaks are precise. The broadening of this spectrum leads to fig. 3.54

Neutrons and protons energy deposits in organic scintillators need to be converted into their electron/gamma equivalent. Electrons and protons do not deposit their energy the same manner in scintillators, and the same energy deposit from an electron or a proton will not generate the same response from organic scintillators. Electrons and gamma rays are treated together because gamma rays interact by creating an electron that will deposit its transferred energy. Protons and neutrons are treated together because neutrons interact with a proton that will deposit its transferred energy. A simulation computes the energy deposits without regard to their origin. Converting the energy deposits originating from a proton or a neutron to its electron equivalent has to be performed in the post-event analysis. The data necessary for the conversion can be found in the literature, see Knoll Ch. 8.I.C.1 [49]. For FACTEL, this issue concerned the three D1 detectors and the six anti-coincidence panels. For example, a proton or neutron needs to deposit 430 keV to

match a 40 keV deposit from a gamma ray interaction in a D1 detector, or deposit 1.82 MeV to match a 400 keV deposit from an electron in an anti-coincidence panel.

Ordering the hit collections is also a non-trivial problem requiring explanations. Geant 4 treats generated particles in a "last in first out" fashion. For example, an incoming gamma ray Compton scatters in a D1 detector ejecting an electron, and then is photoelectrically absorbed in a D2 detector generating another electron. These initial electrons themselves generate dozens of other electrons. Geant 4 will first process the track of the gamma ray, then treat the last generated particle (the D2 photoelectric electron) and all its generated particles in a "last in first out" fashion, then go back to the first generated electron (the Compton D1 electron) and treat its subsequent interactions. This treatment generates detectors hit collections unsorted in time. This is a problem for an application such as FACTEL where the thresholds crossing times are critical. The detectors hits collections thus need to be time ordered, which is a non-trivial problem for hit collections containing tens of thousands of hits. This is a sorting problem, and a basic solution such as the "Bubble sort" algorithm is hopeless in this case. Other well known algorithms such as "Pigeon sort" are completely impractical. The algorithm retained for ordering the detectors hit collections is "Merge sort": this algorithm is quick, efficient, well adapted to this problem, and pseudo-code can easily be found.

The physics list used by a simulation is also a critical choice. In previous Geant 4 versions, the physical processes included in a simulation used to be added manually to a physics list the developer built himself, and this was performed for early versions of the FACTEL simulations. However Geant 4 evolved throughout the years and its complexity increased with time. Physics lists creation and maintaining throughout software versions became cumbersome for the developer. To alleviate this problem, the physics lists creation and maintaining was removed from the developer's tasks by

using reference physics lists developed and maintained by the Geant 4 collaboration. Physics lists thus became "black boxes" and the developer has to choose the most appropriate for his application. The last FACTEL simulations used a physics list called "QGSP_BIC_HP" with a modification to use low-energy electromagnetic processes instead of the standard option. FACTEL simulations needed low-energy electromagnetic physics because deposits can be as low as a few tens of keV, yet during the balloon flight the instrument was bombarded by background particles with energies in the tens of GeV, and neutrons were critical for the instrument.

The generation of the incoming particles (primary particles) is critical for simulations. The basic Geant 4 primaries generator is the "particle gun" class, where the user directly inputs a particle definition, initial position, momentum direction, and energy. The more evolved Geant 4 primaries generator is the GPS (General Particle Source) class that can handle various source distributions and energy distributions. Unfortunately, neither particle generators could meet the requirements of the FACTEL project. For example the gamma ray background at balloon altitude has different fluxes and spectra depending on the zenith angle. A custom made primaries generator was thus developed for the FACTEL project. The developed generator is powerful yet simple enough that it has been successfully taught and used for other of our group simulation projects.

A "trivial yet not so trivial" error was recently found and corrected in the developed primaries generator. However, the flight background simulation results presented in this work used the flawed previous version of the generator. We will now review the mistake and explain why it does not impact the simulations results adversely. The primaries generator uses a sphere centered on the instrument as the source, as seen in figure 3.78. An error in direction choosing made primaries directed on the sphere side a little more favored (+5%) than primaries directed towards the

sphere center (-5%). Fortunately, FACTEL detectors are around the 0% region, and the error margins from the flight data are larger than the possible effect the error could have had. We thus remain confident the simulation results presented in the next chapter are valid.

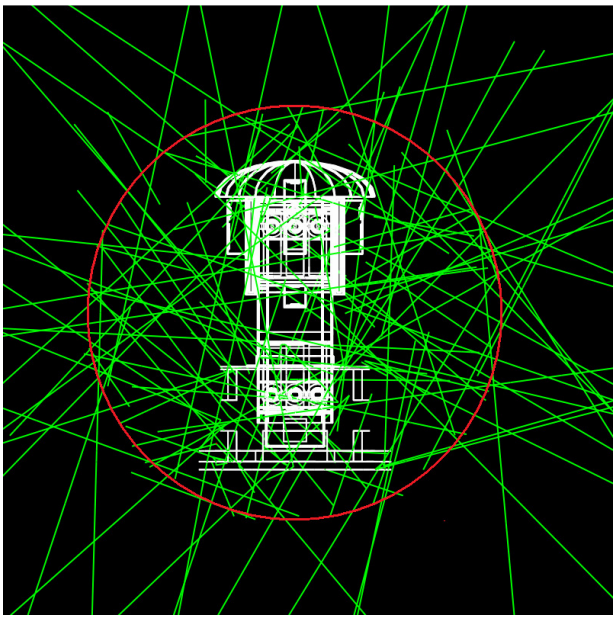

Figure 3.78: Simulations source sphere (red) around the FACTEL instrument (white), and generated primaries (green)

3.4.1 Comparison between Laboratory Runs and Simulations

The validation of the developed simulations tools is done by comparing their results to equivalent laboratory runs. The results presented in figures 3.53 and 3.54 from R402 and S015 are not valid for the final instrument. Laboratory run 402 only involved one D1 detector, one D2 detector, and used standard NIM equipment for the data acquisition and signal analysis. The final instrument had three D1 detectors and three D2 detectors and used custom made electronic boards for the data acquisition and signal analysis. This section will compare R667, a ^{22}Na at 70°

laboratory scatter run using the final calibrated FACTEL instrument, to its equivalent Geant 4 simulation S046.

The results presented *en masse* in figure 3.79 will now be explained. Figure 3.79a shows the initial D1-D2 energy scatter plot from the simulation, the sharp diagonal comes from 1275 keV gamma rays scattering from a D1 detector to a D2 detector, and the thinner extension comes from multiple Compton scatters. Once broadened, fig. 3.79a becomes fig. 3.79d with the scatter spots apparent. Fig. 3.79d it is to be compared to fig. 3.79g from the laboratory run, the difference is coming from the random coincidences occurring in reality. (The simulation generates only one primary per event and completely resolves it before generating another. In reality a source can emit multiple gamma rays within a short time period. For example the ^{22}Na source emits one 1275 keV gamma ray and shortly afterwards the two 511 keV gamma rays from the positron annihilation in opposite directions.) Figure 3.79a is then projected into "Total Energy versus Angle" space in fig. 3.79b, the diagonals are now narrow vertical lines at a precise energy and multiple Compton scatters extend the line to higher angles, other cases account for the rest of the plot. Once broadened, fig. 3.79b becomes fig. 3.79e, with the scatter spots well placed at their correct energy and angle. Fig 3.79e is to be compared to fig. 3.79h from the laboratory run. Finally, an angle cut from 60° to 80° is taken from fig. 3.79b data to produce the fig. 3.79c spectrum, the scatters are now the two sharp spectral lines of the source. Once broadened, fig. 3.79c becomes the spectrum of fig. 3.79f. The simulated fig. 3.79f spectrum is in very good agreement with the result coming from the real FACTEL instrument shown in fig. 3.79i.

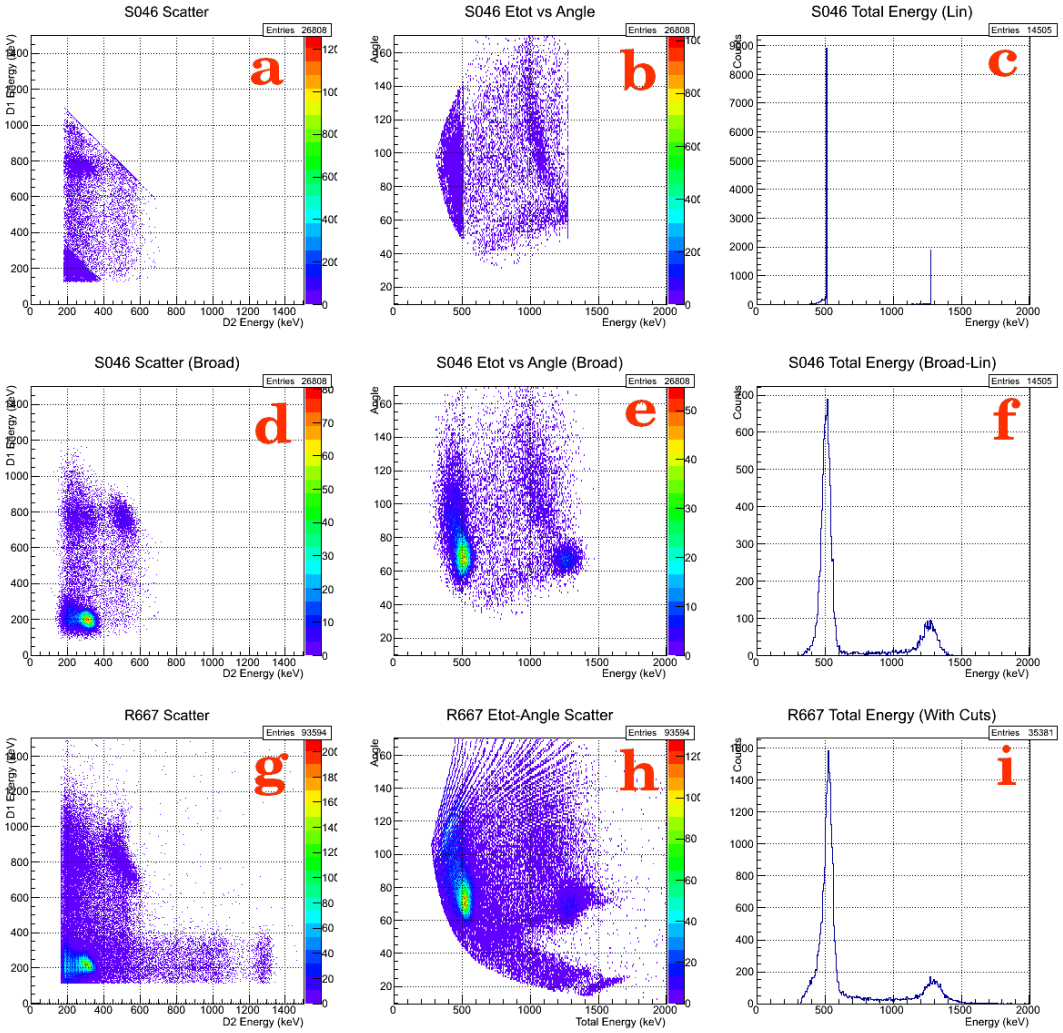

Figure 3.79: Comparison between results from a laboratory ^{22}Na at 70° scatter run (R667) using the final FACTEL instrument and its Geant 4 simulation (S046). The agreement between the (f) and (i) spectra is excellent; see text for explanations.

These results validates our FACTEL simulations and makes us confident that the simulations satisfactorily represents the actual FACTEL instrument prototype, and that simulations can be reliably used to predict and diagnose the performance of FACTEL.

3.5 Summary

This chapter characterized the FACTEL instrument prototype. The components and materials were reviewed and detailed: the $LaBr_3$ D2 crystal scintillator detectors, the deuterated organic liquid scintillator D1 detectors, the R4998 photomultiplier tubes, the anti-coincidence panels and the fiberglass reinforced plastic frame. The calibration procedure was reviewed: the sources, the procedures, the fitting curves, the detectors resolution, the Time of Flight calibration, correction and resolution.

The FACTEL prototype has an energy range from roughly 300 keV to 7 MeV, an energy resolution under 5% above 1 MeV (dominated by the D1 detectors low resolution), and a ToF resolution in the 1 ns range. ^{22}Na and ^{137}Cs spectra from the final instrument are shown in figures 3.80 and 3.81 respectively:

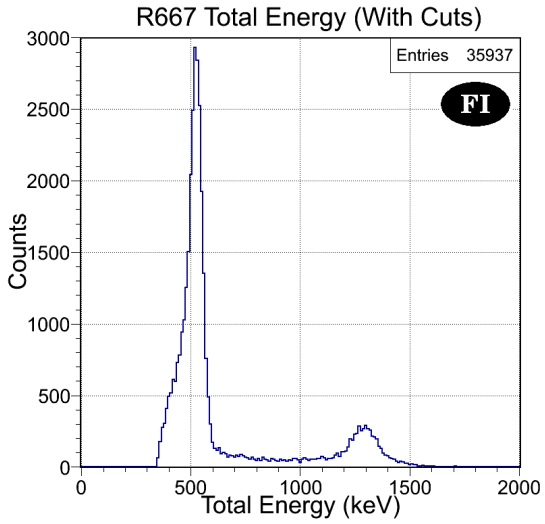

Figure 3.80: FACTEL ^{22}Na spectrum with the final instrument, energy resolution is 13.4% at 511 keV and 12.3% at 1275 keV, see text for comments.

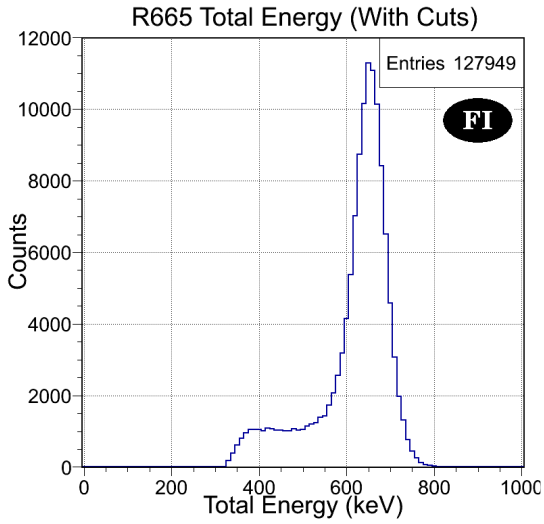

Figure 3.81: FACTEL ^{137}Cs spectrum with the final instrument, energy resolution is 12.9% at 662 keV, see text for comments.

The energies resolutions in figures 3.80 and 3.81 spectra are 13.4% at 511 keV, 12.9% at 662 keV and 12.3% at 1275 keV. The total energy resolution of the telescope

is a combination of the D1 and D2 detectors resolution. The laboratory runs of those results presented in figures 3.80 and 3.81 involved high angles scatters, thus leaving a significant amount of energy in the low resolution D1 detector. R665 was a ^{137}Cs at 80° laboratory run while R667 a ^{22}Na at 70° run. For example, a 1275 keV gamma ray Compton scattering at 70° from a D1 detector to a D2 detector will leave 792 keV in the D1 detector and 483 keV in the D2 detector. It is then not surprising to see a very wide 1275 peak in the total energy spectrum of fig. 3.80 because most of its energy comes from the low resolution D1 detector. Smaller scatter angles lead to smaller energy deposits in the D1 detector, leading to sharper total energy peaks as shown in fig. 3.53.

This chapter showed that the FACTEL instrument is a functioning small Compton Telescope with a Time of Flight resolution in the nanosecond range.

CHAPTER 4

The FACTEL Flight Simulations

4.1 Introduction

This chapter focuses on the simulations performed to analyze and assess the performance of the FACTEL instrument during the balloon flight. The FACTEL flight simulation involved subjecting the developed FACTEL instrument mass model, see fig. 3.75, to an estimation of the expected background during the flight. This process involved eleven different simulations to account for each type of background present in the upper atmosphere that could generate a significant response from the FACTEL instrument. In details, the background types were gamma rays, neutrons, cosmic protons, atmospheric protons, alpha particles, cosmic electrons, atmospheric electrons, cosmic positrons, atmospheric positrons, negative muons and finally positive muons. All the "cosmic" particles are also referred to as "primary" particles, while "atmospheric" particles are also referred to as "secondary" particles. Each simulation involved programming the incident spectrum and flux, and running the simulation to get the instrument response to that background type. Once all simulations were finished, the results were summed to get the simulated FACTEL instrument response during the flight. Each simulation will now be detailed before summing the results.

4.2 Gamma Rays Simulation

The gamma-ray background flux spectrum was taken from Gehrels' paper "Instrumental background in balloon-borne gamma-ray spectrometers and techniques for its reduction" [61], section 3.2. The gamma-ray flux described applies to our case because the 39 km altitude corresponds to an atmospheric depth of 3.5 g cm^{-2}. The inbound spectrum is different depending on the incoming direction of the gamma ray: there are four different spectra for four regions depending on the zenith angle. The four regions are: the cosmic gamma rays from 0° to 65°, the photons coming from the upper sides from 65° to 95°, those coming from the atmosphere on the lower sides from 95° to 130°, and finally those coming from under the instrument from 130° to 180°. The spectra are power law-functions of energy $\boldsymbol{E}$ parametrized by a constant and a spectral index given by eq. 4.1. A plot of these spectra is shown in figure 4.1:

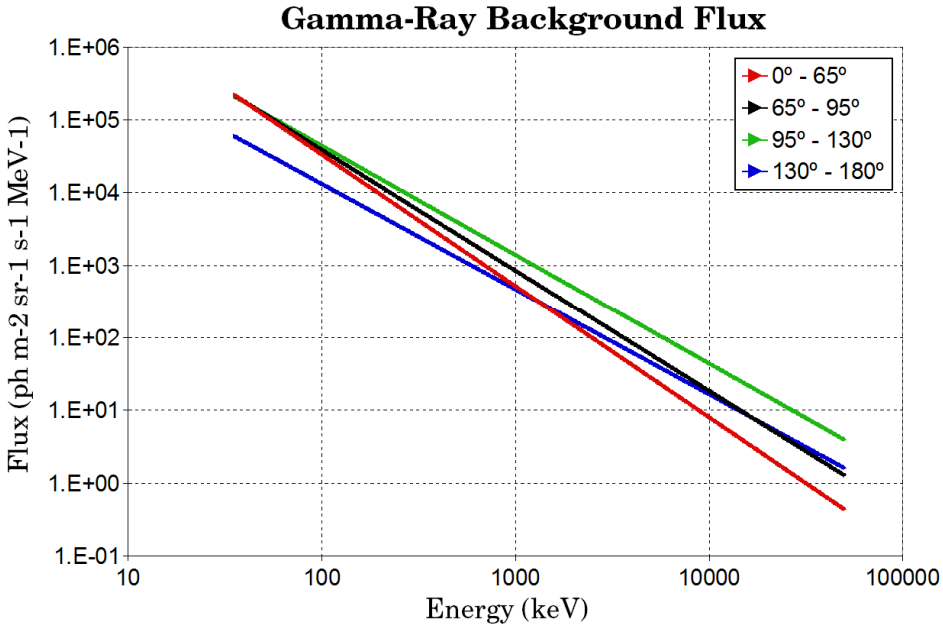

Figure 4.1: Gamma-Ray Background Fluxes

$$
\begin{aligned}
0° \rightarrow 65° &: \quad 0.052\, E^{-1.81} \ (\text{photons cm}^{-2}\ \text{sr}^{-1}\ \text{s}^{-1}\ \text{MeV}^{-1}) \\
65° \rightarrow 95° &: \quad 0.085\, E^{-1.66} \ (\text{photons cm}^{-2}\ \text{sr}^{-1}\ \text{s}^{-1}\ \text{MeV}^{-1}) \\
95° \rightarrow 130° &: \quad 0.140\, E^{-1.50} \ (\text{photons cm}^{-2}\ \text{sr}^{-1}\ \text{s}^{-1}\ \text{MeV}^{-1}) \\
130° \rightarrow 180° &: \quad 0.047\, E^{-1.45} \ (\text{photons cm}^{-2}\ \text{sr}^{-1}\ \text{s}^{-1}\ \text{MeV}^{-1})
\end{aligned}
\tag{4.1}
$$

The simulation generated inbound gamma rays with energies between 35 keV and 50 MeV.

The fluxes (eq. 4.1) being different, we now explain the calculation to generate the primaries with the correct ratio according to the regions (see the result eq. 4.5), and most importantly to know how many seconds of real time each simulated particle is worth (see the result eq. 4.4). Since this is the first background simulation reviewed, this calculation will be detailed, however we will skip directly to the results for the following background types.

The fluxes are in units of [photons cm^{-2} sr^{-1} s^{-1} MeV^{-1}] and the ultimate result in units of [photons s^{-1}]. The first step is to integrate the fluxes (eq. 4.1) over the energy window, changing the area unit to m^{-2} this gives eq. 4.2:

$$
\begin{aligned}
0° \rightarrow 65° &: \quad 9567.46 \quad \text{photons m}^{-2}\ \text{sr}^{-1}\ \text{s}^{-1} \\
65° \rightarrow 95° &: \quad 11567.49 \quad \text{photons m}^{-2}\ \text{sr}^{-1}\ \text{s}^{-1} \\
95° \rightarrow 130° &: \quad 14469.25 \quad \text{photons m}^{-2}\ \text{sr}^{-1}\ \text{s}^{-1} \\
130° \rightarrow 180° &: \quad 4512.87 \quad \text{photons m}^{-2}\ \text{sr}^{-1}\ \text{s}^{-1}
\end{aligned}
\tag{4.2}
$$

Next, the surface of a sphere is integrated to compute the angular surface of each region:

$$
\begin{aligned}
0° \rightarrow 65° &: \quad 3.627796 \text{ sr} \\
65° \rightarrow 95° &: \quad 3.203005 \text{ sr} \\
95° \rightarrow 130° &: \quad 3.491138 \text{ sr} \\
130° \rightarrow 180° &: \quad 2.244432 \text{ sr}
\end{aligned}
\tag{4.3}
$$

The source is a R = 0.5 m sphere, previously shown in fig. 3.78, of $\pi/4$ m^2 cross-section. Multiplying eq. 4.2 with eq. 4.3 and the cross-section value, the final result is:

$$
\begin{aligned}
0° \rightarrow 65° &: \quad 27260.23 \quad \text{photons s}^{-1} \\
65° \rightarrow 95° &: \quad 29099.58 \quad \text{photons s}^{-1} \\
95° \rightarrow 130° &: \quad 39673.73 \quad \text{photons s}^{-1} \\
130° \rightarrow 180° &: \quad 7955.16 \quad \text{photons s}^{-1}
\end{aligned}
\tag{4.4}
$$

Summing these, a value of 103988.70 photons s^{-1} is found for the simulation (meaning that simulating 103989 photons is equivalent to 1 second of real time). Then, one finds the ratio per region of incoming gamma rays by dividing eq. 4.4 with the total value:

$$
\begin{aligned}
0° \rightarrow 65° &: \quad 26.215\ \% \\
65° \rightarrow 95° &: \quad 27.983\ \% \\
95° \rightarrow 130° &: \quad 38.152\ \% \\
130° \rightarrow 180° &: \quad 7.650\ \%
\end{aligned}
\tag{4.5}
$$

The simulation primaries generator will then pick a region according to the ratios of eq. 4.5, pick a position on the source sphere, an energy according to the energy spectrum of the region (eq. 4.1), and finally pick a direction that satisfies the region requirement.

4.3 Neutrons Simulation

The neutron background at flight altitude is isotropic but broken into three sections covering 12 orders of magnitude in energy: from thermal to cosmic neutrons. The data for the spectrum comes from [62] and [63], and is given by eq. 4.6:

$$
\begin{aligned}
&0.01\ \text{eV} \rightarrow 0.1\ \text{eV} : && 7.96\times10^{8}\, \boldsymbol{E} && (\text{neutrons m}^{-2}\ \text{sr}^{-1}\ \text{s}^{-1}\ \text{keV}^{-1}) \\
&0.1\ \text{eV} \rightarrow 60\ \text{MeV} : && 24\, \boldsymbol{E}^{-0.88} && (\text{neutrons m}^{-2}\ \text{sr}^{-1}\ \text{s}^{-1}\ \text{keV}^{-1}) \\
&60\ \text{MeV} \rightarrow 10\ \text{GeV} : && 3.023\times10^{6}\, \boldsymbol{E}^{-1.94} && (\text{neutrons m}^{-2}\ \text{sr}^{-1}\ \text{s}^{-1}\ \text{keV}^{-1})
\end{aligned}
\tag{4.6}
$$

A plot of this flux is shown in figure 4.2:

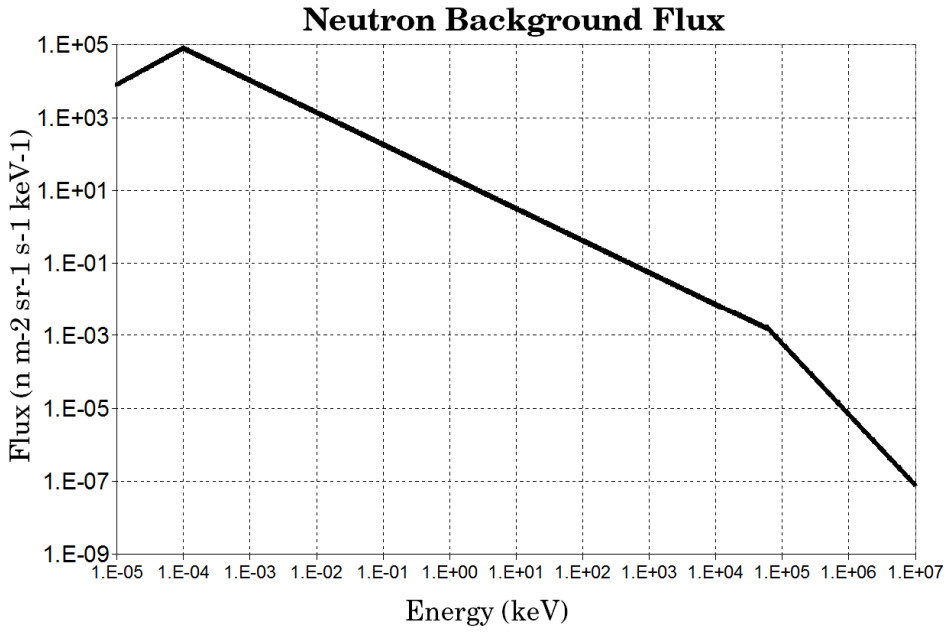

Figure 4.2: Neutron Background Flux

For a source sphere of $\boldsymbol{R}$ = 0.5 m, this flux leads to a 789.6188 neutrons/s events to time conversion factor (meaning that simulating 790 neutrons is equivalent to 1 second of flight time).

4.4 Cosmic Protons Simulation

The data for the cosmic protons flux comes from T. Mizuno et al.'s paper "Cosmic-ray background flux model based on a Gamma-ray Large Area Space Telescope balloon flight engineering model" [64] and is given by their equations 1, 4 and 6, here equations 4.7, 4.8 and 4.9:

$$\begin{aligned}\mathrm{Primary}(E_\mathrm{k}) = \mathrm{Unmod}(E_\mathrm{k} + Z\,e\,\phi) \\ \times \frac{(E_\mathrm{k}+M\,c^2)^2-(M\,c^2)^2}{(E_\mathrm{k}+M\,c^2+Z\,e\,\phi)^2-(M\,c^2)^2} \\ \times \frac{1}{1-(R/R_\mathrm{cut})^{-r}}\end{aligned} \tag{4.7}$$

$$\mathrm{Unmod}(E_\mathrm{k}) = A\left[\frac{R(E_\mathrm{k})}{\mathrm{GV}}\right]^{-a} \tag{4.8}$$

$$R_\mathrm{cut} = 14.9 \times \left(1 + \frac{h}{R_\mathrm{Earth}}\right)^{-2.0} (\cos\theta_M)^4\ \mathrm{GV} \tag{4.9}$$

The result from eq. 4.7 is in units of [protons s^{-1} m^{-2} sr^{-1} MeV^{-1}], $\boldsymbol{E}_\mathrm{k}$ is the proton kinetic energy, the atomic number $\boldsymbol{Z}$ is 1 for protons and $\boldsymbol{e}$ is the elementary charge magnitude. $\boldsymbol{\phi}$ is a parameter representing the solar modulation, it varies from ~550 MV at minimal solar activity to ~1100 MV at maximal solar activity. A good measure of the state of the solar cycle is the number of sunspots on the sun at a given time, figure 4.3 shows the number of sunspots in the months prior to the balloon flight and predicted values. This figure led to setting $\boldsymbol{\phi}$ = 850 MV for our simulations ($\boldsymbol{\phi}$ = 1100 MV when N=125, $\boldsymbol{\phi}$ = 550 MV when N=0, then $\boldsymbol{\phi}$ = 4.4 N + 550. We estimated N would be 70 for September 2011, then $\boldsymbol{\phi}$ = 858 MV ≈ 850 MV).

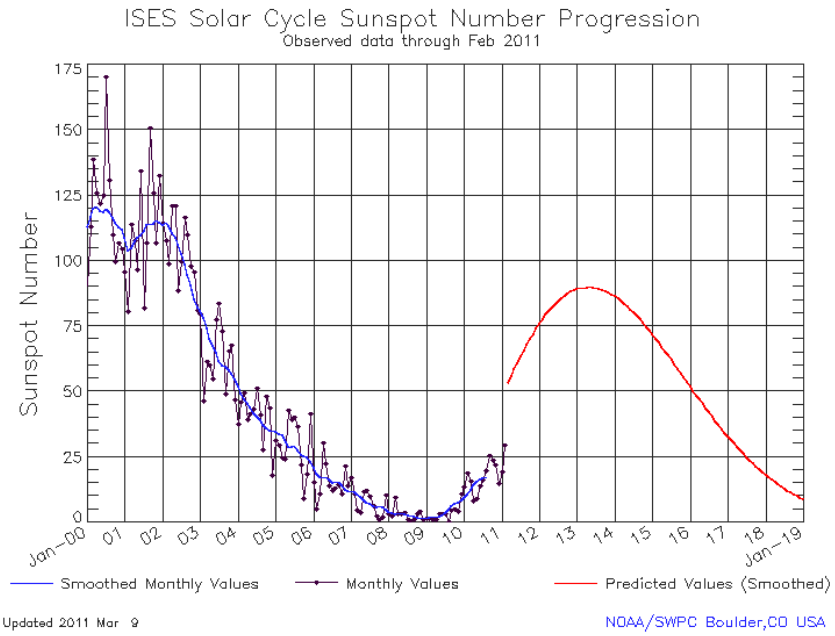

Figure 4.3: Solar Cycle Sunspot Number Progression prior to the balloon flight with predicted values (the x axis is in years). It is used to set the solar modulation factor ϕ for the simulations (see text).

M is the proton mass equal to 938.272 MeV/c^2 and c the speed of light. The rigidity R is defined as a particle momentum divided by its charge p/q. For a proton, q is 1 so the rigidity R is E_k. The parameter r is 12. For the second equation 4.8, A = 23.9 [protons s^{-1} m^{-2} sr^{-1} MeV^{-1}], $R(E_k) = E_k + Ze\phi$, "GV" just removes the unit and a = 2.83. The last equation 4.9 is the cutoff rigidity where h is the flight altitude, 39 km in our case, R_{Earth} the Earth radius, and θ_M the geomagnetic latitude, 42° in our case, which gives an R_{cut} value of 4.48934 GV.

Everything needed to compute the cosmic proton flux for the balloon flight is in place and the result is shown in figure 4.4.

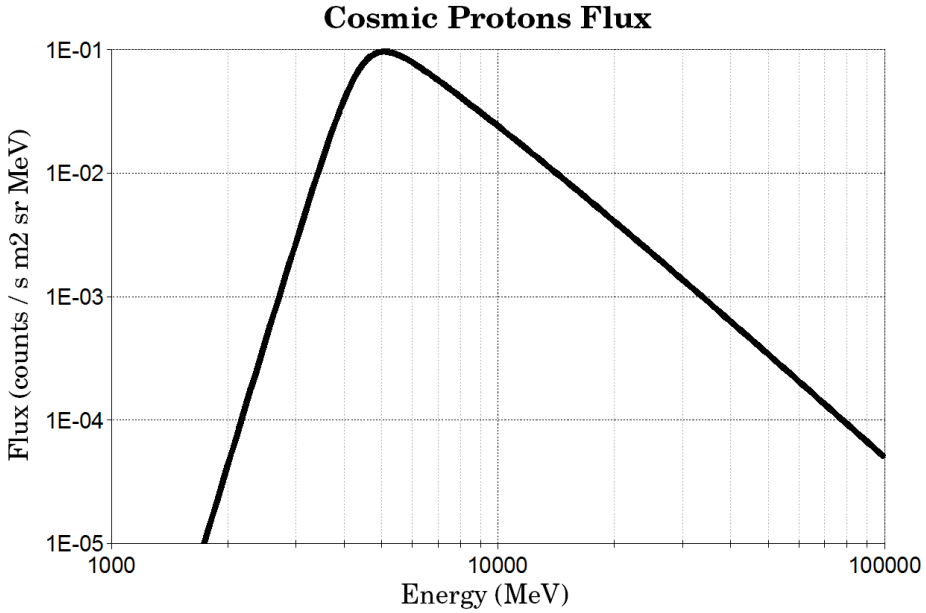

Figure 4.4: Cosmic Protons Background Flux

The effect of air attenuation must now be computed. The cosmic protons come downwards from the upper direction, with zenith angles from 0° to 90°, and the flux will be attenuated by the air it crosses before reaching the instrument. In order to simulate the air attenuation, we first assume that the shape of the spectrum is not be affected by the attenuation, but that its magnitude is. The upper hemisphere of the sky is separated into four regions for which the incoming protons cross different air depths before reaching the instrument, and thus are differently attenuated. The four regions were arbitrarily chosen to be from 0° to 25°, 25° to 50°, 50° to 78.5° and 78.5° to 90°. The proton spectrum remains the same for each region, but the atmospheric attenuation factor to modulate each region needs to be computed. The attenuated flux is given by eq. 4.10:

$$I = I_0 \mathrm{e}^{-\frac{x}{l}} \tag{4.10}$$

where I_0 is the initial flux, I the attenuated flux, l the nuclear interaction length in air (90 g cm^{-2} [64]), and x the effective atmospheric depth. The atmospheric depth at an altitude of 39 km is 3.8 g cm^{-2}, and the effective atmospheric depth in function of the zenith angle θ given by eq. 4.11 :

$$x = 3.8 \frac{1}{\cos\theta} \text{ [g cm}^{-2}\text{]} \quad (4.11)$$

The angle taken for each region was the median angle: 12.5° for the first region, 37.5° for the second, 64.25° for the third and 84.25° for the fourth. Using equations 4.10 and 4.11, the modulation coefficient for each region is computed and the results shown in eq. 4.12:

$$\begin{aligned} 0° \rightarrow 25° &: \quad 95.767\ \% \\ 25° \rightarrow 50° &: \quad 94.817\ \% \\ 50° \rightarrow 78.5° &: \quad 90.739\ \% \\ 78.5° \rightarrow 90° &: \quad 41.789\ \% \end{aligned} \quad (4.12)$$

With these coefficients and the flux given by eq. 4.7 and shown in fig. 4.4, everything necessary to conduct the cosmic proton background simulation is at hand. Further calculations shows that 10.8725 % of the events will come from the first region, 30.2769 % from the second, 48.7551 % from the third, and 10.0955 % from the fourth (the regions do not have the same angular area). For a source sphere of $\boldsymbol{R}$ = 0.5 m, these fluxes leads to a 2070.5842 protons/s events to time conversion factor.

4.5 Atmospheric Protons Simulation

The atmospheric proton fluxes are based on Mizuno et al.'s paper [64]. In this case, four regions are taken: downwards close to the zenith (0° to 60°), downwards close to the horizon (60° to 90°), upwards close to the horizon (90° to 120°), and upwards close to the nadir (120° to 180°). Each flux is broken into a low-energy part and a high-energy part, giving eight sections to consider. In reality, only three functions and two modulation factors are needed. For the downwards regions

between 100 keV and 4 GeV, and for the upwards regions between 100 keV and 100 MeV, the initial flux is given by eq. 4.13:

$$0.17\left(\frac{E_k}{100\ \text{MeV}}\right)^{-1.0} \qquad \text{(protons m}^{-2}\ \text{sr}^{-1}\ \text{s}^{-1}\ \text{MeV}^{-1}\text{)} \qquad (4.13)$$

For the downwards regions above 4 GeV, the initial flux is given by eq. 4.14 :

$$0.222\left(\frac{E_k}{100\ \text{MeV}}\right)^{-2.83} \qquad \text{(protons m}^{-2}\ \text{sr}^{-1}\ \text{s}^{-1}\ \text{MeV}^{-1}\text{)} \qquad (4.14)$$

For the upwards regions above 100 MeV, the initial flux is given by eq. 4.15 :

$$0.17\left(\frac{E_k}{100\ \text{MeV}}\right)^{-1.6} \qquad \text{(protons m}^{-2}\ \text{sr}^{-1}\ \text{s}^{-1}\ \text{MeV}^{-1}\text{)} \qquad (4.15)$$

These three fluxes now need modulation factors to account for two cases. The fluxes for the horizon regions need to be multiplied by a factor 2 to account for atmospheric saturation (or horizon buildup), while the zenith and nadir region fluxes have to be multiplied by 1.1547 to account for the atmospheric depth in the line of sight (1/(cos 30°)=1.1547). The four resulting fluxes are plotted in figure 4.5.

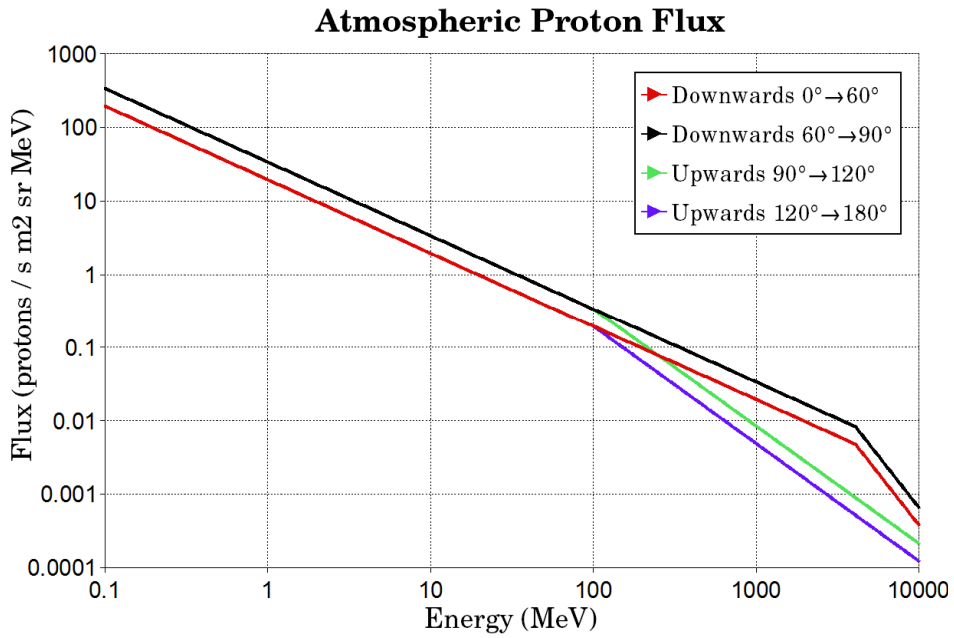

Figure 4.5: Atmospheric Protons Background Flux

Applying the same calculations outlined in the gamma-ray background section, these fluxes lead for a source sphere of R = 0.5 m to a 2583.8881 protons/s events to time conversion factor.

4.6 Alpha Particles Simulation

The alpha particles flux is based on Mizuno et al.'s paper [64]. It follows the same procedure detailed for the cosmic protons case, see section 4.4, with the appropriate modifications. In the alpha particles case, Z is now 2, M is now 3.727379 GeV/c^2, A is now 1.5 [alphas s^{-1} m^{-2} sr^{-1} MeV^{-1}], and α is now 2.77. The rigidities R and $R(E_k)$ need now to be computed with q = 2. The resulting flux is shown in figure 4.6. Afterwards, the analysis follows the same breakup in regions to account for the atmospheric attenuation, resulting in one initial flux supplying four regions with different attenuation coefficients. Except for the number changes outlined above, the procedure is the same as in the cosmic proton case. For a source sphere of R = 0.5 m, the events to time conversion factor for the alpha particles simulations is 297.0046 alphas/s.

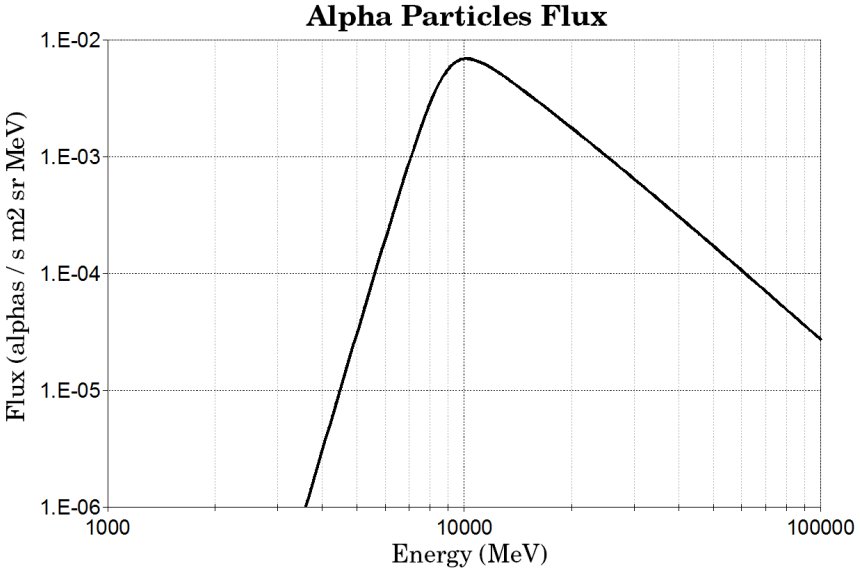

Figure 4.6: Alpha Particles Background Flux

4.7 Cosmic Electrons Simulation

The treatment for the cosmic electrons simulation follows the same treatment as the cosmic protons already outlined in section 4.4 with the following modifications: M is now 511 keV/c^2, r is 6, A is 0.65 [electrons s^{-1} m^{-2} sr^{-1} MeV^{-1}], and α is 3.3. The resulting flux is shown in figure 4.7. To account for the atmospheric attenuation, the same four regions were used, however the constant l is now the radiation length in air and equal to 36.6 g cm^{-2}. The rest of the procedure is the same and for a source sphere of R = 0.5 m, the events to time conversion factor for the cosmic electrons simulations is 19.1507 electrons/s.

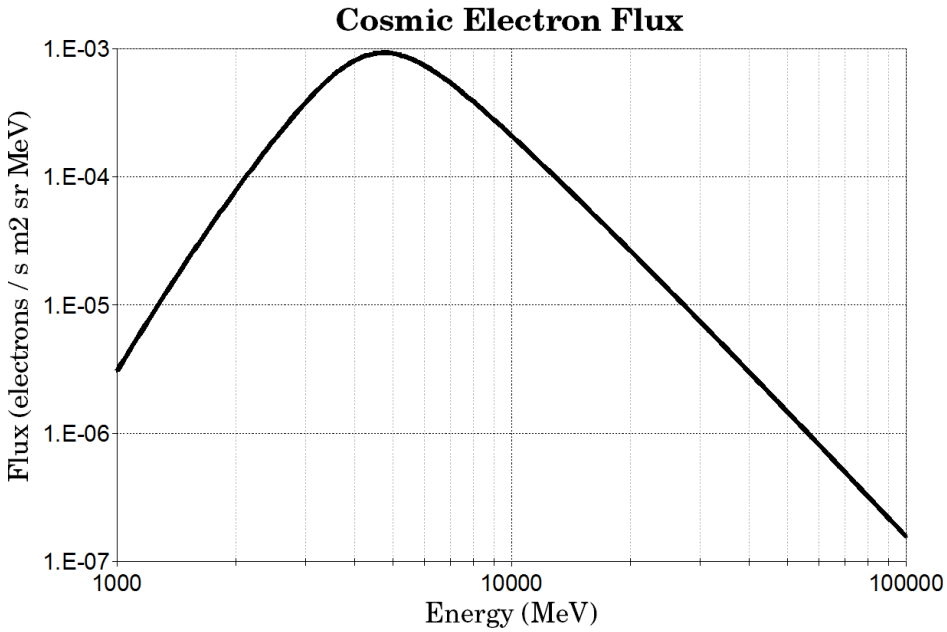

Figure 4.7: Cosmic Electrons Background Flux

4.8 Cosmic Positrons Simulation

The cosmic positron background flux treatment is the same as the cosmic electron background flux with only one change in the flux modulation. Mizuno's paper [64] refer to a measurement from Golden et al. [65] that the fraction of positrons in the (e^-+e^+) cosmic flux is 0.078 ± 0.016 between 5 and 50 GeV. A trivial

calculation leads to the appropriate A = 0.055 [positrons s^{-1} m^{-2} sr^{-1} MeV^{-1}]. The resulting flux is about 10% of the cosmic electron flux and is shown in figure 4.8. For a source sphere of R = 0.5 m, the events to time conversion factor for the cosmic positrons simulations is 1.6204 positrons/s.

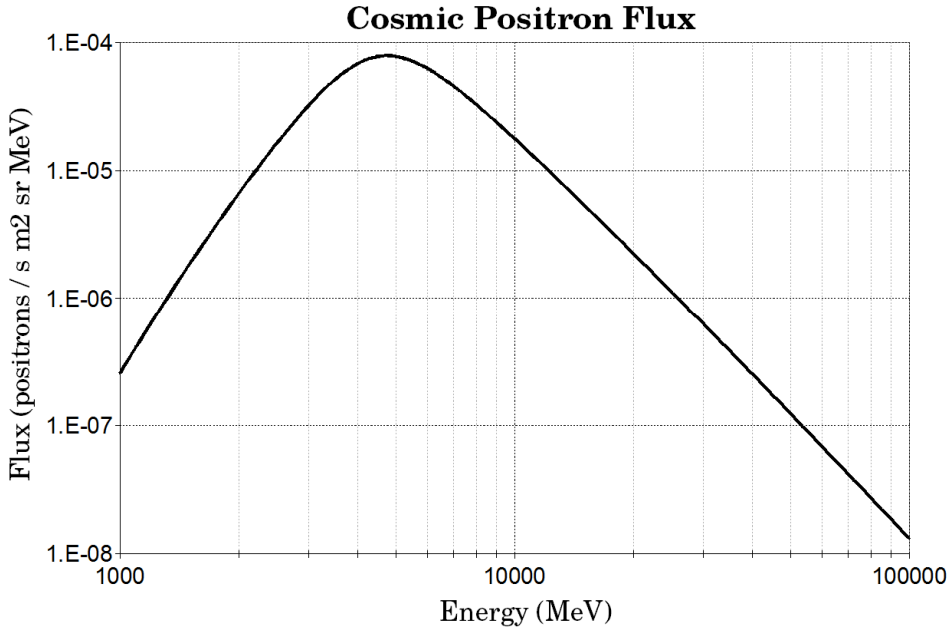

Figure 4.8: Cosmic Positron Background Flux

4.9 Atmospheric Electrons and Positrons Simulation

Atmospheric electrons and positrons are two types of atmospheric radiation background simulated for the FACTEL balloon flight treated in the same way prior to the simulation. Both atmospheric electrons and positrons are created in pairs from incoming energetic particles interacting within the atmosphere, they have the same mass, charge amplitudes, and interaction channels. The only difference between the two was to set the second simulation to generate positrons instead of electrons. The simulations will lead to different results because positrons will annihilate readily within the instrument creating two 511 keV gamma rays.

For the fluxes, the treatment of Mizuno et al. [64] was followed. As for the atmospheric protons case, four regions were defined: downwards close to the zenith (0° to 60°), downwards close to the horizon (60° to 90°), upwards close to the horizon (90° to 120°), and upwards close to the nadir (120° to 180°). The fluxes near the horizon have to be multiplied by 2 while the fluxes near the instrument axis are multiplied by 1.1547 for the same reasons described in section 4.5. Then the same flux is used for both downwards and upwards directions (see [64], sections 3.4 and 6), it is broken into 3 parts and given by 4.16:

100 keV → 100 MeV: $0.41\left(\frac{E_k}{100\ \text{MeV}}\right)^{-0.5}$ (counts m^{-2} sr^{-1} s^{-1} MeV^{-1}) (4.16)

100 MeV → 4 GeV: $0.41\left(\frac{E_k}{100\ \text{MeV}}\right)^{-2.1}$ (counts m^{-2} sr^{-1} s^{-1} MeV^{-1})

4 GeV → 10 GeV: $0.613\left(\frac{E_k}{100\ \text{MeV}}\right)^{-2.83}$ (counts m^{-2} sr^{-1} s^{-1} MeV^{-1})

Actually, since the downwards and upwards fluxes are the same, only two regions could have been used: the horizon region from 60° to 120°, and the vertical region ((0° to 60°) ∪ (120° to 180°)). In practice, the previously programmed regions for the atmospheric protons were reused by replacing the flux supplying the already programmed regions with the one from eq. 4.16. A plot of the "Horizon Flux" and "Vertical flux" is shown in figure 4.9. For a source sphere of $\boldsymbol{R}$ = 0.5 m, the events to time conversion factor for the atmospheric electrons and positrons simulations is 1811.5836 particles/s.

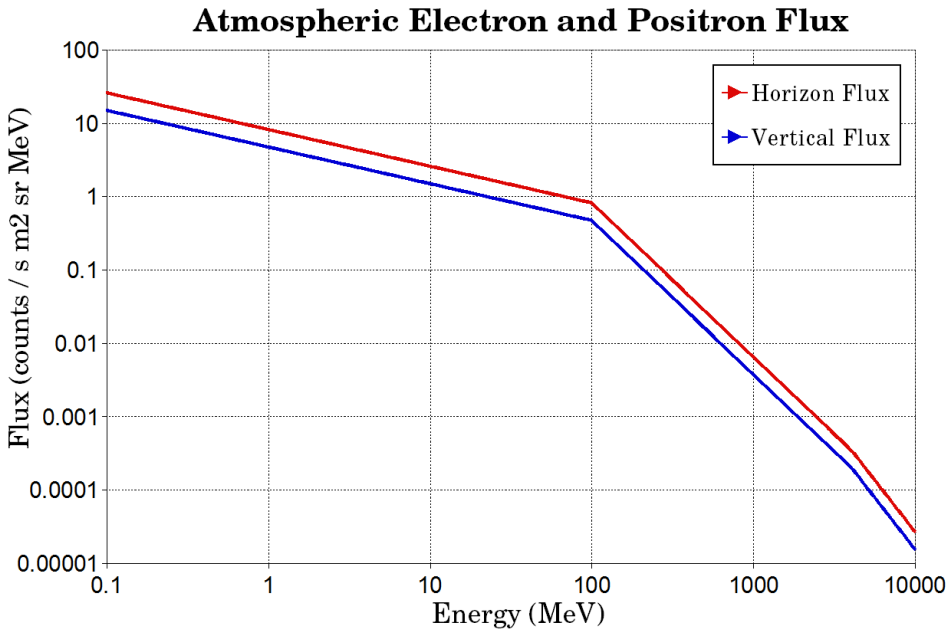

Figure 4.9: Atmospheric Electrons and Positrons Background Flux

4.10 Atmospheric Negative Muons Simulation

The data for the atmospheric negative muon flux was based on Mizuno et al.'s paper [64]. As for atmospheric electrons and positrons, we used the four regions already programmed where a "Horizon Flux" and a "Vertical Flux" could have been used. The initial unmodulated flux is broken in two parts given by eq. 4.17:

100 keV → 380 MeV : 1.65×10^{-2} (muons m^{-2} sr^{-1} s^{-1} MeV^{-1}) (4.17)

380 MeV → 4 GeV: $$0.0065\left(\frac{E_k}{\text{GeV}}\right)^{-2.2}\exp\left[-\left(\frac{E_k}{0.43\ \text{GeV}}\right)^{-1.5}\right]$$

The "Horizon Flux" is modulated by a factor 2, while the "Vertical Flux" is multiplied by a factor 1.1547, giving the fluxes shown in figure 4.10. For a source sphere of R = 0.5 m, the events to time conversion factor for the atmospheric negative muons simulations is 263.0264 muons/s.

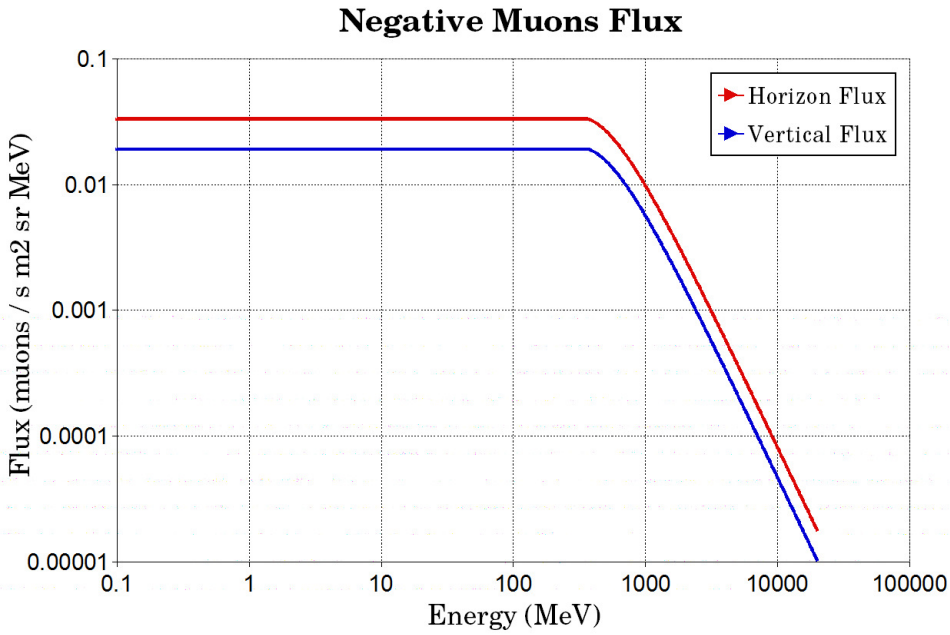

Figure 4.10: Atmospheric Negative Muons Background Flux

4.11 Atmospheric Positive Muons Simulation

The last background type considered for the FACTEL balloon flight simulations was the atmospheric positive muons. For this final case, the treatment is the same as the negative muons just reviewed with a 1.6 modulation factor. Mizuno et al. [64] cite Boezio et al. [66] as the source for the ratio μ^+/μ^- to be 1.6. The flux for the atmospheric positive muons is thus given by multiplying eq. 4.17 by a factor 1.6 and gives eq. 4.18 :

100 keV → 380 MeV : $\mathbf{2.64\times10^{-2}}$ (muons m^{-2} sr^{-1} s^{-1} MeV^{-1}) (4.18)

380 MeV → 4 GeV: $$0.0104\left(\frac{E_k}{\text{GeV}}\right)^{-2.2}\exp\left[-\left(\frac{E_k}{0.43\ \text{GeV}}\right)^{-1.5}\right]$$

The "Horizon Flux" is multiplied by a factor 2 and the "Vertical Flux" multiplied by 1.1547, giving the fluxes shown in figure 4.11. These two fluxes were applied to the four regions already discussed: the "Horizon Flux" to the downwards horizon region (60° to 90°) and upwards horizon region (90° to 120°), and the

"Vertical Flux" to the downwards zenith region (0° to 60°) and upwards nadir region (120° to 180°). After calculations, the events to time conversion factor for a source sphere of $\boldsymbol{R}$ = 0.5 m for the atmospheric positive muons simulations is 420.8422 muons/s.

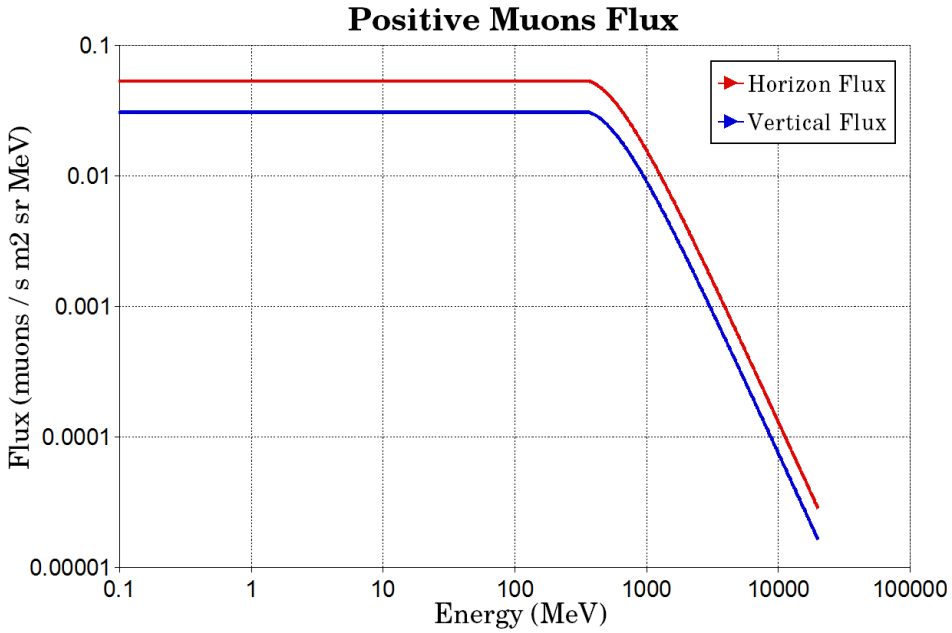

Figure 4.11: Atmospheric Positive Muons Background Flux

4.12 FACTEL Balloon Flight Simulations Results

The results of these simulations will be shown to be in good agreement with the flight data in the next chapter, see figures 5.10, 5.11, 5.14, 5.16 and 5.24. Some of the intermediate results prior to the summation are now presented. An initial way to assess the relative importance of the contribution of each background type is to compare their particles/second value:

Gamma-Rays:	103988.70 photons/s
Neutrons:	789.62 neutrons/s
Cosmic Protons:	2070.58 protons/s
Atmospheric Protons:	2583.89 protons/s
Alpha Particles:	297.00 alphas/s
Cosmic Electrons:	19.15 electrons/s
Cosmic Positrons:	1.62 positrons/s
Atmospheric Electrons:	1811.58 electrons/s
Atmospheric Positrons:	1811.58 positrons/s
Atmospheric Negative Muons:	263.03 n-muons/s
Atmospheric Positive Muons:	420.84 p-muons/s

This comparison is possible as a side benefit of having programmed all the sources to be the same $\boldsymbol{R}$ = 0.5 m sphere shown in fig. 3.78. Still, all the fluxes are different with different shapes, energy ranges, and most importantly particles type, so all simulations had to be run to at least once to an equivalent time as the flight duration. A first series of eleven simulations was performed, noted S035 to S045. Then, because Geant4 and the simulation physics evolved, a second series of six simulations was performed, noted S049 to S054. One of the results from the first simulation cycle was to show that the alpha particles, cosmic electrons and positrons, and muons had no significant impact on FACTEL results. So in order to save time and processing power, these background types were not simulated in the second cycle of simulations. The backgrounds types kept for the second series were gamma rays, cosmic protons, atmospheric protons, electrons and positrons, and finally neutrons. Neutrons were shown by the first simulation cycle not to be a significant contributor to the instrument response, they were however kept for the second cycle because neutrons are usually an important source of background for Compton Telescopes.

The D1 layer simulation of singles without anti-coincidence veto results are shown in figure 4.12. (The summation of these six data sets gives the curves shown in figures 5.10 and 5.11.) The prime contributor to the D1 layer singles is gamma rays.

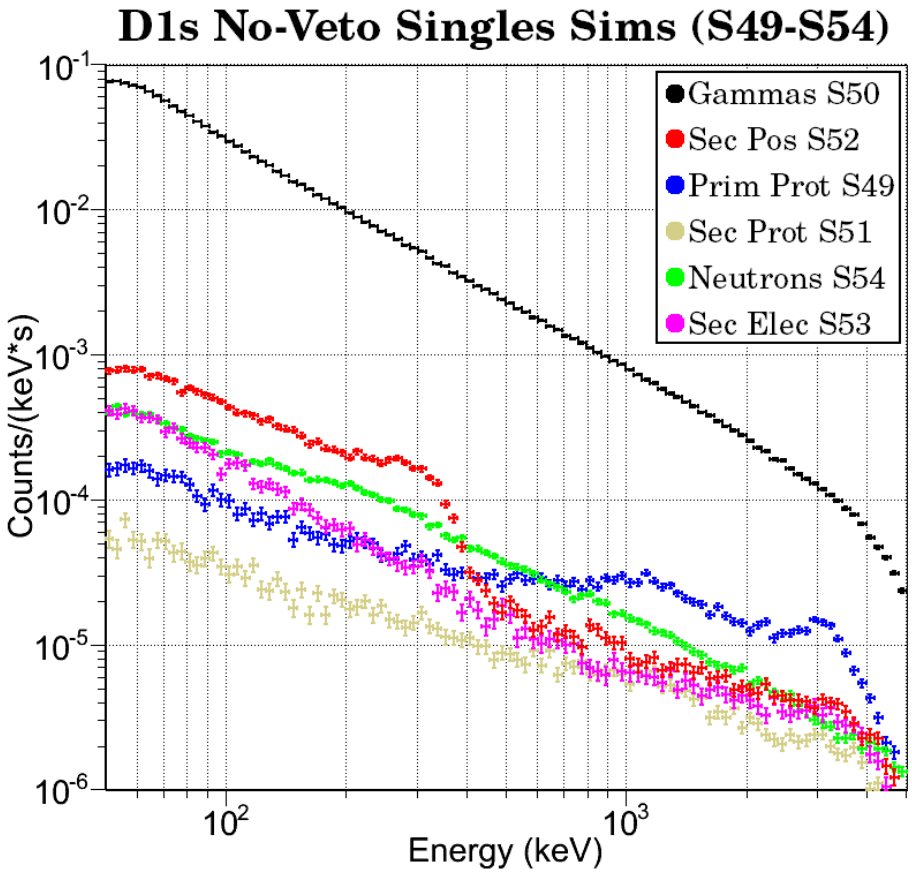

Figure 4.12: FACTEL Flight Simulations D1 Layer Singles without AC Veto results. Gamma rays are the prime contributor to the spectrum.

The D2 layer set of results used to create the line shown in fig. 5.14 is shown in figure 4.13. The prime contributor to the D2 layer singles are gamma rays and the cosmic protons match the gamma rays events rate at 5 MeV. Also of notice is the 511 keV peak for positrons.

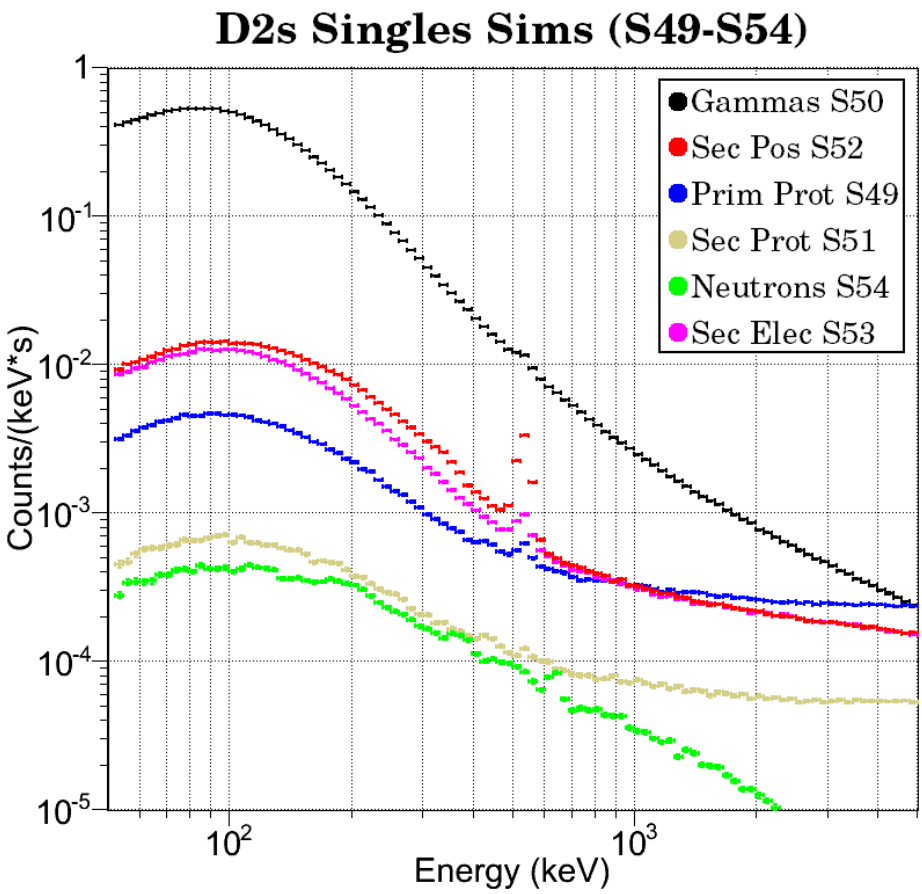

Figure 4.13: FACTEL Flight Simulations D2 Layer Singles results. Gamma rays are the prime contributor to the spectrum.

The self-background of $LaBr_3$ shown in fig. 5.15 is then added to these results to get the result shown in fig. 5.16.

The set of results used to create the telescope mode coincidence energy spectrum shown in fig. 5.24 is shown in figure 4.14, these are the "No Anti-Coincidence Veto" and ToF ≥ 0 events.

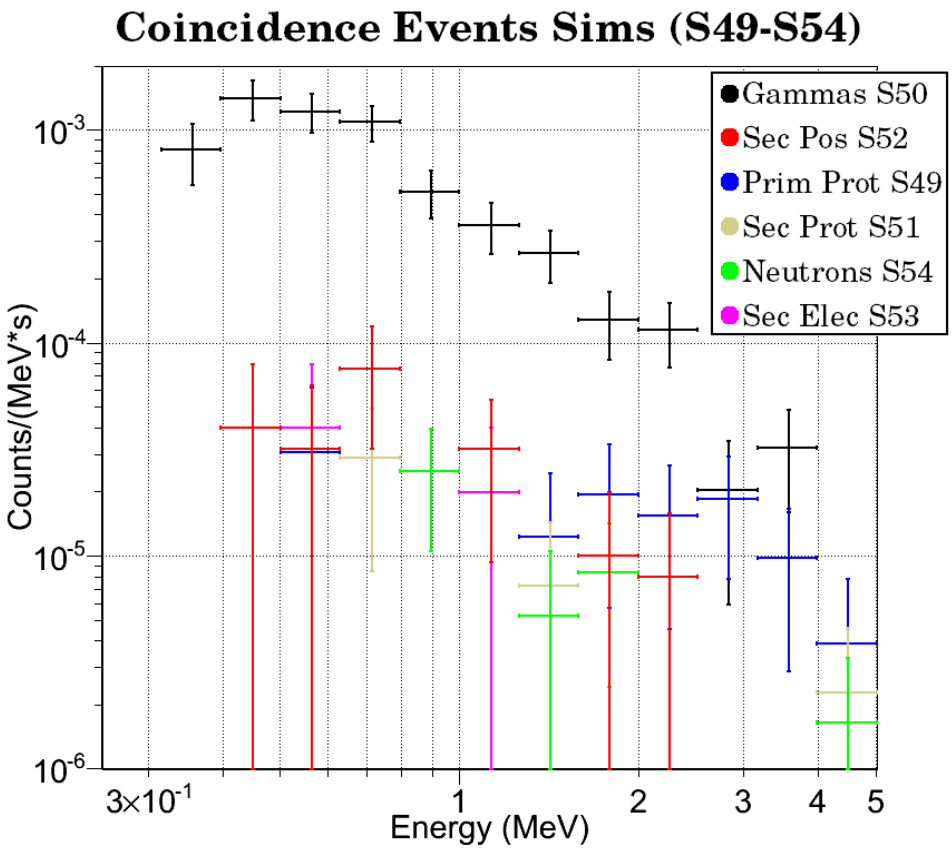

Figure 4.14: FACTEL Flight Simulations Coincident Events results (No AC Veto and ToF≥0) Gamma rays are the prime contributor to the spectrum.

For all three cases shown, figures 4.12, 4.13 and 4.14, gamma rays are the primary source of signal, which is an expected result for a gamma-ray telescope. The fact that the other particles types are struggling to produce any signal in the last fig. 4.14 is precisely what our goal was: mitigating the background signal. In all three cases, the secondary source of events at low-energy is atmospheric positrons, and cosmic protons above 1 MeV.

In terms of evaluating the effectiveness of the new background mitigation techniques implemented for the FACTEL instrument prototype (borating the top anti-coincidence panel, deuterating the D1 detectors liquid scintillator material, limiting metals and passive materials in the D1 region, using $LaBr_3$ scintillator D2 detectors), the results show that the instrument did not suffer from any background

related issue. In all three cases (figures 4.12, 4.13 and 4.14), gamma-rays are the primary source of signal while all background sources stay in most cases well below that of the gamma-rays. Of particular interest are the neutron results: three of the four new background suppression techniques concern mitigating neutrons. The results show the neutrons response to be two orders of magnitude lower than that of gamma-rays in singles results, see figures 4.12 and 4.13, while it remains one order of magnitude lower in the coincidence results (fig. 4.14). This shows that even while the PSD capability of the D1 detectors was not available for the FACTEL instrument, neutrons were not detrimental.

4.13 Summary

This chapter reviewed the background simulations performed to show that the FACTEL instrument responded correctly to the radiation environment during the flight. The background types modeled were gamma rays, neutrons, cosmic protons, atmospheric protons, alpha particles, cosmic electrons, atmospheric electrons, cosmic positrons, atmospheric positrons, negative muons and finally positive muons. We reviewed the expected flux at the balloon altitude for each background type and detailed how each was simulated. The simulation results from the 6 principal contributors to the instrument response were shown in figures 4.12, 4.13 and 4.14. Then the summation of these results is compared to the flight data in figures 5.10, 5.11, 5.14, 5.16 and 5.24. The flight data and the simulation analysis show that the FACTEL instrument performed as expected for a prototype of that size.

CHAPTER 5

The FACTEL Flight

5.1 Introduction

The FACTEL balloon flight was conducted September 23, 2011, from NASA Columbia Scientific Balloon Facility (CSBF) in Fort Sumner, New Mexico USA, to test the FACTEL instrument prototype capabilities in the radiation environment of the high atmosphere. This chapter focuses on the FACTEL balloon flight itself. We will present the results of the flight [84], and assess the effectiveness of the new background mitigation techniques implemented for FACTEL. This chapter will present the flight basic environmental data, discuss FACTEL data acquisition cycle, and present the flight results. The FACTEL prototype was flown with the larger GRAPE instrument, a Gamma RAy Polarimeter Experiment [60], also built at UNH, see figure 5.2.

The FACTEL instrument is a prototype built to test, on a small scale, the new techniques of background mitigation developed from the lessons learned from the COMPTEL instrument. We note that the sensitivity of COMPTEL was ultimately limited by its background rejection capacity. The sources of background events for Compton telescopes have already been described in section 2.5 of this work as well as the background suppression methods in section 2.6. The FACTEL instrument was not a focusing camera, and was too small, to make any observation of any gamma-ray

astronomical source. The goal of the flight was to see what the instrument would measure in the intense radiation background environment above the atmosphere, analyze the characteristics of the various energy and Time of Flight spectra, and ultimately to investigate the effectiveness of the background mitigation techniques developed for the instrument. The high atmosphere is a good testing environment for space telescopes prototypes because it is relatively easily accessed and because it provides conditions similar to those in space.

As detailed in section 2.6, the four background mitigation methods for Compton telescopes are the dome and anti-coincidence panels, the Time of Flight measurement, Pulse Shape Discrimination, and material choices. The FACTEL prototype implemented four new background mitigation techniques outlined in the third chapter of this work and concerns the Time of Flight measurement and material choices. The four techniques are:

- Borate the top anti-coincidence panel
- Deuterate the D1 detectors liquid scintillator material
- Limit passive materials, particularly metals, in the D1 layer region
- Use $LaBr_3$ scintillator D2 detectors

5.2 Basic Environmental Data

The NASA Columbia Scientific Balloon Facility (CSBF) is in Fort Sumner, New Mexico USA (34°28'23" N, 104°14'32" W). The flight provided 26 hours of data from an average altitude of 36 km. The flight path is shown in figure 5.1. For the CSBF, the flight was "GRAPE/FACTEL Flight #624N," for our experimental runs numbering, the flight was R654.

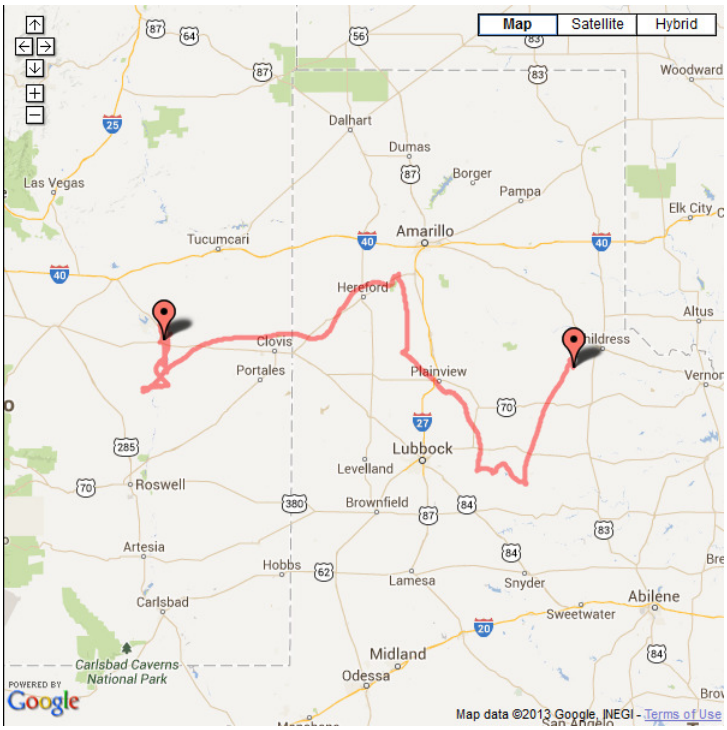

Figure 5.1: GRAPE/FACTEL Flight 624N Flight Path.

Figure 5.2 is comprised of photographs of the final mounted instrument, the full gondola and the balloon launch.

The balloon was launched in the morning and flew for 26 hours at the average float altitude of 36 km. The altitude data is shown in figure 5.3.

Figure 5.2: The FACTEL instrument mounted in its gondola frame (left), the GRAPE/FACTEL gondola (middle), the balloon launch (right)

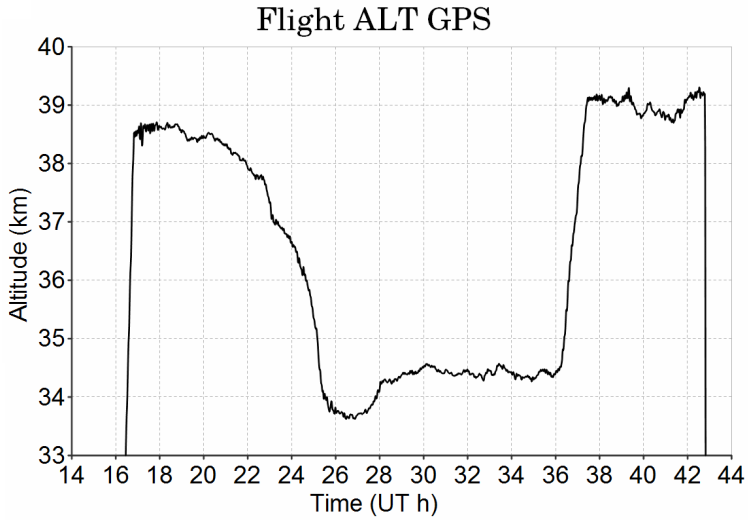

Figure 5.3: FACTEL Flight Altitude, the balloon floated during the day, dipped during the night, and rose again the next day.

The altitude data shows the balloon climbed close to 39 km of altitude, then slowly dipped during the day, then dipped and stabilized during the night (sunset at ~24h) before raising back (sunrise at ~36h) slightly above 39 km during the next day before flight termination. At that altitude, more than 99% of the atmosphere is beneath the balloon and this provides an environment resembling real space conditions. Figure 5.4 shows the external pressure and temperature during the flight, the pressure stays under 0.01 bar, 1 bar being one atmosphere. The internal pressure and temperature inside the instrument dome were also monitored during the flight and the results are presented in figure 5.5.

The internal pressure plot in fig. 5.5 shows that the pressure stayed between 14.6 and 15 psi (1 atmosphere = 14.7 psi), indicating that the pressure vessel had no significant leaks, while the temperature plot shows it stayed between 21 and 27 °C. Of note are the heaters triggering about once per two hours during the day and triggering 18 times during the 12 hours of night time. The data from figures 5.1, 5.3, 5.4 and 5.5 show that the flight was successful in terms of basic environmental data:

the external data show that the flight itself was successful while the internal data shows the instrument operated within the normal conditions it experienced in the laboratory.

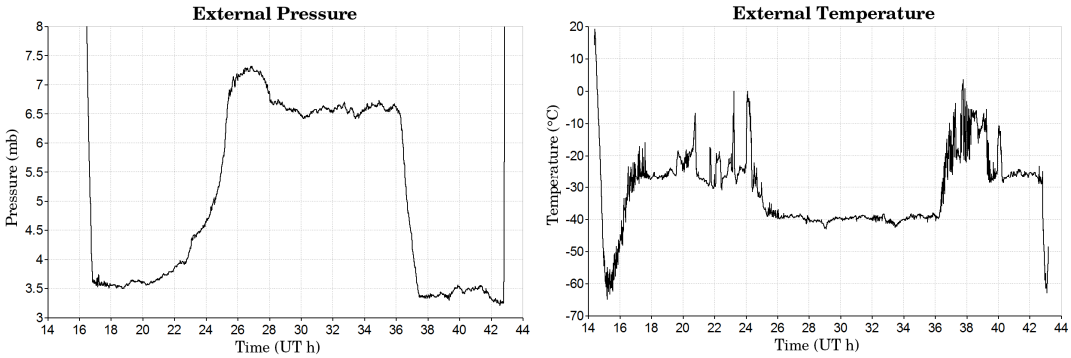

Figure 5.4: FACTEL Flight External Parameters.
The Pressure stayed under 0.01 bar (left) and Temperature (right)

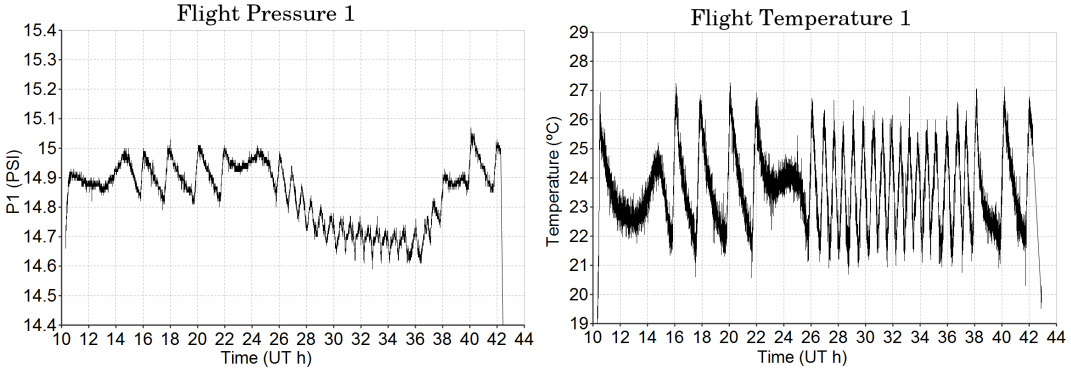

Figure 5.5: FACTEL Flight Internal Parameters. The Pressure stayed close to the ground pressure (left), and the Temperature stayed between 21 and 27 °C (right)

5.3 FACTEL Data Acquisition Cycle

The FACTEL data acquisition routine cycled through four modes during the flight: 5 minutes in coincidence mode, 10 seconds in D1 singles mode, 10 seconds in D2 singles mode, and finally 10 seconds in rates counting mode. The cycle theoretically sums up to 330 seconds, however the flight data shows that in practice one cycle lasted 372.8 seconds. The part of the flight used for data analysis was the

float portion lasting from hour 16.5 to hour 42.27, see fig. 5.3. 248 full cycles were analyzed, the first coincident event considered had a time stamp of 37807.239 s while the last one had a time stamp of 44172.207 s the next day, leading to 25.77 hours of data acquisition. (The time stamp here is the local time in seconds given by the PC-104 computer. New-Mexico is in the Mountain Time Zone, which is at UTC-6h during summer time. Here, 37807.239 s is 10h30 in the morning, about 2 hours after launch, and 16.5 h in Universal Time.)

5.4 Rates during the flight

The first scientific data of interest from the balloon flight are the rates in the detector layers and anti-coincidence panels. The rates in the anti-coincidence panels were monitored by the instrument housekeeping routine while the rates in the detector layers were monitored through the FACTEL data acquisition cycle. Figure 5.6 shows the sum of the rates in the six anti-coincidence panels, while figure 5.7 shows the rates in the detector layers.

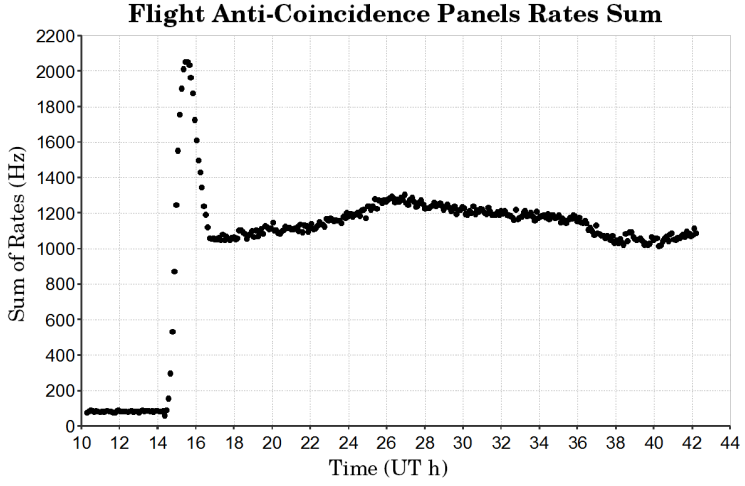

Figure 5.6: FACTEL Flight anti-coincidence panels rates sum. The rates spike at the Pfotzer maximum, then are correlated with the balloon altitude.

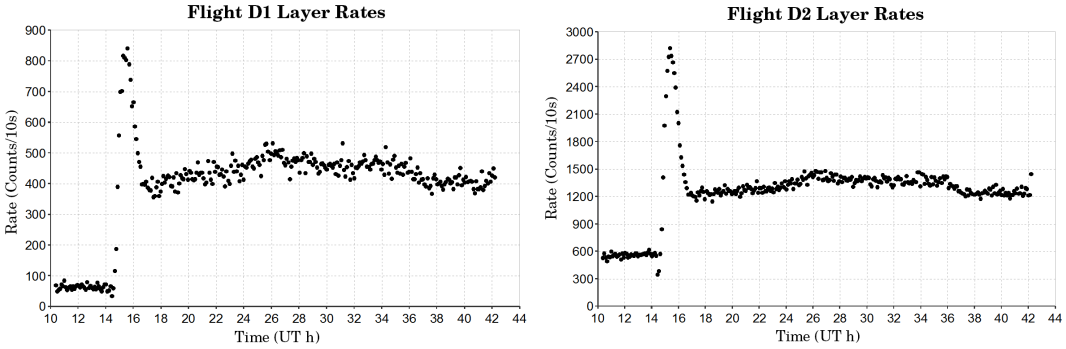

Figure 5.7: FACTEL Flight detector layers rates: D1 (left) and D2 (right). The rates spike at the Pfotzer maximum, then are correlated with the balloon altitude.

The spike around hour 15 is the Pfotzer maximum, the atmosphere layer during ascension where cosmic radiation produces a maximum of omnidirectional radiation. The rest of the plots show the rates are correlated with the balloon altitude. The 372.8 seconds per complete data acquisition cycle result comes from the D2 layer rates: the first one considered had a time stamp of 37917.360 s and the last one 247 values later had a time stamp of 43973.729 s the next day, leading to 248 full cycles lasting 372.8 s in average.

The rates in the D1 and D2 layer have a further importance because they are used to correct the dead time in the singles data: the D1 layer had 43.566 Hz average rate and the D2 layer a 130.646 Hz average rate.

5.5 D1 Singles Results

Although the balloon was launched around 8h20 (local), the instrument was powered and started acquiring data around 4h20, see fig. 5.6. This leads to 307 full data acquisition cycles and the D1 layer results files contained 77788 entries. The analyzed events ranged from 10h30 (time stamp > 37800 s) until the flight

termination. Removing the overflow events in the last bin (1023), 41785 events remained and their address plot is shown in figure 5.8.

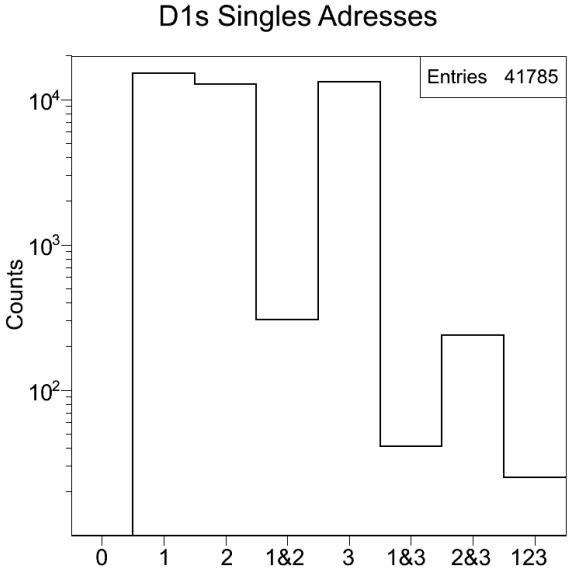

Figure 5.8: FACTEL flight D1 layer singles addresses, the plot is as expected, see text for details

The fig. 5.8 plot is as expected. The D11 and D13 detectors have the most events, the D12 detector recorded slightly less events because it is centered and thus more shielded from the environment. Multiple hits events by close detectors (D11 & D12, D12 & D13) follow in terms of counts, then with a lower probability the opposed detectors (D11 & D13). Finally, the events where all detectors of the layer were triggered have the lowest event count.

Keeping the events where only one detector is triggered, and converting the amplitude value (integer) to energy using eq. 3.13 and the parameters of table 3.4, the count vs. energy spectrum shown in figure 5.9 is produced. The total count is 41174.

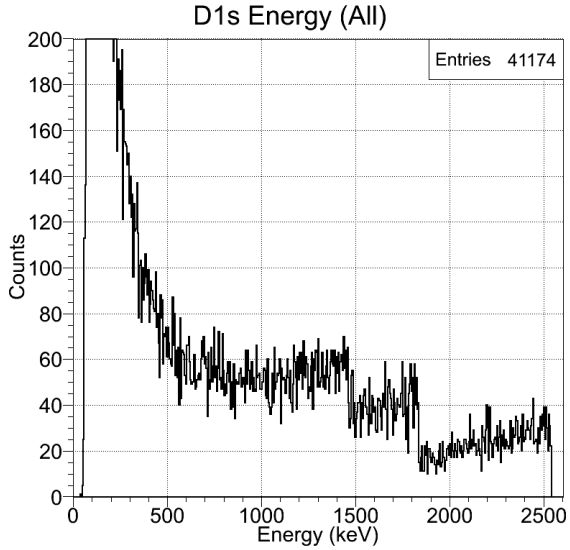

Figure 5.9: FACTEL flight D1 layer singles energy spectrum, the jumps arise from the different energy ranges of the three detectors.

The jumps around 1450 and 1850 keV arise from the different energy ranges of the three detectors, see eq. 3.14. (The end values in eq. 3.14 are computed for Ch1 = 975, the data shown in fig. 5.9 includes data up to Ch1 = 1022.)

To compare this result to the simulation results, a few steps were taken. First, the simulations did not have calibration endpoints for each detector (the total energy deposit in one detector can be arbitrarily small or large). However, the real detectors have an energy range, see eq. 3.14. To compare the two sets of data, the flight data were corrected by multiplying portions of the spectrum by appropriate factors. Under 1450 keV ($E_3(Ch_3=1022)=1465$ keV, see table 3.4), both simulations and flight had 3 detectors operating, the multiplying factor is then 1. Between 1450 and 1850 keV ($E_1(Ch_1=1022)=1837$ keV, see table 3.4), the simulations had 3 detectors operating while the flight only had 2 (D11 and D12), the flight data is then multiplied by a factor 3/2. Above 1850 keV, the simulations had 3 detectors operating while the flight only

had D12, the flight data is then multiplied by a factor 3. Secondly, the dead time correction: the rates shown in fig. 5.7 lead to a rate of 43.5661 Hz in the D1 layer, while the 41785 events recorded in 2480 s lead to a 16.8487 Hz recording rate, the singles data was thus multiplied by 2.5857. Finally, the events that had an anti-coincidence veto flag were removed and the y axis was converted from "Counts" to "Counts/(keV s)". The resulting spectrum is compared to the simulations results in figure 5.10.

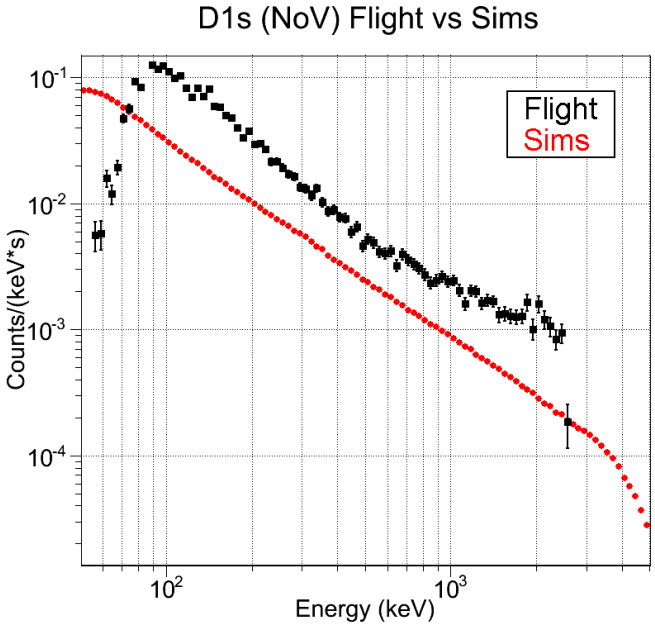

Figure 5.10: Comparison of FACTEL flight D1 layer singles to simulations, see text for comments

Figure 5.10 shows that the spectral indexes are comparable, but the flight data has a higher amplitude than the simulations results. Many factors could explain this discrepancy: the presence in reality of a signal not simulated, or inaccurate simulation amplitudes. However, it is our belief that the dead time correction was unnecessary for the D1 layer data. A comparison of the flight data without the dead time correction with the simulations is shown in figure 5.11.

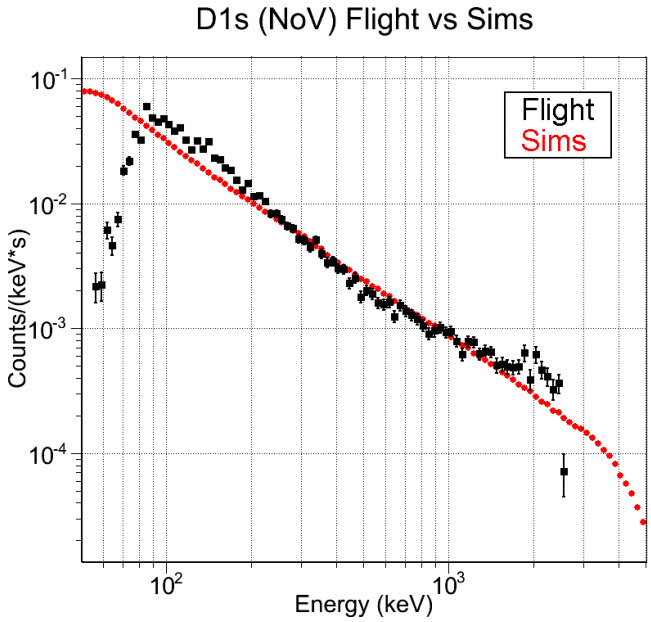

Figure 5.11: Comparison of FACTEL flight D1 layer singles without dead time correction to simulations, the agreement is excellent

The agreement between the flight data and the simulations shown in fig. 5.11 is more satisfactory. The difference factor between figures 5.10 and 5.11 being precisely the dead time correction factor gives credentials to the notion that the dead time correction was unnecessary for the D1 layer. It is our belief that the singles recording rate was correct while the rates from the rates routine, see the left part of fig. 5.7, were erroneous. Two factors can explain the error. First, the electronic noise issue experienced from the PC-104 computer was directly affecting the rates in the D1 layer. As previously stated, "the increased baseline noise caused the D1 sub-system to trigger continuously at a ~5 kHz rate while the normal background rate in the D1 layer is in the ~5 Hz range." The aluminum foil inside the D1 anti-coincidence box and the grounding alleviated the problem making the instrument viable, but no one can say how well the problem was resolved. The aluminum foil and grounding shielded the D1 layer from a noise source that still existed, but no one can say with certainty if the shielding protected the layer at 100% or at 99.5%. For a 5 kHz noise

rate, maybe a few tens of events still triggered the D1 layer per second. The recording rate of 16.8 Hz is then believed to be correct, while the 43.6 Hz rate from the rates routine is believed to be influenced by the noise issue. Also, the trigger threshold for the rate routine could have been lower than the recording routine threshold: the rates routine triggering on more electronic noise while the signal recording routine had a higher threshold.

In terms of evaluating the effectiveness of the four new background mitigation techniques implemented for the FACTEL prototype, the D1 singles results do not give us much information. The use of $LaBr_3$ scintillator D2 detectors is irrelevant here, while the limitation of passive materials can only be truly addressed with the ToF spectrum. We can however say, with the simulation results of figure 4.12, where all other signal sources are well below that of gamma rays, that the passive materials did not provide any significant background channels sources to non-gamma-ray particles.

Borating the top anti-coincidence panel and deuterating the D1 detectors material was done to prevent neutron capture and the emission of 2.2 MeV gamma rays by the instrument. The results of fig. 5.11 do not show any significant 2.2 MeV peak, nor do the neutrons simulation results shown in fig. 4.12. In fact, we have already discussed in section 3.3.5 that the FACTEL D1 detectors were too small to efficiently thermalize and capture neutrons (neutrons would frequently only interact once before escaping the detector), while any eventually produced 2.2 MeV gamma ray would most likely escape the detector before interacting. The only result supporting the presence of a 2.2 MeV line would be that of figure 5.9, where a few events stack precisely at 2.2 MeV to form what looks like a small peak, but this is inconsistent with the resolution of an organic liquid scintillator detector.

5.6 D2 Singles Results

The singles results analysis from the D2 layer follows the same method presented for the D1 layer. The complete data files had 71386 entries. Keeping the entries after 10h30 and with an amplitude Ch ≤ 975 leaves 54127 entries with an address plot shown in figure 5.12. The plot is very similar to the one from the D1 layer, see fig. 5.8, in this case the central detector D22 had more events than the border ones and there are more D21 & D23 double hits events.

Removing the multiple hits events and making an energy spectrum of the 53739 remaining events gives the spectrum shown in figure 5.13. Of note in this spectrum are the 511 keV peak, the self-background 1471 keV peak and the alpha continuum from 1700 to 2300 keV (see fig. 3.33). Fits of the peaks gives 503.8 keV for the 511 keV peak and 1475.0 keV for the 1471 keV peak, validating the calibration performed in section 3.3.2.2.

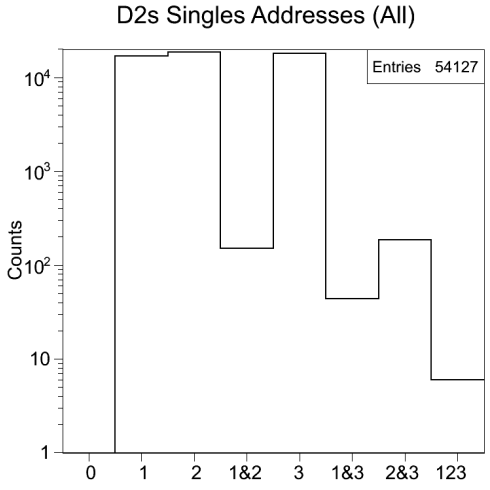

Figure 5.12: FACTEL flight D2 layer singles addresses, the plot is as expected, see text for details

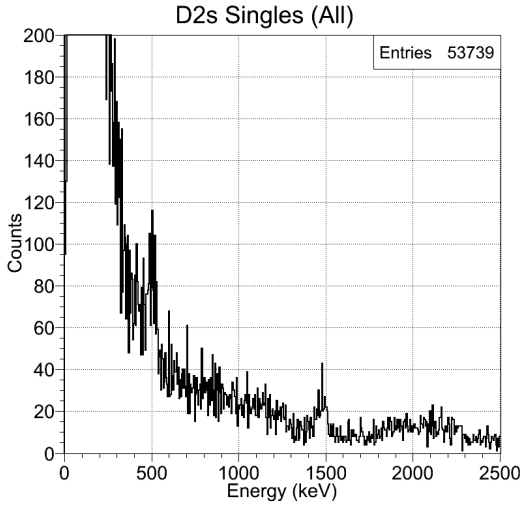

Figure 5.13: FACTEL flight D2 layer singles energy spectrum, of note are the 511 keV peak, the 1471 keV peak, and the alpha continuum

To compare the fig. 5.13 spectrum to simulations, the dead time correction must be applied. The 54127 events recorded in 2480 s leads to a 21.8254 Hz recording rate while the rates from fig. 5.7 leads to a real 130.646 Hz rate. In this case the dead time correction is relevant because the D2 layer triggering electronics were not affected by the electronic noise issue. The values from the fig. 5.13 spectrum were thus multiplied by a factor 5.986. The D2 layer events had no anti-coincidence veto flag because the detectors were outside the anti-coincidence box. The units of the y axis were also converted from "Counts" to "Counts/(keV s)." The resulting spectrum compared to the simulations results is shown in figure 5.14. The discrepancy seen in fig. 5.14 comes from the fact that the simulations did not include the self-background from $LaBr_3$, which needs to be added to the simulation data. The self-background data comes from the laboratory run R659, a spectrum from that run was shown in fig. 3.33, and is re-expressed in the units used in this analysis in figure 5.15.

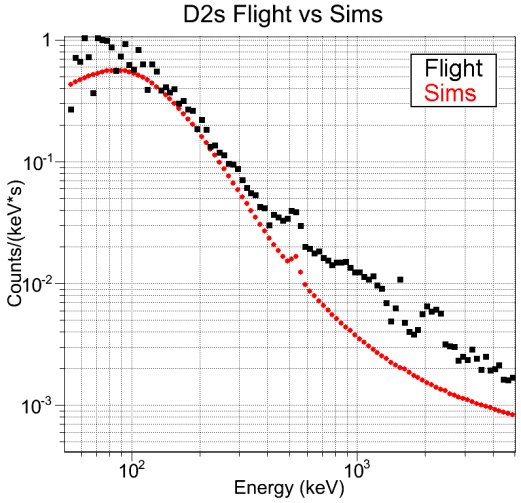

Figure 5.14: Comparison of FACTEL flight D2 layer singles to simulations without the $LaBr_3$ self-background

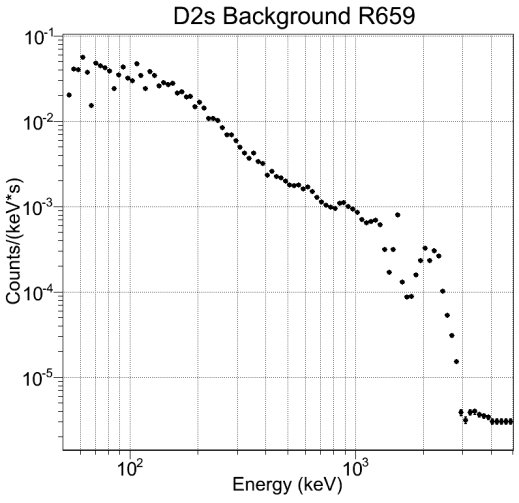

Figure 5.15: Figure 3.33 re-expressed with logarithmic axes

The self-background of $LaBr_3$ has to be added to the simulations results in an *ad hoc* fashion. For the laboratory run the PIC data was fed directly to the laboratory

PC running the Hyper-Terminal software that was recording the D2 layer continuously. In flight mode, the PIC data was fed to the PC-104 running the flight data acquisition routine. In flight mode the instrument would spend 10 seconds every 330 seconds recording singles events from the D2 layer, while R659 was a weekend run that lasted ~92 hours recording only D2 layer events (self-background and laboratory background). Thus, the flight data and laboratory data do not involve the same hardware (different PCs) or the same software. The criteria then used was to add the self-background spectrum to the simulations spectrum until the 1471 keV peak height would match the flight spectrum, which turned out to be a factor 12, resulting in the comparison shown in figure 5.16.

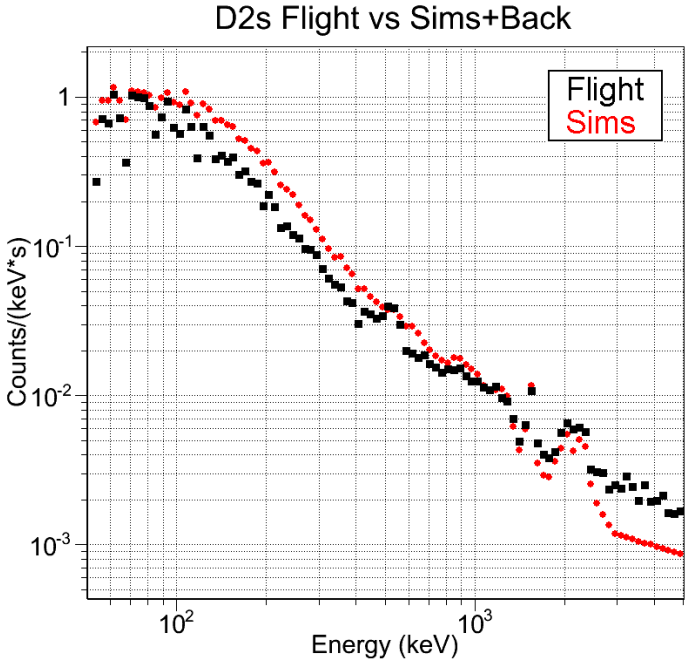

Figure 5.16: Comparison of FACTEL flight D2 layer singles to simulations with the $LaBr_3$ self-background added, the agreement is satisfactory.

Some features of fig. 5.16 can be highlighted. First, a few of the first flight points have lower values because of artifacts of logarithmic binning. The data acquisition electronics assign an integer value to signal amplitudes, meaning that

ultimately the computed energy values are discrete. Logarithmic bins under 70 keV can be narrow in a way that only one channel from one detector can fill the bin, leading to low points. The problem solves itself above 100 keV. Secondly, the simulations plus the self-background is consistently higher than the flight data between 100 keV and 500 keV, this comes from the fact that the self-background run (R659) was done at ground level and also recorded the laboratory background. One can get a sense of that low-energy extra background by comparing the spectrum from our laboratory run shown in fig. 3.33 to the self-background result from Saint-Gobain shown in fig. 3.6. Thirdly, the simulations curve is missing a clear 511 keV peak as a 511 keV dedicated simulation was not performed. Finally, the end of the flight data has a consistent excess of events, which could come from sources that were not simulated or inaccurate amplitudes.

In terms of evaluating the effectiveness of the four new background mitigation techniques implemented for the FACTEL prototype, the D2 singles results are even less useful than the D1 singles results. Borating the top anti-coincidence panel, deuterating the D1 detectors, and limiting the passive materials around the D1 layer are all issues more relevant for the D1 part of the instrument. Still, we can note that there is no significant 2.2 MeV line in the flight spectrum or the simulation results, implying no significant neutron capture in the upper parts of the instrument.

As for the use of $LaBr_3$ scintillator for the D2 detectors, we see from fig. 5.13 that the main features of the D2 singles spectrum comes from the $LaBr_3$ self-background. Then the simulation results, fig. 4.13 and 5.14, along the self-background spectrum, fig. 5.15, all show in figure 5.16 that the D2 singles spectrum is a combination of the signals from the environment radiation and from the self-background. Figure 5.14 show that the self-background is an important contributor to

the D2 events, thus that it could become problematic for the overall telescope if the telescope was not able to reject those events through the ToF measurement.

Otherwise, the data provided in section 3.2.2 shows that $LaBr_3$ detectors performance is superior in all aspects to previously used NaI detectors. Finally, the fact that the 511 keV peak was measured at 503.8 keV (Δ=7.2 keV, 1.4%) and the 1471 keV peak was measured at 1475.0 keV (Δ=4.0 keV, 0.3%) from the fig. 5.13 spectrum show that an accurate calibration of multiple $LaBr_3$ detectors over a good energy range can be achieved.

5.7 Flight Coincidence and ToF results

The telescope coincidence mode results hold the Time of Flight result validating the FACTEL project. The flight coincidence files contained 24166 entries in total, of which 22115 entries were within the flight afloat time period, the addresses plot of these events is shown in figure 5.17.

The plot of fig. 5.17 is conventional, see fig. 3.55, each detector pair recording about 2000 events. 19478 (88%) of those events had an anticoincidence veto flag and were removed leaving 2637 events. Then 176 events in the 2637 remaining events have multiple detectors triggered in one detector layer (addresses 3, 5, 6 and 7) and were removed. The address plot of the remaining 2461 events from detectors pairs is shown in figure 5.18.

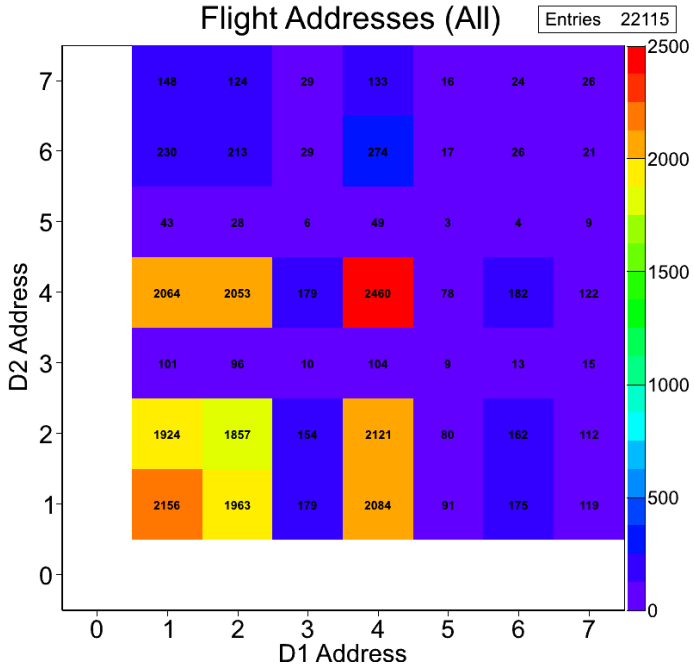

Figure 5.17: FACTEL Flight Addresses plot of all coincidence events

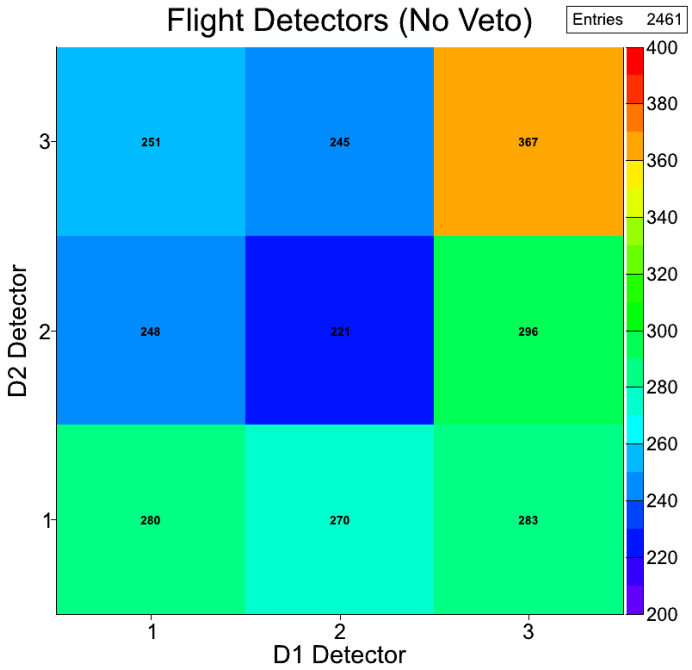

Figure 5.18: FACTEL Flight Addresses Plot of the "good" events

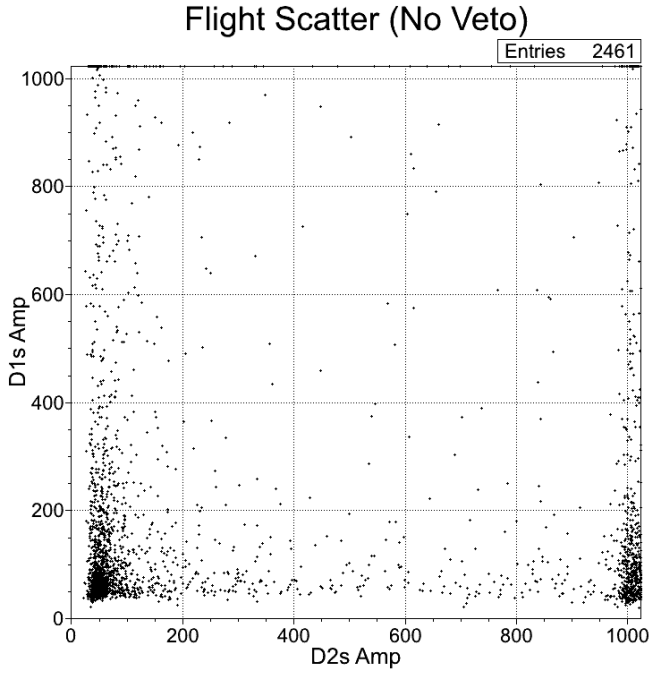

Figure 5.19: Scatter Plot of the "good" events from the FACTEL flight, most are low-energy events, and overflow events can be seen at the borders

A scatter plot of these 2461 events is shown in figure 5.19. Note that fig. 5.19 is not an energy plot but a plot of the amplitudes in channel numbers (0 to 1023). The events at D1 Ch1=1023 are overflow events and have to be rejected, so only the events with a D1 Ch1≤1000 were retained. The same logic applies to the D2 channel axis and only the events under Ch2≤975 were retained: the events above Ch2=975 are overflow events. This is also the region where the D2 detectors calibration curves are flattening and becoming unreliable. This leaves most of the events in the under (100, 100) region. The difficulty here is not the energy calibration curves, see figures 3.34 and 3.41, which are sufficiently reliable under Ch 100, but the ToF delay correction curves, see fig. 3.68. This is a region where the delay correction is significant for both detectors: over 40 channels for the D1 detectors and about 20 channels for the D2 detectors. The delay correction curves are diverging in that region and there are no data under Ch 40. The low-energy region is also subject to random background. The lower channel cut for both layers was then chosen arbitrarily to be channel 75. The

region kept for Time of Flight analysis was thus from channel 75 to 1000 for the D1 detector layer and from channel 75 to 975 for the D2 detector layer; this procedure left 406 events to analyze.

The uncorrected raw ToF spectrum of these 406 events is shown in figure 5.20. The corrected ToF spectrum of the selected coincident events from the FACTEL balloon flight is shown in figure 5.21, yielding the desired result.

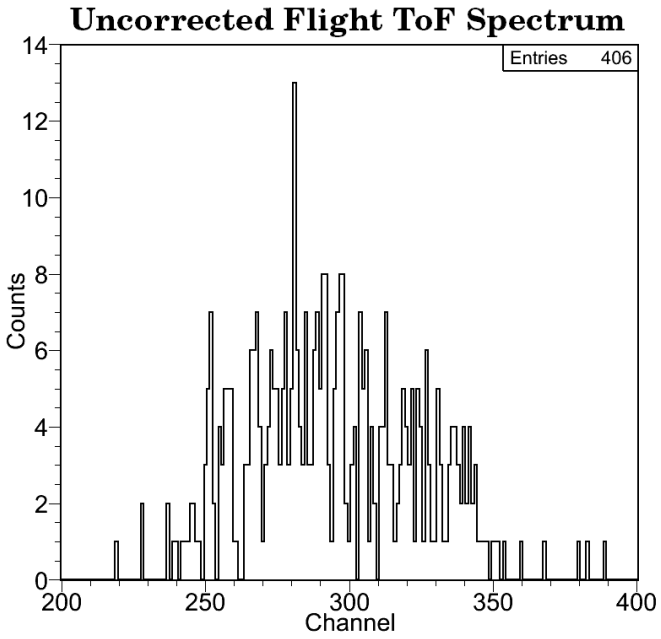

Figure 5.20: Uncorrected ToF spectrum of the selected coincident events from FACTEL balloon flight

The figure 5.21 result is unprecedented and should be compared to fig. 2.16 from COMPTEL to appreciate the FACTEL improvement. The fact that the ToF spectrum is fitted with only two Gaussians shows that the other background sources were effectively mitigated to only have the forward and backward peaks left. The two Gaussians sigmas were forced to be the same for both peaks, which led to a final ToF resolution of 1.3 ns. Considering all the difficulties that have arisen during the FACTEL project construction, a ToF resolution slightly above 1 ns is considered a

success. Figure 5.21 shows we have successfully built a small Compton telescope prototype with a ToF resolution in the 1 ns range.

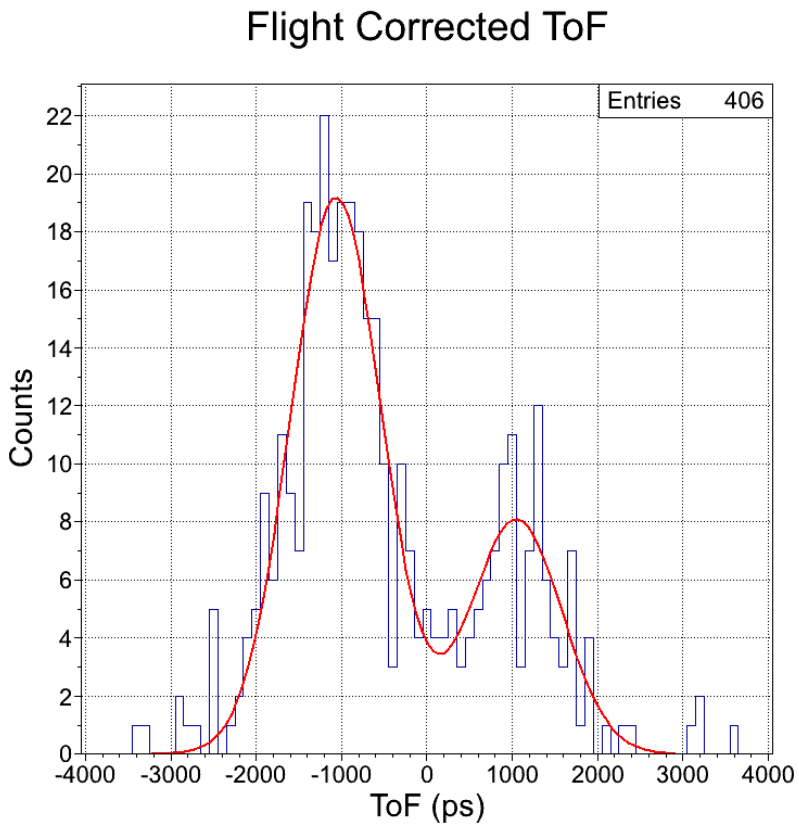

Figure 5.21: Corrected ToF spectrum of the selected coincident events from FACTEL balloon flight, the spectrum is described by two Gaussians of 1.3 ns resolution.

A few analysis steps between the uncorrected ToF spectrum of fig. 5.20 and the corrected spectrum of fig. 5.21 have to be detailed. The correction with the delay curves did lead to the two peaks shown in fig. 5.21 as they are displayed. However, this correction is still in channel space and has to be translated to time space.

The first correction was to set the zero of the ToF axis. It turns out that for some undetermined reason the zero of the axis was drifting with time. The laboratory run used to create the delay correction curves was the laboratory run R668, a $ToF=0$ run with a ^{60}Co source placed at the center of the instrument. This run was also used

to define ***ToF*=0** in channel space for each detector pair, see figures 3.69 and 3.70. (There is also a small correction to account for the different pair separation distances to have all pairs on the same scale.) The corrections extracted from R668 have been successful in correcting the ToF values for all runs performed during the same time period. Laboratory run R668 was conducted five months after the flight and lasted 7 days. Then, the laboratory run R642, another ***ToF*=0** run with a ^{60}Co source placed at the center of the instrument, was also available. R642 was performed 2 weeks before the balloon flight, but lasted 5 hours and was insufficient to generate the delay correction curves. Applying the correction script extracted from R668 to R642 did correct the raw ToF spectrum, yielding a Gaussian ToF peak, however the peak center was not at Ch = 0, but at Ch = -21.3242, as shown in figure 5.22.

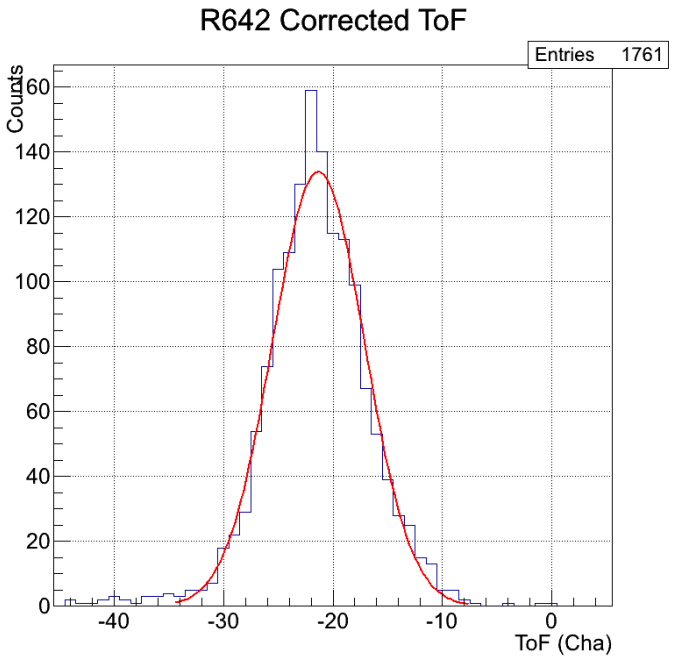

Figure 5.22: Laboratory run R642 Corrected ToF spectrum, the center of the Gaussian should have been at 0 and not -21.3

For the flight data, the initial channel value for the point between the two means of the Gaussians of fig. 5.21 was Ch = -17.2348. This is consistent with the

zero of the ToF axis drifting monotonically with time: -21.3 two weeks before the flight, -17.2 during the flight, and 0 five months later. The cause of the ToF drift is unknown. The ToF drift being revealed and documented, and the point between the backward and forward peaks needing to be zero, the correction provided by the script from laboratory run R668 was further corrected by adding a +17.2384 channel value to the first correction.

The second correction step was to pass from channel space to time space, which was done using the 63.691 ps/ch value previously calibrated, see fig. 3.71. This value has been successfully used previously and both our project engineer and electronics engineer were confident that this calibration should not have changed. However, applying the 63.691 ps/ch conversion factor led the peaks to be misplaced in time space. The distance between the two detector layers is known to be 31.75 cm on center, thus that the time separation between the two peaks is 2.118 ns. The channel separation between the two centers of the Gaussians was 22.786 channels, then the conversion factor to properly place the peaks at their right time is 92.95 ps/ch.

These two further corrections might appear arbitrary, however the first "standard" ToF correction procedure did produce the spectrum shown in fig. 5.21, albeit expressed in channels and around channel -15 on the axis. The spectrum had the exact characteristics of a Compton telescope ToF spectrum, see fig. 2.16. The ToF correction procedure worked properly and the resulting spectrum was as expected but misplaced. Then, the ToF axis zero drift was clearly exposed by comparing laboratory runs R668 and R642, and the needed correction consistent with the comparison. The point between the two Gaussians has to be $ToF=0$. Then the conversion factor is an "end product" conversion, all the analysis is performed in terms of channels and the results converted to physical units (keV, ps) at the end. The spectrum shown in fig.

5.21 in channel space was reliable, and the only thing needed was a translation factor. The time separation between the two peaks has to be 2.118 ns because the detector layers are separated by 31.75 cm, then the new conversion factor was necessary. This particular problem will be further discussed. We believe the two further corrections justified, and the fig. 5.21 spectrum correct.

The next step of the analysis is to analyze the 121 events in the forward peak ($ToF \geq 0$, the D1→D2 events). Figure 5.23 shows the computed theta of these events using eq. 2.17, it is consistent with the uniform background the instrument was exposed to.

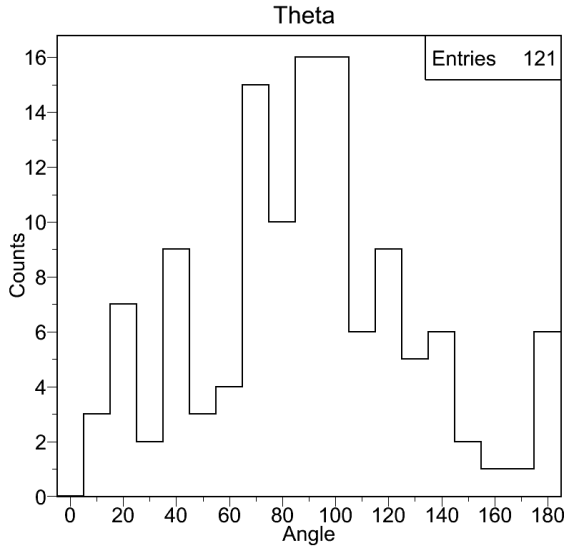

Figure 5.23: Theta spectrum of the forward events, it is consistent with a uniform background

The final step of the analysis is to compare the energy spectrum of these events to the simulated energy spectrum, this is shown in figure 5.24.

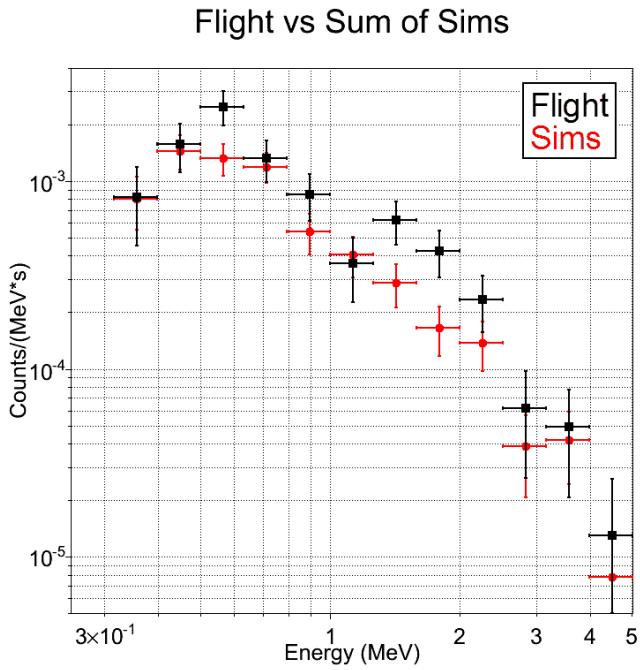

Figure 5.24: Comparison of FACTEL flight energy spectrum of the forward events to simulations, the agreement is very acceptable.

The units of the y axis were converted from "Counts" to "Counts/(MeV s)" and no dead time correction was required in the coincidence mode. The agreement between the FACTEL flight data and the simulations is satisfactory considering only 121 events were available. The flight data is usually higher than the simulations, showing the presence of unsimulated sources, for example the third bin contains the unsimulated 511 keV line, as already shown in fig. 5.16, or inaccurate simulations amplitudes.

In terms of evaluating the effectiveness of the four new background mitigation techniques implemented for the FACTEL prototype, the 121 events of the flight spectrum cannot tell us much more than validating the simulations. The data from fig. 5.24 cannot be used to assess the effectiveness of borating the top anti-coincidence panel, deuterating the D1 detectors, limiting the passive materials around the D1 layer, or using $LaBr_3$ scintillator D2 detectors. The only thing we can say by

comparing fig. 5.24 and 4.14 is that the vast majority of the 121 downward events recorded during the flight come from gamma-ray interactions, which in turn tells us that the sources of background events from other particle types have been successfully mitigated.

The main result of the FACTEL project is the ToF spectrum presented in figure 5.21, and it is to be compared to its COMPTEL equivalent shown in figure 2.16. In terms of evaluating the effectiveness of the four new background mitigation techniques implemented for the FACTEL prototype, the ToF result can be used to assess all of them. The fact that the flight data can be modeled by only two Gaussians, see fig. 5.21, and without a third component, the B, C* and D events of fig. 2.16, does imply that those sources of background events have been successfully mitigated using the three first techniques (Borating the top anti-coincidence panel, deuterating the D1 detectors, and limiting passive materials and metals around the D1 layer).

The advantage of using $LaBr_3$ scintillator D2 detectors is clearly demonstrated by comparing the FWHM of the peaks of fig. 5.21 compared to the peaks of fig. 2.16. COMTPEL had a ToF resolution (FWHM) of 4 ns while FACTEL shows a ToF resolution of about 1 ns, implying a direct improvement of the background rejection capabilities of the instrument, see fig. 3.2, leading to an improved signal to noise ratio, finally achieving an improved sensitivity.

A 31.75 cm distance separation between the two detector layers led to the fig. 5.21 spectrum, where the forward and backward peaks are already well separated. One can clearly understand that a Compton telescope using $LaBr_3$ D2 detectors with a distance separation of 60 cm, or even 50 cm, between the two detector layers would completely separate the two ToF peaks, leading to a forward peak comprising of only the celestial events, type A background events, and the remaining C_1 events.

The final point to discuss is the actual ToF resolution of the FACTEL instrument. One could point out the discrepancy between the ToF resolution of 875 ps (with the 92.95 ps/ch conversion factor) shown in fig. 3.70 and the ToF resolution of 1.3 ns shown in fig. 5.21. This discrepancy is a consequence of the delay correction curves shown in fig. 3.68. The >500 k events shown in fig. 3.70 from the ^{60}Co $ToF=0$ laboratory run 668 are all above channel 100 in both detectors, while most of the 406 events from the flight shown in fig. 5.21 are under channel 100 in both detectors, as seen in fig. 5.19. Most of the flight events fall in the divergent portion of the correction curves, implying large corrections for both D1 and D2 detectors, and are less than 2 MeV of total energy, see fig. 5.24. All the events in fig. 3.70 imply one 1173 keV and one 1333 keV gamma rays, totaling for 2.5 MeV, and fall into regions of the correction curves where we are confident in. In fact, most the flight events fall into the D2 region where the "backscatter bump correction" was applied, see fig. 3.67. With a conversion factor between 50 and 100 ps/ch, an error of 3 channels on the D2 correction is enough to account for the discrepancy between the two ToF resolutions. This only shows again how critical are the correction curves.

This fact can also cast doubt on the 92.95 ps/ch channel-to-time conversion value. This value was derived from the fact that the forward and backward peaks of the flight ToF spectrum must be separated by 2.118 ns. However, the corrected spectrum in channel space has made use of the correction curves, for which an error of a few channels imply hundreds of picoseconds of error. Perhaps the 63.69 ps/ch is the correct value all along, and the misplacement of the peaks in time space due to a systematic error of a few channels in the correction curves, which is a real possibility. For example, looking at fig. 3.68, we note the zeros of the curves were chosen arbitrarily, and an error of a few channels a distinct possibility there. The backscatter bump in the D2 correction curves was corrected arbitrarily, see fig. 3.67, another error

of a few channels could lead to hundreds of picoseconds in time space. In effect, the correction curves are precise enough to convert the uncorrected fig. 5.20 spectrum into the 5.21 spectrum, but perhaps not accurate enough to accurately place the peaks in time space. The 92.95 ps/ch value comes from the peaks being physically separated by 2.118 ns and a 22.786 channels separation in the corrected spectrum. With the 63.69 ps/ch value, the initial peaks separation was 1.451 ps, implying a 333 ps misplacement per peak, implying a 5.2 channels per peak mis-correction. This is a real possibility considering the scope of the corrections (tens of channels for each detector) and the accuracy of the curves. Then the peaks should have been separated by 33.25 channels instead of 22.79, and the 63.69 ps/ch value would have correctly placed the peaks in time space. To conclude the argument, the delay correction curves are critical, they were precise enough to lead to the fig. 5.21 spectrum, but perhaps imprecise enough to misplace the peaks. Then the 92.95 ps/ch value becomes more an *ad hoc* valid further correction to a faulty delay correction rather than a proper new conversion factor.

If the 63.69 ps/ch is correct, then the ~13 channels width of the ToF peaks of fig. 5.21 would rather lead to an 830 ps ToF resolution instead of the 1.3 ns ToF resolution we reported.

To conclude this discussion about the actual ToF resolution of the FACTEL instrument, the fairest statement would be that it is 1.0±0.2 ns, as in 800 ps in the best case and 1.2 ns at worst. The broad goal of the project was to achieve a Time of Flight resolution in the 500 ps range. The best result we ever attained was 450 ps, see fig. 3.61. That test used only two detectors, NIM laboratory electronics, and precise energies deposits were selected in both detectors. The best result obtained with the final instrument was 600 ps, see fig. 3.70 (with the 63.69 ps/ch conversion factor). This result is good compared to the flight results because it involved higher energy

gamma rays. For lower energy interactions, such as the flight results, assuming the delay correction curves are imprecise and the 63.69 ps/ch conversion factor is correct, then the Time of Flight resolution is of the order of 800 ps. What degrades the final resolution compared to the best case scenario are the facts that 6 detectors forming 9 pairs are used, low-power (more noisy) electronic boards are used, the final instrument experienced a digital noise issue, see fig. 3.62, and the final instrument uses delay correction curves in order to measure the complete energy range. The delay correction curves, see fig. 3.68, have their zero chosen arbitrarily, diverge at lower energies, and the D2 detectors delay correction curves need a further backscatter peak correction, see fig. 3.67.

{NOTE. When the FACTEL instrument was dismantled, over a year after the flight, a delay cable was found to have been mislabeled. (The author was not present at that time.) A cable labeled with a delay time of 65 ps had an actual value closer to 95 ps, precisely the values debated here (63.69 ps/ch and 92.95 ps/ch). Somehow, when the final instrument was assembled a cable would have been changed, inducing the new factor that had to be used for the analysis. A quick time/dimension analysis reveals more about this potential issue: 65 ps at the speed of light is about 2 cm (1.95 cm), and 95 ps about 3 cm (2.85 cm). Then, a cable length difference of 0.9 cm induces a 30 ps signal propagation difference (at the speed of light). The author's opinion could be summarized as "perhaps". It is an intriguing issue. Perhaps if some delay cable was changed to one 1 cm longer in the ToF circuit a new 30 ps delay could be added and the 63.69 ps/ch value pass to 92.95 ps/ch. On the other hand, the correction curves shown in fig. 3.68 have their limits: the curves are "as precise as they could be". It is evident that errors of a few channels are present, for example the zero of the D12 curve is clearly not the one that has been chosen (the curve goes lower). Data were not available, so even wrong, the chosen zero was the best choice

when following a clear procedure. Whether the 92.95 ps/ch factor comes from inaccurate delay correction curves or from a delay cable change, it seems the 63.69 ps/ch value has its window of application (the fig. 3.71 calibration was correct), and the 92.95 ps/ch a necessary change to correctly place the peaks in fig. 5.21. Which factor to apply in which circumstance seems arbitrary considering how well the issue is understood. Without further clear understanding, both factors should be considered somewhat equally valid, this is why both possibilities are usually mentioned in this work. The next paragraph will explain why this discussion this is not critically important.}

In the end, whether the Time of Flight resolution is closer to 800 ps or 1.3 ns does not matter critically. What does matter is the fig. 5.21 result: the ToF forward and backward peaks are well separated for 31.75 cm between the detector layers, and only two Gaussians adequately describe the results. This result is impressive and shows that the FACTEL project is a success.

5.8 Two further tests on the Flight ToF result

Two further tests can be conducted with the fig. 5.21 flight ToF result.

The first test is to compute how many events from the backscatter peak are within the forward peak one sigma window. The two Gaussians fit function used to analyze the flight ToF data is given by eq. 5.1:

$$\mathbf{F}(x) = \mathbf{A}\, e^{-\frac{1}{2}\left(\frac{x-\mathbf{B}}{\mathbf{C}}\right)^2} + \mathbf{D}\, e^{-\frac{1}{2}\left(\frac{x-\mathbf{E}}{\mathbf{C}}\right)^2}, \qquad (5.1)$$

where $\mathbf{F}$ [Counts], x [ps], $\mathbf{A}$=19.1012 [Counts], $\mathbf{B}$=-1064.73 [ps], $\mathbf{C}$=540.175 [ps], $\mathbf{D}$=8.08331 [Counts], and $\mathbf{E}$=1063.46 [ps]. Note that both sigmas are chosen to

be the same value **C**. The function of eq. 5.1 with these parameters values lead to the fit shown in fig. 5.21. Figure 5.25 shows this fit with its components and the one sigma window of the forward peak:

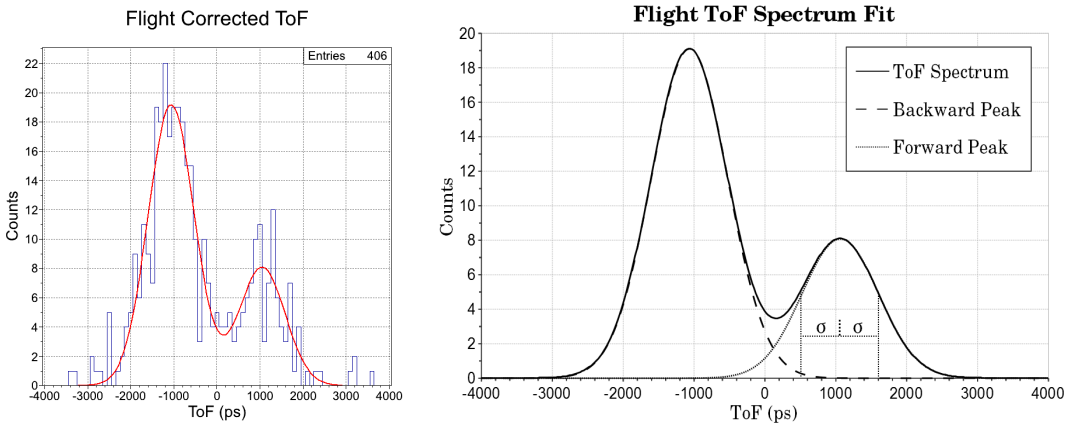

Figure 5.25: Figure 5.21 (Left), the fit components and the one sigma window of the forward peak (Right).

Integrating both Gaussians over the one sigma ToF window of the forward peak leads to 99.43% of the events coming from the forward peak and 0.57% of the events coming from the backward peak. This implies the forward peak one sigma window is almost devoid of events from the backward peak.

The second test is to actually force a third Gaussian component to the fit, in the spirit of fig. 2.16, and try to quantify a third component (the material B, C* and D background events). The first attempt was to add the third Gaussian to the fit function (eq. 5.1), relax the parameters already found, and let the fitting routine quantify the third Gaussian. This leads to the result shown in fig. 5.26:

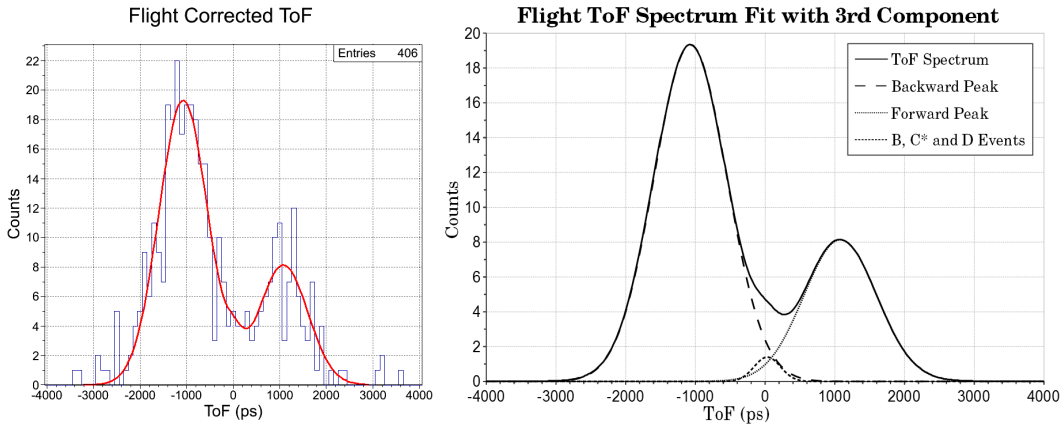

Figure 5.26: Fit of the flight ToF data with a 3 Gaussians function (Left), the fit components (Right)

The data are well expressed by only two Gaussians and the small third component imply the vast majority of the B, C* and D background events have been successfully mitigated, see fig. 2.16. A second attempt to add a third Gaussian component to the fig. 5.21 fit is to seed the fitting routine with three Gaussians starting with equal amplitudes and widths, with a large window of possible values to allow the third component to find its share, centered on zero and the two peaks. The fitting routine then finds a local minimum in the parameter space shown in fig. 5.27:

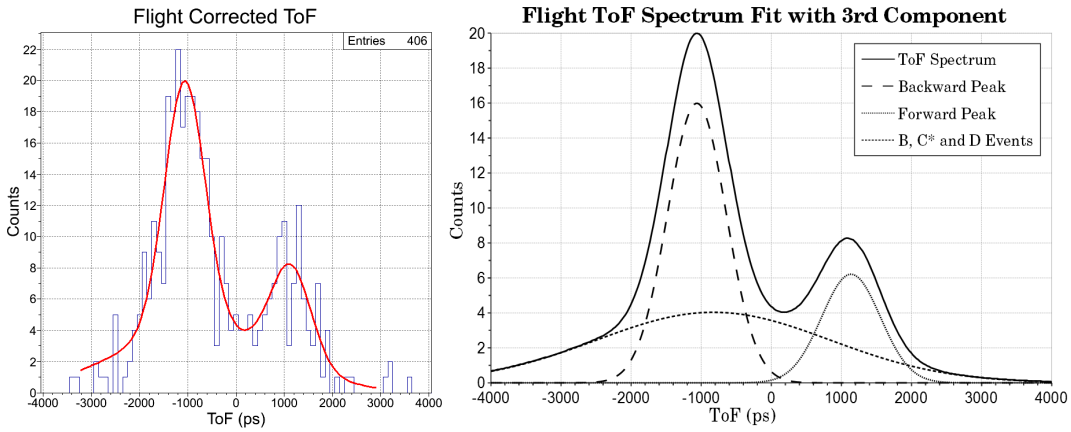

Figure 5.27: Fit of the flight ToF data with a 3 Gaussians function (Left), the fit components (Right)

This result closely resembles the COMPTEL ToF spectrum shown in fig. 2.16, shown side by side in fig. 5.28:

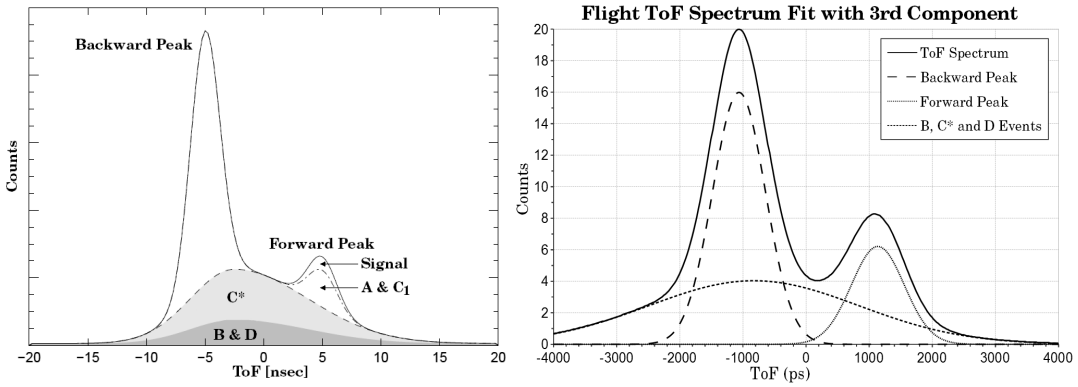

Figure 5.28: COMPTEL ToF Distribution from fig. 2.16 (Left), 3 Gaussians fit of the FACTEL flight ToF data from fig. 5.27 (Right)

The fig. 5.21 result is compelling; however the fig. 5.27 result cannot be immediately discarded because it closely resembles the fig. 2.16 COMPTEL distribution. The three Gaussians fit function with two sigmas linked is given by eq. 5.2:

$$\mathrm{F}(x) = \mathrm{A}\, e^{-\frac{1}{2}\left(\frac{x-\mathrm{B}}{\mathrm{C}}\right)^2} + \mathrm{D}\, e^{-\frac{1}{2}\left(\frac{x-\mathrm{E}}{\mathrm{C}}\right)^2} + \mathrm{G}\, e^{-\frac{1}{2}\left(\frac{x-\mathrm{H}}{\mathrm{I}}\right)^2}, \qquad (5.2)$$

where F [Counts], x [ps], A=15.9886 [Counts], B=-1062.45 [ps], C=418.982 [ps], D=6.21114 [Counts], E=1136.66 [ps], G=4.03531 [Counts], H=-827.334 [ps], and I=1666.34 [ps].

This very preliminary result suggests that the material background mitigation was not as successful as thought. A ToF spectrum from a previous instrument at balloon altitude is shown in fig. 5.29 [83, Figure 5, p.22], a third component is evident.

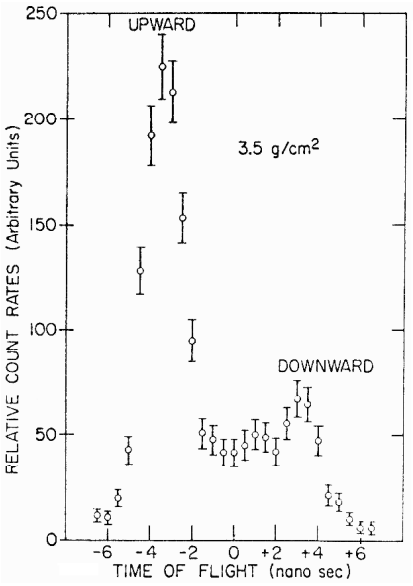

Figure 5.29: ToF spectrum from a previous Compton telescope [83] at balloon altitude, a third component between the upward and downward peak is evident.

Without considerable further study, we leave these results to stand on their own and interpret our data in the context of the good-fitting two Gaussians. To conclude this section, although the two Gaussians fit result of fig. 5.21 seems the most appropriate, the three Gaussians fit deserves further study.

5.9 Summary

This chapter presented the FACTEL flight results. The basic environmental data presented in section 5.2 showed that the flight was a success in terms of the flight itself (path and altitude) and instrument operating conditions (temperature and pressure within the dome). We presented the sum of the rates within the anti-coincidence panels and for each detector layer, showing that after the Pfotzer maximum during the ascension, the rates followed the altitude of the balloon. We presented the singles energy spectra results for the D1 and D2 detector layers,

showing good agreement with simulations. We presented the energy spectrum of a selection of the coincident events, again showing good agreement with simulations. The Time of Flight spectrum of a selection of the coincident events was presented, displaying the ToF spectrum of an improved Compton telescope with a ToF resolution of ~1 ns.

The goal of the FACTEL project and the flight was to evaluate new background mitigation techniques developed to improve the sensitivity of Compton telescopes. The four new techniques implemented with the FACTEL prototype are:

- Borating the top anti-coincidence panel
- Deuterating the D1 detectors liquid scintillator material
- Limiting passive materials, particularly metals, in the D1 layer region
- Use $LaBr_3$ scintillator D2 detectors

The flight results showed the four new background mitigation techniques implemented for the FACTEL instrument prototype were successful. Borating the top anti-coincidence panel was mainly validated by "not measuring" neutron capture at all. The second technique of deuterating the D1 material was mainly validated through the simulations results shown in section 3.3.6. The simulations showed that neutron capture was not an issue for small detectors, and showed deuteration mitigated neutron capture problem for larger detectors (figures 3.74 and 3.75). We also showed experimentally that Pulse-Shape Discrimination is preserved from deuteration (fig. 3.72). The third technique of limiting passive materials, particularly metals, in the D1 layer region can be considered successful through the figures 5.21, 5.25 and 5.26 results. The use of $LaBr_3$ scintillator D2 detectors was validated by the ToF spectrum fit result of figures 5.21 and 5.27 displaying a ToF resolution in the 1 ns range, clearly separating the upwards and downwards peaks for a ~30 cm detector

layer separation. This in turn proves the superior sensitivity a next generation instrument using $LaBr_3$ D2 detectors would possess.

The goals we wanted to achieve by building the FACTEL prototype was to reduce background generation in the instrument through the first three material techniques, and achieve a telescope ToF resolution in the nanosecond range using $LaBr_3$ for the D2 detectors, with an aim for 500 ps. The three first techniques have been evaluated as successful through the flight results, laboratory tests and simulations. The best ToF resolution we achieved was 450 ps (fig. 3.61) in ideal conditions; in normal conditions or for the test flight (figures 5.25 and 5.21), the ~1 ns ToF resolution is a fair assessment of FACTEL capability. In the end, we greatly improved the Time of Flight resolution of Compton telescopes, allowing us to build smaller and less massive instruments with much improved background suppression capabilities. Time of Flight resolution is the key to background rejection, which is the key to sensitivity. The FACTEL results have shown that we improved COMPTEL 4-ns ToF resolution to a ~1 ns ToF resolution, making FACTEL a success.

CHAPTER 6

The future ASCOT and the larger picture

6.1 Introduction

This last chapter presents a discussion about the larger gamma-ray astronomy picture and how a fast Compton telescope would contribute to the field. We showed in the previous chapter that a fast Compton telescope was a reality and how a ~1 ns ToF resolution improved the sensitivity by filtering more background events than earlier instruments. The FACTEL instrument is a small prototype meant to demonstrate that a Compton telescope with a 1-ns ToF was possible, this chapter focuses on what comes next. The first part of the chapter is a preliminary inquiry on a larger instrument called the "Advanced Scintillator COmpton Telescope" (ASCOT) based on the FACTEL prototype. It will show ASCOT to be a much more efficient version of FACTEL. ASCOT is a design that accommodates the new techniques developed with FACTEL and will be shown to produce results comparable to COMPTEL. The second part will be a broader discussion on the state of the medium energy gamma-ray astronomy field, how a fast Compton telescope fits in, and how it compares to other instrument concepts. We will discuss about why an ASCOT instrument would be the best next generation instrument to address the observational needs of the field.

6.2 ASCOT concept and Comments

Ground laying work on a future instrument called the "Advanced Scintillator COmpton Telescope" (ASCOT) was performed with a few basic simulations based on the FACTEL prototype work. The goal was to outline what instrument could be proposed within a ~80-cm cube, following NASA's SMEX guideline. For comparison, the dimensions of the "Large Area Telescope" (LAT) of the Fermi Gamma-ray Space Telescope are 1.8×1.8×0.72 m [67], the Chandra X-ray observatory has a 1.2 m diameter and a 10 m focal length, and COMPTEL was 2.6 m tall with a 1.7 m diameter.

The concept for the ASCOT instrument has two 25×25 detectors layers separated by 60 cm (center to center) with a 3-cm pitch between the detectors. This gives 625 detectors per layer and 1250 detectors in total. The detectors are cylinders ~1 inch (2.5 cm) in diameter and ~2 inches (5 cm) long. The modeled PMTs are based on Hamamatsu R1924a PMTs which are 1 inch (2.54 cm) in diameter for a 4.3 cm length. The two layers are enclosed in an anti-coincidence box, and an aluminum dome contains the instrument. A general picture of the ASCOT mass model is shown in figure 6.1.

The 80-cm box requirement from the SMEX program was the basis of this layout. The anti-coincidence panels are 80×80×0.65 cm, each detectors layer is 74.54 cm wide with 25 one inch (2.54 cm) detectors separated by 3 cm center to center. The distance between a D1 detector center to its corresponding D2 detector center is 60 cm, and the distance from the top end of a D1 detector PMT to the lower end of a D2 detector PMT is 73.68 cm. Other pictures of the mass model are shown in figure 6.2.

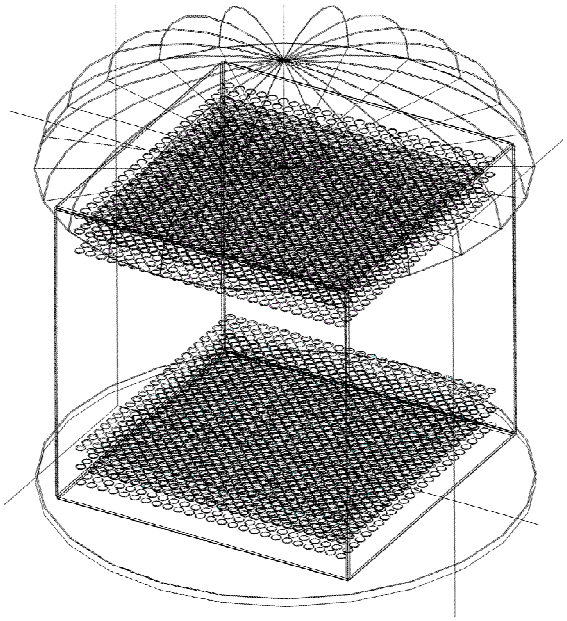

Figure 6.1: ASCOT Mass Model, the two layers of 625 detectors are separated by 60 cm

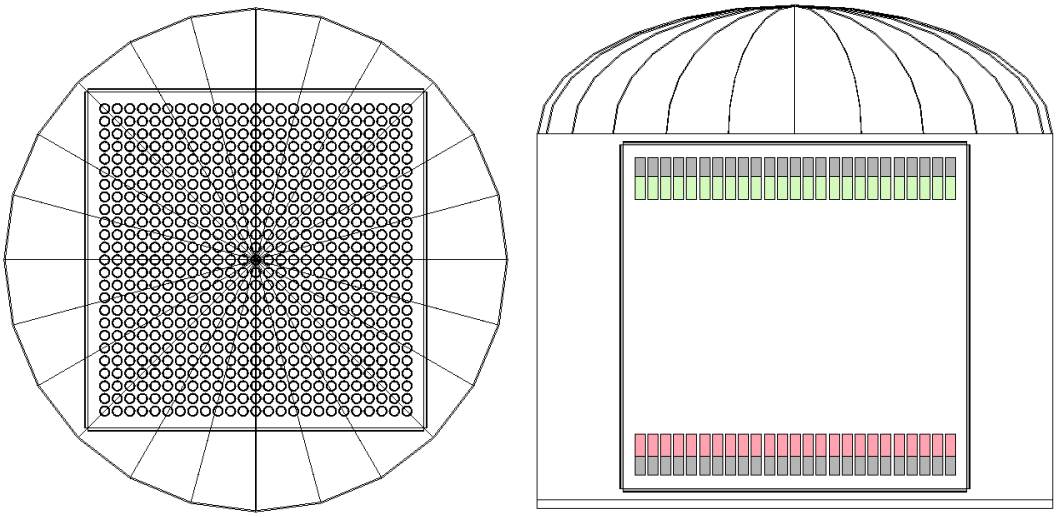

Figure 6.2: Views of the ASCOT mass model: Top view (left) and Side view (right). The D1 detectors are in green and the D2 detectors in red.

To contain the anti-coincidence box, the aluminum dome has a 1.2 m diameter and is 1.17 m from its bottom to its top, the base is 2 cm thick while the dome is 3 mm thick. The detectors materials are the same as FACTEL: the D1 detectors are

composed of EJ-315 deuterated liquid scintillator and the D2 detectors are composed of $LaBr_3$.

A first comment on this ASCOT concept is that the 60 cm between the detector layers leads to 4 ns between the downwards ToF peak and the upwards ToF peak. Considering the results from the FACTEL prototype, see fig. 5.21, the peaks would clearly be separated with almost no events in a 2 ns window. This in turn relaxes the ToF requirement for ASCOT. The FACTEL prototype had its difficulties (the digital noise issue, a signal treatment method needing correction curves) and better results are certainly achievable through a second cycle of engineering development. Yet, the FACTEL prototype achieved a 600 to 800 ps ToF resolution at higher energies (see fig. 3.70) and a 800 ps to 1.3 ns ToF resolution at lower energies (see fig. 5.21). If the 0.8 to 1.3 ns ToF resolution can be improved to 0.5 to 0.8 ns, which is not unreasonable, then a 4 ns distance between the ToF peaks puts ASCOT in an advantageous situation. Either the detectors layers could be placed closer to each other, or the ToF resolution requirement could be relaxed. An instrument using slower PMTs with a ToF resolution in the nanosecond range, coupled with the other background mitigation techniques developed for FACTEL, would still lead to a clear separation between the two peaks of a ToF spectrum for an instrument with a 60 cm distance between the layers. Then, a next generation in sensitivity instrument using slower PMTs could be built at a much lower cost than one using the fastest PMTs.

A second comment is that the anti-coincidence box now enclosing both detector layers is a sound choice. The removal of material between the two detector layers is critical, while placing the D2 detectors inside the anti-coincidence box would further help suppress unwanted events.

The third and most serious comment about this version of the ASCOT instrument is about the PMT layer directly above the D1 detectors. A full PMT layer with the associated electronic boards directly in the instrument field of view is detrimental. Any incoming astronomical gamma ray would first have to cross that passive material layer before reaching the detectors. The PMT layer in front of the D1 detectors leads to two significant drawbacks: the layer would attenuate the already weak flux of incoming celestial gamma rays, and then the gamma rays interacting in the passive layer would directly become a source of background. This aspect of this version of the ASCOT instrument is what led to a rethinking of the concept, and why simulations efforts did not go further than a few basic tests showing the instrument would perform as expected.

Two opinions are opposing each other in this assessment of a significant passive layer of material in front of the D1 detectors. The first opinion is that the passive layer is not really significant: it would attenuate the incoming flux and create background events, however the rest of the instrument would perform admirably and still constitute an exceptional Compton telescope. The opposing opinion is that the PMT passive layer in front of the D1 detectors absolutely needs to be removed. It is not a sound choice to attenuate an already weak flux while generating new background events. The goal is to achieve the best Compton telescope possible and removing any passive material layer in the track of the gamma rays is the best choice.

A possible solution to the PMT layer in front of the D1 detectors problem is the recent development Silicon Photomultipliers (SiPM) [68]. SiPMs are not susceptible to magnetic fields, they operate at much lower voltages compared to PMTs, and most importantly are compact. For example, the diagram of a 6×6×2 mm SiPM from Hamamatsu, model S10985 [69 and 70], is shown in figure 6.3:

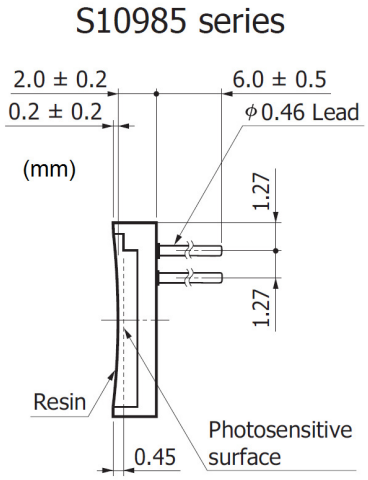

Figure 6.3: Schematic diagram of a Hamamatsu S10985 SiPM

This particular SiPM (Hamamatsu S10985) operates at ~70 V and is 2 mm thick. For the purpose of building a new generation fast Compton telescope, such SiPMs solve the problem of a significant passive material layer in front of the D1 detectors. SiPMs are still a relatively new technology undergoing intense development. However, a ToF resolution of 100 ps has been achieved between two $LaBr_3$:Ce detectors coupled to SiPMs for 511 keV gamma rays [71, figure 3]. SiPMs may be a viable avenue for Compton telescopes, providing a solution to the first version of the ASCOT instrument concept problem of having a significant passive layer of material in the telescope field of view. For an ASCOT instrument using SiPMs, an incoming gamma ray would only have the dome and anti-coincidence panels to cross before reaching the D1 detector layer, then no material has to be crossed to reach the D2 detector layer, while retaining the sub-nanosecond ToF resolution. Furthermore, replacing the aluminum dome with a lighter non-metallic material, such as Kevlar, would provide better background reduction.

6.3 ASCOT Simulation Results

This section presents the results of the simulations performed using the first version of the ASCOT instrument concept shown in figures 6.1 and 6.2. The PMT layer in the field of view problem and the evolution of the ASCOT concept presented in the last section brought a halt to the first model simulations. To summarize the goal and results of these simulations, the ASCOT instrument would perform as intended and constitute a superior Compton telescope. The FACTEL instrument has two layers of three 2.5 cm detectors totaling 9 pairs, while the ASCOT instrument would have two layers of 625 5-cm detectors totaling 390625 pairs, which is ~$4x10^4$ times more pairs than FACTEL and twice the material for each pair. The main difference between the two instruments is that the ASCOT instrument would possess a much larger efficiency than the FACTEL prototype. And indeed, a simulation (not shown here) shows ASCOT to be about 82000 times more efficient than the FACTEL prototype at 1 MeV, which is the expected number.

The second test performed was to compute the effective area for the ASCOT instrument at various energies to then compare the results with the simulated effective area of COMPTEL (figure 4 of [72]). The simulation was basic and involved generating gamma rays of various energies aimed directly downwards at the central D1 detector and counting how many coincident events were generated. A plot of the results compared to COMPTEL is shown in figure 6.4:

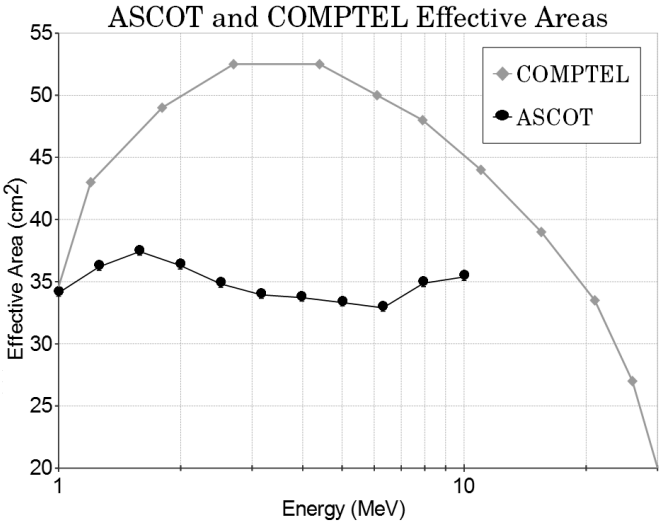

Figure 6.4: ASCOT and COMPTEL simulated Effective Areas in function of Energy

For example, for the peak data point, the simulation generated 1 million 1.585 keV gamma rays towards the central D1 detector, which generated 17287 coincident events. There are 625 D1 detectors with a circular cross-section of 1.05 cm in radius, the effective area calculation is then given by equation 6.1.

$$\frac{17287}{1000000} \times 625 \times 1.05^2 \times \pi \text{ cm}^2 = 37.422 \text{ cm}^2 \qquad (6.1)$$

The ASCOT instrument results of fig. 6.4 are between 33 and 38 cm^2, which places ASCOT a bit under COMPTEL in terms of effective area, but with a much smaller instrument volume and mass. The ASCOT effective area drops after 2 MeV while the effective area of COMPTEL stays high because of ASCOT smaller detectors. The effective area of COMPTEL goes down under 3 MeV because of a threshold effect: the detecting threshold in a COMPTEL D2 detector was 300 keV. The rise in ASCOT effective area above 5 MeV comes from pair production: the pair production cross section is proportional to Z^2 (eq. 2.9), NaI average Z is 32 while $LaBr_3$ average Z is 40.5 (section 3.2.2). This effective area simulation was basic and could be improved in two ways: broadening the incoming beam to the whole area of

the telescope would lower the effective area (geometric factors), while using multiple scatters events in the D2 layer would increase the effective area.

This simple test shows that the ASCOT instrument would be a superior Compton telescope when compared to COMPTEL, which was the goal of performing these quick evaluations. The ASCOT instrument is not as massive as COMPTEL, but the ToF resolution improvement would lead to a better sensitivity by filtering much more background. An ASCOT instrument using SiPMs instead of PMTs, with a Kevlar dome instead of an aluminum one, and perhaps with a larger area and thicker detector layers could outperform COMPTEL in every aspect: angular resolution, energy resolution, effective area and most importantly sensitivity.

6.4 ASCOT in the larger Gamma-Ray astronomy picture

The introduction and first chapter of this work showed that sensitivity was the primary need of the medium-energy gamma-ray field. The FACTEL prototype results have shown that a Compton telescope with a 1-ns Time of Flight resolution was possible, and figure 5.21 showed its superior background rejection capabilities. Background rejection capabilities lead to superior sensitivity by increasing the signal to noise ratio. An ASCOT instrument based on the FACTEL prototype was presented and a first performance assessment showed that the ASCOT instrument would be superior to COMPTEL in every aspect, especially in sensitivity. A discussion about the pertinence of an ASCOT instrument within the medium-energy gamma-ray field and how it would contribute to the research in the field is now presented.

As shown in fig. I.1 in the introduction, no instrument has outperformed COMPTEL in the 1 to 10 MeV range although the CGRO mission was launched 24

years ago and ended in June 2000. The sensitivity in that energy band is trailing compared to the other bands, and the first chapter of this work showed more sensitive observations were needed to further our knowledge of a vast range scientific topics.

This state of the field explains why so much work is being devoted to developing a new generation instrument that would bring the sensitivity threshold in the medium-energy gamma-ray range one or two orders of magnitude down. This is where the FACTEL/ASCOT development effort comes from.

Many have wondered why the sensitivity in that 1 to 10 MeV energy range has not improved as other energy ranges have benefited from recent missions: the X-ray range with Chandra or the high-energy gamma-ray range with Fermi. The answer is the intense background present in the medium-energy range. X-Ray instruments can be shielded as X-rays are not as penetrative as gamma rays, and high-energy instruments do not suffer from as much background because sources of >100 MeV gamma rays are rather rare. Gamma rays between 1 and 10 MeV are penetrative, sources close to the spacecraft are abundant, and this is the energy range within which most nuclear interactions will produce gamma rays. The spacecraft, the instrument, and the detector material are background sources. The 1 to 10 MeV range is an energy range where substantial improvements are hard to achieve.

This is where the FACTEL/ASCOT project becomes pertinent as the goal was to reject as much background as possible by improving the Time of Flight window of the instrument. We believe this concept can gain factors in sensitivity compared to COMPTEL by rejecting much more background events and improving the signal to noise ratio. We believe ASCOT to be the most sensitive 1 to 10 MeV telescope concept up to date.

The "sensitivity hole" between 1 to 10 MeV seen in fig. I.1 is prompting a huge developmental effort: this is the next step for gamma-ray astronomy, this is where the next discoveries will be made. A leap in sensitivity implies the unveiling of a whole new facet of the Universe. Dozens of fields are waiting for new sensitive observations to progress. It is then no surprise to find dozens of serious instrument concepts and proposals competing to provide that next sensitivity step for the medium-energy gamma-ray field.

It is not the goal of this work to present all concepts and describe their advantages and weaknesses. However if an ASCOT instrument is to be placed within this competition, its advantages and weaknesses should at least be discussed. Weaknesses of such a "classic Compton Telescope" are efficiency and energy resolution, while advantages are sensitivity, concept simplicity, it is a significant improvement built upon an already successful mission, the electronic channels count, and being the most appropriate instrument for a deep survey.

The efficiency of a Compton telescope is a weakness compared to other concepts because a classic Compton telescope uses two steps (the D1 and the D2 steps), and the D1 detector needs to let the scattered gamma ray escape towards the D2 detector. Consequently, many of the incoming gamma rays will go through the D1 detector layer without interacting. For example, for the ASCOT instrument, the numbers used in eq. 6.1 lead to a 1.7% efficiency for ~1.6 MeV gamma rays. This is a weakness compared to a stack of semi-conductors detectors that will absorb a much larger fraction of the incoming gamma rays. However, a better efficiency does not lead to better results because what really matters in this energy range is the background rejection capability of an instrument: absorbing more of the incoming radiation is not an advantage if the background cannot be filtered.

The second perceived weakness is the energy resolution. The D2 absorber detectors can usually display an energy resolution of a few percent, however the organic liquid scintillator used for the D1 detectors is notorious for its low energy resolution. The instrument total energy resolution is a combination of both detector layers resolutions. Compton telescopes then usually display lower energy resolutions than, for example, gamma-ray telescopes using semi-conductors (Ge, Si, CdTe, CZT, etc.). The notion of energy resolution being a weakness for Compton telescopes can be challenged because energy resolution is not critical for a general purpose gamma-ray telescope. Energy resolution is only pertinent to resolve two close nuclear lines, it is not a necessity to observe a lone nuclear line or a continuum emission. A classic Compton telescope is totally adequate to observe a single line such as the 1809 keV gamma-ray line from ^{26}Al (see fig. 1.4), the 2223 keV gamma-ray line from neutron capture, or the 511 keV annihilation line from positron annihilation. Furthermore, above 1 MeV a Compton telescope energy resolution (around 4%) is adequate to resolve two lines separated by over a hundred keV, for example fig. 3.53 shows that an ASCOT telescope would resolve the two lines from ^{60}Co (1173 and 1333 keV).

The ASCOT concept first advantage is its sensitivity, which is the need of the medium-energy gamma-ray astronomy field. We have striven to build an instrument rejecting as much background as possible by using PSD, reducing metals and passive material around the D1 detector layer, deuterating the D1 detectors, borating the top anti-coincidence panel, and most importantly by reaching an unmatched Time of Flight resolution. By focusing on background rejection, many "good" events recorded by an ASCOT instrument would be celestial events. This gives an ASCOT instrument an excellent signal to noise ratio, which in turn gives the telescope an unmatched sensitivity.

The ASCOT concept second advantage is its simplicity in data processing. The data recorded in a Compton telescope event is simple: D1 address, D1 amplitude, D2 address, D2 amplitude, ToF value, PSD value, Anti-coincidence flag. The undesired events are removed through ToF, PSD, anti-coincidence, and angle cuts. The event is then reconstructed using equations 2.16 and 2.17. The image reconstruction is more complicated, but every instrument concept has to deal with that problem.

Another advantage is that ASCOT is the logical step building upon an already known quantity. The COMPTEL instrument has already been flown and has been a very successful mission with its results still unmatched in its energy range. The ASCOT concept is then a sound choice as it is a direct improvement of the already successful COMPTEL instrument.

The number of electronic channels is an advantage for an ASCOT instrument. The ASCOT instrument concept presented in section 6.2 has 1250 detectors, leading to 1250 electronic channels to process. The main competitors to such classic Compton telescope concepts like ASCOT are semi-conductor based concepts typically using multiple stacked double-sided semi-conductor detectors. Typically, the electrodes pitch of a double-sided semi-conductor detector is in the millimeter range. This leads to thousands to hundreds of thousands of electronic channels to be processed by larger instruments. Comparatively, the low electronic channels count of a classic Compton telescope is an advantage.

Finally, semi-conductor based instruments are more appropriate than classical Compton telescopes for nuclear lines studies. However, through sensitivity, classical Compton telescopes are more appropriate for continuum emission studies. The need of the medium-energy gamma-ray astronomy field is for a new sensitive deep survey of the universe in this energy range, making continuum emission studies more

appropriate than nuclear lines studies. This makes classical Compton telescopes the instrument class to be favored.

The advantages and weaknesses of the ASCOT instrument concept having been detailed, we will now succinctly point out a few of the weaknesses of the main competitors to classical Compton telescope concepts, which are typically semi-conductor based detector stacks. To provide a concrete example, the "Nuclear Compton Telescope" (NCT) is a stack of germanium double-strip detectors devices. A diagram and a picture of the NCT the instrument are shown in figure 6.5. An overview of the Nuclear Compton Telescope can be found in [74], a study on its expected sensitivity in [75], observational results of the Crab nebula in [76], future prospects for its development in [77], and a reference for event reconstruction in such instrument is [78].

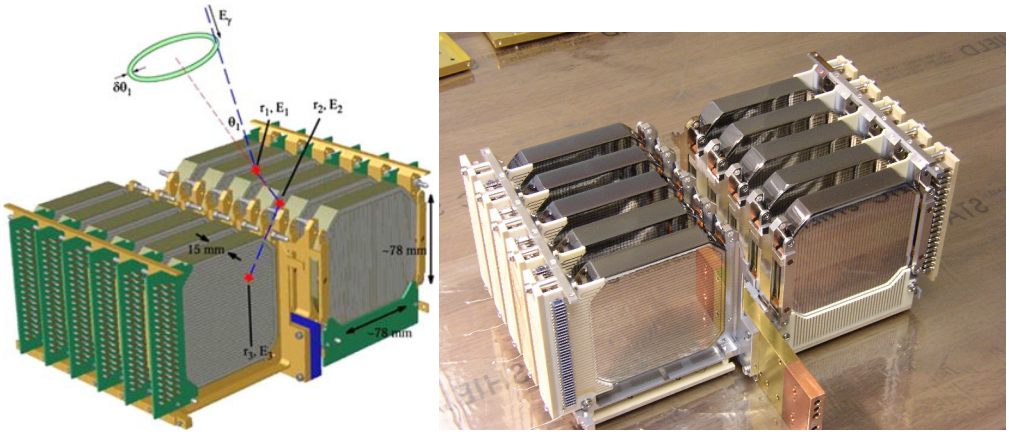

Figure 6.5 NCT concept diagram (left), NCT detectors picture (right)

The main weakness of such instrument concepts is their inferior background rejection capabilities compared to a fast Compton telescope. Such instruments rely on multiple scatters (triple and more) in multiple detectors to record an event. The timing resolution of the detectors precludes the time ordering of the scatters, leading to the use of probabilistic treatments to reconstruct an event. Instruments not using ToF

have to treat all hits of an event indiscriminately, and figure 2.16 shows that most events will be background. While they have to contend with the background "in" the data and treat it after its recording, the ToF measurement of an ASCOT instrument provides an intrinsic background rejection capability. Another weakness is the fact that in an environment dominated by background, the unavoidable errors of a probabilistic treatment allow many background events in the valid data stream (the base rate fallacy), leading to an inferior signal to noise ratio and sensitivity compared to an ASCOT instrument. Then, as the size of the instrument increases, the background signals rate increases with the volume of the instrument.

The debate about the advantages and weaknesses of instruments concepts could be expanded much more, however it is not the goal of this work to make a full comparison of the many instrument proposals existing.

To conclude this section about how an ASCOT telescope would place itself within the current 1 to 10 MeV gamma-ray astronomy field and how it competes with other instrument concepts, we believe that through its simplicity and sensitivity, an ASCOT telescope would be the best suited instrument to address the vast majority of the needs of the field. Sensitivity is the priority, and background rejection is key to sensitivity. Time of Flight resolution is key to background rejection, making ASCOT the preferred future instrument.

6.5 Summary

The FACTEL prototype was successful in showing that a ~1 ns Compton telescope was possible. This chapter presented how an Advanced Scintillator Compton Telescope (ASCOT) instrument based on the FACTEL prototype would

perform and how it would fit within the current gamma-ray astronomy field. The ASCOT instrument would be a classic two detecting layers Compton telescope with a much improved ToF resolution. Each layer would be a 2D array of scintillator detectors, organic liquid for the D1 detectors and $LaBr_3$ for the D2 detectors, the detectors would be coupled to either PMTs or more probably to Silicon Photo-Multipliers. Simulations based on FACTEL simulations show that the first version of the ASCOT instrument would perform as expected and constitute a superior Compton telescope with an unprecedented sensitivity provided by its ToF resolution. Finally the ASCOT instrument was placed within the current medium-energy gamma-ray astronomy field. Figure I.1 shows the current hole in sensitivity between 1 and 10 MeV, and we have shown how through its superior sensitivity ASCOT would be the best suited instrument to address the current needs of the field.

CONCLUSION

The current medium-energy gamma-ray astronomy field needs a new more sensitive telescope for observations between 1 and 10 MeV. As shown in fig. I.1, the development of new more sensitive telescopes for observations in this band has been difficult due to the high amount of background events. The development of new "fast" scintillators such as $LaBr_3$:Ce has allowed our research group here at the University of New Hampshire to build a FAst Compton TELescope (FACTEL) prototype which would be the basis for an Advanced Scintillator COmpton Telescope (ASCOT). We showed how an ASCOT instrument, a Compton telescope with a Time of Flight resolution under 1 ns, whether coupled to classic Photo-Multipliers Tubes or new Silicon Photo-Multipliers, would be a good answer to the field sensitivity need by being able to filter the environment background events at an unprecedented level.

There are many astronomical gamma-ray sources to observe with such a telescope. Topics in the nuclear astrophysics field are nuclear lines from the galactic center, the positron annihilation 511 keV line, SN Ia supernovae, core collapse SN, the ^{44}Ti isotope, classical novae, nuclear gamma-ray lines from cosmic rays, gamma-ray lines from X-ray binaries, supernovae remnants, solar flares lines, long lived radioactive isotopes diffusing within the galactic media, radioactive isotopes within celestial objects without atmosphere, and possibly dark matter annihilation and decay. Topics in the relativistic particle accelerators field are the continuum emission from the galactic center, the galactic bulges, novae, the high-energy inter stellar media, X-

ray and gamma-ray binaries, black holes and accreting objects, gamma-ray bursts (GRB), active galactic nuclei (AGN), magnetars and isolated pulsars, pulsars wind nebulae, starbursts galaxies, the Sun at high energy, terrestrial gamma-ray flashes, and possibly limits of modern physics. With the exception of observing close nuclear lines, the overarching priority for all topics is new more sensitive observations, and background rejection is the key to sensitivity.

The FACTEL instrument prototype we built is an evolution upon the successful COMPTEL instrument. The goal of the FACTEL project and flight was to implement and evaluate the new background mitigation techniques needed to build a successful more sensitive next generation instrument for observations in the medium-energy gamma-ray range. The four new techniques implemented in the FACTEL prototype are:

- Borating the top anti-coincidence panel (plastic scintillator) to mitigate neutrons incoming in the field of view of the instrument.
- Deuterating the D1 detectors liquid scintillator material to avoid neutron capture in the D1 detectors.
- Limiting passive materials, particularly metals, in the D1 layer region to limit material background events and material activation.
- Using $LaBr_3$ scintillator D2 detectors to suppress more background events by narrowing the Time-of-Flight window.

These new techniques were evaluated through simulations, laboratory tests, and the FACTEL balloon flight conducted from NASA's Columbia Scientific Balloon Facility (CSBF) in Fort Sumner, New Mexico, on September 23, 2011. We now finalize this work with the evaluation of these techniques.

We cannot see the effect of borating the top anti-coincidence panel because we cannot distinguish between the Signal, A, and C_1 events in the forward ToF peak, see fig. 5.28, and we have not measured any sign of neutron capture at all in the flight data. The goal of this technique was to prevent neutron capture in the anti-coincidence panel in the field of view of the telescope. There is no great need to borate the side panels because those events would be rejected through an angle calculation. We cannot see an adverse effect on the telescope performance from this change, for example an increase of the background. Thus without further information, borating the top anti-coincidence panel can be considered successful, and definitely not detrimental to the telescope performance. Actually, one laboratory test could have been performed to assess the effectiveness of borating the top anti-coincidence panel. We could have placed a slow neutron source in front of the telescope, perform a signal acquisition run, then perform the exact same run while exchanging the AC1 and AC4 panels (both have the same dimensions, AC4 is borated, AC1 is not). Or we could have performed the runs while completely removing the panel between the detector layers and just changing the AC4 panel for the AC1 panel in the setup. This test is a missed opportunity no one thought of performing, but could still be performed in future tests because all the components still exist.

Deuterating the liquid scintillator material of the D1 detectors was validated by the simulations presented in section 3.3.6. This technique aimed at preventing neutron capture within the D1 detectors. Simulations have shown that neutron capture would not be a problem for the small FACTEL D1 detectors: incoming neutrons would only interact once within the detector and then escape (they do not have the time and space to thermalize). Then, even if a 2.2 MeV gamma-ray would be produced within the detector, it would escape the detector before interacting in the majority of cases.

The neutron capture problem is evident for larger undeuterated D1 detectors, the COMPTEL data and the result from a laboratory test shown in fig. 3.73 confirm the problem. Then, simulations of that test, those results are shown in figures 3.74 and 3.75, gives evidence that deuterating the material of the D1 detectors mitigates the neutron capture spectral line. Finally, the test results presented in fig. 3.72 demonstrates that deuterating the liquid scintillator material of the D1 detectors still provides successful pulse-shape discrimination.

The new material choices for the FACTEL prototype were validated by the ToF spectrum of the coincident events recorded during the balloon flight. The material choices implied limiting metals and passive material around the D1 detectors by using fiberglass reinforced plastic instead of aluminum for the frame and using Bakelite for the mechanical support close to the D1 detectors. These changes aimed at reducing the material background (B, C and D background events) generated close to the D1 detector layer. Whether we favor the fig. 5.21 result or the fig. 5.27 result, the material choices have been successful as all results show a reduction of the background signal in the forward peak of the ToF spectrum. As much as neutron capture was a problem for COMPTEL, activation of aluminum leading to ^{24}Na (see equations 2.18, 2.19, and 2.20) also plagued COMPTEL [51]. No definitive statement can be made over this issue from the FACTEL balloon flight: no 1369, 2754 or 4123 keV peaks are evident in figures 5.13 and 5.16, and fig. 5.24 does not have enough statistics to prove the point.

Using $LaBr_3$ for the D2 detectors was obviously successful. The ~1-ns ToF resolution of the FACTEL prototype is easy to recognize: the two detector layers are physically separated by ~30 cm and the forward and backward ToF peaks are well separated (separation of ~2 ns at the speed of light), see fig. 5.25. The goal of using $LaBr_3$ for the D2 detectors was to improve the ToF resolution from COMPTEL 4-ns

resolution to a resolution under 1 ns, which through the ToF technique would filter much more of the unwanted background events. Throughout the history of the project, from laboratory tests of the components, laboratory tests with the final instrument, and the balloon flight, the ToF resolution value has consistently revolved under or close to 1 ns. The best case scenario found a 450 ps ToF resolution (fig. 3.61), laboratory tests with the final instrument give a 600 ps (perhaps 975 ps) ToF resolution (fig. 3.70), and the balloon flight ToF resolution is 1.27 ns at worst. Perhaps not clearly demonstrated by the FACTEL project, because of the small scale of the project, the ~1-ns ToF resolution clearly measured still theoretically lead to a substantial improvement in the background rejection capability of a next generation instrument. The ToF resolution of a telescope leads to a better isolation and then rejection of background features. For example, the ^{24}Na background ToF peak in COMPTEL was 0.5 ns closer to zero than the actual forward peak (4.5 vs 5 ns). With a ToF resolution of 4 ns, this feature was complex to address in COMPTEL data [51]; a 1-ns ToF would definitely make this issue easier to address. Hopefully, the ^{24}Na issue can also be suppressed by using as little aluminum as possible in the instrument design.

The goals we wanted to achieve by building the FACTEL prototype were to reduce background generation in the instrument through the first three material techniques we evaluated, and to improve background rejection by building a telescope with a ToF resolution in the nanosecond range using $LaBr_3$ for the D2 detectors. All the four new background mitigation techniques we implemented can be considered successful either by simulation or demonstration. In the end, we greatly improved the Time of Flight resolution of Compton telescopes, allowing us to build smaller and less massive instruments, such as ASCOT, with much improved background suppression capabilities. Time of Flight resolution is the key to background rejection, which is the

key to sensitivity, which is the priority for the majority of the required observations in the field. Based on the successful FACTEL instrument prototype we built and evaluated, an ASCOT telescope would be a good, and possibly the best, instrument to provide the medium-energy gamma-ray astronomy field the needed sensitivity to allow its many fields to progress.

REFERENCES

[1] Schönfelder V. et al., **"Instrument Description and Performance of the Imaging Gamma-Ray Telescope COMPTEL aboard the Compton Gamma-Ray Observatory"**,
The Astrophysical Journal Supplement Series, 86:657-692, June 1993.

[2] Bloemen H. et al., **"The revised COMPTEL Orion results"**, Astrophysical Journal, 521, L137, 1999.

[3] Weisskopf M. C. et al., **"An Overview of the Performance and Scientific Results from the Chandra X-Ray Observatory"**,
Publications of the Astronomical Society of the Pacific, Vol. 114, pp. 1-24, January 2002

[4] A brief Chandra Observatory Bibliography can be found on the site: http://cxc.harvard.edu/cdo/biblio/chandra_bib.html

[5] Michelson P. F., Atwood W. B. and Ritz S., **"Fermi Gamma-Ray Space Telescope: High-Energy Results from the First Year"**, Reports on Progress in Physics, Vol. 73, Issue 7, id. 074901, arXiv:1011.0213v2, 2010-11

[6] Nakazawa K. et al., **"Concept of a small satellite for sub-MeV & MeV all sky survey: the CAST Mission"**, Proceedings of SPIE, Vol. 8443, 84430E, 2012-09

[7] Ryan J. M. et al., **"Using LaX scintillator in a new low-background Compton Telescope"**, Proc. of SPIE, Vol. 6707, 670703, 2007-09

[8] S. Bowyer, E. T. Byram, T. A. Chubb and H. Friedman, **"Cosmic X-ray Sources"**, Science, New Series, Vol. 147, No. 3656, January 1965, pp. 394-398

[9] Reid M. J. et al., **"The Trigonometric parallax of Cygnus X-1"**,
The Astrophysical Journal, Vol. 742:83, December 2011

[10] Nolan R. Walborn, **"The Spectrum of HDE 226868 (Cygnus X-1)"**,
The Astrophysical Journal, 179:L123-L124, February 1973

[11] Orosz J. A. et al., **"The Mass of the Black Hole in Cygnus X-1"**,
The Astrophysical Journal, Vol. 742:84, December 2011

[12] LaSala J. et al., **"The orbital period of HDE 226868/Cyg X-1"**, Monthly Notices of the Royal Astronomical Society, Volume 301, Issue 1, pp. 285-288, 1998

[13] Jourdain E., Roques J. P., Malzac J., **"The Emission of Cygnus X-1: Observations with *INTEGRAL* SPI from 20 keV to 2 MeV"**, The Astrophysical Journal, 744:64, January 2012

[14] McConnell M. L. et al., **"The Soft Gamma-Ray Spectral Variability of Cygnus X-1"**, The Astrophysical Journal, 572:984-995, June 2002

[15] Sabatini S. et al., **"Gamma-Ray Observations of Cygnus X-1 above 100 MeV in the Hard and Soft States"**, The Astrophysical Journal, 766:83, April 2013

[16] Bodaghee A. et al., **"Gamma-ray observations of the microquasars Cygnus X-1, Cygnus X-3, GRS 1915+105, and GX 339-4 with the *Fermi* Large Area Telescope"**, The Astrophysical Journal, 775:98, October 2013

[17] Albert J. et al., **"Very High Energy Gamma-Ray Radiation from the Stellar Mass Black Hole Binary Cygnus X-1"**, The Astrophysical Journal, 665:L51, August 2007

[18] Esin A. A. et al., **"Spectral Transitions in Cygnus X-1 and other Black Hole X-ray Binaries"**, The Astrophysical Journal, 505:854-868, October 1998

[19] Palacios A. et al., **"New estimates of the contribution of Wolf-Rayet stellar winds to the Galactic ^{26}Al"**, Astronomy and Astrophysics, Vol. 429, pp. 613-624, January 2005

[20] Plüschke S. et al., **"The COMPTEL 1.809 MeV Survey"**, Proceedings of the 4th INTEGRAL Workshop, ESA SP-459, p. 55, September 2001

[21] Prantzos N., **"Radioactive ^{26}Al and ^{60}Fe in the Milky Way: Implications of the RHESSI detection of ^{60}Fe"**, Astronomy & Astrophysics, Vol. 420, pp. 1033-1037, 2004

[22] Mahoney W. A. et al., **"HEAO 3 Discovery of 26Al in the interstellar medium"**, The Astrophysical Journal, 286:578-585, November 1984

[23] Prantzos Nikos, Diehl Roland, **"Radioactive ^{26}Al in the Galaxy: Observations versus Theory"**, Physics Reports, Vol. 267, pp. 1-69, 1996

[24] Woosley S. E. et al., **"The evolution and explosion of massive stars. II. Explosive Hydrodynamics and Nucleosynthesis"**,
The Astrophysical Journal Supplement Series, 101:181-235, November 1995

[25] Timmes F. X. et al., **"^{26}Al and ^{60}Fe from Supernova Explosions"**,
The Astrophysical Journal, 449:204-210, August 1995

[26] Smith D. M., "**RHESSI results on γ-ray lines from diffuse radioactivity"**,
New Astronomy Reviews, Vol. 48, Issue 1-4, pp. 87-91.

[27] Prantzos Nikos, **"Nucleosynthesis and gamma-ray lines"**,
Proceedings of the 8th INTEGRAL Workshop, September 2010

[28] Klebesadel R. W., Strong I. B., Olson R. A.,
"Observations of Gamma-Ray Bursts of Cosmic Origin",
The Astrophysical Journal, 182:L85-L88, June 1973

[29] Gehrels N., Ramirez-Ruiz E., Fox D. B.,
"Gamma-Ray Bursts in the Swift Era",
Annual Reviews of Astronomy and Astrophysics, 47:567-617, 2009

[30] De Shong J. A., Hildebrand R. H., Meyer P.,
"Ratio of Electrons to Positrons in the Primary Cosmic Radiation",
Physical Review Letters, Vol. 12, pp. 3-6, 1964

[31] Johnson W. N., Harnden F. R., Haymes R. C., **"The spectrum of low-energy gamma radiation from the galactic-center region"**,
The Astrophysical Journal, 172:L1-L7, February 1972

[32] Chupp E. L., Forrest D.J., Suri A. N., **"High Energy Gamma-Ray Radiation above 300 keV associated with Solar Activity"**, Proceedings of the Symposium on Solar gamma-, X-, and EUV radiation, Buenos Aires, Argentina, June 11-14 1974;
Dordrecht, D. Reidel Publishing Co., pp. 341-359, 1975

[33] Prantzos N., Boehm C., Bykov A. M., Diehl R., et al.,
"The 511 keV emission from positron annihilation in the Galaxy",
Reviews of Modern Physics, Vol. 83, Issue 2, pp. 1001-1056, 2011

[34] Weidenspointner G. et al., **"An asymmetric distribution of positrons in the Galactic disk revealed by γ-rays"**, Nature, 451, pp. 159-162, January 2008

[35] Fletcher L. et al., **"An Observational Overview of Solar Flares"**,
Space Science Reviews, Vol. 159, Issue 1-4, pp. 19-106, September 2011

[36] Shih A. Y., Lin R. P., Smith D. M., **"*RHESSI* Observations of the Proportional Acceleration of Relativistic >0.3 MeV electrons and >30 MeV protons in Solar Flares"**,
The Astrophysical Journal, 698:L152-L157, June 2009

[37] Graham Woan, **"The Cambridge Handbook of Physics Formulas"**,
Cambridge University Press, 2003, ISBN 0-521-57507-1

[38] Volker Schönfelder (Ed.), **"The Universe in Gamma Rays"**,
Springer-Verlag Berlin Heidelberg, 2001, ISBN 3-540-67874-3

[39] John David Jackson, **"Classical Electrodynamics, Third Edition"**,
John Wiley & Sons, Inc., 1999, ISBN 0-471-30932-X

[40] Blumenthal G. R., Gould R. J., **"Bremsstrahlung, Synchrotron Radiation, and Compton Scattering of High-Energy Electrons Traversing Dilute Gasses"**, Reviews of Modern Physics, Vol. 42, Issue 2, pp. 237-270, 1970

[41] Robley D. Evans, **"The Atomic Nucleus"**, McGraw-Hill Inc., 1955

[42] Einstein A., **"Über einen die Erzeugung und Verwandlung des Lichtes betreffenden heuristischen Gesichtspunkt"**,
Annalen der Physik, Vol. 322, Issue 6, pp.132-148, 1905

[43] Harald A. Enge, **"Introduction to nuclear physics"**,
Addison-Wesley, 1966, ISBN 0-201-01870-5

[44] Arthur H. Compton, **"A Quantum Theory of the Scattering of X-Rays by Light Elements"**, Physical Review, Vol. 21, Issue 5, pp. 483-502, May 1923

[45] Ryan J. M., **"Astrophysics challenges of MeV-astronomy instrumentation"**, New Astronomy Reviews, Vol. 48, pp. 199-204, 2004

[46] Hebert T., Leahy R., Singh M., **"Three-dimensional maximum-likelihood reconstruction for an electronically collimated single-photon-emission imaging system"**,
Journal of the Optical Society of America A: Optics, Image Science, and Vision, Vol. 7, Issue 7, pp.1305-1313, July 1990

[47] Parra L. C., **"Reconstruction of cone-beam projections from Compton scattered data"**, IEEE Transactions on Nuclear Science, Vol. 47, Issue 4, pp. 1543-1550, August 2000

[48] Much R., et al., **"Preliminary Performance Characteristics of Comptel"**, Proceedings of the 21st International Cosmic Ray Conference, Vol. 4, p. 158, 1990

[49] Glenn F. Knoll, "**Radiation Detection and Measurement 4th ed."**, John Wiley & Sons, Inc., 2010, ISBN 978-0-470-13148-0

[51] Srinivas Cheenu Kappadath, **"Measurement of the cosmic diffuse gamma-ray spectrum from 800 keV to 30 MeV"**, University of New Hamsphire, 1998

[52] Weidenspointner et al., **"The COMPTEL instrumental line background"**, Astronomy and Astrophysics, 368:347-368, March 2001

[53] Bollinger L. M. and Thomas G. E., **"Measurement of the Time Dependence of Scintillation Intensity by a Delayed-Coincidence Method"**, Review of Scientific Instruments, Volume 32, Issue 9, September 1961

[54] http://www.eljentechnology.com/index.php/products/liquid-scintillators/75-ej-315

[55] Saint-Gobain Crystals, Scintillation Products Technical Note, BrilLanCe™ Scintillators Performance Summary, January 2009 Revision

[56] Hamamatsu's technical paper for the R4998 PMT: http://www.hamamatsu.com/resources/pdf/etd/R4998_TPMH1261E02.pdf

[57] http://www.phys.ufl.edu/courses/phy4803L/group_I/muon/bicron_bc400-416.pdf

[58] Bloser P. F., Ryan J. M., Legere J. S., Julien M., Bancroft C. M., McConnell M. L., Wallace, M., Kippen M. R., Tornga S.; **"A fast scintillator Compton telescope for medium-energy gamma-ray astronomy"**; Proceedings of the SPIE, Volume 7732, pp. 773222-773222-12, July 2010

[59] S. Agostinelli et al., **"GEANT4 - a simulation toolkit"**, Nuclear Instruments and Methods in Physics Research A, Vol. 506, p. 250-303, July 2003

[60] McConnell M. L. et al., **"Plans for the next GRAPE balloon flight"**, Proceedings of the SPIE, Volume 8859, id. 885909, September 2013

[61] Gehrels N., **"Instrumental background in balloon-borne gamma-ray spectrometers and techniques for its reduction"**, Nuclear Instruments and Methods in Physics Research A239 (1985), pp. 324-349

[62] Armstrong T. W., Chandler K. C., Barish J., **"Calculations of Neutron Flux Spectra Induced in the Earth's Atmosphere by Galactic Cosmic Rays"**, Journal of Geophysical Research, Vol. 78, No. 16, pp. 2715-2726, June 1973

[63] Swartz D. A., Chen Y. Z., Ramsey B. D., **"Background simulation for a balloon-borne gas scintillation proportional counter"**, Proceedings of the SPIE, Volume 4140, pp. 520-531, December 2000

[64] T. Mizuno et al., **"Cosmic-ray background flux model based on a Gamma-ray Large Area Space Telescope balloon flight engineering model"**, The Astrophysical Journal, 614:1113-1123, 2004 October 20

[65] R. L. Golden et al., **"Observations of Cosmic Ray Electrons and Positrons Using an Imaging Calorimeter"**, The Astrophysical Journal, Vol. 436, p. 769, 1994

[66] M. Boezio et al., **"New Measurement of the Flux of Atmospheric Muons"**, Physical Review Letters, vol. 82(24), pp. 4757-4760, 1999

[67] Atwood W. B. et al., **"The Large Area Telescope on the Fermi Gamma-Ray Space Telescope Mission"**, The Astrophysical Journal, Vol. 697, Issue 2, pp. 1071-1102, June 2009

[68] P. Buzhan et al., **"Silicon photomultiplier and its possible applications"**, Nuclear Instruments and Methods in Physics Research A, Vol. 504, p. 48, 2003

[69] P. F. Bloser et al., **"Balloon-flight test of a lanthanum bromide gamma-ray detector with silicon photolustiplier readout"**, IEEE Nuclear Science Symposium and Medical Imaging Conference (NSS/MIC), pp. 912-917, 10.1109/NSSMIC.2012.6551239, 2012

[70] Hamamatsu's technical paper for the S10984/S10985 SiPMs http://www.hamamatsu.com/resources/pdf/ssd/s10984_series_etc_kapd1024e03.pdf

[71] Schaart D. R. et al., **"LaBr3:Ce and SiPMs for time-of-flight PET: achieving 100 ps coincidence resolving time"**, Physics in Medicine and Biology, Vol. 55, pp. 179-189, 2010

[72] Stacy J. G., et al., **"The response of the CGRO COMPTEL determined from Monte Carlo simulation studies"**, Astronomy and Astrophysics Supplement, v.120, pp. 691-694, December 1996

[73] R. B. Firestone[1] and L. P. Ekström[1,2]
[1] Laurence Berkeley National Laboratory, Berkeley, USA
[2] Department of Physics, Lund University, Sweden
http://ie.lbl.gov/toi/

[74] Bellm E. C., et al., **"Overview of the Nuclear Compton Telescope"**, IEEE Transactions on Nuclear Science, Vol. 56, Issue 3, pp. 1250-1256, June 2009

[75] Chang H.-K., et al., **"The Nuclear Compton Telescope (NCT): Scientific goals and expected sensitivity"**,
Advances in Space Research, Vol. 40, Issue 8, pp. 1281-1287, 2007

[76] Bandstra M. S., et al., **"Detection and Imaging of the Crab Nebula with the Nuclear Compton Telescope"**, The Astrophysical Journal, Vol. 738, Issue 1, article id. 8, 9 pp., September 2001

[77] Lowell A., et al., **"Prospects for the 2014/2015 Nuclear Compton Telescope balloon campaign"**, Proceedings of the SPIE, Vol. 8443, article id. 84434U, 8 pp., September 2012

[78] Boggs S. E. and Jean P.,
"Event reconstruction in high resolution Compton Telescopes",
Astronomy and Astrophysics Supplement, Vol. 145, pp. 311-321, August 2000

[79] Heristchi D., **"Hard X-ray and gamma-ray bremsstrahlung production by high-energy protons in solar flares"**,
The Astrophysical Journal, Vol. 311, pp. 474-494, December 1986

[80] Klein O. and Nishina Y., "**Über die Streuung von Strahlung durch freie Elektronon nach der neuen relativistischen Quantendynamik von Dirac"**,
Zeitschrift für Physik, Volume 52, Issue 11-12, pp. 853-868, September 1929

[81] Bradley W. Carroll and Dale A. Ostlie,
"An Introduction to Modern Astrophysics",
Addison-Wesley Publishing Company, Inc., 1996, ISBN 0-201-54730-9

[82] Wang W., et al.,
"SPI observations of the diffuse ^{60}Fe emission in the Galaxy",
Astronomy and Astrophysics, Vol. 469, Issue 3, pp. 1005-1012, July 2007

[83] James Ryan, **"Energy and Angle Distributions for Atmospheric and Cosmic Diffuse Gamma Rays from 2 to 25 MeV"**,
University of California, June 1978

[84] Julien M., et al.,
"Balloon Flight Results of a FAst Compton TELescope (FACTEL)",
IEEE 2012 NSS/MIC Conference Record, pp. 1893-1900, November 2012

FIGURES CREDITS

I.1 Credits and Source, see reference [6]
Copyright: Fair Use for Scholarly work under Section 107 of the 1976 United States Copyright Act
http://www.copyright.gov/title17/92chap1.html#107

I.2 Credit: COMPTEL Collaboration
Source: http://heasarc.gsfc.nasa.gov/docs/cgro/images/epo/gallery/skymaps/1_to_30_mev.gif
Copyright: "NASA still images generally are not copyrighted"
http://www.nasa.gov/audience/formedia/features/MP_Photo_Guidelines.html

I.3 Credit: NASA/DOE/Fermi LAT Collaboration
Source: http://www.nasa.gov/images/content/585379main_2-year-all-sky_GT1_GeV_labels.jpg
Copyright: "NASA still images generally are not copyrighted"
http://www.nasa.gov/audience/formedia/features/MP_Photo_Guidelines.html

1.1 Credit: ESA
Source: http://sci.esa.int/science-e-media/img/cc/CM_016_1778_1000.jpg
Copyright: http://www.esa.int/About_Us/Industry/Intellectual_Property_Rights/ESA_copyright_notice

1.2 Credit: Reference [15] and [14]
Source: [15]
Copyright: Fair Use under Section 107 of the 1976 United States Copyright Act: http://www.copyright.gov/title17/92chap1.html#107

1.3 Credit: Reference [14]
Source: [14]
Copyright: Fair Use, see copyright of fig. 1.2

1.4 Credit: Reference [20]
Source: [27]
Copyright: Fair Use, see copyright of fig. 1.2

1.5 Credit: Reference [28]
Source: [28]
Copyright: Fair Use, see copyright of fig. 1.2

1.6 Credit: Reference [29]
Source: [29]
Copyright: Fair Use, see copyright of fig. 1.2

1.7 Credit: Reference [34]
Source: [33]
Copyright: Fair Use, see copyright of fig. 1.2

1.8 Credit: Reference [32]
Source: [32]
Copyright: Fair Use, see copyright of fig. 1.2

1.9 Credit: Reference [36]
Source: [36]
Copyright: Fair Use, see copyright of fig. 1.2

1.10 Credit: C. Alex Young
Source: http://www.thesuntoday.org/wp-content/uploads/2012/02/rhessi_stereo_HSD_fig.png
Copyright: Fair Use, see copyright of fig. 1.2

1.11 Credit: Graham Woan
Source: [37], page 121
Copyright: Fair Use, see copyright of fig. 1.2

1.12 Author : Manuel Julien

1.13 Author : Manuel Julien

1.14 Credit: Graham Woan
Source: [37], page 159
Copyright: Fair Use, see copyright of fig. 1.2

1.15 Author: R. Bartolini
Modifications: Manuel Julien
Source: http://upload.wikimedia.org/wikipedia/commons/d/de/Syncrotron_radiation_energy_flux.png
Copyright: The original file is ineligible for copyright and therefore in the public domain, because it consists entirely of information that is common property and contains no original authorship.

1.16 Author : Manuel Julien

1.17 Credit: J. J. Condon and S. M. Ransom
Modifications: Manuel Julien
Source: http://www.cv.nrao.edu/course/astr534/InverseCompton.html
Copyright: The original comes from a United-States ".edu" internet page;
Fair Use, see copyright of fig. 1.2

1.18 Author : Manuel Julien

1.19 Author : Manuel Julien

1.20 Author : Manuel Julien

1.21 Credit: Reference [81]
Source: [81]
Copyright: Fair Use, see copyright of fig. 1.2

2.1 Credit: Robley D. Evans
Modifications: Manuel Julien
Source: [41], page 712
Copyright: Fair Use, see copyright of fig. 1.2

2.2 Author: Manuel Julien

2.3 Author: Manuel Julien

2.4 Author: Manuel Julien

2.5 Credit: James Ryan and Peter Bloser
Source: http://spie.org/x19645.xml?pf=true&ArticleID=x19645
Permission: James is my advisor and Peter on my thesis committee, they both are aware of my usage of the picture and consent to it.

2.6 Credit: James Ryan
Source: [45]
Permission: James is my advisor, he is aware of my usage of the picture and consent to it.

2.7 Credit: Much R. et al.
Source: [48]
Copyright: Fair Use, see copyright of fig. 1.2

2.8 Credit: Glenn F. Knoll
Source: [49], Figure 4.5, page 116
Modified all text: Manuel Julien
Copyright: Fair Use, see copyright of fig. 1.2

2.9 Credit: NASA
Source: http://upload.wikimedia.org/wikipedia/commons/8/83/Atmospheric_electromagnetic_transmittance_or_opacity.jpg
Copyright: "NASA still images generally are not copyrighted". http://www.nasa.gov/audience/formedia/features/MP_Photo_Guidelines.html

2.10 Credit: NASA
Modifications: Manuel Julien
Source: http://heasarc.gsfc.nasa.gov/docs/cgro/images/epo/gallery/cgro/cgro_cut-away.jpg
Copyright: See copyright of fig. 2.9

2.11 Credit: NASA
Modifications: Manuel Julien
Source: http://heasarc.gsfc.nasa.gov/docs/cgro/images/epo/gallery/cgro/comptel_schematic.gif
Copyright: See copyright of fig. 2.9

2.12 Author: Manuel Julien
Credit/Copyright: I created a figure by reproducing Kappadath's thesis [51] Figure III.6

2.13 Author: Manuel Julien
Credit/Copyright: I created a figure by reproducing Kappadath's thesis [51] Figure III.6

2.14 Author: Manuel Julien
Credit/Copyright: I created a figure by reproducing Kappadath's thesis [51] Figure III.6

2.15 Author: Manuel Julien
Credit/Copyright: I created a figure by reproducing Kappadath's thesis [51] Figure III.6

2.16 Credit: Weidenspointner et al.
Source: [52], Fig. 3
Modifications: Manuel Julien
Copyright: Fair Use, see copyright of fig. 1.2

2.17 Credit: Bollinger and Thomas
Modified Text: Manuel Julien
Source 1: I scanned [49], figure 8.5, page 235
Source 2: Knoll took his version from [53]
Copyright: Fair Use, see copyright of fig. 1.2

2.18 Credit: Steve Payne
Source: https://str.llnl.gov/JanFeb10/images/payne4.jpg
Copyright: This is a U.S. Government source, see:
https://www.llnl.gov/disclaimer.html

2.19 Credit: U.S. Department of Energy
Source: http://techportal.eere.energy.gov/images/tech/
Delayed%20Charge%20graph%20for%20Plastic%20Scintillators.png
Copyright: Same as fig. 2.18

3.1 Credit: James Ryan, UNH High Energy Astrophysics Group
Source: Development on an Advanced Scintillator Compton Telescope
Document submitted to NASA NNH07ZDA001N-APRA
March 28, 2008
Copyright: Our research group

3.2 Credit: James Ryan, UNH High Energy Astrophysics Group
Source: Development on an Advanced Scintillator Compton Telescope
Document submitted to NASA NNH07ZDA001N-APRA
March 28, 2008
Copyright: Our research group

3.3 Author: Jason Legere
Source: Our research group material
Copyright: Our research group

3.4 Credit: CRH (Initials), Eljen Technologies
Source: The product drawing Eljen sent us, GV10x10-2/3XX Cell
Copyright: There is no copyright in the document Eljen sent us

3.5 Credit: CJ (Initials), Saint-Gobain Crystals
Source: The product drawing Saint-Gobain sent us:
Detecteur N 20x20 /B380
Copyright: There is no copyright in the document Saint-Gobain sent us

3.6 Credit: Saint-Gobain Crystals
Source: [55]
Copyright: Fair Use, see copyright of fig. 1.2

3.7 Credit: Hamamatsu
Modifications: Manuel Julien; I have made very minor modifications
Source: [56]
Copyright: Fair Use, see copyright of fig. 1.2

3.8 Author: Manuel Julien

3.9 Author: Manuel Julien

3.10 Author: Manuel Julien

3.11 Author: Manuel Julien

3.12 Author: Manuel Julien

3.13 Author: Manuel Julien

3.14 Author: Jason Legere
Source: Our research group material
Copyright: Our research group

Figures 3.15 to 3.81 Author: Manuel Julien

4.1 Author: Manuel Julien

4.2 Author: Manuel Julien

4.3 Author: NOAA/Space Weather Prediction Center
Source: http://www.swpc.noaa.gov/SolarCycle/
Copyright: NOAA is a governmental organization

Figures 4.4 to 4.14 Author: Manuel Julien

5.1 Author: Google/CSBF
Source: http://towerfts.csbf.nasa.gov/Maps/ConvGps624N.htm
Copyright: CSBF is a governmental facility. For Google, this fall into fair use for a work of scholarship, see:
http://www.google.com/permissions/geoguidelines.html

5.2 Author: Manuel Julien and our Research Group
Source : Our research group material
Copyright : Our research group

Figures 5.3 to 5.27 Author: Manuel Julien

5.28 See Fig. 2.16 credit, and Manuel Julien

5.29 Author: James Ryan
Source : [83]
Copyright : [83] is James Ph. D. Thesis, James is my advisor, he is aware of my usage of the picture and consent to it.

6.1 Author: Manuel Julien

6.2 Author: Manuel Julien

6.3 Credit: Hamamatsu
Modifications: Manuel Julien; I did very minor modifications
Source: [70]
Copyright: Fair Use, see copyright of fig. 1.2

6.4 Author: Manuel Julien

6.5 Credit: NCT Collaboration
Source: Web material
Copyright: Fair Use, see copyright of fig. 1.2